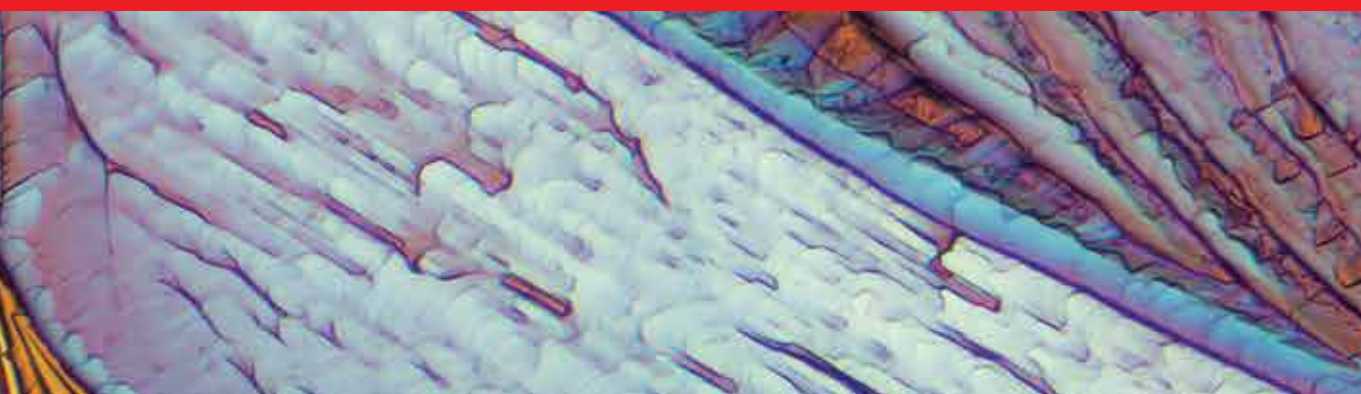


IntechOpen

Microscopy and Analysis

Edited by Stefan G. Stanciu



MICROSCOPY AND ANALYSIS

Edited by **Stefan G. Stanciu**

Microscopy and Analysis

<http://dx.doi.org/10.5772/61531>

Edited by Stefan G. Stanciu

Contributors

Frank Winterroth, Katsutoshi Miura, Andrea Falqui, Alberto Casu, Cristiano Di Benedetto, Alessandro Genovese, Sergio Lentijo Mozo, Elisa Sogne, Efsio Zuddas, Francesca Pagliari, John Miller, Paola Pesantéz Cabrera, Marianne Sowa, Wei Song, Naoki Fukutake, Hisashi Miyafuji, Toru Kanbayashi, Juan M. Bueno, Francisco J. Avila, Pablo Artal, Kenji Mizoguchi, Hirokazu Sakamoto, Eiichi Mori, Hiroyuki Tahara, Toshio Naito, Taka-Aki Hiramatsu, Hideki Yamochi, Hideyuki Arimoto, Keiichiro Namai, Javier Adur, Hernandes Carvalho, Carlos Cesar, Víctor Hugo Casco, Reema Adel Khorshed, Cristina Lo Celso, Marco Wiltgen, Marcus Bloice, Leonid Bolotov, Toshihiko Kanayama, Gitanjal Deka, Fu-Jen Kao, Shi-Wei Chu, Fan Wu, Nan Yao, Alexander Chaika

© The Editor(s) and the Author(s) 2016

The moral rights of the and the author(s) have been asserted.

All rights to the book as a whole are reserved by INTECH. The book as a whole (compilation) cannot be reproduced, distributed or used for commercial or non-commercial purposes without INTECH's written permission.

Enquiries concerning the use of the book should be directed to INTECH rights and permissions department (permissions@intechopen.com).

Violations are liable to prosecution under the governing Copyright Law.



Individual chapters of this publication are distributed under the terms of the Creative Commons Attribution 3.0 Unported License which permits commercial use, distribution and reproduction of the individual chapters, provided the original author(s) and source publication are appropriately acknowledged. If so indicated, certain images may not be included under the Creative Commons license. In such cases users will need to obtain permission from the license holder to reproduce the material. More details and guidelines concerning content reuse and adaptation can be found at <http://www.intechopen.com/copyright-policy.html>.

Notice

Statements and opinions expressed in the chapters are those of the individual contributors and not necessarily those of the editors or publisher. No responsibility is accepted for the accuracy of information contained in the published chapters. The publisher assumes no responsibility for any damage or injury to persons or property arising out of the use of any materials, instructions, methods or ideas contained in the book.

First published in Croatia, 2016 by INTECH d.o.o.

eBook (PDF) Published by IN TECH d.o.o.

Place and year of publication of eBook (PDF): Rijeka, 2019.

IntechOpen is the global imprint of IN TECH d.o.o.

Printed in Croatia

Legal deposit, Croatia: National and University Library in Zagreb

Additional hard and PDF copies can be obtained from orders@intechopen.com

Microscopy and Analysis

Edited by Stefan G. Stanciu

p. cm.

Print ISBN 978-953-51-2578-5

Online ISBN 978-953-51-2579-2

eBook (PDF) ISBN 978-953-51-5076-3

We are IntechOpen, the world's leading publisher of Open Access books Built by scientists, for scientists

3,800+

Open access books available

116,000+

International authors and editors

120M+

Downloads

151

Countries delivered to

Our authors are among the
Top 1%

most cited scientists

12.2%

Contributors from top 500 universities



WEB OF SCIENCE™

Selection of our books indexed in the Book Citation Index
in Web of Science™ Core Collection (BKCI)

Interested in publishing with us?
Contact book.department@intechopen.com

Numbers displayed above are based on latest data collected.
For more information visit www.intechopen.com



Meet the editor



Dr. Stefan G. Stanciu received a PhD degree in Electronics and Telecommunications from the University Politehnica of Bucharest (UPB) in 2011. Currently, he is conducting his research activities as Scientific Researcher at the Center for Microscopy-Microanalysis and Information Processing of UPB. His main research interests revolve around scanning laser and scanning probe microscopies and connected image processing and computer vision topics. Stefan's current research agenda focuses not only on optical characterization of cells, tissues and biomaterials using combined biophotonics approaches but also on the design and development of novel image classification frameworks for automated disease diagnostics.

Contents

Preface XI

Section 1 Optical Microscopy 1

Chapter 1 **Quantum Image-Forming Theory for Calculation of Resolution Limit in Laser Microscopy 3**

Naoki Fukutake

Chapter 2 **Kinetic Model of Development and Aging of Artificial Skin Based on Analysis of Microscopy Data 31**

Paola Pesantez-Cabrera, Marianne B. Sowa and John H. Miller

Chapter 3 **Automatic Interpretation of Melanocytic Images in Confocal Laser Scanning Microscopy 51**

Marco Wiltgen and Marcus Bloice

Chapter 4 **Super-Resolution Confocal Microscopy Through Pixel Reassignment 81**

Longchao Chen, Yuling Wang and Wei Song

Chapter 5 **Second Harmonic Generation Microscopy: A Tool for Quantitative Analysis of Tissues 99**

Juan M. Bueno, Francisco J. Ávila, and Pablo Artal

Chapter 6 **Nonlinear Microscopy Techniques: Principles and Biomedical Applications 121**

Javier Adur, Hernandes F. Carvalho, Carlos L. Cesar and Víctor H. Casco

Chapter 7 **Skin Wound Healing Revealed by Multimodal Optical Microscopies 151**

Gitanjal Deka, Shi-Wei Chu and Fu-Jen Kao

- Chapter 8 **Automated Identification and Measurement of Haematopoietic Stem Cells in 3D Intravital Microscopy Data 181**
Reema Adel Khorshed and Cristina Lo Celso
- Chapter 9 **Microscopic Investigations on Woody Biomass as Treated with Ionic Liquids 203**
Toru Kanbayashi and Hisashi Miyafuji
- Section 2 Non-Optical Microscopy 221**
- Chapter 10 **The New Youth of the In Situ Transmission Electron Microscopy 223**
Alberto Casu, Elisa Sogne, Alessandro Genovese, Cristiano Di Benedetto, Sergio Lentijo Mozo, Efisio Zuddas, Francesca Pagliari and Andrea Falqui
- Chapter 11 **In Situ Transmission Electron Microscopy Studies in Gas/Liquid Environment 267**
Fan Wu and Nan Yao
- Chapter 12 **Advanced Scanning Tunneling Microscopy for Nanoscale Analysis of Semiconductor Devices 299**
Leonid Bolotov and Toshihiko Kanayama
- Chapter 13 **Electron Orbital Contribution in Distance-Dependent STM Experiments 329**
Alexander N. Chaika
- Chapter 14 **Wavefunction Analysis of STM Image: Surface Reconstruction of Organic Charge Transfer Salts 355**
Hirokazu Sakamoto, Eiichi Mori, Hideyuki Arimoto, Keiichiro Namai, Hiroyuki Tahara, Toshio Naito, Taka-aki Hiramatsu, Hideki Yamochi and Kenji Mizoguchi
- Chapter 15 **Application of Scanning Acoustic Microscopy to Pathological Diagnosis 381**
Katsutoshi Miura
- Chapter 16 **Applying High-Frequency Ultrasound to Examine Structures and Physical Properties of Cells and Tissues 405**
Frank Winterroth

Preface

The word “microscopy” has its origins in the Greek language where the term “mikro” means “small” or “little”, while “skopein” means “to look at”, so literally “microscope” means *an instrument for looking at small things*. So why the interest in such instruments? That’s because *humans* have a deeply *curious* nature, and an infinity of questions that cross their minds cannot be answered without looking at small objects and scenes that are impossible to be seen with the naked eye. Although the underlying mechanisms of curiosity are not yet well understood, no one can argue that curiosity is equivalent to the desire to learn and to gain knowledge. This desire made Zacharias Jansen and his father, Hans, two Dutch spectacle makers, to be thrilled to see in the 1590s that by placing several lenses in a tube, an enlarged view of an object near its end could be observed, much larger than it was possible with any simple magnifying glass. Not much later, in the seventeenth century, the Englishman Robert Hooke was constructing the first microscope and using it to see and describe biological organisms. His book *Micrographia*, published in 1665, was the first illustrated volume on microscopy containing detailed accounts of 60 “observations” of objects examined microscopically. *Micrographia’s* illustrations of a world were not accessible to the human eyes before created sensation, taking its readers by storm. For example, Samuel Pepys, a Fellow of the Royal Society, was writing in his diary: “Before I went to bed, I sat up till 2’o clock in my chamber, reading of Mr. Hookes Microscopical Observations, the most ingenious book that I ever read in my life.” It is in *Micrographia* where the term “cell” was first introduced, a term that is currently used to describe the basic structural and functional biological unit of living organisms, the smallest unit of life that can replicate independently. Looking at thin cork slices, Hooke remarked structures resembling to pores, which to him looked similar to the small room in which a monk inhabited, the cellula, thus deriving the name: “. . . I could exceedingly plainly perceive it to be all perforated and porous, much like a Honey-comb, but that the pores of it were not regular. . . . these pores, or cells, . . . were indeed the first microscopical pores I ever saw, and perhaps, that were ever seen, for I had not met with any Writer or Person, that had made any mention of them before this. . . .” These structures that puzzled Hooke were the dead cells of cork; although Hooke himself was going to observe as well living cells later, it was someone else who was to witness for the first time a live cell under a microscope, Antonie van Leeuwenhoek. The Royal Society in London was releasing a first letter from this self-educated Dutch scientific explorer 8 years later after *Micrographia* had been published. This letter, entitled “A specimen of some Observations made by a Microscope”, contrived by M. Leewenhoek in Holland, lately communicated by Dr. Regnerus de Graaf”, presented microscopic observations on mold, bees, and lice. Further letters followed in which he provided his findings on different subjects using microscopes developed by him, the details of most of which he refused to reveal, preferring instead to provide his interpretations of the imaged scenes. Many of his letters dealt

with the description of specific forms of microorganisms, which he referred to as “animalcules.” These included protozoa and other unicellular organisms, like bacteria. Some of Leeuwenhoek’s initial findings were met with both skepticism and open ridicule, but this was until Hooke was to return to his microscopes, which he had given up because of eye strain, and verify Leeuwenhoek’s observations and confirm his findings. Leeuwenhoek was also the first to find and describe in his letters the sperm cells of animals and humans and to see that the fertilization process requires the sperm cell to enter the egg cell, which put an end to previous theories of spontaneous generation that revolved around the idea that certain forms of life such as fleas could arise from inanimate matter. Antonie van Leeuwenhoek was elected to the Royal Society in February 1680, and although he considered this to be a high honor, he did not attend the induction ceremony in London and never attended the meetings of the Royal Society. By the time of his death in 1723, Leeuwenhoek had written more than 550 letters to different scientific institutions, of which around 200 letters had been published by the Royal Society. Ever since those times, microscopes represent tools of the utmost importance for a wide range of disciplines. Without them, it would have been impossible to stand where we stand today in terms of understanding the structure and functions of organelles and cells, tissue composition and metabolism, or the causes behind various pathologies and their progression. Our knowledge on basic and advanced materials is also intimately intertwined to the realm of microscopy, and progress in key fields of micro- and nanotechnologies critically depends on high-resolution imaging systems. While Hooke and Leeuwenhoek were placing efforts on looking at small things with microscopes that relied on optical magnification, at this time a wide variety of imaging systems are available, relying on various contrast mechanisms. Light and optical magnification remain fundamental for the microscopy realm, but “looking” at small things is now possible also by using nanostructured probes that are scanned across a sample’s surface to assess its topography or sense various other properties, by using beams of accelerated electrons to interact with a sample of interest and provide information on its structure, by exploiting sound interaction with matter, and by many other approaches. This volume includes 16 chapters that address highly significant scientific subjects from diverse areas of microscopy and analysis. Nine of these chapters deal with optical microscopy topics, while the remaining seven refer to nonoptical microscopy subjects. The authors present in this volume their work or review recent trends, concepts, and applications, in a manner that is accessible to quite a broad readership audience from both within and outside their specialist area. I am confident that this volume will be of great value not only to those actively involved in the addressed fields but also to those with passive but constant interest in these scientific areas and to those who will have their first encounter with microscopy and analysis when reading the contained chapters. In the end, I would like to express my deepest thanks to each of the authors for his or her fine contributions to this project.

Stefan G. Stanciu, PhD

Center for Microscopy-Microanalysis and Information Processing
University Politehnica of Bucharest
Romania

Optical Microscopy

Quantum Image-Forming Theory for Calculation of Resolution Limit in Laser Microscopy

Naoki Fukutake

Additional information is available at the end of the chapter

<http://dx.doi.org/10.5772/63494>

Abstract

Here we show what determines the optical resolution in laser microscopy. We define the expanded resolution limit (spatial frequency cutoff) that includes the classic Abbe definition as $2 NA/\lambda$, where λ is the wavelength. The resolution limit can approximately be redefined as the frequency cutoff $\alpha NA/\lambda$, where α is the constant that depends on the optical process occurring in the sample. In the case of the optical process originating from the linear susceptibility $\chi^{(1)}$, the resolution limit is well known as the Abbe definition, namely, $\alpha = 2$. However, when other optical processes are harnessed to form the image through laser microscopy, the resolution limit can differ. We formulate a theoretical framework that can calculate the expanded resolution limits of all kinds of laser microscopy utilizing coherent, incoherent, linear, and nonlinear optical processes.

Keywords: image-forming theory, nonlinear optical microscopy, optical transfer function, optical resolution limit, light-matter interaction

1. Introduction

The resolution limit (spatial frequency cutoff) of optical microscopy is usually described as $2 NA/\lambda$, where λ is the wavelength [1]. For example, bright field microscopy indicates the resolution limit of $2 NA/\lambda$ at a maximum. However, this resolution limit is restricted to optical microscopy that utilizes the optical process derived from the linear susceptibility $\chi^{(1)}$, such as bright field microscopy. Since fluorescence is a $\chi^{(3)}$ -derived optical process, the resolution limit of optical microscopy with fluorescence can differ from that of bright field microscopy. Although conventional fluorescence microscopy exhibits the resolution limit of $2 NA/\lambda$, microscopy that achieves the full potential of fluorescence, such as structured illumination

microscopy (SIM), can reach $4 NA/\lambda$ [2]. In general, the resolution limit in optical microscopy becomes different according to the kind of optical process.

Laser microscopy is composed of an excitation optical system and a signal-collection optical system, and the signals are acquired point by point to reconstruct an image. One of the typical examples of laser microscopy is confocal fluorescence microscopy, which has been widely used as an optical imaging technique. Confocal fluorescence microscopy can acquire high-resolution optical images with depth sectioning by means of focused laser excitation and a pinhole in front of a detector, which eliminates out-of-focus signals. Confocal fluorescence microscopy harnesses fluorescence as an optical process to increase the optical resolution, compared with microscopy with a $\chi^{(1)}$ -derived optical process. Confocal microscopy that utilizes a $\chi^{(1)}$ -derived optical process has a resolution limit (frequency cutoff) of $NA_{ex}/\lambda_{ex} + NA_{col}/\lambda_{ex}$, where λ_{ex} is the wavelength of the excitation beam, NA_{ex} is the numerical aperture of the objective in the excitation system, and NA_{col} is the numerical aperture of the objective in the signal-collection system [3, 4], while confocal fluorescence microscopy theoretically indicates the resolution limit of $2NA_{ex}/\lambda_{ex} + 2 NA_{col}/\lambda_{fl}$, where λ_{fl} is the wavelength of the fluorescence. Note that in conventional (wide field) fluorescence microscopy, since the entire specimen is excited evenly, which corresponds to the condition $NA_{ex} = 0$, the resolution limit becomes $2 NA_{col}/\lambda_{fl}$.

In addition to confocal fluorescence microscopy, various laser microscopy techniques have recently been used to visualize biological specimens in three dimensions by harnessing many kinds of optical processes, such as two-photon excited fluorescence (TPEF), second-order harmonic generation (SHG), third-order harmonic generation (THG), coherent anti-Stokes Raman scattering (CARS), and stimulated Raman scattering (SRS) [5–11]. Depending on the optical process, each microscopy exhibits its own feature of image formation. In incoherent optical processes, such as fluorescence and TPEF, since the vacuum field is involved in the phenomena along with the excitation beam, the signals emitted from different molecules in the specimen do not interfere. In contrast, in coherent optical processes, such as $\chi^{(1)}$ -derived phenomenon, SHG, THG, CARS, and SRS, because the processes are caused only by coherent excitation laser beams, the signals emitted from different molecules interfere. Although the coherence of the optical process influences the image-forming properties of laser microscopy, the basic concept is that the image of the linear or nonlinear susceptibility distribution $\chi^{(i)}(x, y, z)$ in the specimen is formed by microscopy regardless of coherence. From a perspective other than coherence, laser microscopy can be categorized into two types. In the first type, as the wavelength of the signal is different from that of the excitation beam, the signal can be separated from the excitation beam, resulting in the image being formed only by the signal. In the second type, since the signal has the same wavelength as the excitation beam, interference between the signal and the excitation beam is observed. It will be shown that the image-forming properties and resolution limits of both types can be dealt with in the identical framework.

Although the image-forming properties of each microscopy technique are well known, the unified theory does not exist that can deal with the image-forming properties and the resolution limits of all kinds of laser microscopy in the identical framework. If the unified image-forming theory is developed, it enables one to overview all microscopy techniques with any

optical processes, such as linear, nonlinear, coherent, and incoherent processes, which can lead to the invention of a new microscopy technique. In this chapter, we formulate a unified framework that utilizes double-sided Feynman diagrams to discuss all microscopy applications by use of a unique technique. With our framework, the resolution limits of laser microscopy techniques will be able to be redefined with respect to each optical process. Moreover, we will lead to some important conclusions about laser microscopy. Although only laser microscopy is discussed here, our theory can be applied to any type of optical microscopy.

2. Theoretical framework

2.1. Model description

We begin by defining the imaging system (laser microscopy) in our model. Laser microscopy is composed of an excitation system to focus the laser beam onto a sample and a signal-collection system to gather the signal generated from the sample. A schematic of laser microscopy is shown in **Figure 1**, in which the coordinate systems are given. We assume in what follows that three-dimensional (3-D) sample-stage scanning is conducted instead of laser scanning, but it does not influence the optical resolution. In laser microscopy, usually one or two excitation beams are employed to generate the signal. The electric field of the signal is emitted from the molecule excited by the electric fields of excitation beams, and the signal field propagates through the signal-collection system. The signals are acquired point by point with a photodetector to reconstruct the 3-D image.

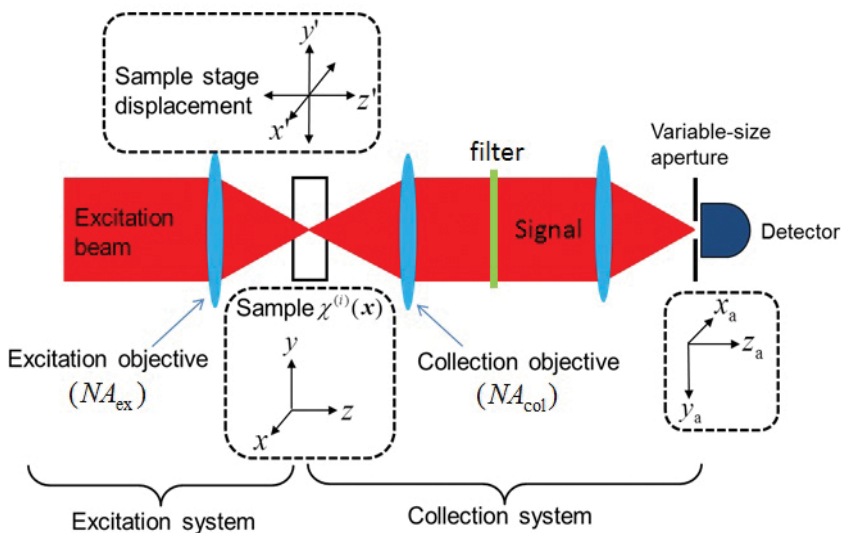


Figure 1. Schematic of laser microscopy (transmission type).

For simplicity, the first Born approximation is applied to understand the true nature of the optical resolution. In this approximation, the multiple scattering and depletion of the beam are neglected, which usually holds true for nearly transparent samples, such as a biological specimen. If the multiple scattering and depletion were intense, the image acquired would become deformed to some degree. We assume that both the excitation and signal-collection systems are $1\times$ magnification systems with no aberration, which does not change the essence of their image-forming properties. In our model, the scalar diffraction theory is employed. The linear or nonlinear susceptibility distribution $\chi^{(i)}(x, y, z)$ in the sample plays a role as the object in the imaging system. The polarization $P(x, y, z)$ is induced by the excitation electric field, and the induced polarization emits the signal electric field. Hereafter, we express the electric field as a complex function.

2.2. Transmission linear confocal microscopy

We start with transmission linear confocal microscopy, in which a $\chi^{(1)}$ -derived optical process occurs in the sample. **Figure 2** shows the double-sided Feynman diagram and the energy-level diagram describing the $\chi^{(1)}$ -derived optical process. The polarization is induced by the excitation beam focused onto the sample, and the signal emitted by the polarization is gathered and delivered into the photodetector through the signal-collection system. We express the electric field distribution in the sample formed by the focused excitation beam as $E_{\text{ex}}(x, y, z)$. The Fourier transform of $E_{\text{ex}}(x, y, z)$ is shaped like a portion of a spherical shell, as shown in **Figure 3**, which represents the distribution of the wavenumber vector. When the sample-stage displacement (x', y', z') is zero, the polarization distribution becomes

$$P(x, y, z) = \chi^{(1)}(x, y, z)E_{\text{ex}}(x, y, z), \quad (1)$$

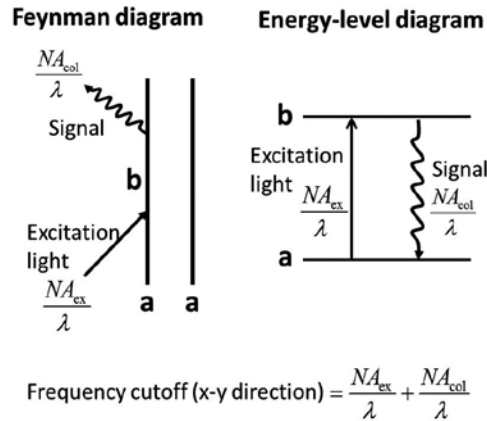


Figure 2. Double-sided Feynman diagram and energy-level diagram for the $\chi^{(1)}$ -derived optical process. λ is the wavelength. The frequency cutoff (x-y direction) can be calculated by using the diagrams, which will be discussed in more detail in a later section.

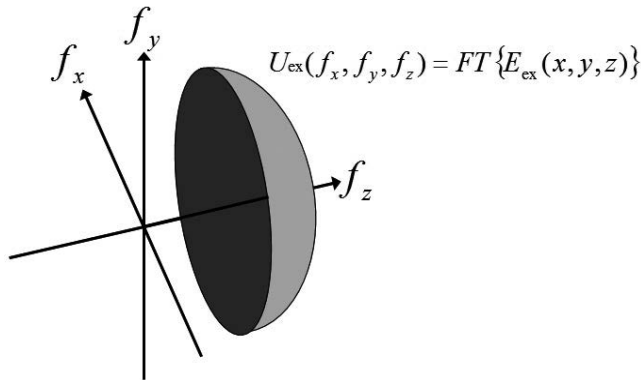


Figure 3. Distribution of the wavenumber vector for the beam focused by the objective. This is referred to as the “3-D pupil function”.

where $\chi^{(1)}(x, y, z)$ is the linear susceptibility distribution in the sample and we presume that the electric permittivity ϵ_0 of free space is unity: $\epsilon_0 = 1$. We assume that the signal emitted from a single point in the sample located at the origin $((x, y, z) = (0, 0, 0))$ of the object coordinate forms the electric field distribution $E_{col}(x_a, y_a, z_a)$ in the detection space through the signal-collection system. The Fourier transform of $E_{col}(x_a, y_a, z_a)$ is also shaped like a portion of a spherical shell located on the $+k_z$ side. Using $E_{col}(x_a, y_a, z_a)$ and $P(x, y, z)$, the electric field distribution $E_T(x_a, y_a, z_a)$ in the detection space in the case of arbitrary $\chi^{(1)}(x, y, z)$ is given by

$$E_T(x_a, y_a, z_a) = \iiint P(x, y, z) E_{col}(x_a - x, y_a - y, z_a - z) dx dy dz, \quad (2)$$

when $(x', y', z') = (0, 0, 0)$. Taking into account the sample-stage displacement (x', y', z') , we recast Eq. (2) as

$$E_T(x', y', z'; x_a, y_a, z_a) = \iiint \chi^{(1)}(x + x', y + y', z + z') E_{ex}(x, y, z) E_{col}(x_a - x, y_a - y, z_a - z) dx dy dz. \quad (3)$$

In addition to the signal, we need to consider the electric field distribution formed in the detection space by the excitation beam itself through the excitation system and signal-collection system, which functions as the local oscillator.

For simplicity, we consider the case of the condition $NA_{ex} = NA_{col}$. The image intensity $I(x', y', z')$ acquired by our imaging system can be written as

$$I(x', y', z') = \iiint | \{-iE_{ex}(x_a, y_a, z_a) + E_T(x', y', z'; x_a, y_a, z_a)\} |^2 a(x_a, y_a) \delta(z_a) dx_a dy_a dz_a, \quad (4)$$

where $a(x_{ar}, y_a)$ is the two-dimensional function representing the detector size, $\delta(z_a)$ stands for the Dirac delta function, the excitation beam $E_{\text{ex}}(x_{ar}, y_{ar}, z_a)$ acts as the local oscillator, and $-i$ before $E_{\text{ex}}(x_{ar}, y_{ar}, z_a)$ stems from the Gouy phase shift. To obtain the image intensity $I_c^t(x', y', z')$ for confocal microscopy, we can substitute $\delta(x_a)\delta(y_a)$ into $a(x_{ar}, y_a)$ in Eq. (4). From Eqs. (3) and (4), we obtain

$$\begin{aligned}
& I_c^t(x', y', z') \\
&= \left| -iE_{\text{ex}}(0, 0, 0) + \iiint \chi^{(1)}(x+x', y+y', z+z') E_{\text{ex}}(x, y, z) E_{\text{col}}(-x, -y, -z) dx dy dz \right|^2 \\
&\approx |E_{\text{ex}}(0, 0, 0)|^2 \\
&\quad + i \{E_{\text{ex}}(0, 0, 0)\}^* \iiint \chi^{(1)}(x+x', y+y', z+z') E_{\text{ex}}(x, y, z) E_{\text{col}}(-x, -y, -z) dx dy dz \\
&\quad - iE_{\text{ex}}(0, 0, 0) \iiint \{ \chi^{(1)}(x+x', y+y', z+z') \}^* \{E_{\text{ex}}(x, y, z)\}^* \{E_{\text{col}}(-x, -y, -z)\}^* dx dy dz.
\end{aligned} \tag{5}$$

Although $E_{\text{ex}}(x, y, z)$ and $E_{\text{col}}(x, y, z)$ are complex functions, $E_{\text{ex}}(x, y, z) E_{\text{col}}(-x, -y, -z) \equiv \text{ASF}_t(x, y, z)$ approaches a real function under the condition $\text{NA}_{\text{ex}} = \text{NA}_{\text{col}}$. Regarding $\text{ASF}_t(x, y, z)$ as the real function, Eq. (5) reduces to

$$I_c^t(x', y', z') \approx |E_{\text{ex}}(0, 0, 0)|^2 - 2E_{\text{ex}}(0, 0, 0) \iiint \text{Im} \{ \chi^{(1)}(x+x', y+y', z+z') \} \text{ASF}_t(x, y, z) dx dy dz. \tag{6}$$

This equation shows that only absorbing objects can be observed and phase objects cannot be visualized. The first term in Eq. (6) leads to low-contrast images. The function $\text{ASF}_t(x, y, z)$ is referred to as the amplitude spread function (ASF), and the coherent transfer function (CTF) is calculated by Fourier transforming the ASF.

2.3. Reflection linear confocal microscopy

Next, we deal with reflection linear confocal microscopy (see **Figure 4**), in which a $\chi^{(1)}$ -derived optical process is harnessed. The excitation beam focused onto the sample by the excitation objective induces the polarization, and the signal generated from the polarization is gathered and delivered into a photodetector with the same objective. The excitation and signal-collection systems share a common objective. Unlike in transmission linear confocal microscopy, the excitation beam does not interfere with the signal. For reflection microscopy, the electric field distribution of the signal emitted from a single-point object in the sample $E_{\text{col}}(x_{ar}, y_{ar}, z_a)$ formed in the detection space through the signal-collection system is replaced by $E'_{\text{col}}(x_{ar}, y_{ar}, z_a)$, where the Fourier transform of $E'_{\text{col}}(x_{ar}, y_{ar}, z_a)$ is located on the $-k_z$ side (see **Figure 5**). With the arbitrary sample-stage displacement (x', y', z') , the electric field distribution $E_{\text{R}}(x', y', z'; x_{ar}, y_a, z_a)$ in the detection space is given by

$$E_R(x', y', z'; x_a, y_a, z_a) = \iiint \chi^{(1)}(x + x', y + y', z + z') E_{\text{ex}}(x, y, z) E'_{\text{col}}(x_a - x, y_a - y, z_a - z) dx dy dz. \quad (7)$$

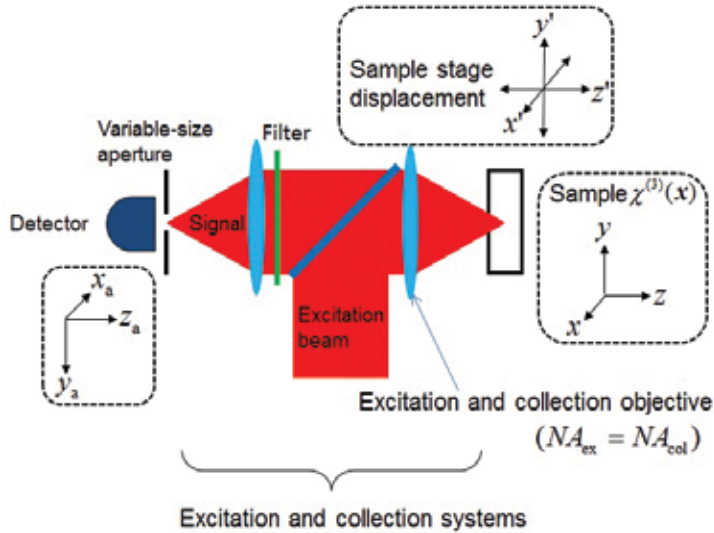


Figure 4. Schematic of reflection microscopy.

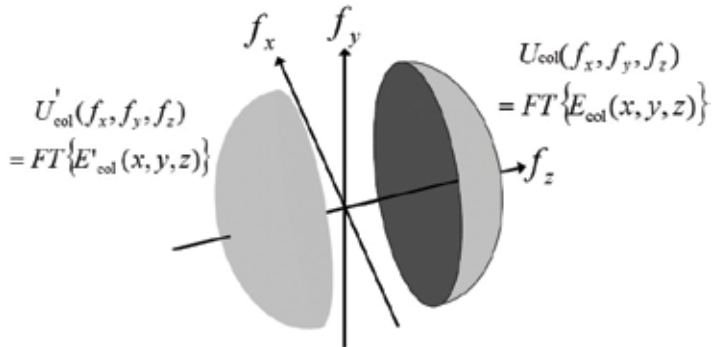


Figure 5. Distribution of the wavenumber vector (3-D pupil function) for the signal focused by the signal-collection objective.

As only the signal with no local oscillator forms the image, the image intensity $I_c^I(x', y', z')$ acquired by reflection linear confocal microscopy is written as

$$\begin{aligned} I_c^I(x', y', z') &= \iiint \left| \{ E_R(x', y', z'; x_a, y_a, z_a) \} \right|^2 \delta(x_a) \delta(y_a) \delta(z_a) dx_a dy_a dz_a \\ &= \left| \iiint \chi^{(1)}(x + x', y + y', z + z') E_{\text{ex}}(x, y, z) E'_{\text{col}}(-x, -y, -z) dx dy dz \right|^2. \end{aligned} \quad (8)$$

The function $E_{\text{ex}}(x, y, z)E'_{\text{col}}(-x, -y, -z) \equiv \text{ASF}_r(x, y, z)$ is defined as the ASF for reflection linear confocal microscopy. Since we have the relation $E_{\text{col}}(x, y, z) = E'_{\text{col}}(-x, -y, -z)$, the ASF in reflection linear confocal microscopy $\text{ASF}_r(x, y, z)$ becomes equal to $E_{\text{ex}}(x, y, z)E_{\text{col}}(x, y, z)$. While the ASF in transmission linear confocal microscopy $\text{ASF}_t(x, y, z)$ approaches a real function, that in reflection linear confocal microscopy $\text{ASF}_r(x, y, z)$ is inevitably a complex function. In reflection linear confocal microscopy, the mixture image of the real and imaginary parts of the linear susceptibility is visualized.

2.4. Coherent nonlinear microscopy

We expand the image-forming formulas for $\chi^{(1)}$ -derived optical processes to the general formulas for $\chi^{(3)}$ -derived optical processes. In this subsection, we deal with coherent microscopy, which utilizes coherent optical processes. As an example, we first consider coherent anti-Stokes Raman scattering (CARS) microscopy, in which the two excitation beams (pump and Stokes) are used to generate the CARS signal (see **Figure 6**). In CARS microscopy, the pump and Stokes beams are temporally and spatially overlapped to generate the CARS signal such that the frequency difference between the pump and Stokes is tuned to match a particular Raman-active vibration frequency. The resonant CARS emission is several orders of magnitude greater than that from spontaneous Raman scattering. CARS microscopy provides chemically selective image contrast based on the intrinsic vibrational modes of molecular species, avoiding the need for labels. In addition, CARS imaging systems also employ near-infrared lasers to maximize imaging depth and minimize photodamage to cells. When the sample-stage displacement is zero, $(x', y', z') = (0, 0, 0)$, the polarization distribution becomes

$$P_{\text{CARS}}(x, y, z) = \chi_{\text{CARS}}^{(3)}(x, y, z)E_{\text{p}}(x, y, z)\{E_{\text{s}}(x, y, z)\}^* E_{\text{p}}(x, y, z), \quad (9)$$

where $\chi_{\text{CARS}}^{(3)}(x, y, z)$ denotes the nonlinear susceptibility for CARS and $E_{\text{p}}(x, y, z)$ and $E_{\text{s}}(x, y, z)$ stand for the electric field distributions in the sample formed by the pump and Stokes beams focused through the excitation system, respectively. In the same manner as in the previous subsection, taking into account the sample-stage displacement (x', y', z') , in transmission microscopy, the electric field distribution $E_{\text{CARS}}(x', y', z'; x_{\text{a}}, y_{\text{a}}, z_{\text{a}})$ in the detection space can be written as

$$E_{\text{CARS}}(x', y', z'; x_{\text{a}}, y_{\text{a}}, z_{\text{a}}) = \iiint \chi_{\text{CARS}}^{(3)}(x + x', y + y', z + z')E_{\text{p}}(x, y, z)\{E_{\text{s}}(x, y, z)\}^* E_{\text{p}}(x, y, z) \times E_{\text{col}}(x_{\text{a}} - x, y_{\text{a}} - y, z_{\text{a}} - z) dx dy dz, \quad (10)$$

where $E_{\text{col}}(x, y, z)$ is calculated by using the wavelength of the CARS signal. Note that for reflection microscopy, $E_{\text{col}}(x, y, z)$ is replaced by $E'_{\text{col}}(x, y, z)$. As the wavelength of the CARS signal is different from those of the pump and Stokes beams, only the CARS signal can be

detected by using a filter. The image intensity $I_{\text{CARS}}(x', y', z')$ acquired by CARS microscopy is given by

$$I_{\text{CARS}}(x', y', z') = \iiint |\{E_{\text{CARS}}(x', y', z'; x_a, y_a, z_a)\}|^2 a(x_a, y_a) \delta(z_a) dx_a dy_a dz_a. \quad (11)$$

Coherent anti-Stokes Raman scattering (CARS)

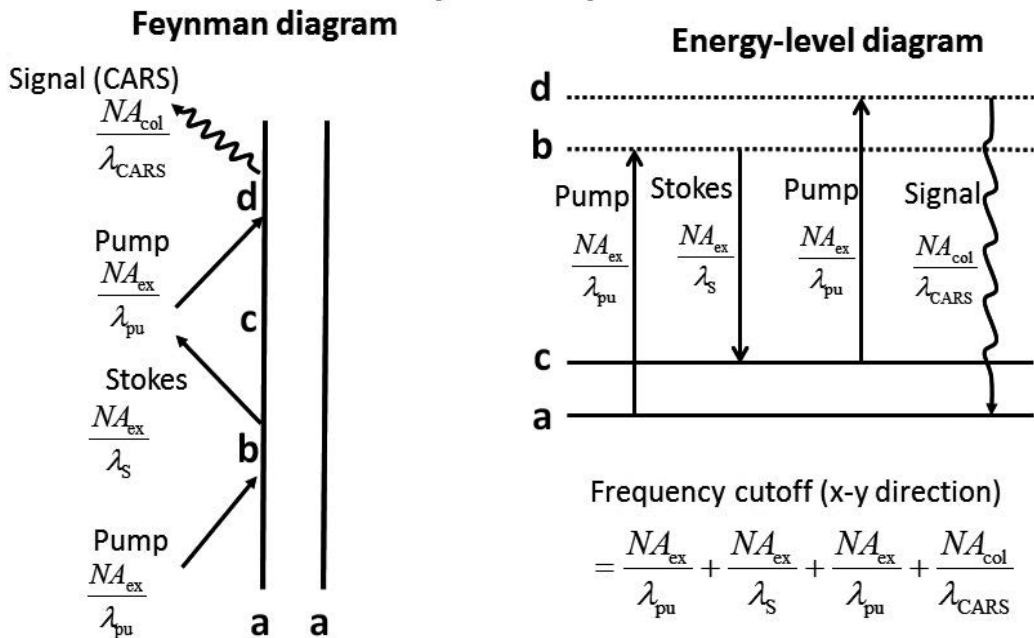


Figure 6. Double-sided Feynman diagram and energy-level diagram for CARS. λ_{pu} is the wavelength of the pump beam, λ_{S} is the wavelength of the Stokes beam, and λ_{CARS} is the wavelength of the CARS signal. The relation $2/\lambda_{\text{pu}} - 1/\lambda_{\text{S}} = 1/\lambda_{\text{CARS}}$ is satisfied.

In confocal CARS microscopy, the image intensity $I_{\text{CARS}}^{\text{c}}(x', y', z')$ reduces to

$$\begin{aligned} I_{\text{CARS}}^{\text{c}}(x', y', z') &= |\{E_{\text{CARS}}(x', y', z'; 0, 0, 0)\}|^2 \\ &= \left| \iiint \chi_{\text{CARS}}^{(3)}(x + x', y + y', z + z') E_{\text{p}}(x, y, z) \{E_{\text{S}}(x, y, z)\}^* E_{\text{p}}(x, y, z) E_{\text{col}}(-x, -y, -z) dx dy dz \right|^2 \quad (12) \\ &= \left| \iiint \chi_{\text{CARS}}^{(3)}(x + x', y + y', z + z') \text{ASF}_{\text{CARS}}(x, y, z) dx dy dz \right|^2. \end{aligned}$$

where $\text{ASF}_{\text{CARS}}(x, y, z) \equiv E_{\text{p}}(x, y, z) \{E_{\text{S}}(x, y, z)\}^* E_{\text{p}}(x, y, z) E_{\text{col}}(-x, -y, -z)$. The CTF of CARS microscopy is calculated by Fourier transforming $\text{ASF}_{\text{CARS}}(x, y, z)$. The maximum value of the

frequency cutoff, which means the grating with the largest grating vector that can be resolved, is determined by the CTF. It is proven that the frequency cutoff of nonconfocal CARS microscopy does not change compared with that of confocal CARS microscopy [4]. In general, in coherent microscopy, the theoretical resolution limits (frequency cutoffs) are identical between confocal and nonconfocal systems.

Stimulated Raman gain (SRG)

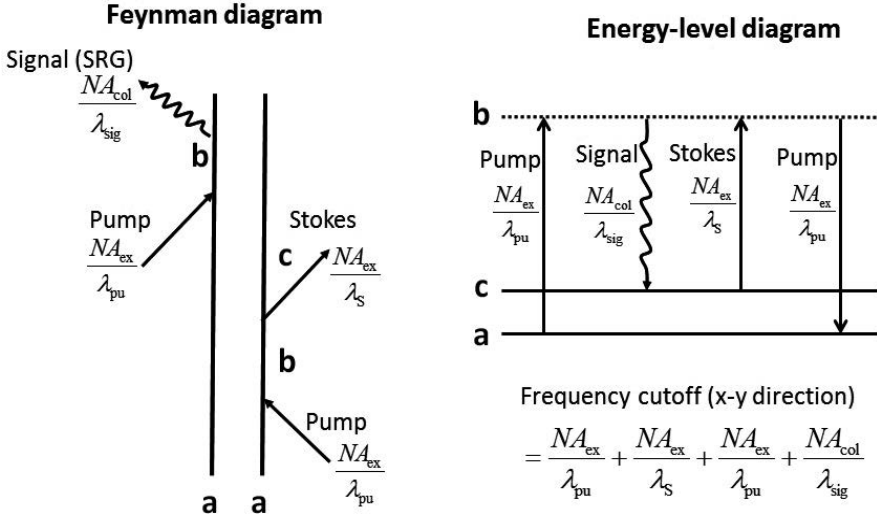


Figure 7. Double-sided Feynman diagram and energy-level diagram for SRG. λ_{sig} is the wavelength of the SRG signal. Note that $\lambda_{\text{S}} = \lambda_{\text{sig}}$.

As the next example, we consider stimulated Raman gain (SRG) microscopy, in which the pump and Stokes beams are employed as the excitation beams in common with CARS microscopy. As the wavelength of the SRG signal is identical with that of the Stokes beam (see **Figure 7**), the SRG signal interferes with the Stokes beam, which acts as the local oscillator in transmission microscopy. The pump beam is modulated and the SRG signal with the same wavelength as the Stokes beam can be extracted by demodulating the Stokes beam with the lock-in amplifier. In the signal-collection system, the pump beam is blocked by the filter. When $(x', y', z') = (0, 0, 0)$, the polarization distribution is given by

$$P_{\text{SRG}}(x, y, z) = \chi_{\text{SRG}}^{(3)}(x, y, z) \{E_p(x, y, z)\}^* E_S(x, y, z) E_p(x, y, z), \quad (13)$$

where $\chi_{\text{SRG}}^{(3)}(x, y, z)$ represents the nonlinear susceptibility for SRG. With the sample-stage displacement (x', y', z') , in transmission microscopy, the electric field distribution of the SRG signal $E_{\text{SRG}}(x', y', z'; x_a, y_a, z_a)$ in the detection space is written as

$$E_{\text{SRG}}(x', y', z'; x_a, y_a, z_a) = \iiint \chi_{\text{SRG}}^{(3)}(x+x', y+y', z+z') \{E_p(x, y, z)\}^* E_s(x, y, z) E_p(x, y, z) \times E_{\text{col}}(x_a - x, y_a - y, z_a - z) dx dy dz, \quad (14)$$

where $E_{\text{col}}(x, y, z)$ in this case must be calculated by using the wavelength of the SRG signal. With the filter that blocks the pump beam, the total intensity $I_{\text{SRG}}^{\dagger}(x', y', z')$ identified by the detector of transmission SRG microscopy is given by

$$I_{\text{SRG}}^{\dagger}(x', y', z') = \iiint | -iE_s(x_a, y_a, z_a) + E_{\text{SRG}}(x', y', z'; x_a, y_a, z_a) |^2 a(x_a, y_a) \delta(z_a) dx_a dy_a dz_a, \quad (15)$$

where the Stoke beam $-iE_s(x_a, y_a, z_a)$ with the Gouy phase shift ($-i$) functions as the local oscillator. In confocal transmission SRG microscopy, substituting $\delta(x_a) \delta(y_a)$ into $a(x_a, y_a)$, $I_{\text{SRG}}^{\dagger}(x', y', z')$ reduces to

$$\begin{aligned} & I_{\text{SRG}}^{\dagger}(x', y', z') \\ &= \left| -iE_s(0, 0, 0) + \iiint \chi_{\text{SRG}}^{(3)}(x+x', y+y', z+z') \right. \\ & \quad \left. \times \{E_p(x, y, z)\}^* E_s(x, y, z) E_p(x, y, z) E_{\text{col}}(-x, -y, -z) dx dy dz \right|^2 \\ &\approx |E_s(0, 0, 0)|^2 \\ & \quad + i \{E_s(0, 0, 0)\}^* \iiint \chi_{\text{SRG}}^{(3)}(x+x', y+y', z+z') |E_p(x, y, z)|^2 E_s(x, y, z) E_{\text{col}}(-x, -y, -z) dx dy dz \\ & \quad - iE_s(0, 0, 0) \iiint \{ \chi_{\text{SRG}}^{(3)}(x+x', y+y', z+z') \}^* |E_p(x, y, z)|^2 \{E_s(x, y, z)\}^* \\ & \quad \quad \times \{E_{\text{col}}(-x, -y, -z)\}^* dx dy dz \\ &= |E_s(0, 0, 0)|^2 - 2E_s(0, 0, 0) \iiint \text{Im} \{ \chi_{\text{SRG}}^{(3)}(x+x', y+y', z+z') \} \text{ASF}_{\text{SRG}}(x, y, z) dx dy dz, \end{aligned} \quad (16)$$

where we used the fact that $\text{ASF}_{\text{SRG}}(x, y, z) \equiv |E_p(x, y, z)|^2 E_s(x, y, z) E_{\text{col}}(-x, -y, -z)$ approaches a real function under the condition $\text{NA}_{\text{ex}} = \text{NA}_{\text{col}}$. Note that the sign of $\text{Im} \{ \chi_{\text{SRG}}^{(3)} \}$ is negative in SRG. The first term in Eq. (16) can be eliminated with lock-in detection. The CTF is calculated by Fourier transforming $\text{ASF}_{\text{SRG}}(x, y, z)$.

We also consider “nonconfocal” transmission SRG microscopy, which is normally used to achieve a high signal intensity. Although the detector is normally placed at the plane conjugate to the pupil of the collection objective in nonconfocal microscopy, we deal with microscopy in which the detector is placed at the image plane conjugate to the sample plane to discuss confocal microscopy and nonconfocal microscopy in the same theoretical framework. Note that in nonconfocal microscopy, the image does not change regardless of detector position. Therefore, to simplify the equation, we calculate the intensity value at a certain sample-stage displacement (x', y', z') by three-dimensionally integrating the signal intensity in the detection

space. The image intensity is proportional to the above-mentioned calculation result. The image intensity $I_{\text{SRG}}^{\text{nct}}(x', y', z')$ acquired by the detector of nonconfocal transmission SRG microscopy is given by

$$\begin{aligned}
& I_{\text{SRG}}^{\text{nct}}(x', y', z') \\
& \propto \iiint \left| \{-iE_S(x_a, y_a, z_a) + E_{\text{SRG}}(x', y', z'; x_a, y_a, z_a)\} \right|^2 dx_a dy_a dz_a \\
& = \iiint \left[|E_S(x_a, y_a, z_a)|^2 + i \{E_S(x_a, y_a, z_a)\}^* \right. \\
& \quad \times \iiint \chi_{\text{SRG}}^{(3)}(x+x', y+y', z+z') |E_p(x, y, z)|^2 E_S(x, y, z) E_{\text{col}}(x_a-x, y_a-y, z_a-z) dx dy dz \\
& \quad - i E_S(x_a, y_a, z_a) \iiint \chi_{\text{SRG}}^{(3)}(x+x', y+y', z+z') |E_p(x, y, z)|^2 \{E_S(x, y, z)\}^* \\
& \quad \times \left. \{E_{\text{col}}(x_a-x, y_a-y, z_a-z)\}^* dx dy dz \right] dx_a dy_a dz_a \\
& = \iiint |E_S(x_a, y_a, z_a)|^2 dx_a dy_a dz_a \\
& \quad + i \iiint \chi_{\text{SRG}}^{(3)}(x+x', y+y', z+z') |E_p(x, y, z)|^2 |E_S(x, y, z)|^2 dx dy dz \\
& \quad - i \iiint \{ \chi_{\text{SRG}}^{(3)}(x+x', y+y', z+z') \}^* |E_p(x, y, z)|^2 |E_S(x, y, z)|^2 dx dy dz \\
& = \iiint |E_S(x_a, y_a, z_a)|^2 dx_a dy_a dz_a \\
& \quad - 2 \iiint \text{Im} \{ \chi_{\text{SRG}}^{(3)}(x+x', y+y', z+z') \}^* |E_p(x, y, z)|^2 |E_S(x, y, z)|^2 dx dy dz.
\end{aligned} \tag{17}$$

Stimulated emission (SE)

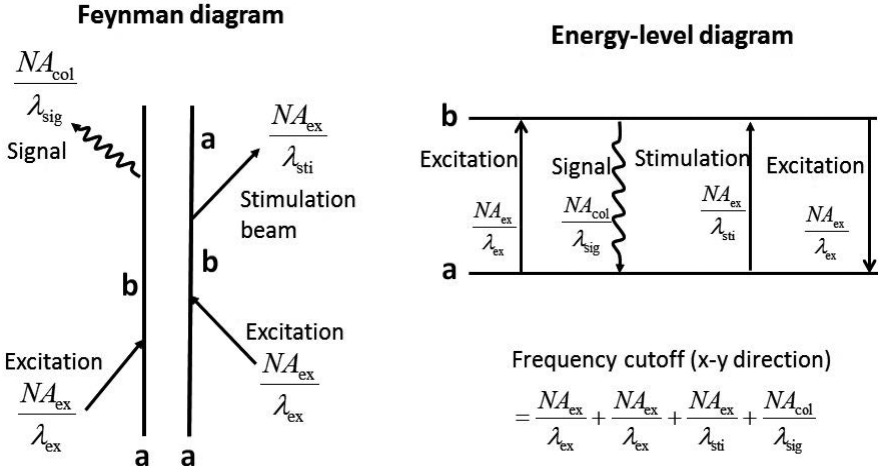


Figure 8. Double-sided Feynman diagram and energy-level diagram for stimulated emission. λ_{ex} is the wavelength of the excitation beam, λ_{sti} is the wavelength of the stimulation beam, and λ_{sig} is the wavelength of the SE signal. A two-level system is assumed.

Here we used the relations $E_{\text{col}}(-x, -y, -z) = \{E_{\text{col}}(x, y, z)\}^*$ and $E_S(x_a, y_a, z_a) \otimes E_{\text{col}}(x_a, y_a, z_a) = E_S(x_a, y_a, z_a)$ under the condition $\text{NA}_{\text{ex}} = \text{NA}_{\text{col}}$, where \otimes represents the convolution. The first term in Eq. (17) can be eliminated with lock-in detection. The ASF for nonconfocal SRG microscopy is $|E_p(x, y, z)|^2 |E_S(x, y, z)|^2$, which is nearly equal to the ASF for confocal microscopy.

We then consider nonconfocal reflection SRG microscopy. Interestingly, in nonconfocal reflection SRG microscopy, the reflection light $E_R(x', y', z'; x_a, y_a, z_a)$ generated by the $\chi^{(1)}$ -derived optical process plays a role as the local oscillator. The image intensity $I_{\text{SRG}}^{\text{ncr}}(x', y', z')$ acquired by the detector of nonconfocal reflection SRG microscopy is given by

$$\begin{aligned}
 & I_{\text{SRG}}^{\text{ncr}}(x', y', z') \\
 & \propto \iiint \left| \{E_R(x', y', z'; x_a, y_a, z_a) + E_{\text{SRG}}(x', y', z'; x_a, y_a, z_a)\} \right|^2 dx_a dy_a dz_a \\
 & = \iiint \left| \iiint \chi^{(1)}(x+x', y+y', z+z') E_S(x, y, z) E'_{\text{col}}(x_a-x, y_a-y, z_a-z) dx dy dz \right. \\
 & \quad \left. + \iiint \chi_{\text{SRG}}^{(3)}(x+x', y+y', z+z') \{E_p(x, y, z)\}^* E_S(x, y, z) E_p(x, y, z) \right. \\
 & \quad \left. \times E'_{\text{col}}(x_a-x, y_a-y, z_a-z) dx dy dz \right|^2 dx_a dy_a dz_a.
 \end{aligned} \tag{18}$$

As the local oscillator in this case does not have a Gouy phase shift, the real part of $\chi_{\text{SRG}}^{(3)}(x, y, z)$ is mainly observed. To see this, we consider a single-point object: $\chi^{(1)}(x, y, z) = \delta(x, y, z)$ and $\chi_{\text{SRG}}^{(3)}(x, y, z) = \varepsilon_r \delta(x, y, z) + i\varepsilon_i \delta(x, y, z)$, where $\varepsilon_r, \varepsilon_i \ll 1$. Eq. (18) reduces to

$$\begin{aligned}
 & I_{\text{SRG}}^{\text{ncr}} \\
 & \propto \iiint \left| E_S(-x', -y', -z') E'_{\text{col}}(x_a+x', y_a+y', z_a+z') \right. \\
 & \quad \left. + \varepsilon_r |E_p(-x', -y', -z')|^2 E_S(-x', -y', -z') E'_{\text{col}}(x_a+x', y_a+y', z_a+z') \right. \\
 & \quad \left. + i\varepsilon_i |E_p(-x', -y', -z')|^2 E_S(-x', -y', -z') E'_{\text{col}}(x_a+x', y_a+y', z_a+z') \right|^2 dx_a dy_a dz_a \\
 & \approx |E_S(-x', -y', -z')|^2 \iiint |E'_{\text{col}}(x_a, y_a, z_a)|^2 dx_a dy_a dz_a \\
 & \quad + 2\varepsilon_r \iiint |E'_{\text{col}}(x_a, y_a, z_a)|^2 dx_a dy_a dz_a \text{Re} \left\{ |E_p(-x', -y', -z')|^2 |E_S(-x', -y', -z')|^2 \right\} \\
 & \quad - 2\varepsilon_i \iiint |E'_{\text{col}}(x_a, y_a, z_a)|^2 dx_a dy_a dz_a \text{Im} \left\{ |E_p(-x', -y', -z')|^2 |E_S(-x', -y', -z')|^2 \right\}.
 \end{aligned} \tag{19}$$

The third term in Eq. (19) becomes zero, and the first term can be eliminated with lock-in detection. Eventually, only the real part ε_r remains.

The last example for coherent nonlinear microscopy is stimulated emission (SE) microscopy, in which the pump beam (electric field distribution: $E_p(x, y, z)$) and the stimulation beam (electric field distribution: $E_{\text{sti}}(x, y, z)$) are employed to generate the signal (see **Figure 8**). In SE microscopy, the SE signal has the same wavelength as that of the stimulation beam, and the SE signal interferes with the stimulation beam, which functions as the local oscillator in transmission microscopy. The pump beam is modulated and the SE signal can be extracted by demodulating the stimulation beam interfering with the SE signal. In analogy with SRG microscopy, replacing $E_S(x_{a'}, y_{a'}, z_a)$ with $E_{\text{sti}}(x_{a'}, y_{a'}, z_a)$ and $E_{\text{SRG}}(x', y', z'; x_{a'}, y_{a'}, z_a)$ by $E_{\text{SE}}(x', y', z'; x_{a'}, y_{a'}, z_a) \equiv \iiint \chi_{\text{SE}}^{(3)}(x+x', y+y', z+z') |E_p(x, y, z)|^2 E_{\text{sti}}(x, y, z) E_{\text{col}}(x_a-x, y_a-y, z_a-z) dx dy dz$, the image intensity $I_{\text{SE}}^{\text{ncf}}(x', y', z')$ acquired by the detector in nonconfocal transmission SE microscopy is written as

$$\begin{aligned}
& I_{\text{SE}}^{\text{ncf}} \\
& \propto \iiint \left[\left\{ -iE_{\text{sti}}(x_a, y_a, z_a) + E_{\text{SE}}(x', y', z'; x_a, y_a, z_a) \right\}^2 dx_a dy_a dz_a \right. \\
& = \iiint \left[\left| E_{\text{sti}}(x_a, y_a, z_a) \right|^2 + i \left\{ E_{\text{sti}}(x_a, y_a, z_a) \right\}^* \right. \\
& \quad \times \iiint \chi_{\text{SE}}^{(3)}(x+x', y+y', z+z') |E_p(x, y, z)|^2 E_{\text{sti}}(x, y, z) E_{\text{col}}(x_a-x, y_a-y, z_a-z) dx dy dz \\
& \quad - iE_{\text{sti}}(x_a, y_a, z_a) \iiint \left\{ \chi_{\text{SE}}^{(3)}(x+x', y+y', z+z') \right\}^* |E_p(x, y, z)|^2 \left\{ E_{\text{sti}}(x, y, z) \right\}^* \\
& \quad \left. \times \left\{ E_{\text{col}}(x_a-x, y_a-y, z_a-z) \right\}^* dx dy dz \right] dx_a dy_a dz_a \quad (20) \\
& = \iiint \left| E_{\text{sti}}(x_a, y_a, z_a) \right|^2 dx_a dy_a dz_a \\
& \quad + i \iiint \chi_{\text{SE}}^{(3)}(x+x', y+y', z+z') |E_p(x, y, z)|^2 |E_{\text{sti}}(x, y, z)|^2 dx dy dz \\
& \quad - i \iiint \left\{ \chi_{\text{SE}}^{(3)}(x+x', y+y', z+z') \right\}^* |E_p(x, y, z)|^2 |E_{\text{sti}}(x, y, z)|^2 dx dy dz \\
& = \iiint \left| E_{\text{sti}}(x_a, y_a, z_a) \right|^2 dx_a dy_a dz_a \\
& \quad - 2 \iiint \text{Im} \left\{ \chi_{\text{SE}}^{(3)}(x+x', y+y', z+z') \right\} |E_p(x, y, z)|^2 |E_{\text{sti}}(x, y, z)|^2 dx dy dz,
\end{aligned}$$

where $\chi_{\text{SE}}^{(3)}(x, y, z)$ represents the nonlinear susceptibility for SE. In Eq. (20), we used the relations $E_{\text{col}}(-x, -y, -z) = \{E_{\text{col}}(x, y, z)\}^*$ and $E_{\text{sti}}(x_{a'}, y_{a'}, z_a) \otimes E_{\text{col}}(x_{a'}, y_{a'}, z_a) = E_{\text{sti}}(x_{a'}, y_{a'}, z_a)$ under the condition $\text{NA}_{\text{ex}} = \text{NA}_{\text{col}}$. The first term can be eliminated with lock-in detection. The ASF for nonconfocal SE microscopy is $|E_p(x, y, z)|^2 |E_{\text{sti}}(x, y, z)|^2$, which is nearly equal to the

ASF for confocal microscopy. Although this equation for SE microscopy is described by the same notation as SRG microscopy, the Feynman diagram differs.

2.5. Incoherent microscopy

To deal with incoherent optical processes, the vacuum field around the sample needs to be reckoned in our calculation. We assume that $|0\rangle_{(x,y,z)}$ denotes the amplitude of the quantum vacuum zero-point effect at the (x,y,z) position in the sample. For spontaneous Raman scattering, the Stokes beam $E_S(x_{a'}, y_{a'}, z_a)$ is replaced by the vacuum field $|0\rangle_{(x_a, y_a, z_a)}$:

$$\begin{aligned}
 I_{\text{Ra}}^t(x', y', z') &= \iiint \left| -i|0\rangle_{(x_a, y_a, z_a)} + E_{\text{SRG}}(x', y', z'; x_a, y_a, z_a) \right|^2 a(x_a, y_a) \delta(z_a) dx_a dy_a dz_a \\
 &= \iiint \left| -i|0\rangle_{(x_a, y_a, z_a)} + \iiint \chi_{\text{SRG}}^{(3)}(x+x', y+y', z+z') \{E_p(x, y, z)\}^* E_p(x, y, z) |0\rangle_{(x,y,z)} \right. \\
 &\quad \left. \times E_{\text{col}}(x_a-x, y_a-y, z_a-z) dx dy dz \right|^2 a(x_a, y_a) \delta(z_a) dx_a dy_a dz_a.
 \end{aligned} \tag{21}$$

We then consider the Fourier expansion of $|0\rangle_{(x,y,z)}$ into the plane wave basis $|0\rangle_{(k_x, k_y, k_z)}$:

$$|0\rangle_{(x,y,z)} = \frac{1}{(2\pi)^3} \iiint |0\rangle_{(k_x, k_y, k_z)} e^{-i(k_x x + k_y y + k_z z)} dk_x dk_y dk_z, \tag{22}$$

$$|0\rangle_{(x_a, y_a, z_a)} = \frac{1}{(2\pi)^3} \iiint C(k_x, k_y, k_z) |0\rangle_{(k_x, k_y, k_z)} e^{-i(k_x x_a + k_y y_a + k_z z_a)} dk_x dk_y dk_z, \tag{23}$$

where (k_x, k_y, k_z) is the wavenumber vector, $|0\rangle_{(k_x, k_y, k_z)}$ stands for the Fourier component of the vacuum field, and $C(k_x, k_y, k_z)$ is the cone-shaped function representing the wave vectors of the Fourier components of the vacuum field that can pass through the signal-collection objective with NA_{col} and reach the detector. In the case of the fixed angular frequency of the

pump, the nonlinear susceptibility of SRG is a function of the angular frequency of the Stokes beam: $\omega_S = c\sqrt{k_x^2 + k_y^2 + k_z^2}$, where c is the light speed in vacuum. Therefore, we can replace $\chi_{\text{SRG}}^{(3)}(x, y, z)$ in Eq. (21) with $\chi_{\text{SRG}}^{(3)}(x, y, z)L(k_x, k_y, k_z)$, where $L(k_x, k_y, k_z)$ is a spherically symmetrical function (typically a complex Lorentzian function of ω_S). We then obtain

$$I'_{\text{Ra}}(x', y', z') = \iiint |A_{\text{Ra}}(x', y', z'; x_a, y_a, z_a)|^2 a(x_a, y_a) \delta(z_a) dx_a dy_a dz_a, \quad (24)$$

with

$$\begin{aligned} & |A_{\text{Ra}}(x', y', z'; x_a, y_a, z_a)|^2 \\ &= \left| -i \langle 0 | 0 \rangle_{(x_a, y_a, z_a)} + \iiint \chi_{\text{SRG}}^{(3)}(x+x', y+y', z+z') L(k_x, k_y, k_z) \{E_p(x, y, z)\}^* E_p(x, y, z) \right. \\ &\quad \times |0 \rangle_{(x, y, z)} E_{\text{col}}(x_a - x, y_a - y, z_a - z) dx dy dz \left. \right|^2 \\ &= \left| -i \frac{1}{(2\pi)^3} \iiint C(k_x, k_y, k_z) |0 \rangle_{(k_x, k_y, k_z)} e^{-i(k_x x_a + k_y y_a + k_z z_a)} dk_x dk_y dk_z \right. \\ &\quad + \iiint \chi_{\text{SRG}}^{(3)}(x+x', y+y', z+z') L(k_x, k_y, k_z) \{E_p(x, y, z)\}^* E_p(x, y, z) \\ &\quad \times \frac{1}{(2\pi)^3} \iiint |0 \rangle_{(k_x, k_y, k_z)} e^{-i(k_x x + k_y y + k_z z)} dk_x dk_y dk_z E_{\text{col}}(x_a - x, y_a - y, z_a - z) dx dy dz \left. \right|^2 \\ &\approx \frac{1}{(2\pi)^6} \iiint \iiint C(k_x, k_y, k_z) C^*(k'_x, k'_y, k'_z)_{(k'_x, k'_y, k'_z)} \langle 0 | 0 \rangle_{(k_x, k_y, k_z)} e^{-i\{(k_x - k'_x)x_a + (k_y - k'_y)y_a + (k_z - k'_z)z_a\}} \\ &\quad \times dk_x dk_y dk_z dk'_x dk'_y dk'_z \\ &+ i \frac{1}{(2\pi)^6} \iiint \iiint \iiint L(k_x, k_y, k_z) C^*(k'_x, k'_y, k'_z)_{(k'_x, k'_y, k'_z)} \langle 0 | 0 \rangle_{(k_x, k_y, k_z)} e^{i(k_x x_a + k_y y_a + k_z z_a)} \\ &\quad \times e^{-i(k'_x x + k'_y y + k'_z z)} dk_x dk_y dk_z dk'_x dk'_y dk'_z \chi_{\text{SRG}}^{(3)}(x+x', y+y', z+z') |E_p(x, y, z)|^2 \\ &\quad \times E_{\text{col}}(x_a - x, y_a - y, z_a - z) dx dy dz \quad + \text{c.c.} \end{aligned} \quad (25)$$

In common with SRG, the fourth term in the above equation is negligible also in spontaneous Raman scattering. Thus, we omitted the fourth term. Carrying on the calculation, we obtain

$$\begin{aligned}
 & \left| A_{\text{Ra}}(x', y', z'; x_a, y_a, z_a) \right|^2 \\
 &= \frac{1}{(2\pi)^3} \iiint \iiint C(k_x, k_y, k_z) P^*(k'_x, k'_y, k'_z) \delta(k_x - k'_x) \delta(k_y - k'_y) \delta(k_z - k'_z) \\
 & \quad \times e^{-i[(k_x - k'_x)x_a + (k_y - k'_y)y_a + (k_z - k'_z)z_a]} dk_x dk_y dk_z dk'_x dk'_y dk'_z \\
 &+ i \frac{1}{(2\pi)^3} \iiint \iiint \iiint L(k_x, k_y, k_z) C^*(k'_x, k'_y, k'_z) \delta(k_x - k'_x) \delta(k_y - k'_y) \delta(k_z - k'_z) \\
 & \quad \times e^{i(k_x x_a + k_y y_a + k_z z_a)} e^{-i(k'_x x_a + k'_y y_a + k'_z z_a)} dk_x dk_y dk_z dk'_x dk'_y dk'_z \chi_{\text{SRG}}^{(3)}(x + x', y + y', z + z') \\
 & \quad \times |E_p(x, y, z)|^2 E_{\text{col}}(x_a - x, y_a - y, z_a - z) dx dy dz + \text{c.c.} \\
 &= \frac{1}{(2\pi)^3} \iiint |C(k_x, k_y, k_z)|^2 dk_x dk_y dk_z \tag{26} \\
 &+ i \frac{1}{(2\pi)^3} \iiint \iiint L(k_x, k_y, k_z) C^*(k'_x, k'_y, k'_z) e^{-i[(x-x_a)k_x + (y-y_a)k_y + (z-z_a)k_z]} dk_x dk_y dk_z \\
 & \quad \times \chi_{\text{SRG}}^{(3)}(x + x', y + y', z + z') |E_p(x, y, z)|^2 E_{\text{col}}(x_a - x, y_a - y, z_a - z) dx dy dz + \text{c.c.} \\
 &= \frac{1}{(2\pi)^3} \iiint |C(k_x, k_y, k_z)|^2 dk_x dk_y dk_z \\
 &+ i \iiint \chi_{\text{SRG}}^{(3)}(x + x', y + y', z + z') |E_p(x, y, z)|^2 |E_{\text{col}}(x_a - x, y_a - y, z_a - z)|^2 dx dy dz + \text{c.c.} \\
 &= \frac{1}{(2\pi)^3} \iiint |C(k_x, k_y, k_z)|^2 dk_x dk_y dk_z \\
 & \quad - 2 \iiint \text{Im} \left\{ \chi_{\text{SRG}}^{(3)}(x + x', y + y', z + z') \right\} |E_p(x, y, z)|^2 |E_{\text{col}}(x_a - x, y_a - y, z_a - z)|^2 dx dy dz.
 \end{aligned}$$

Here we used the following equations:

$$(k'_x, k'_y, k'_z)^{(00)}_{(k_x, k_y, k_z)} = (2\pi)^3 \delta(k_x - k'_x) \delta(k_y - k'_y) \delta(k_z - k'_z), \tag{27}$$

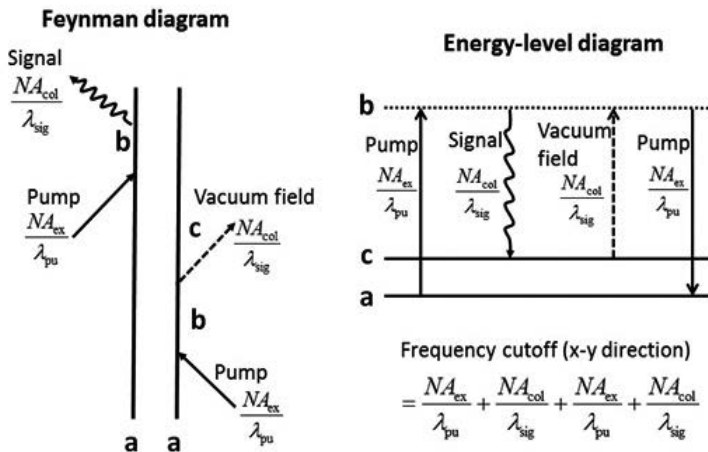
$$\begin{aligned}
 & \frac{1}{(2\pi)^3} \iiint L(k_x, k_y, k_z) C^*(k_x, k_y, k_z) e^{-i[(x-x_a)k_x + (y-y_a)k_y + (z-z_a)k_z]} dk_x dk_y dk_z \\
 &= E_{\text{col}}^*(x_a - x, y_a - y, z_a - z).
 \end{aligned} \tag{28}$$

The first term in Eq. (26) corresponds to the vacuum field that cannot be observed. As only the difference from the vacuum state can be measured, the detected signal becomes

$$\begin{aligned}
 & I_{\text{Ra}}^{\text{de}}(x', y', z') \approx \\
 & \left\{ \iiint \left\{ \iiint \text{Im} \left\{ -2 \chi_{\text{SRG}}^{(3)}(x + x', y + y', z + z') \right\} |E_p(x, y, z)|^2 |E_{\text{col}}(x_a - x, y_a - y, z_a - z)|^2 dx dy dz \right\} \right. \\
 & \quad \left. \times a(x_a, y_a) \delta(z_a) dx_a dy_a dz_a \right\} \tag{29}
 \end{aligned}$$

Note that $\text{Im}\{\chi_{\text{SRG}}^{(3)}(x, y, z)\}$ is a negative value. This equation is well known as the image-forming formula of confocal microscopy with a finite detector size for incoherent optical processes [12]. In incoherent microscopy, the size of the detector influences the optical resolution, according to Eq. (29). In nonconfocal incoherent microscopy, only the pump beam $|E_p(x, y, z)|^2$ determines the optical resolution, while in confocal incoherent microscopy, both the pump beam $|E_p(x, y, z)|^2$ and the signal $|E_{\text{col}}(-x, -y, -z)|^2$ affect the resolution limit, resulting in better resolution.

(a) Spontaneous Raman scattering



(b) Fluorescence

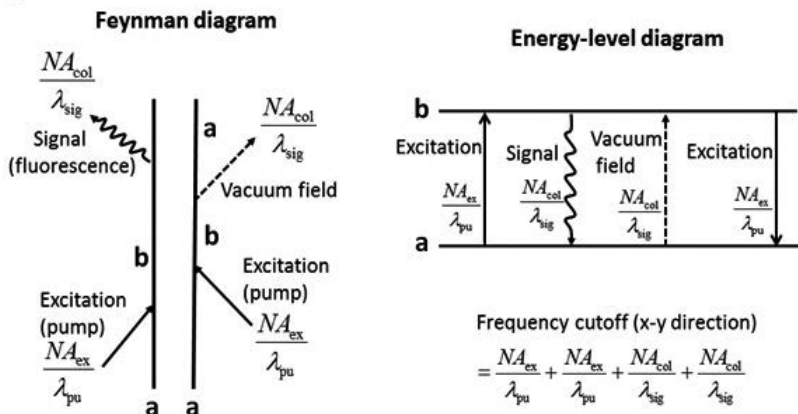


Figure 9. Double-sided Feynman diagram and energy-level diagram for (a) spontaneous Raman scattering and (b) fluorescence.

To discuss the maximum value of the frequency cutoff, we concentrate on confocal microscopy. Substituting $\delta(x_a) \delta(y_a)$ into $a(x_a, y_a)$, we obtain the image-forming formula of confocal Raman microscopy as follows:

$$I_{\text{Ra}}^c(x', y', z') = \iiint \text{Im}\{-2\chi_{\text{SRG}}^{(3)}(x+x', y+y', z+z')\} |E_p(x, y, z)|^2 |E_{\text{col}}(-x, -y, -z)|^2 dx dy dz. \quad (30)$$

Another example of an incoherent optical process is fluorescence. For the image-forming formula of confocal fluorescence microscopy, we only replace $\chi_{\text{SRG}}^{(3)}(x, y, z)$ with $\chi_{\text{SE}}^{(3)}(x, y, z)$, namely,

$$I_{\text{flu}}^c(x', y', z') = \iiint \text{Im}\{-2\chi_{\text{SE}}^{(3)}(x+x', y+y', z+z')\} |E_p(x, y, z)|^2 |E_{\text{col}}(-x, -y, -z)|^2 dx dy dz. \quad (31)$$

Although the ASF of spontaneous Raman scattering and that of fluorescence microscopy are represented by the same notation, it is notable that the double-sided Feynman diagrams or energy-level diagrams for these two processes are different, as described in **Figure 9**.

3. Optical resolution limit

In Section 2, we covered all types of laser microscopy, which include (i) coherent microscopy with the signal wavelength different from the excitation wavelength, (ii) coherent microscopy with the signal wavelength identical with the excitation wavelength, and (iii) incoherent microscopy.

In type (i), the signal can be measured by blocking the excitation beam with the filter. In type (ii), the signal can be extracted by lock-in detection, except linear microscopy that utilizes a $\chi^{(1)}$ -derived optical process. Type (ii) has the local oscillator interfering with the signal, while type (i) does not have the local oscillator. Type (iii) is described in the same fashion as type (ii). Interestingly, in type (iii), the vacuum field plays a role as the local oscillator.

In this section, we form the framework that can discuss the resolution limit for all types of laser microscopy by using double-sided Feynman diagrams and energy-level diagrams. It is well known that the image of the object is formed in three dimensions by laser microscopy with a finite optical resolution, determined by the NA of the excitation and signal-collection systems and the wavelengths of the excitation beams and signal. In addition, we show that the type of optical process occurring in the sample also influences the optical resolution. In our model, the distribution of the linear or nonlinear susceptibility $\chi^{(i)}(x, y, z)$ corresponds to the object we would like to visualize. While the double-sided Feynman diagram was developed to calculate the quantity of susceptibility, which depends on the type of optical process involved, we provide the calculation method for the optical resolution of laser microscopy, which is also linked to the double-sided Feynman diagram.

Our model includes coherent microscopy and incoherent microscopy. Regardless of the coherence, we deal with all types of laser microscopy in the identical framework. In coherent microscopy, the coherent interaction between the excitation laser beam and the molecule occurs, and the corresponding susceptibility distribution is visualized in the image. In incoherent microscopy, an incoherent optical process, which is caused by the excitation beam and the vacuum field lying in the object space, takes place, and the image of the corresponding susceptibility distribution is created. Incoherent microscopy exhibits the incoherent property inherited from the vacuum field. For incoherent microscopy, the equation is formulated by partially using quantum optical notation.

In incoherent microscopy, the definition of the optical resolution becomes straightforward by utilizing the optical transfer function (OTF), while in coherent microscopy, because the OTF does not exist, some definitions are conceivable. In this section, for both coherent microscopy and incoherent microscopy, we define the resolution limit as the largest grating vector that can be resolved, when the three-dimensional grating of the susceptibility is observed as the object. By using our theoretical framework described below, the frequency cutoffs (resolution limits) of coherent microscopy and incoherent microscopy can be compared.

3.1. Diagram technique

We introduce the double-sided Feynman diagram to discuss the frequency cutoff. Originally, this diagram was developed to count and categorize the optical processes and calculate the nonlinear susceptibility of each one. Here we connect the diagram to the frequency cutoffs of linear, nonlinear, coherent, and incoherent microscopy. The diagram can deal with all optical processes, including incoherent processes, such as fluorescence and spontaneous Raman scattering. In coherent microscopy, the resolution limits of confocal and nonconfocal systems are identical, while in incoherent microscopy, the confocal system exhibits the better optical resolution than the nonconfocal system. Note that in coherent microscopy, the images of the confocal and nonconfocal systems indicate the different contrasts. To discuss the theoretical maximum value of the frequency cutoff, we deal with the confocal system for both coherent microscopy and incoherent microscopy. We consider the ASF and its Fourier transform: CTF. For incoherent microscopy, although the point spread function (PSF) is ordinarily used instead of ASF, in this section we refer to PSF for incoherent microscopy as ASF, to integrate coherent microscopy and incoherent microscopy into the identical framework.

The essential part of the image-forming formula for all types of microscopy can be written as

$$I(x', y', z') = \iiint O^{(i)}(x + x', y + y', z + z') \text{ASF}(x, y, z) dx dy dz, \quad (32)$$

or the square of its modulus. Here $O^{(i)}(x, y, z)$ corresponds to the object originating from $\chi^{(i)}(x, y, z)$. To discuss the largest grating vector that can be resolved, we consider 3-D grating as the object. In this case, we can just concentrate on Eq. (32), because the resolution limit does not change regardless of whether Eq. (32) is squared or not. The Fourier transform of Eq. (32) is given by

$$\tilde{I}(f_x, f_y, f_z) = \tilde{O}^{(i)}(f_x, f_y, f_z) \text{CTF}(f_x, f_y, f_z), \quad (33)$$

where \tilde{A} means the Fourier transform of A and $(f_{x'}, f_{y'}, f_z) = (k_x/2\pi, k_y/2\pi, k_z/2\pi)$, which corresponds to the grating vector. For convenience, we use the definition that the Fourier transform of $\{\text{ASF}(x, y, z)\}^*$ is $\{\text{CTF}(f_{x'}, f_{y'}, f_z)\}^*$. The CTF expresses the existence range of the grating vector that can be resolved. In transmission linear confocal microscopy, for example, $\text{ASF}(x, y, z)$ is equal to $E_{\text{ex}}(x, y, z)E_{\text{col}}(-x, -y, -z)$, and Fourier transforming it leads to $\text{CTF}(f_{x'}, f_{y'}, f_z) = U_{\text{ex}}(-f_{x'}, -f_{y'}, -f_z) \otimes U_{\text{col}}(f_{x'}, f_{y'}, f_z)$, where $U_{\text{col}}(f_{x'}, f_{y'}, f_z)$ and $U_{\text{ex}}(f_{x'}, f_{y'}, f_z)$ stand for the Fourier transforms of $E_{\text{col}}(x, y, z)$ and $E_{\text{ex}}(x, y, z)$, respectively. Considering the Ewald sphere helps in understanding the CTF. The Ewald sphere in this case has the same radii as $U_{\text{col}}(f_{x'}, f_{y'}, f_z)$ and $U_{\text{ex}}(f_{x'}, f_{y'}, f_z)$, which are partial spheres (3-D pupil functions) as mentioned above. The phase-matching condition (momentum conservation law), $\mathbf{k}_{\text{sig}} = \mathbf{k}_{\text{ex}} + \mathbf{K}$, is satisfied with the Ewald sphere, where \mathbf{k}_{ex} and \mathbf{k}_{sig} are the wavenumber vectors of the excitation light and the signal, respectively, and \mathbf{K} is the grating vector in the sample. Unless the phase-matching condition is satisfied as shown in **Figure 10**, the signal cannot be generated. Consequently, the resolvable grating vector is restricted to the range determined by the CTF.

In analogy with the above formulation, also for any laser microscopy, the phase-matching condition is taken into account. Since the focused excitation beam is composed of numerous plane waves, all combinations of the excitation plane wave need to be considered. In coherent microscopy, only if the sum of the wavenumber vector of each excitation plane wave and the grating vector of the susceptibility is equal to the wavenumber vector of the signal that can be collected by the signal-collection system, the signal can be generated and detected by the signal-collection system. The phase-matching condition (e.g., $\mathbf{k}_{\text{sig}} = \mathbf{k}_{\text{ex1}} - \mathbf{k}_{\text{ex2}} + \dots + \mathbf{k}_{\text{exn}} + \mathbf{K}$) can be connected to the double-sided Feynman diagram and energy-level diagram as follows:

1. For the right-pointing arrow in the Feynman diagram or the up-pointing arrow in the energy-level diagram, the wavenumber vector of the excitation light corresponds to $+\mathbf{k}_{\text{ex}}$.
2. For the left-pointing arrow in the Feynman diagram or the down-pointing arrow in the energy-level diagram, the wavenumber vector of the excitation light corresponds to $-\mathbf{k}_{\text{ex}}$.

The focused excitation beams and the signal contain many plane waves whose wavenumber vectors lie on the 3-D pupil functions. The ASF (e.g., $E_{\text{ex1}}(\mathbf{x})E_{\text{ex2}}^*(\mathbf{x}) \dots E_{\text{exn}}(\mathbf{x})E_{\text{col}}(-\mathbf{x})$) obeys the following rule.

3. For the right-pointing arrow in the Feynman diagram or the up-pointing arrow in the energy-level diagram, the electric field distribution formed by the excitation beam corresponds to $E_{\text{ex}}(\mathbf{x})$.
4. For the left-pointing arrow in the Feynman diagram or the down-pointing arrow in the energy-level diagram, the electric field distribution formed by the excitation beam corresponds to $E_{\text{ex}}^*(\mathbf{x})$.

5. For the wavy-line arrow, the electric field distribution $E_{\text{col}}(-\mathbf{x})$ formed by the signal through the signal-collection system is applied.

The CTF (e.g., $U_{\text{ex1}}(-f) \otimes U_{\text{ex2}}^*(f) \otimes \dots \otimes U_{\text{exn}}(-f) \otimes U_{\text{col}}(f)$) satisfies the following rule.

6. For the right-pointing arrow in the Feynman diagram or the up-pointing arrow in the energy-level diagram, the 3-D pupil function for the excitation beam corresponds to $U_{\text{ex}}(-f)$.
7. For the left-pointing arrow in the Feynman diagram or the down-pointing arrow in the energy-level diagram, the 3-D pupil function for the excitation beam corresponds to $U_{\text{ex2}}^*(f)$.
8. For the wavy-line arrow, the 3-D pupil function for the signal $U_{\text{col}}(f)$ is applied.

As an example of coherent microscopy, **Figure 10** describes the relation between the CTF and the phase-matching condition represented by the 3-D pupil function. The figure shows the case of linear confocal microscopy, but in the case of nonlinear coherent microscopy, the nonzero region of the CTF becomes larger and the missing cone in the z direction disappears. While the CTF can be calculated by the above rule, the frequency cutoff in the x - y direction can be evaluated more easily with the following rule.

9. Each arrow for the excitation is connected to $\text{NA}_{\text{ex}}/\lambda'$, where λ' is the wavelength of the corresponding beam, such as pump or Stokes.
10. The arrow for the signal is connected to $\text{NA}_{\text{col}}/\lambda_{\text{sig}}$.
11. The maximum possible value of the frequency cutoff in the x - y direction is given by the sum of all the above-mentioned values: $\Sigma\{\text{NA}/\lambda\}$.

In incoherent microscopy, the vacuum field, which contains the virtual photons with the wavenumber vectors in all directions, plays a role as one of the excitation light. The vacuum field is described by the right-pointing dashed arrow in the double-sided Feynman diagram and up-pointing dashed arrow in the energy-level diagram. The vacuum field has its own rule as follows.

12. The wavenumber vector for the vacuum field corresponds to $+\mathbf{k}_{\text{vac}}$.
13. For the ASF, the electric field distribution for the vacuum field corresponds to $E_{\text{col}}^*(-\mathbf{x})$.
14. For the CTF, the 3-D pupil function for the vacuum field corresponds to $U_{\text{col}}^*(-f)$.
15. For the frequency cutoff in the x - y direction, the corresponding value for the vacuum field is $\text{NA}_{\text{col}}/\lambda_{\text{sig}}$ which is the same value as that of the signal.

Note that in incoherent microscopy, the CTF is referred to as the OTF and the ASF becomes the PSF. The vacuum field around the sample includes the Fourier components that have the wavenumber vectors also on the side opposite to the excitation beam. As a result, for reflection microscopy, $|E_{\text{col}}(x_a - x, y_a - y, z_a - z)|^2$ in Eq. (29) can be replaced by $|E_{\text{col}}'(x_a - x, y_a - y, z_a - z)|^2$, but both become the same function if the NAs are identical. Thus,

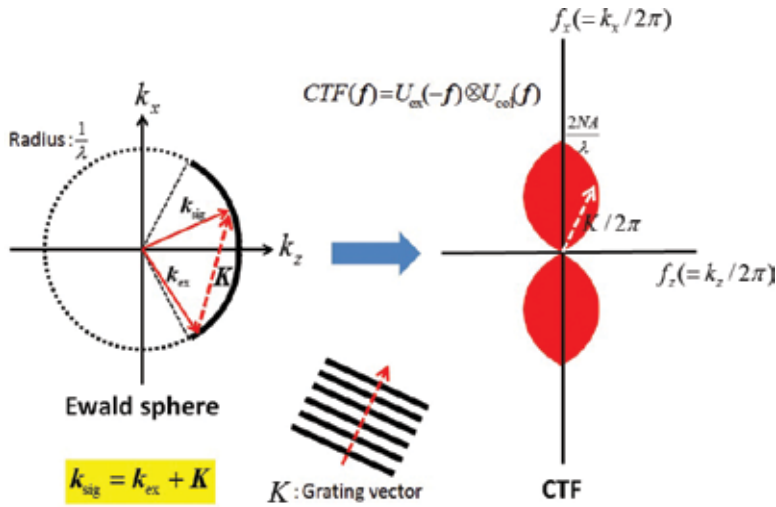


Figure 10. The relation between the phase-matching condition and the CTF for transmission linear confocal microscopy.

unlike in coherent microscopy, it turns out that the OTF of transmission microscopy is identical with that of reflection microscopy in incoherent microscopy. As an example of incoherent microscopy, we take the transmission fluorescence confocal microscopy shown in **Figure 11**, where the relation between the CTF and the phase-matching condition is described with the 3-D pupil function.

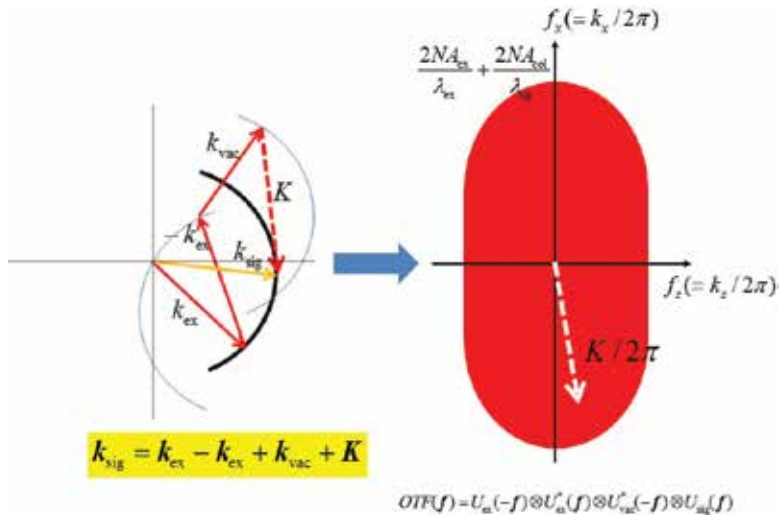


Figure 11. The relation between the phase-matching condition and the CTF for the transmission fluorescence confocal microscopy. Note that $U_{col}^*(-f) = U_{vac}^*(-f)$ and $U_{col}(f) = U_{sig}(f)$

4. Discussion

As stated above, the maximum possible resolution limit is determined by the kind of optical process in force. For illustration, **Figure 12** shows the calculation results of the CTF for CARS, stimulated Raman loss (SRL), SRG, and third-order harmonic generation (THG) microscopy [4]. For reference, the double-sided Feynman diagram and the energy-level diagram describing SRL and THG are shown in **Figure 13**. SRL microscopy and SRG microscopy have the same resolution limit, while CARS microscopy shows better optical resolution than the two former techniques. The CTF of THG microscopy exhibits peculiar properties in which the value of the origin in the spatial frequency domain is zero.

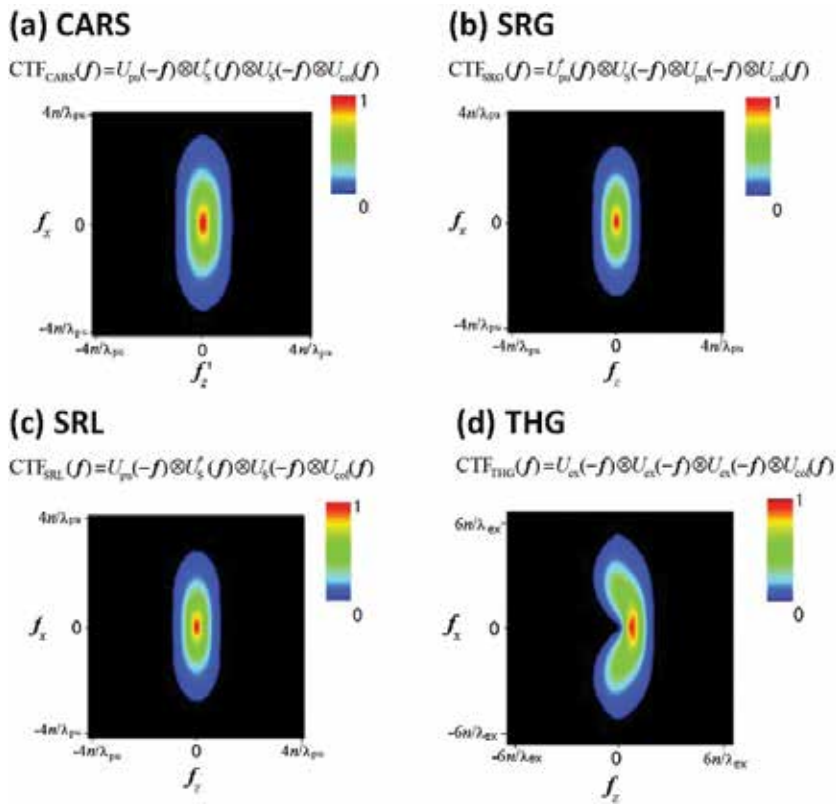


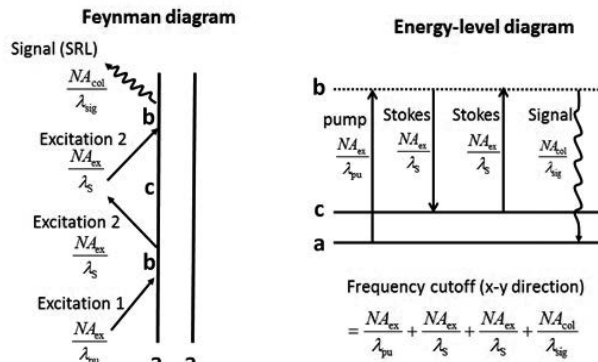
Figure 12. Calculation samples of the CTF for (a) CARS, (b) SRG, (c) SRL, and (d) THG microscopy.

From our theory, some interesting results are also obtained. In reflection coherent microscopy, the uniform region of the susceptibility disappears in the image, as does the interface whose normal is perpendicular to the optical axis. As an example to see the difference between reflection and transmission microscopy, the CTF of transmission and reflection CARS microscopy are shown in **Figure 14** [13]. In transmission THG microscopy, the dot and interface of the susceptibility are emphasized in the image and the uniform region vanishes. In reflection

CARS microscopy and transmission THG microscopy, the grating of susceptibility cannot be resolved, but by assembling the interference microscopy where the signal interferes with the local oscillator generated separately, the grating becomes resolved and then the optical resolution can be defined.

In incoherent microscopy such as fluorescence and spontaneous Raman scattering microscopy, the vacuum field as well as the excitation beam are involved in the optical process and contribute to the increase in the frequency cutoff. It is noteworthy about incoherent microscopy that the OTFs of the transmission and reflection microscopy becomes equal. On the other hand, in coherent microscopy such as SHG, THG, CARS, SRG, and SRL microscopy, the CTFs of transmission and reflection microscopy differ from each other.

(a) Stimulated Raman loss (SRL)



(b) Third harmonic generation (THG)

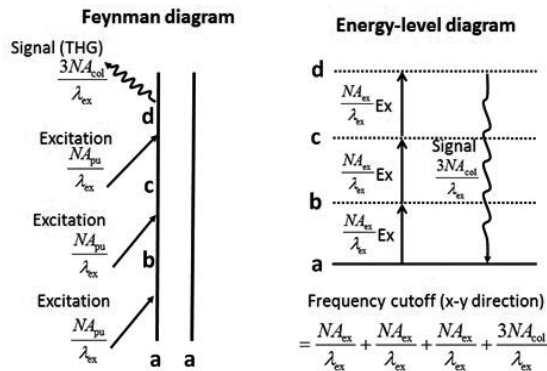


Figure 13. Double-sided Feynman diagram and energy-level diagram for (a) SRL and (b) THG.

Without restricting laser scanning (stage-scanning) microscopy, we can conjecture the following theorem of the resolution limit for all types of microscopy, which visualize $\chi^{(i)}(x, y, z)$ through a variety of optical processes.

4.1. Theorem

- If there is no a priori information on the object (sample), the resolution limit (the maximum value of frequency cutoff) is determined by the diagram describing the optical process. As long as the optical process described by a certain diagram is used to visualize $\chi^{(i)}(x, y, z)$, the resolution limit calculated from the diagram cannot be surpassed regardless of how well the optical apparatus is devised.

The typical exception to the above theorem is localization microscopy, such as photo-activated localization microscopy (PALM) [14] and stochastic optical reconstruction microscopy (STORM) [15], which have a priori information on the object (isolated single-point object). Any microscopy application, including SIM and stimulated emission depletion (STED) microscopy [16], that does not have a priori information on the object should follow this theorem.

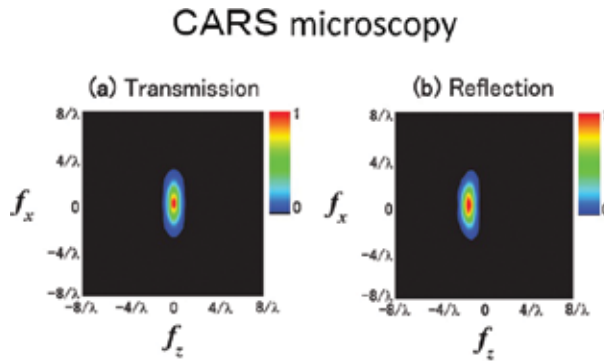


Figure 14. The CTF of transmission and reflection CARS microscopy.

5. Conclusions

We have constructed a theoretical framework to deal with the image formation of all kinds of microscopy by using the double-sided Feynman diagrams and energy-level diagrams describing optical processes. We discovered some rules to evaluate the resolution limit by using these diagrams. Our diagram technique can overview laser microscopy with any optical processes regardless of coherence or linearity. In our framework, the susceptibility distribution is visualized in the image, which blurs based on the optical resolution of each type of microscopy calculated from the diagram technique. Interestingly, in microscopy with an incoherent process, the vacuum field plays a role as part of the excitation light and contributes to the improvement of the optical resolution. In nonconfocal systems, which is commonly used to acquire a high-intensity signal particularly in nonlinear microscopy, the resolution limit of incoherent microscopy is determined by the excitation system only, whereas that of coherent microscopy is determined by both the excitation and signal-collection systems. In SRS microscopy, the transmission type mainly observes the imaginary part of the nonlinear susceptibility, while the reflection type can detect the real part.

Author details

Naoki Fukutake

Address all correspondence to: Naoki.Fukutake@nikon.com

Nikon Corporation, Yokohama, Japan

References

- [1] M. Born and E. Wolf. *Principles of Optics*. 5th ed. Pergamon Press (Oxford); 1974.
- [2] M. G. Gustafsson. Surpassing the lateral resolution limit by a factor of two using structured illumination microscopy. *J. Microsc.* 2000;198:82–87.
- [3] M. Gu. *Principles of three dimensional imaging in confocal microscopes*. World Scientific (Singapore); 1996.
- [4] N. Fukutake. Comparison of image-formation properties of coherent nonlinear microscopy by means of double-sided Feynman diagrams. *J. Opt. Soc. Am. B.* 2013;30:2665–2675.
- [5] W. Denk, J. H. Strickler, and W. W. Webb. Two-photon laser scanning fluorescence microscopy. *Science*. 1990;248:73–76.
- [6] W. R. Zipfel, R. M. Williams, and W. W. Webb. Nonlinear magic: multiphoton microscopy in the biosciences. *Nat. Biotechnol.* 2003;21:1369–1377.
- [7] I. Freund and M. Deutsch. Second-harmonic microscopy of biological tissue. *Opt. Lett.* 1986;11:94–96.
- [8] Y. Barad, H. Eisenberg, M. Horowitz, and Y. Silberberg. Nonlinear scanning laser microscopy by third-harmonic generation. *Appl. Phys. Lett.* 1997;70:922–924.
- [9] M. D. Duncan, J. Reintjes, and T. J. Manuccia. Scanning coherent anti-Stokes Raman microscope. *Opt. Lett.* 1982;7:350–352.
- [10] A. Zumbusch, G. R. Holtom, and X. S. Xie. Vibrational microscopy using coherent anti-Stokes Raman scattering. *Phys. Rev. Lett.* 1999;82:4142–4145.
- [11] W. Freudiger, W. Min, B. G. Saar, S. Lu, G. R. Holtom, C. He, J. C. Tsai, J. X. Kang, and X. S. Xie. Label-free biomedical imaging with high sensitivity by stimulated Raman scattering microscopy. *Science*. 2008;322:1857–1861.
- [12] S. Kawata, R. Arimoto, and O. Nakamura. Three-dimensional optical-transfer-function analysis for a laser-scan fluorescence microscope with an extended detector. *J. Opt. Soc. Am. A.* 1991;8:171–175.

- [13] N. Fukutake. Coherent transfer function of Fourier transform spectral interferometric coherent anti-Stokes Raman scattering microscopy. *J. Opt. Soc. Am. A.* 2011;28:1689–1694.
- [14] E. Betzig, G. H. Patterson, R. Sougrat, O. W. Lindwasser, S. Olenych, J. S. Bonifacino, M. W. Davidson, J. Lippincott-Schwartz, and H. F. Hess. Imaging intracellular fluorescent proteins at nanometer resolution. *Science.* 2006;313:1642–1645.
- [15] M. J. Rust, M. Bates, and X. Zhuang. Sub-diffraction-limit imaging by stochastic optical reconstruction microscopy (STORM). *Nature Methods.* 2006;3:793–796.
- [16] S. W. Hell and J. Wichmann. Breaking the diffraction resolution limit by stimulated emission: stimulated-emission-depletion fluorescence microscopy. *Opt. Lett.* 1994;19:780–782.

Kinetic Model of Development and Aging of Artificial Skin Based on Analysis of Microscopy Data

Paola Pesantez-Cabrera, Cläre von Neubeck,
Marianne B. Sowa and John H. Miller

Additional information is available at the end of the chapter

<http://dx.doi.org/10.5772/63402>

Abstract

Artificial human skin is available commercially or can be grown in the laboratory from established cell lines. Standard microscopy techniques show that artificial human skin has a fully developed basement membrane that separates an epidermis with the corneal, granular, spinosal, and basal layers from a dermis consisting of fibroblasts in an extracellular matrix. In this chapter, we show how modeling can integrate microscopy data to obtain a better understanding of the development and aging of artificial human skin. We use the time-dependent structural information predicted by our model to show how irradiation with an electron beam at different times in the life of artificial human skin affects the amount of energy deposited in different layers of the tissue. Experimental studies of this type will enable a better understanding of how different cell types in human skin contribute to overall tissue response to ionizing radiation.

Keywords: artificial human skin, kinetic model, radiation exposure, protection by corneal layer, selective irradiation of epidermis

1. Introduction

Engineered human tissues provide a bridge between in vivo and in vitro studies by enabling the investigation of fundamental cellular mechanisms at a level of detail that is not possible with whole-animal models, while providing a tissue-like context specific to the organ under investigation (reviewed in reference [1]). Such models are routinely used for toxicology and radiation studies [2–6].

Artificial human skin, a well-known example of engineered human tissue, is available commercially but can also be developed from human cell lines in the laboratory [7, 8]. EpiDermFT™ (MatTek, Ashland, VA) is a widely used commercial product that exhibits a fully developed basement membrane that separates the epidermis, with keratinocytes in the corneal, granular, spinosal, and basal layers, from the dermis consisting of fibroblasts in an extracellular matrix.

Microbeam irradiation of EpiDermFT™ and similar skin-tissue models showed that skin exhibits a “radiation-induced bystander effect” (reviewed in reference [9]); cells that are not directly damaged by ionizing particles in the beam nevertheless exhibit biological responses similar to cell that receive direct damage. Hence, it appears that Interactions layers and cell types plays a role among different layers and cell types play a role in the response of skin to ionizing radiation. Experiments that vary the dose delivered to different layers of artificial skin will contribute to our understand of these interactions.

Cole and coworker [10] showed that, due to its limited penetration in biological materials, the sensitivity of different components of a biological system can be investigated by low-voltage electron-beam irradiation. Recognizing that this technique could be useful in a layered system such as the skin, we calculated the penetration of electron beams of various energies into artificial skin [11] as a basis for the design of experimental studies.

We immediately realized that a detailed analysis of microscopic images of artificial skin was required to ensure accurate calculation of penetration depths. In this chapter, we trace the evolution of our analysis of microscopy data for the purpose of modeling the interaction of artificial skin with electron-beam irradiation. Initially, our focus was on irradiation at a fixed time dictated by experimental procedures coupled with the purchase of EpiDermFT™ from MatTek. Later, we realized that earlier delivery by MatTek and in-house production of artificial skin enabled irradiation studies at different stages in the development of the tissue model. This realization encouraged us to develop a kinetic model of artificial-skin growth and aging that would support simulations of electron-beam exposure at any time during its life cycle.

2. Morphology of the fully developed epidermis of artificial skin

Radiation biology experiments on EpiDermFT™ [6, 12, 14] are usually preformed approximately 3 weeks postseeding of the keratinocytes onto the dermal substrate. At this time, images such as those shown in **Figure 1** reveal the morphology of the mature skin model.

Image A in **Figure 1** (kindly provided by MatTek [13]) uses hematoxylin and eosin (H&E) staining to show the structure of EpiDermFT™ at the time of shipping, about 17 days postseeding of keratinocytes onto the dermal substrate. Horizontal lines added by us approximately delineate layers of the epidermis and suggest that, on average, the spinosal layer is about twice as thick as the basal layer, and granular layers have about the same thickness as the basal layer. Using the scale mark shown in **Figure 1A**, we estimate that the basal, spinosal, and granular layers are about 17, 37, and 17 μm thick, respectively. In this chapter, we refer to

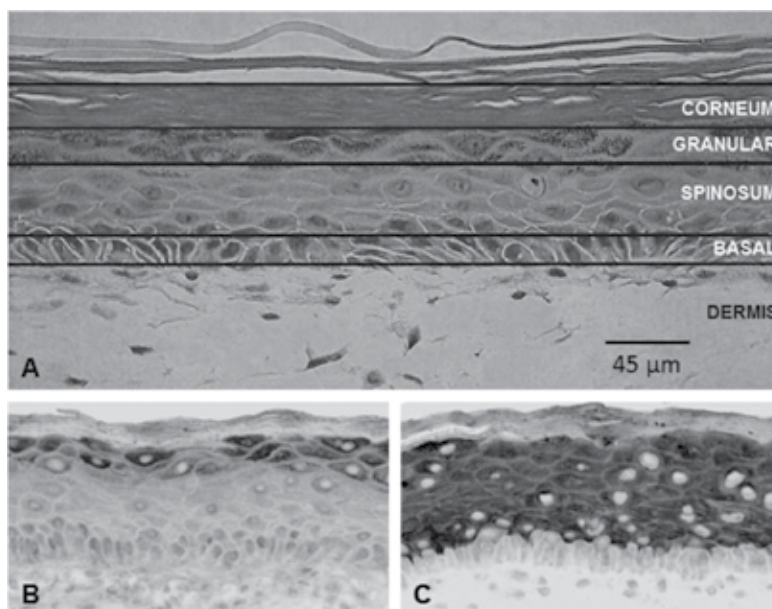


Figure 1. Representative histological sections showing morphology and differentiation in the EpiDermFT™ skin model 17–20 days after the seeding of keratinocytes onto the dermal substrate. Samples A, B, and C were stained for eosin, filaggrin, and keratin10, respectively. For filaggrin and keratin10, positive DAB staining appears dark in the image. All tissues were counterstained with hematoxylin. The scale bar in A applies to B and C as well.

the combined basal, spinosal, and granular layers as the “viable” epidermis to contrast it from the corneal layer of dead cells.

Cells in the stratum corneum have lost most of their intercellular adhesion so that even careful sample handling is likely to induce small air gaps such as those seen in the lower part of the corneal layer in **Figure 1A**. Experimental procedures involved in microscope slide preparation can destabilize the stratum corneum and are, most likely, responsible for large air gaps, such as those seen in the upper part of the corneal layer in **Figure 1A**. Consequently, these images are not a reliable source of data on corneal thickness.

MatTek also provided valuable information about the production of their human skin model. A nutrient layer is seeded with neonatal foreskin basal cells. It is unlikely that this population contains stem cells; hence, the basal layer has finite replication capacity due to transiently amplifying (TA) cell, about 80% of which are in a resting state at any one time. Ca^+ ions in the nutrient layer diffuse into the epidermis but are trapped beneath the corneal layer, which creates a Ca^+ gradient since water can diffuse into the liquid-air interface. As in normal skin, this Ca^+ gradient is most likely responsible for the differentiation of keratinocytes as they are pushed toward the stratum corneum by cell replication in the basal layer.

Images B and C in **Figure 1** are prepared in Dr. Sowa’s laboratory approximately 3 weeks postseeding of keratinocytes onto the dermal substrate [14]. When EpiDermFT™ skin samples were received from MatTek, they were placed in 2 ml of maintenance media and incubated at

37°C and 5% CO₂ as the manufacturer instructed. After 2 days, tissues were fixed in 4% paraformaldehyde, dehydrated, and embedded in paraffin wax using standard methods [15].

Five-micrometer sections were prepared using a Leica microtome and mounted onto coated slides (IMEB, Inc., San Marcos, CA). Sections were deparaffinized in xylene and rehydrated via a series of alcohol rinses. Sections were processed for antigen retrieval by immersion in a citrate acid solution (pH 6.0, 99°C) for 30 min, followed by immersion in 3% H₂O₂ for 10 min to block endogenous peroxidase activity. Slides were then washed three times in phosphate-buffered saline (PBS) for 10 min, blocked with 0.3% bovine serum albumin (BSA) for 1 h, and incubated in the primary antibody overnight at 4°C.

Immunofluorescence staining was performed in triplicate to ensure consistent results. Individual tissue sections were imaged using a Nikon Eclipse TE300 microscope with a Nikon Plan APO VC 60x/1.20 water immersion objective. A Retiga 1300 cooled charge-coupled device (CCD) camera (Qimaging) controlled by QCapture software was used to acquire the image. Image processing was performed in Image J (NIH; Bethesda, MD).

Images B and C in **Figure 1** show differentiation profiles for nonirradiated EpiDermFT™ skin-model samples using filaggrin and Keratin10, respectively. Filaggrin-positive staining defines the granular layer only. Keratin10-positive staining defines the combined spinosum and granular layers but is excluded from the basal layer. Image B seems to indicate that the granular layer contains cells both with and without a nucleus. Furthermore, granular cells with nuclei appear to be adjacent to the stratum corneum. Image C shows that cells in the spinosal layer vary in size with smaller cells nearer to the basal layer. We interpret this as evidence for cell growth as keratinocytes traverse the spinosal layer.

Thicknesses of the basal, spinosal, and granular layers revealed by images B and C in **Figure 1** are roughly in the same proportions as that suggested by the horizontal lines in **Figure 1A**. However, absolute thicknesses cannot be compared due to both sample variability and differences in ages of the sample when the images were acquired. Due to the time spent in shipping and equilibration, images B and C are for samples approximately 4 days older than the sample shown in **Figure 1A**. A significant shrinkage of the viable epidermis (basal, spinosal, and granular layers) during this time was reported in reference [14].

The thickness of the viable epidermis at any given point is stochastic, depending on the particular arrangement of cells in the basal, spinosal, and granular layers. One way to average over this intrinsic variability is to measure area over a fixed width, also called “field of view.” This technique was used in reference [14] to measure the thickness of the viable epidermis in samples stained using a standard H&E protocol [15]. As stated above, MatTek normally ships EpiDermFT™ 17 days postseeding of keratinocytes onto the dermal substrate; however, they will ship samples at earlier time points in sample production if requested. Early shipment was desirable for some of the radiation biology studies conducted by Sowa and coworkers [9, 14], which allowed them to measure the thickness viable layers of the epidermis starting on day 17 postseeding. Results of these measurements are shown in **Table 1**.

Day	Relative thickness
17	1.00 ± 0.04
18	1.14 ± 0.06
19	0.93 ± 0.05
20	0.93 ± 0.06
21	0.76 ± 0.04
22	0.90 ± 0.16
23	0.64 ± 0.08
24	0.42 ± 0.06

Table 1. Relative thickness of the viable epidermis as a function of sample age.

In **Table 1**, the data have been normalized by the mean of areas observed on day 17 and uncertainties are ± 1 standard deviation. Shrinkage starts between days 18 and 19 after an increase in thickness between days 17 and 18. With the exception of day 21, shrinkage of the viable epidermis is relatively minor between days 19 and 22. After day 22, shrinkage is linear with the thickness decreasing about 25% each day.

The biological reason for these changes in the thickness of the combined basal, spinosal, and granular layers is not clear. This is particularly true between days 17 and 22 when the variation is not systemic. The severe shrinkage after day 22 suggests that a dramatic change has occurred in the viable epidermis, possibly due to the exhaustion of replication capacity in the basal layer. If we assume that shrinkage is uniform across the basal, spinosal, and granular layers, we can easily include this shrinkage when we convert cell count from our kinetic model into layer thickness.

3. Properties of artificial skin epidermis revealed by confocal microscopy

The microscope images described in the previous section provide the quantitative information needed to model the viable layers of EpiDermFT™ skin-tissue samples at about 20 days after keratinocytes were seeded onto the dermal substrate. These images of stained vertical slices through the epidermis frequently display large air gaps in the corneal layer, such as those shown in **Figure 1A**, which we attribute to sample preparation. Hence, these images cannot provide reliable quantitative information about the thickness of the corneal layer. To obtain this type of information, we analyzed three-dimensional (3D) confocal microscopy of live samples [6].

Samples were stained overnight with SYTO13 and SYTO59 fluorescent nucleic acid stains (Invitrogen). Two colors (red and green) were chosen because of their high contrast and strong overlap with the excitation lasers of the confocal microscope. Both dyes were used at a final concentration of 10 μM in 3 ml of media. Stained samples were washed with PBS and placed in a 35-mm culture plate containing sufficient PBS to cover the tissue. To minimize sample movement during imaging, samples were placed on a thin coating of autoclaved petroleum

jelly prior to the addition of the PBS. Images were acquired in 1- μm z-steps on a Zeiss laser scanning microscope (LSM) 710 scanning head confocal microscope with a Zeiss plan apo 40 \times /1.1 objective. Excitation lasers were 488 and 633 nm for the green and red emission channels, respectively. Laser dwell times were 1.27 μs for both channels. Two-dimensional (2D) and 3D image analyses were carried out using Volocity (Perkin Elmer, Waltham, MA).

Confocal microscopy of EpiDermFT™ skin-model samples treated with fluorescent nucleic acid stains, as described above, revealed the location of nuclei in the samples. **Figure 2** illustrates a detailed analysis of a confocal microscopy image designed to measure the thicknesses of the corneal layer and the viable epidermis at 20 days after seeding of keratinocytes onto the dermal substrate.

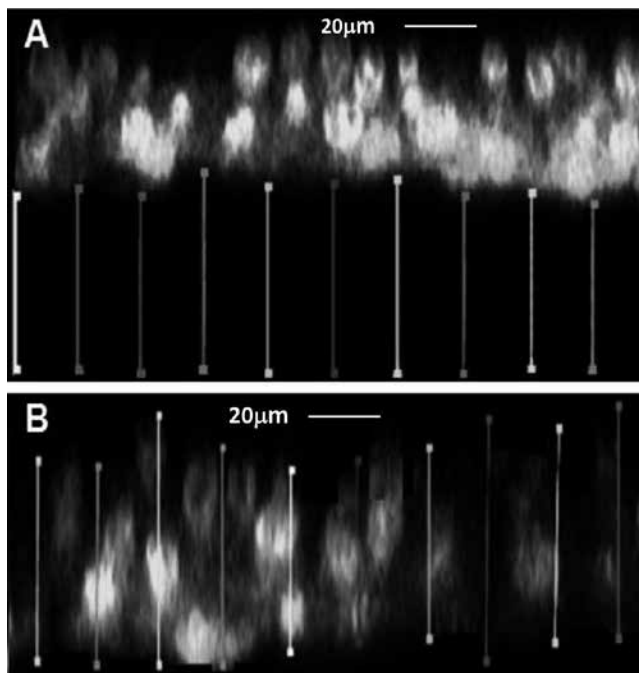


Figure 2. Side view of a 3D image of EpiDermFT™ epidermis obtained by confocal microscopy following treatment with fluorescent nucleic acid stains at 20 days after seeding of keratinocytes onto the dermal substrate. Vertical lines illustrate repeated measurements of the thickness of regions that did (B) and did not (A) take up the stain.

Vertical lines in panel B of **Figure 2**, which span the thickness of the epidermis where stained nuclei were observed by confocal microscopy, have an average length of $45.2 \pm 0.7 \mu\text{m}$. This distance agrees with the thickness of the combined basal and spinosal layers from **Figure 1A** after we allow for shrinkage between days 17 and 20, shown in **Table 1** ($0.93 \pm 0.06 \times 54 \mu\text{m} = 50.2 \pm 3.2 \mu\text{m}$). For this association between information derived by two different types of microscopy to be valid, we must assume that granular cells do not take up the DNA stains, even though, as mentioned above, H&E-stained tissue sections seem to show nuclei in some granular cells.

Vertical lines in panel A of **Figure 2**, which span the thickness of the epidermis where DNA staining is not observed, have an average length of $55.0 \pm 0.41 \mu\text{m}$. Based on the assumption that granular cells do not take up the DNA stain, the combined granular and corneal layers have a thickness of $55.0 \pm 0.41 \mu\text{m}$ on day 20. Assuming further that the shrinkage observed on day 20 is uniform across the viable epidermis, we calculate the thickness of $16 \pm 1 \mu\text{m}$ ($17 \times 0.93 \pm 0.06$) for the granular layer on day 20, which allows us to estimate the corneal-layer thickness as $39 \pm 1.41 \mu\text{m}$ ($55 \pm 0.41 - 16 \pm 1$) on day 20.

By itself, this estimate of the corneal-layer thickness on day 20 is not extremely useful; however, in conjunction with a kinetic model for the number of cells in the stratum corneum, it can be used to estimate the thickness of the corneal layer at all times after its first appearance 7–10 days postseeding of keratinocytes onto the dermal substrate. If we assume that the thickness of corneal cells is constant, then the ratio of cell number to layer thickness on day 20 is the same at all times. Our kinetic model, described in Section 5, was developed to predict corneal cell populations, which can be converted into corneal thickness.

Figure 3 shows the distribution of nuclei in the region of the epidermis that took up the DNA stains. To determine the number of nuclei in a specific volume at a specific depth, Z-stacks of optical sections were reconstructed in 10- μm sections starting at the bottom of the basal layer. Individual nuclei were identified by a threshold on the fluorescence intensity and the number in each 10- μm section was counted. The 2D image area was approximately $60,000 \mu\text{m}^2$.

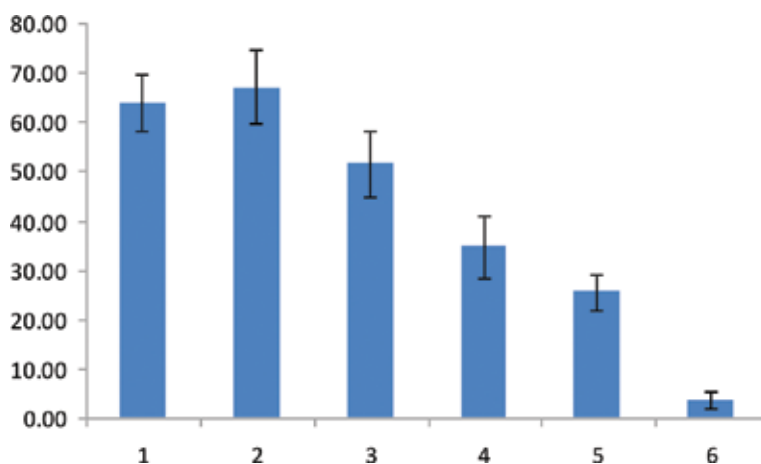


Figure 3. Number of nuclei (vertical axis) in successive 10- μm thick slices numbered 1-6 on the horizontal axis of a 3D confocal microscope image of EpiDermFT™ skin model starting on the basement membrane and ending in the granular layer.

The first two bars of the histogram in **Figure 3** are counts of nuclei in the basal layer and the start of the spinosal layer. Between 20 and 50 μm above the basal membrane, the number of nuclei counted in 10- μm sections decreases linearly. We interpret this decrease in nuclei per unit area as evidence for increasing cell volume as keratinocytes pass through the spinosal layer. A significant departure from this linear behavior occurs in the count of nuclei between

50 and 60 μm above the basal membrane. We associate the small number of nuclei in this 10- μm section as a small number of cells at the base of the granular layer that took up the DNA stain. The deviation from the linearity of nuclei counts between 50 and 60 μm is interpreted as a decrease in the number of cells susceptible to DNA staining, not to an increase in cell volume. Our kinetic model assumes that keratinocytes in the granular layer have the same volume as those cells at the top of the spinous layer.

4. Simulation of electron-beam penetration into skin

PITS [16] is a radiation transport code that performs an event-by-event simulation of charged particles transferring their kinetic energy to electronic excitations of a medium. Simulated tracks are data objects containing, among other things, the Cartesian coordinates of energy deposition events. Properties of elastic collisions are not retained in the track object except as they influence the position of inelastic interactions in the stopping medium. Condensed phase effects [17] are included as described by Wilson et al. [18]. Primary electrons and all generations of secondary electrons are followed until their energy falls below 10 eV, the lowest ionization threshold in Dingfelder's model [17], after which residual kinetic energy is assigned to a final transfer point cast in an isotopically random direction and at an exponentially random distance.

For each electron-beam energy considered, 10^5 independent primary electrons were simulated as they transferred their energy to a liquid-water medium. For layers of the epidermis containing live cells, liquid-water provides a reasonable approximation due to their high water content; however, this approximation may not be valid for the corneal layer due to the low water content and small air gaps.

The density of the cellular material in the stratum corneum is slightly greater than water [19] but the presence of air gaps makes the average corneal density less than that of its cellular material. To allow for these competing factors in determining a water thickness with equivalent mass per unit area as the corneal layer, we used microscope images such as in **Figure 4**, to quantify the relative area of small air gaps. We consider these small air gaps as intrinsic to the corneal layer under normal sample handling during experiments.

Microscope slides of Vertical slices through EpiDermFT™ were prepared by methods described in Section 2 and stained with H&E (IMEB, Inc.). A Nikon Eclipse TE300 inverted microscope with a Nikon Plan APO 20/0.75 objective was used to image individual tissue slices. A Retiga 1300 cooled CCD camera (Qimaging) controlled by Volocity Acquisition (Improvision) software was used to acquire images and to take area measurements. A 12-bit gray scale of intensity determined the relative proportions of high- and low-density materials in the image. High-density material was associated with pixels with normalized gray scale intensity between 0.5 and 15%. The air pockets in the stratum corneum layer were associated with pixels in the 23–100% gray level intensity range.

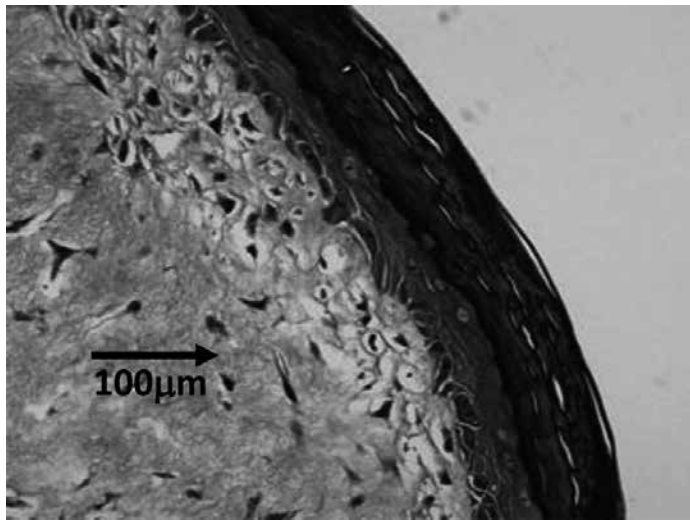


Figure 4. Microscope image of a vertical slice through the EpiDermFT™ skin-tissue model showing small air gaps in the corneal layer.

Area measurements of high and low intensity performed on 14 distinct regions of the stratum corneum gave a mean relative area of low-density material of 9.53% with a standard deviation of the mean 0.81%. Given the large number of cross-sections sampled, it is reasonable to assume that the relative volume of air in the stratum corneum is about 10%.

Weigand et al. [19] measured the buoyant density of the stratum corneum cellular material from Caucasian and Black subjects by several techniques. They concluded that the sucrose density gradient method gave values closest to that of the natural state. Averages of repeated experiments with Caucasian samples, which should apply to the EpiDermFT™ skin model, ranged from 1.075 to 1.145 g/ml. Consequently, the increase in equivalent water thickness to account for the higher density of cellular material in the stratum corneum is approximately equal to the decrease in the thickness of water to account for air pockets. We conclude from these results that calculations of electron-beam penetration in a uniform water medium provide a reasonable approximation to the penetration of the EpiDermFT™ skin model, including the corneal layer.

Figure 5 shows the cumulative probability distribution of samples of the largest z-coordinate of energy transfer points in simulated tracks of 90-keV electrons stopping in a uniform liquid-water medium. Percentile points of this distribution give the thickness of water required to stop a specified fraction of electrons injected into the medium. For example, about 40 μm of water is required to stop about half of the electrons in a 90-keV beam. The dashed curve in **Figure 5** shows the fraction of beam energy deposited by events not exceeding a specified depth. The point a zero depth shows that about 12% of the beam energy is backscattered. By interpolation between calculations at 60 and 70 μm , we estimate that 4% of the beam energy is deposited at depths that exceed the 90th percentile of penetration.

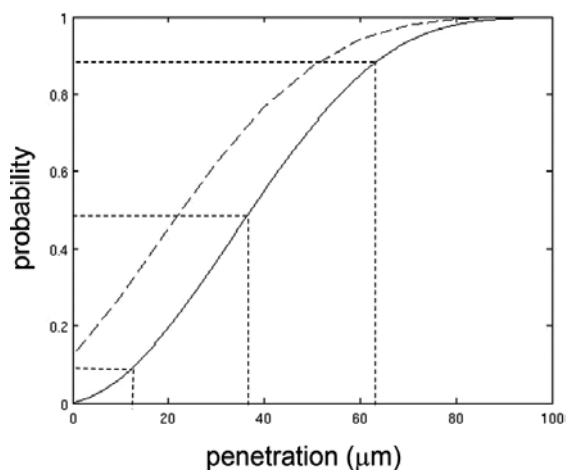


Figure 5. Penetration and energy deposited by a 90-keV electron beam in water. Solid curve is the cumulative probability of maximum z-coordinate of energy transfer points. Intersecting horizontal and vertical dashed lines show 10th, 50th, and 90th percentiles of penetration. Dashed curve shows the fraction of beam energy deposited by events not exceeding a specified depth, with the point a zero depth showing the fraction of beam energy backscattered. Reprinted with permission from Radiation Research.

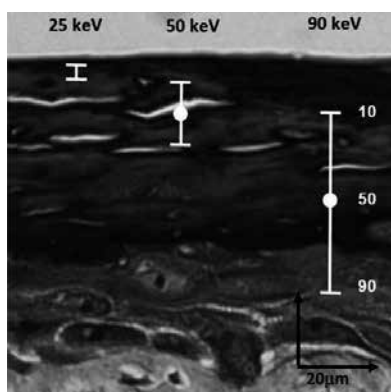


Figure 6. Microscope image of a vertical slice through the EpiDermFT™ skin-tissue model overlay showing calculated penetration of 25-, 50-, and 90-keV electron beams. Bars cover the 10–90th percentile of penetration with the 50th percentile at the center. Reprinted with permission from Radiation Research.

The overlay in **Figure 6** shows the penetration of 25-, 50-, and 90-keV electron beams superimposed on a microscope image of a vertical slice through the EpiDermFT™ skin model. The uncertainty bar is centered on Z_{p50} and the upper and lower extremes are Z_{p10} and Z_{p90} respectively, where Z_{pX} is the depth to which $X\%$ of the electron beam is expected to penetrate. It is clear from the overlay in **Figure 6** that beam energies near 90 keV are required to irradiate keratinocytes in the epidermis that are undergoing active cell division, which is usually the population of greatest interest in radiation biology.

5. Kinetic model of epidermis formation and aging

In this section, we present a kinetic model for the development of the basal, spinosal, granular, and corneal layers of the EpiDermFT™ skin-tissue model. The main purpose for developing this model is to estimate the corneal layer thickness from the start of its formation 7–10 days after seeding of keratinocytes onto the dermal substrate to the end of the useful life of the sample for radiation biology studies due to shrinkage. Our model predicts the kinetics of the number cells in the corneal layer. If we assume that the thickness of a corneal cell is constant, then the measure of corneal layer thickness at 20 days (see Section 3) can be used to convert cell count into layer thickness at any time.

A kinetic model of artificial-skin development was reported in reference [9] that focused on the viable epidermis for comparison with experimental studies of skin homeostasis after exposure to ionizing radiation [9, 14]. The model in reference [9] starts with a rapid expansion of TA basal cells, with the population increasing sixfold in about 12 days. By contrast, the kinetic model described here starts with a confluent monolayer of the basal cells and the total basal-cell population, consisting of cycling TAs, noncycling TAs with replication potential, and the basal cells that have exhausted their replication capacity, is constant throughout the simulation.

As in reference [9], we assume that TA cells exhaust their replication capacity after five to three cycles, but the current model includes the information from MatTek that only about 20% of TA cells are cycling at any given time. This means that as individual TA cells exhaust their replication capacity, they are replaced by a TA cell with full replication capacity that has been held in reserve. The biological mechanism for delayed cycling of TA cells with replication capacity is unclear; however, as **Figure 7** shows, this modeling assumption allows the cycling TA population to be constant throughout most of our kinetic simulation. Replication in the

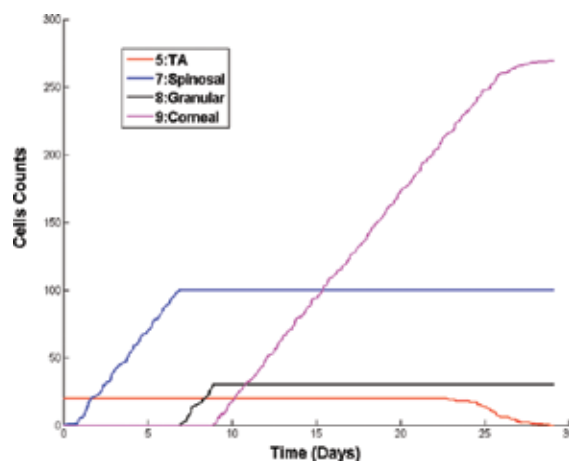


Figure 7. Predicted kinetics of cell count in the basal (orange), spinosal (blue), granular (black), and corneal (red) layers of the epidermis of an artificial-skin tissue, starting from the time with the basal layer is confluent.

basal layer goes to zero after about day 23 when reserve replication capacity is no longer available.

In the current model, the differentiation of keratinocytes is determined by their height above the basement membrane. We think this more correctly models differentiation driven by a Ca⁺ gradient than the purely time-dependent transitions of the kinetic model in reference [9]. Height-dependent differentiation means that a spinosal cell is the consequence of each TA-cell replication. TA cycling produces two daughter TA cells, but some basal cells must move to the spinosal layer because the basal-cell layer is confluent

As can be seen in **Figure 7**, the spinosal-cell population is non-zero after the first TA-cell replication, which occurs at TA cycle time chosen randomly from a lognormal distribution with a mean TA cycle time of 31.2 h. The lognormal distribution of TA cycle times and its variance are the same as in reference [9] but the mean TA cycle time in the current model is significantly shorter. A shorter mean cycling time for TA cells in the current model is a direct consequence of our assumption, based on information from MatTek [15] that only about 20% of TA cell with replication potential are cycling at any given time. Consequently, a shorter mean cycling time is required to generate complete spinosal and granular layers 7–10 days postseeding of keratinocytes than is the case when all TAs with replication potential are cycling.

In our kinetic model, the corneal layer begins to form as soon as the granular layer reaches its full thickness. Exposure to air is crucial to the formation of a corneal layer but this requirement is not explicitly included in our model. **Figure 7** also shows that the rates of increase of spinosal, granular and corneal cell populations are all nearly equal, aside from random fluctuations, to a constant value determined by the rate of TA-cell replication in the basal layer. The rates of increase in the thickness of the spinosal, granular, and corneal layers are not the same because the volumes of individual cells in those layers are different. In addition, the volume of a spinosal cells is increasing with time since it entered the stratum spinosum.

Sharp transitions between increasing and constant cell populations in the spinosal and granular layers are an artifact of our model in which cell type is determined by a specified height of the cell above the basement membrane. If a TA cycle, which adds a cell to the stratum spinosum, makes the upper boundary of the spinosal layer exceed the height above the basement membrane allowed for spinosal cells, the oldest cell in the current stratum spinosum becomes a granular cell. A similar modeling assumption governs the transition of granular to corneal cells.

The transition between linearly increasing to constant corneal cell population is not sharp. This transition mirrors the loss of replication capacity in the basal layer, which occurs over about a 4-day time period. In **Figure 7**, this loss of replication capacity occurs between days 23 and 29. Various model parameters, including the mean TA cycle time and the fraction of cycling TA cells, determine the duration of replication capacity in the basal layer. parameters affect the time when replication capacity is exhausted relative seeding of keratinocytes onto the dermal substrate. We think that the decay of replication seen in **Figure 7** is reasonable because it correlates roughly with the onset of significant shrinkage of the viable epidermis observed

experimentally [14] (see **Table 1**). After replication capacity is exhausted, cell count in all layers is constant. Cell count in the basal layer is always constant but transitions between cycling, resting with replication potential, and sterile TA cells occur throughout the kinetic simulation.

Even though cell count in the viable epidermis remains constant after complete formation of spinosal and granular layers, its thickness is not constant due to shrinkage. On converting cell count to layer thickness after shrinkage begins, we assume that its effect is uniform across all three layers, basal, spinosal, and granular, of the viable epidermis. After day 18, we assume that the volume of all cells in the viable epidermis decreases in accordance with the shrinkage fractions in **Table 1**. Although no data are available, it seems reasonable that corneal cells do not shrink since they are dead and have lost most of their water content. Hence, we can use the corneal thickness of $39 \pm 1.41 \mu\text{m}$ deduced from confocal microscopy on day 20 to convert corneal cell count to corneal thickness at any time after its appearance, about day 8.5 shown in **Figure 7**.

A typical simulation begins by assigning a maximum of 3, 4, or 5 replications randomly to 100 basal cells, 20 of which are chosen randomly to be expressing this replication potential at the beginning of the simulation. The 20 active TA cells are assigned cycle times randomly drawn from a lognormal distribution with a variance of 0.2 and a mean cycling time chosen to generate complete spinosal and granular layers 7–10 days postseeding of keratinocytes, as reported by MatTek [15].

The active TA cell with the shortest cycling time is selected for replication, which forces a randomly selected TA cell off the basement membrane to become a spinosal cell and leaves a TA cell on the basement membrane that is capable of one less replication. The current simulation time is upgraded and a new random cycle time is assigned to the TA cell that just replicated, if it still has replication capability. If not, the TA cell that just replicated becomes a permanently resting TA cell and is replaced by a TA cell that can replicate, if the pool of TA cells with replication capacity is not empty.

If we knew the growth rate of spinosal cells, we would assign the spinosal cell generated by TA-cell replication a birth time equal to the current simulation time and volume equal to that of a basal cell. The age of any preexisting spinosal cells would increase by the TA cycle time and their volume would increase to reflect growth during that cycle time. The growth rate of spinosal cells cannot be determined from the available data; however, as discussed below, the difference in the volume of spinosal cells at different heights in the spinosal layer can be estimated from the data in **Figure 3**. This allows us to calculate the average volume of a spinosal cell, which we assign to all cells in the spinosal population.

After each TA-cell replication, we find the active TA cells with the shortest cycling time, which determine the size of the next time step in the simulation. However, before that time step can be taken, we must determine if a spinosal cell needs to transition to a granular cell, based on the current thickness of the spinosal layer. From the microscopy images in **Figure 1**, it is clear that the spinosal and granular layers are confluent; hence, the volume of the spinosal and granular layers at any time in the simulation is the sum of the volumes of the cells in those layers. The current thickness of the spinosal and granular layers is their current total volume

divided by the area of skin being simulated, which is 100 times the cross-sectional area of a basal cell. If the current thickness of the spinosal layer exceeds the observed thickness of a fully formed spinosal layer, a spinosal cell transitions to a granular cell with an appropriate average volume change.

We assume that all granular cells have the same volume that does not change with time. As with the spinosal layer, we estimate the current thickness of the granular layer as its population volume divided by the simulation area. If this total thickness exceeds that observed for a fully developed granular layer, a granular cell transitions to a corneal cell. Updating the count of corneal cells, if needed, completes a simulation time step.

To conduct the series of steps in the simulation described above requires parameters derived from the analysis of microscopy data. A vertical slice through the skin-tissue model imaged by H&E staining 17 days postseeding of keratinocytes allowed us to estimate values of 17, 37, and 17 μm for the thickness of the basal, spinosal, and granular layers, respectively, after they are fully developed and before shrinkage begins. We compare these thicknesses to layer thicknesses after each time step of the simulation to determine if changes in cellular populations are needed. To conduct this test, we need the area of artificial skin being modeled. In our simulation, the basal-cell layer is always a confluent monolayer; hence, the mean separation of basal-cell nuclei, observed to be 14.9 μm by confocal microscopy after DNA staining [6], is an estimate of the mean lateral thickness of the basal cells. By this method, we estimate the cross-sectional area of the basal cells to be 14.9 μm^2 , so a typical area of skin in our simulations is $100 \times (14.9 \mu\text{m})^2 = 2.22 \times 10^4 \mu\text{m}^2$.

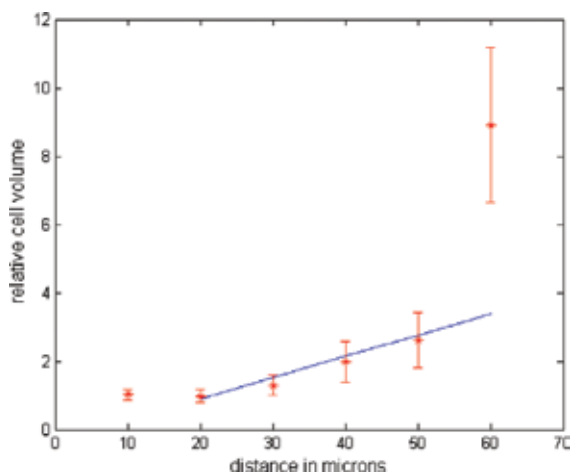


Figure 8. Change in the volume per cell as a function of distance above the basement membrane. Data were normalized to the volume of the basal cells by averaging the results for slices of 3D confocal microscopy data 0–10 and 10–20 μm above the basement membrane. The line fit to data at heights greater than 20 μm mainly reflects the changing volume of spinosal cells.

The analysis of microscopy data discussed in this chapter does not yield a direct measure of spinosal-cell growth rate. However, the analysis of confocal microscopy data for the distribution

of nuclei as a function of height above the basement membrane, shown in **Figure 3**, can be used to estimate the change in spinosal-cell volume as a function of height above the basement membrane. As discussed in Section 3, the number of nuclei at various heights above the basement membrane was estimated by counting the number of stained object in a 10- μm slice with an image area of 60,000 μm^2 . Dividing the volume of the slice, 600,000 μm^3 , by the observed count, we get an estimate of the volume per cell, assuming that each cell has a single nucleus. The counts of nuclei in slices 10 and 20 μm above the basement membrane mainly reflect the volume of the basal cells. The average of calculated volume per cell at 10 and 20 μm was used to normalize the data; hence, the data shown in **Figure 8** are the relative change in cell volume versus height above the basement membrane.

The linear trend in the relative volume per cell between 20 and 50 μm above the basement membrane is not reflected in the data at 60 μm . Based on **Figure 1A** and allowing for shrinkage on day 20 (see **Table 1**), we estimate that the combined thickness of the basal and spinosal layers on day 20, when the confocal data were obtained, is 50.2 μm . Hence, the data shown in **Figure 8** at 60 μm are mainly due to nuclear staining in the granular layer and reflect the uptake of the DNA stains more than the size of cells in the granular layer.

As the results in **Figure 8** show, a linear model is reasonable for the change of spinosal-cell volume as a function of their height in that layer. We express this model as

$$v_s(h) = v_b(1 + (g - 1)(h - \Delta_b) / \Delta_s) \quad (1)$$

where v_b is the volume of a basal cell, $v_s(h)$ is the volume of a spinosal cell at height h above the basement membrane, Δ_b is the thickness of the basal layer, and Δ_s is the total thickness of the spinosal layer. The parameter g is the ratio of the volume of a granular cell to a basal cell, which can be verified by applying Eq. (1) at the maximum height of the spinosal layer. This parameter can be estimated by setting $(g-1)/\Delta_s$ to the slope of the linear fit shown in **Figure 8**, which gives a value of $g = 3.32$.

Equation (1) is not directly useful in our kinetic simulation because we do not know the height above the basement membrane of individual cells in the spinosal layer; however, since $v_s(h)$ is linear, we can easily calculate the average volume of a spinosal cell:

$$\langle v_s \rangle = (v_b + v_g) / 2 = v_b(1 + g) / 2 = 2.16v_b \quad (2)$$

We assign this average volume to every spinosal cell, which allows us to calculate the thickness of the spinosal layer at any time from the number of spinosal cells at that time. As explained above, knowing the thickness of the spinosal layer at any time is sufficient to determine when a spinosal cell makes a transition to a granular cell.

Using an average volume of spinosal cells also simplifies the relationship between the mean TA-cell cycling time and the mean time t_0 required in our kinetic simulation to produce a fully developed via epidermis, which marks the beginning of a corneal layer by exposed to the

liquid-air interface. If the confluent basal-cell population is N and a fraction p of basal cells is cycling with a mean time T_c , then

$$t_0 = (T_c / p)(N_s / N + N_g / N) \quad (3)$$

where N_s and N_g are the number of spinosal and granular cells, respectively, in the fully developed spinosal and granular layers. Since $N = A\Delta_b/v_b$, where A is the area of epidermis being simulated, $N_s = A\Delta_s/v_s$, and $N_g = A\Delta_g/v_g$, where Δ_g is the thickness of the granular layer, Eq. (3) becomes

$$t_0 = (T_c / p)[(\Delta_s / \Delta_b)(v_b / v_s) + (\Delta_g / \Delta_b)(v_b / v_g)] \quad (4)$$

Taking the average of 7 and 10 days as the typical time when the corneal layer begins [15], Eq. (4) predicts the mean TA cycling time of 31.2 h. This completes the parameter estimates for our kinetic simulation.

6. Effect of corneal screening on irradiation of the viable epidermis

The results of our kinetic simulation of epidermis development shown in **Figure 7** together with the estimate of $39 \pm 1.41 \mu\text{m}$ for corneal layer thickness at 20 days postseeding of keratinocytes onto the dermal substrate enable the calculation of the protection that the corneal layer provides to live cells in the viable epidermis. We only model radiation exposure delivered after day 8.5, model radiation exposures delivered after day 8.5, the day selected in our model for first appearance of the corneal layer based on information from MatTek [15] that viable epidermis (basal, spinosal, and granular layers) is completed 7–10 days postseeding of keratinocytes onto the dermal substrate.

The thickness of the corneal layer on the day of irradiation was obtained from the results for cell count in the corneal layer, shown in **Figure 7**, after combining several simulations to reduce random fluctuations and normalizing to a thickness of $39 \mu\text{m}$ on day 20. From day 8.5 to about day 25, the increase in corneal thickness is linear. Beyond day 30, its thickness is constant since the replication capacity of the basal layer has been exhausted.

Based on results from simulations of a 90-keV electron beam stopping in a liquid-water medium [11], we developed an interpolation procedure for the amount of energy deposited in a layer of a given thickness at a given depth in the medium. As shown in Section 4, a liquid-water medium is a reasonable approximation to the epidermis of skin, including the corneal layer. Hence, our interpolation procedure allows the accurate prediction of radiation exposure to specified regions of the epidermis without the computationally intense, event-by-event simulation of 90-keV electrons penetrating an aqueous medium. The dermal substrate, which is composed of human fibroblast in a collagen matrix, is thick enough to stop a 90-keV electron

beam; hence, we estimate the energy deposited in the dermal substrate as the residual energy of electrons if they are not stopped in the epidermis.

The curve in **Figure 9** referred to the left-hand vertical axis shows our prediction for the energy deposited in the combined spinosal and basal layers depending on the day when the tissue was treated relative to the seeding of keratinocytes onto the dermal substrate. Spinosal and basal layers contain most of the cells with nuclei and that are undergoing growth and replication; consequently, they are the most sensitive to radiation exposure.

The results shown in **Figure 9** allow for the shrinkage of the viable epidermis observed to start on day 19 but with little significance until day 23, with the exception of day 21 where shrinkage is greater than on days 20 or 22 (see **Table 1**). The energy deposited in layers that contain nucleated cells decreases from a value about 50 keV per incident electron for irradiation on day 8.5, when the corneum is just beginning to form, to a value about 1 keV for irradiation on day 25. The lack of smoothness in these calculations after day 18 is due to observed shrinkage of the viable epidermis that begins on day 19.

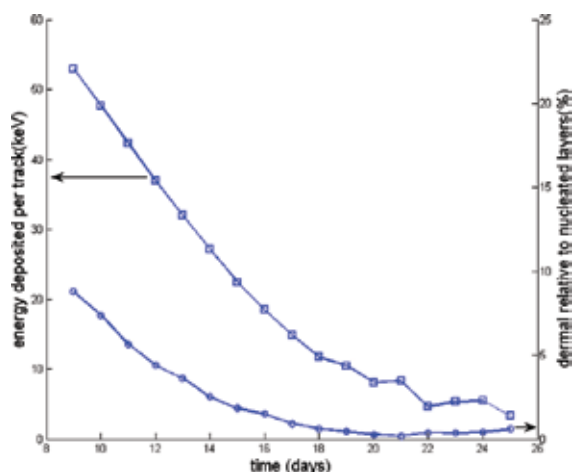


Figure 9. Effects of increasing corneum thickness on energy deposition in the combined basal and spinosum layers where keratinocytes are undergoing cell division and growth (left-hand vertical axis). The curve referred to the right-hand vertical axis is the energy deposited in the dermal substrate relative to that deposited in the combined basal and spinosal layers.

The curve in **Figure 9** referred to the right-hand vertical axis shows the energy deposited in the dermal substrate relative to that deposited in nucleated cells of the epidermis. When the corneal layer is thin, a significant fraction of the energy deposited reaches the fibroblast in the dermal substrate but this exposure is near zero for irradiation on day 21 when the corneal thickness has increased to about 40 μm . Comparing tissue responses at these different exposure times will not only show how screening by the corneal layer protects viable skin cells but may also reveal interactions between dermis and epidermis that are present when both components are exposed and absent when essentially all the radiation exposure is to epidermis alone.

Figure 9 suggests that irradiations performed around day 20 would deposit significant energy in the basal and spinosal layers with minimal exposure to the dermal substrate.

7. Conclusions

As artificial organotypic cell cultures become more widely used in research, their characterization becomes increasingly important. Morphology is a fundamental part of this characterization that can be accomplished through quantifiable microscopy techniques with sample preparation that preserves organ structure. The research described in this chapter concerned a part of artificial skin, the corneal layer, which is particularly prone to distortion in standard microtome-based slide preparation. To circumvent this difficulty, we correlated data from histologic staining methods [14] with data from 3D images of artificial-skin samples acquired by confocal microscopy [6]. However, this correlation of different types of microscope data required assumptions about the uptake of DNA stains by granular cells and a kinetic model to amplify the usefulness of confocal microscope data obtained at only one time point. In future work, direct measurements of corneal thickness can be obtained by new non-destructive techniques [20]. Despite these limitations on the available data, we achieved our objective of modeling the decrease in radiation exposure to live cells in the epidermis with increasing corneal thickness as the age of artificial skin samples increases.

Author details

Paola Pesantez-Cabrera¹, Cläre von Neubeck^{2,3}, Marianne B. Sowa⁴ and John H. Miller^{5*}

*Address all correspondence to: jhmiller@tricity.wsu.edu

1 School of Electrical Engineering and Computer Science, Washington State University, Pullman, WA, USA

2 German Cancer Consortium (DKTK), Dresden and German Cancer Research Center (DKFZ), Heidelberg, Germany

3 OncoRay, National Center for Radiation Research in Oncology, Faculty of Medicine and University Hospital Carl Gustav Carus, Technische Universität Dresden, Dresden, Germany

4 Space Biosciences Research Branch, NASA Ames Research Center, Moffett Field, CA, USA

5 School of Electrical Engineering and Computer Science, Washington State University Tri-Cities, Richland, WA, USA

References

- [1] Griffith LG, Swartz MA. Capturing complex 3D tissue physiology in vitro. *Nat Rev Mol Cell Biol* 2006; 7:211–24.
- [2] Belyakov OV, Mitchell SA, Parikh D, Randers-Pehrson G, Marino SA, Amundson SA, et al. Biological effects in unirradiated human tissue induced by radiation damage up to 1 mm away. *Proc Natl Acad Sci U S A* 2005; 102:14203–8.
- [3] Sedelnikova OA, Nakamura A, Kovalchuk O, Koturbash I, Mitchell SA, Marion SA, et al. DNA double-strand breaks form in bystander cells after microbeam irradiation of three-dimensional human tissue models. *Cancer Res* 2007; 67:4295–302.
- [4] Prise KM, Schettino G, Vojnovic B, Belyakov O, Shao C. Microbeam studies of the bystander response. *J Radiat Res (Tokyo)* 2009; 50 Suppl A:A1–6.
- [5] Sowa MB, Chrisler WB, Zens KD, Ashjian EJ, Opresko LK. Three-dimensional culture conditions lead to decreased radiation induced cytotoxicity in human mammary epithelial cells. *Mutat Res* 2010; 687:78–83.
- [6] von Neubeck C, Shankaran H, Geniza M, Kauer P, Robinson J, Chrisler W, et al., Integrated experimental and computational approach to understand the effects of heavy ion radiation on skin homeostasis. *Integr Biol* 2013; 5:1229–45.
- [7] Gangatirkar P, Paquet-Fifield S, Li A, Rossi R, Kaur P. Establishment of 3D organotypic cultures using human neonatal epidermal cells. *Nat Protoc* 2007; 2:178–86.
- [8] Vaughan MB, Ramirez RD, Brown SA, Yang JC, Wright WE, Shay JW. A reproducible laser-wounded skin equivalent model to study the effects of aging in vitro. *Rejuvenation Res* 2004; 7:99–110.
- [9] Hei TK, Ballas LK, Brenner DJ, Geard CR. Advances in radiobiological studies using a microbeam. *J Radiat Res (Tokyo)* 2009; 50 Suppl A: A7–12.
- [10] Zermeno A, Cole, A. Radiosensitive structures of metaphase and interphase hamster cells as studied by low-voltage electron beam irradiation. *Radiat Res* 1969; 39:669–84.
- [11] Miller JH, Suleiman A, Chrisler WB, Sowa MB. Simulation of electron beam irradiation of skin tissue model. *Radiat Res* 2011; 175:113–8.
- [12] Yang F, Waters KW, Miller JH, Gristenko MA, Zhao R, Du X, et al Phosphoproteomic profiling of human skin fibroblast cells reveals pathways and proteins affected by low doses of ionizing radiation. *PLoS One* 2010; 5(11) e14152 DOI: 10.1371/journal.pone.0014152
- [13] Mat Tek Corporation. The EpiDermFT™ skin model.<http://www.mattek.com/pages/products/epidermft/October 2, 2012>

- [14] von Neubeck C, Geniza M, Kauer P, Robinson J, Chrisler W, Sowa MB. The effect of low dose ionizing radiation on homeostasis and functional integrity in an organotypic human skin model. *Mut Res* 2015; 775:10–18.
- [15] Luna LG (ed). *Manual of histologic staining methods of the armed forces institute of pathology*. 3rd edition. McGraw-Hill, New York; 1968.
- [16] Wilson WE, Nikjoo H. A Monte-Carlo code for positive ion track simulation. *Radiat Environ Biophys* 1999; 38:97–104.
- [17] Dingfelder M, Hantke D, Inokuti M, Paretzke HG. Electron inelastic-scattering cross sections in liquid water. *Radiat Phys Chem* 1998; 53:1–18.
- [18] Wilson WE, Miller JH, Lynch DJ, Lewis RR, Batdorf M. Analysis of low-energy electron track structure in liquid water. *Radiat Res* 2004; 161:591–6.
- [19] Weigand DA, Haygood C, Gaylor JR. Cell layers and density of Negro and Caucasian stratum coreum. *J Invest Dermatol* 1974; 62:563–8.
- [20] Mateus R, Abdalghafor H, Oliverira G, Hadgraft J, Lane ME. A new paradigm in dermatopharmacokinetics – confocal Raman spectroscopy. *Int J Pharm* 2013; 444:106–8.

Automatic Interpretation of Melanocytic Images in Confocal Laser Scanning Microscopy

Marco Wiltgen and Marcus Bloice

Additional information is available at the end of the chapter

<http://dx.doi.org/10.5772/63404>

Abstract

The frequency of melanoma doubles every 20 years. The early detection of malignant changes augments the therapy success. Confocal laser scanning microscopy (CLSM) enables the noninvasive examination of skin tissue. To diminish the need for training and to improve diagnostic accuracy, computer-aided diagnostic systems are required. Two approaches are presented: a multiresolution analysis and an approach based on deep layer convolutional neural networks. For the diagnosis of the CLSM views, architectural structures such as micro-anatomic structures and cell nests are used as guidelines by the dermatologists. Features based on the wavelet transform enable an exploration of architectural structures at different spatial scales. The subjective diagnostic criteria are objectively reproduced. A tree-based machine-learning algorithm captures the decision structure explicitly and the decision steps are used as diagnostic rules. Deep layer neural networks require no a priori domain knowledge. They are capable of learning their own discriminatory features through the direct analysis of image data. However, deep layer neural networks require large amounts of processing power to learn. Therefore, modern neural network training is performed using graphics cards, which typically possess many hundreds of small, modestly powerful cores that calculate massively in parallel. Readers will learn how to apply multiresolution analysis and modern deep learning neural network techniques to medical image analysis problems.

Keywords: confocal laser scanning microscopy, skin lesions, multiresolution image analysis, convolutional neural networks, machine learning, computer-aided diagnosis

1. Introduction

The skin is the largest organ of the body. Its surface comprises up to two square meters. It is the organ that is in direct contact to the environment and is therefore exposed to several environmental influences such as sun radiation, temperature, infections. The skin consists of three main layers: the epidermis, the dermis and the hypodermis (subcutis), whereby each layer is subdivided into several sublayers (strata) [1]. As the outermost layer, the epidermis provides a protective barrier of the body's surface which keeps water in the body, protects against heat and ultraviolet radiation and prevents infections (caused by bacteria, fungi, parasites, etc.) [2, 3]. The horny layer (stratum corneum), which is the top layer of the epidermis, undergoes a continuous process of renovation (every 4 weeks). Keratinocytes, which represents 90% of the cell types in the epidermis, protect the body against ultraviolet radiation. Keratinocytes are derived from epidermal stem cells residing in the lower part of the epidermis (stratum basalis). During their lifetime, they migrate through the different strata of the epidermis. Via this process, they are pressed to the epidermis surface by the continuously succeeding cells. During the migration through the different strata, the keratinocytes cells undergo multiple stages of differentiation, whereby they change shape and composition and are filled with keratin. Different stages and corresponding strata are represented in **Figure 1**. Keratin, a structural protein, is the key structural material making up the outer layer of the epidermis and protects the cells from damage or stress. On their way to the outermost strata, the keratinocytes lose liquid and become hornier. Corneocytes are keratinocytes that have completed their differentiation program. They are dead cells in the stratum corneum and are shed off (by desquamation) as new ones come in. Keratinocytes protect against ultraviolet radiation by taking up melanosomes from epidermal melanocytes. The melanosomes are vesicles which contain the endogenous photo protectant molecule melanin. Melanocytes are melanin producing cells which comprise between 5 and 10% of the cells in the basal layer (stratum basalis) of the epidermis. The production of the skin pigment melanin is stimulated by ultraviolet radiation (melanogenesis). Melanocytes have several arm-like structures (dendrites) that stretch out to connect them with many keratinocytes. Once synthesized, melanin is contained in the melanosomes and moved along the dendrites to reach the keratinocytes. The melanin molecules are stored within keratinocytes (and melanocytes) in the perinuclear area, around the nucleus, where they protect the DNA against ultraviolet radiation. Thereby, a melanin molecule transforms nearly all the radiation energy in to heat. This is done by ultrafast internal conversion of the energy from the excited electronic states into vibrational modes. The ultrafast conversion shortens the lifetime of the excitation states and therefore prevents the formation of harmful free radicals.

The dermis is connected to the epidermis through a basement membrane (a thin sheet of fibres) and provides anchoring and nourishment for the epidermis. The dermis contains collagen (stability), elastic fibres (elasticity) and an extrafibrillar matrix as structural components. The papillary region (stratum papillae) in the dermis is composed of connective tissue which extends towards the epidermis. These finger-like projections are called papillae and strengthen the connection between the dermis and the epidermis. In addition to the structural components, blood vessels are present in the dermis providing nourishment for the dermal and

epidermal cells. Furthermore, the dermis contains hair follicles, sweat glands and lymphatic vessels. (In addition to the presented components, the dermis also contains mechanoreceptors that enable the sense of touch and thermoreceptors that provide the sense of heat). The hypodermis is beneath the dermis. Its tasks comprise energy storage, heat insulation and the connection of the skin with inner structures like muscles and bones. The hypodermis consists primarily of loose connective tissue and adipocytes (fat cells), which are grouped together in lobules (subcutaneous fat). Furthermore, the hypodermis contains larger blood vessels and nerves than those found in the dermis.

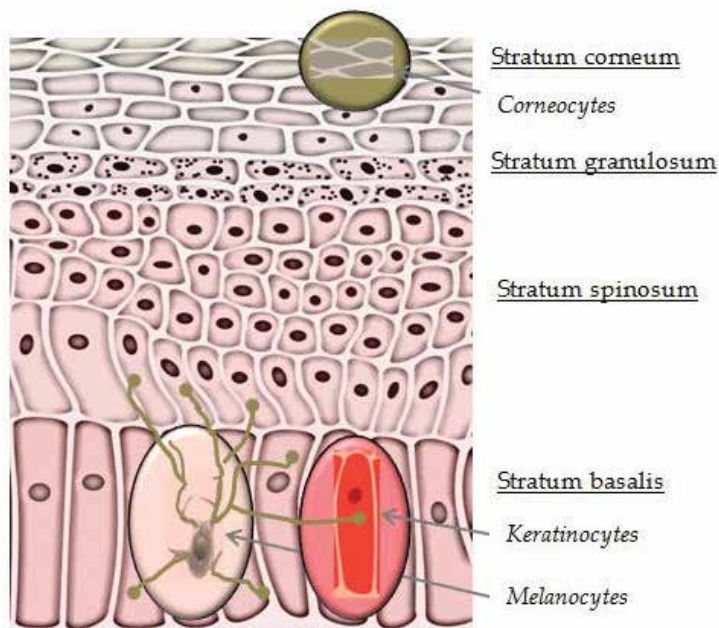


Figure 1. The layer architecture of the epidermis.

2. Malignant melanoma and benign nevi

The primary cause for the increasing number of melanomas is the extreme sun exposure during sun-bathing (especially for people with low levels of skin pigment). The malignant melanoma is a type of cancer that develops from the pigment containing melanocytes [4]. Melanomas are mainly caused by DNA damage resulting from the ultraviolet radiation [5]. It is observed that strongly pigmented people are less susceptible to (sun induced) melanomas, which demonstrates the protection function of melanin. At the early stage, melanocytes begin an out-of-control growth [5]. In a posterior stage (invasive melanoma), the melanoma may grow into the surrounding tissue and can spread out around the body through lymph or blood vessels deeper in the skin. People with melanomas at the early stage are treated by surgical removal of the skin lesion. In cases where the melanoma has spread out, patients are treated by

immunotherapy or chemotherapy. Most people are cured if spreading has not occurred. Therefore, the early and reliable recognition of melanomas at the early stage is of special importance [6]. The difference between a benign or malignant tumour is its invasive potential. If a tumour lacks the ability to invade adjacent tissues and to metastasize then it is benign, whereas a malignant tumour is invasive or metastatic. A nevus (birthmark) is a sharply circumscribed and benign chronic lesion of the skin. The melanocytic nevus results from benign proliferation of the dendritic melanocytes. Due to the pigment melanin, they are mostly brown. Nevus cells are related to the melanocytes, but they show a lack of the dendrites and are oval in shape. They are typically arranged in cell nests. The majority of acquired nevi appear during the childhood up to young adults (the first two decades of life). A melanocytic nevus present at birth is called a congenital nevus. They are rarely about one in every 100 newborns. Nevi are harmless. However, 25% of malignant melanomas arise from pre-existing nevi.

3. Confocal laser scanning microscopy

In conventional microscopy, the entire field of a tissue sample is simultaneously illuminated by light and displayed. Although the brightest light intensity results from the focal point of the objective lens, other parts of the tissue are still illuminated, resulting in a large unfocused background section. This background noise diminishes the image quality. Both conventional and confocal laser scanning microscopy (CLSM) can use reflected light to image a tissue sample. The reflected light from the illuminated spot is then re-collected by the objective lens. In addition to the reflected light from the focal point, the scattered light from sample points outside the focus light (coming from places above or below the focus) is projected by the optical system of the microscope and therefore contributes to the image assembly. This causes a blurring and obscuring of the resulting image. Confocal microscopy overcomes this problem by placing a pinhole in the conjugate focal plane (hence the designation confocal) that allows only the light emitting from the desired focal spot to pass through [7]. Any light outside of the focal plane (the scattered light) is blocked. **Figure 2** shows the principle: the out of focus light (red), coming from places above the selected focal plane, is blocked by the pinhole in the conjugate focal plane. The (in focus) light from focal plane (blue) can pass through the pinhole and is detected. Therefore, a blurring is avoided and sharp and detailed images are produced (in other words: the image information from multiple depths in the sample is not superimposed). In confocal microscopy, a light beam is directed by a dichroic mirror to the objective lens where it is focused into a small focal volume at a layer within the tissue sample (**Figure 3**). A laser, with a near-infrared wavelength, is used as a coherent monochromatic light source. The same microscope objective gathers the reflected light from the illuminated spot in the sample. The dichroic mirror separates the reflected light from the incident light and deflects it to the detector. Before the light reaches the detector, the out of focus sections are blocked by the pinhole in the conjugate focal plane. The in focus light that passes through the pinhole is measured.

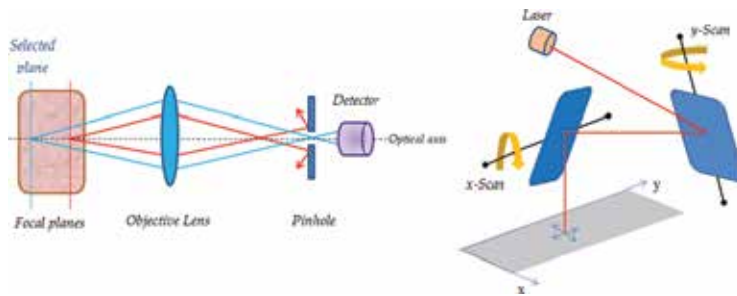


Figure 2. Principle of the confocal (left) and laser scanning (right) microscopy.

The detector, which is usually a photomultiplier tube or avalanche photodiode, amplifies and transforms the intensity of the reflected light signal into an electrical one that is recorded by a computer. In contrast to conventional microscopy, there is never a complete image of the sample at any given instant; rather only one point in the selected plane of the sample is observed. In order to create an image, light from every point in the plane (x-axis, y-axis) must be recorded. This can be done by a raster scanning mechanism which uses two motor driven high-speed oscillating mirrors, which pivot on mutually perpendicular axes. Coordination of the two mirrors, one scanning along the x-axis and the other on the y-axis, produces the rectilinear raster scan (**Figure 2**). During the scanning process, the detected signal is transferred to a computer that collects all the 'point images' of the sample and serially constructs the image pixel by pixel. The brightness of a resulting image pixel corresponds to the relative intensity of the reflected light. The contrast in the images results from variations in the refractive index of microstructures within the tissue. Information can be collected from different focal planes by raising or lowering the objective lens. Then successive planes make up a 'z-stack'. A stack

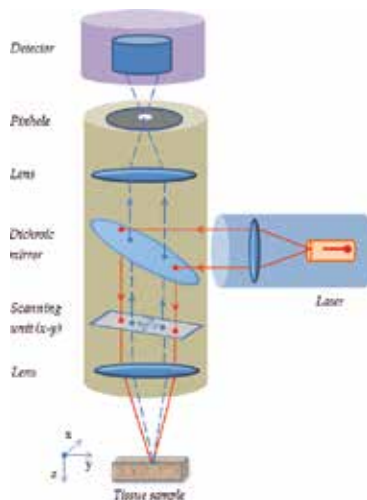


Figure 3. Principle of the confocal laser scanning microscope.

is a sequence of images captured at the same horizontal position (x- and y-axes) at different depths (z-axis). The images are taken enface (horizontally). The confocal laser scanning microscopy is performed with a Vivascope 1000 (Lucid Inc., USA) which uses a diode laser at 830 nm wavelength and a power of <35 mW at tissue level. A $\times 30$ water-immersion objective lens with a numerical aperture of 0.9 is used with water as an immersion medium. The spatial resolution is 0.5–1.0 μm in the lateral and 3–5 μm in the axial dimension.

The images contain a field-of-view of 0.5×0.5 mm. Up to 16 layers per lesion can be scanned. All images, stored in BMP file format, are monochrome images with a spatial resolution of 640×480 pixels and a grey level resolution of 8 bits.

4. Interpretation of confocal laser scanning microscopic images

The reflectivity of the tissue depends on chemical structures. Melanin and melanosomes have a high refractive index which contributes strongly to the contrast of the resulting image [8–10]. Due to such dominating variations of the refractive index, only a certain part of the in falling light is reflected. This makes the appearance of the tissue in a CLSM image so different from conventional histological views. The power of the 830 nm laser limits the imaging depth to a maximum of 350 μm , corresponding to the papillary dermis (higher power could damage the skin). **Figure 4** shows the views of different skin layers [11]. The stratum corneum shows large polygonal anucleated corneocytes (A). Skin folds and marks appear as dark structures. The next layer is the stratum granulosum (B). The stratum spinosum (C) contains keratinocytes in a honeycomb pattern. In the stratum basalis (D), the basal cells are uniform in size and show higher reflections than spinous keratinocytes and appear very intensively. The dermatological guidelines for the interpretation of melanocytic skin lesions in CLSM views are as follows.

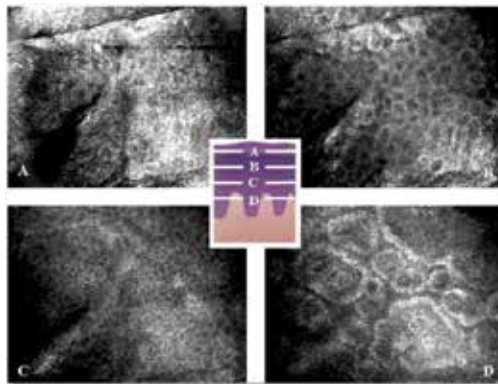


Figure 4. CLSM views of normal skin.

For the diagnosis of CLSM views of benign common nevi and malignant melanoma, architectural structures such as micro-anatomic structures; cell nests, etc., play an important role [12].

Monomorphic melanocytic cells, melanocytic cell nests and readily detected keratinocyte cell borders are suggestive of benign nevi, whereas polymorphic melanocytic cells, disarray of melanocytic architecture and poorly defined keratinocyte cell borders are suggestive of melanoma (**Figure 5**). The images are taken from the centre of the tumours.

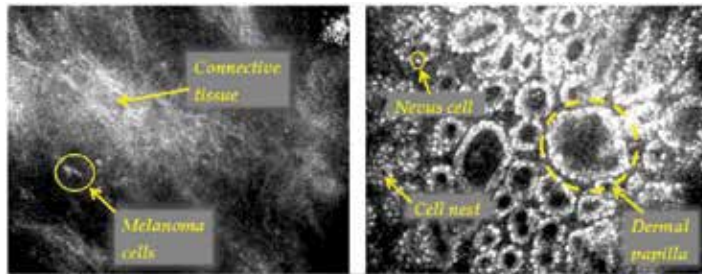


Figure 5. CLSM images of malignant melanoma (left) and common benign nevi (right).

Layers from the plane of the spinous keratinocytes (polygonal cells) to the plane of the basal cells (dermo-epidermal junction) are used for diagnosis.

5. Analysis of tissue structures at different scales

As shown in the previous section, the information at different scales (from coarse structures to details) plays a crucial role in the diagnosis of CLSM images of skin lesions. Wavelet analysis is a method to analyse visual data by taking into account scale information [13].

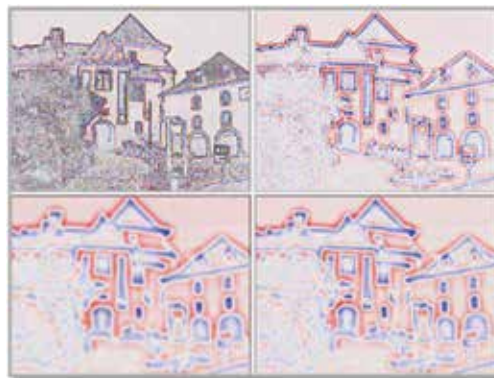


Figure 6. Scale-space sequence of a successively Laplacian of Gaussian-filtered image.

The multiple resolutions enable a scale invariant interpretation of an image. **Figure 6** illustrates the principle of scale space analysis for four levels of scale (clockwise direction). In the top left

image (scale 1), the feature detection responds to fine texture. The images at higher scales are generated by a Laplacian of Gaussian filter ($\text{LoG}(x, y)$), which is also known as Marr-Hildreth operator or Marr wavelet (**Figure 7**), whereby the kernel size (σ) of the Gaussian increases step by step.

$$\text{LoG}(x, y) = \frac{1}{\pi\sigma^4} \left(\frac{x^2 + y^2}{2\sigma^2} - 1 \right) \cdot e^{-\frac{x^2 + y^2}{2\sigma^2}}$$

The blue and red colours indicate positive and negative values. The images become increasingly blurred and smaller details (or regions) progressively disappear. The detected features are then associated with a larger scale scene structure. The multiresolution analysis is closely analogous to the human vision system which seems to prefer methods of analysis that run from coarse to fine and, repeating the same process, obtain new information at the end of each cycle [14] (**Figure 6** counter clockwise direction). The wavelet decomposition can be realized as a convolution of the image with a filter bank, consisting of high pass and low pass filters [15]. Whereby, for example a first-order derivative can be used as a convolution kernel for the high-pass filter and a moving average as a kernel for the low-pass filter. In our study, the filter coefficients are defined by the Daubechies 4 wavelet transform.

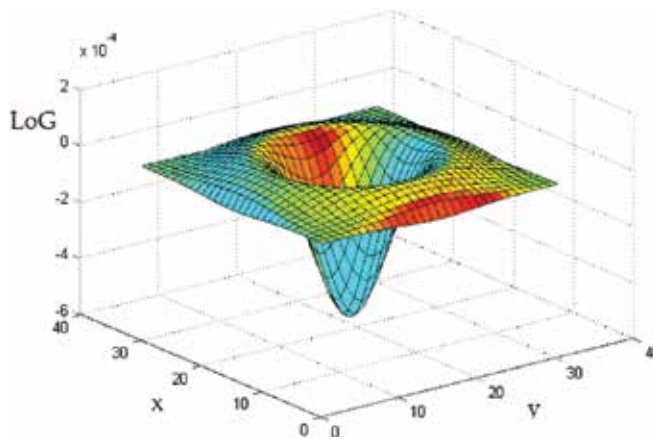


Figure 7. Shape of the Laplacian of Gaussian convolutional filter kernel.

The wavelet decomposition performs a multi resolution analysis, whereby the image is successively decomposed by the filter operations followed by sub-sampling. The (pyramidal) algorithm consists of several steps and operates as follows: at the beginning, the image rows are filtered by the high-pass filter and in parallel by the low-pass filter (**Figure 8**). From both operations result two images (which are called sub-bands), one shows details (high pass) and the other is smoothed out (low pass). The sub-sampling is done by removing every second column in both sub-bands. Subsequently, the columns of both sub-bands are high-pass and

independently low-pass filtered. This results in four sub-bands, which differ by the kind of filtering. Again a sub-sampling is done by removing every second row in each sub-band. This is the end of the first step. The mixed filtered (high-low pass, etc.) sub-bands are stored. Only the double low-passed sub-band is processed in the second step (**Figure 8**). The second step repeats the operations of the first step. Again this results in four sub-bands and the fourth smoothed sub-band is used as entry for the following step. At every step, the resulting sub-bands are reduced to half the resolution. The sub-bands with higher spatial resolution contain the detailed information (high pass), whereas the sub-bands with the low-resolution represent the large scale coarse information (low pass). The output of the wavelet decomposition consists of the remaining ‘smooth-...-smooth’ components and all the accumulated ‘detail’ components. In other words, via the wavelet decomposition, the image array is decomposed into several sub-bands representing information at different scales. The output of the last low-pass filtering is the mean gray level of the image.

After the dissection of the quadratic sub-bands, they are usually arranged in a quadratic configuration, whereby the three sub-bands of the first step fill 3/4 of the square, the three sub-bands of the second step fill 3/16 of the square, etc. The sub-bands representing successively decreasing scales are labelled with increasing indices (**Figure 9**). Then, the architectural structure information is accumulated along the way of the sub-bands (from coarse to fine). In image processing, it is convenient to display the smoothed image as lowest sub-band in the upper left corner of the quadratic sub-band configuration. The coefficients values in the different sub-bands reflect architectural and cell structures at different scales.

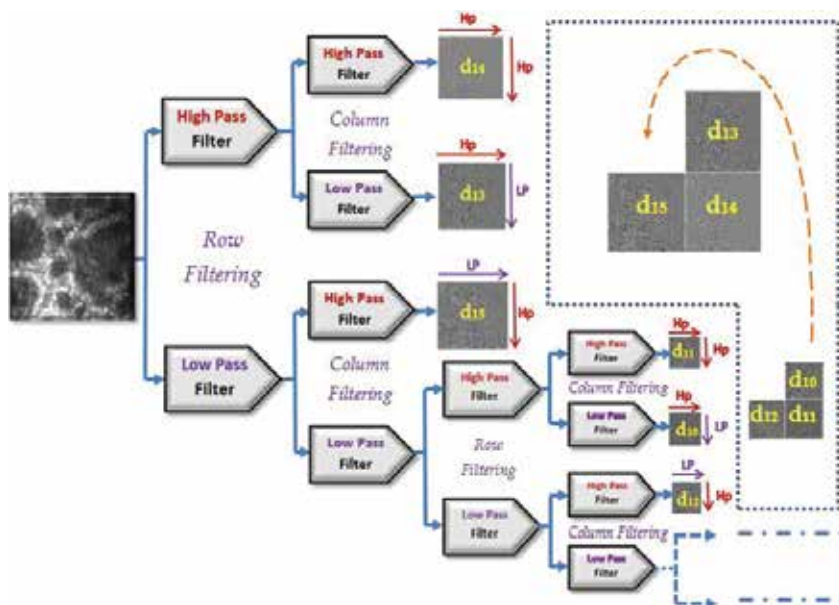


Figure 8. The multiresolution filter bank of the wavelet decomposition.

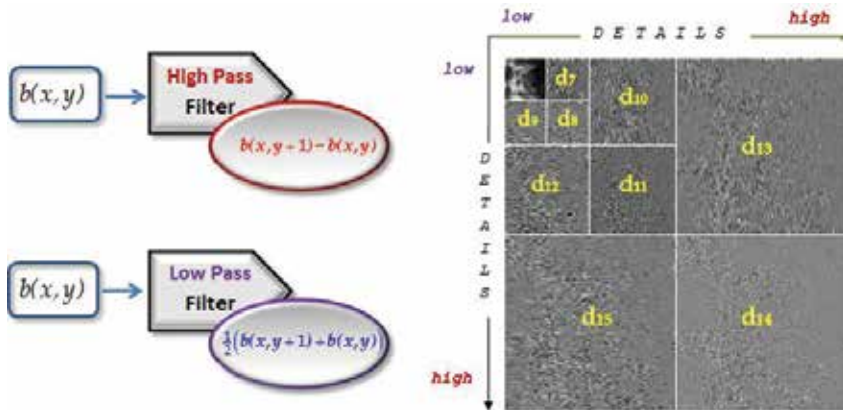


Figure 9. The sub-bands resulting from the successive high and low pass filter operations.

The tissue features are derived from statistical properties of the sub-band coefficients. For the i th sub-band of size $N \times N$, the coefficients are given by:

$$d_i = \{d_i(k, l) | k, l = 1, N\}$$

The texture features are based on the variations of the coefficients within each sub-band and the weighted sum of all the coefficients into each sub-band. The standard deviations of the coefficients inside the single sub-bands and the energy and entropy of the different sub-bands are calculated and used as features (for details see: [16]). The standard deviation of the coefficients represents how exposed the tissue structures in the considered sub-band at the given scale are. The total energy of the coefficients in a given sub-band shows to what degree the structures at the corresponding scale contribute to the image. The distribution of the energy of the sub-bands is represented in a power spectrum, enabling an evaluation of their relative contributions.

The next task in automated image analysis is the use of machine-learning algorithms for classification purposes on hand of the feature values [17]. The algorithm learns, by use of a training set, how to assign the tissue images to given classes. Then, in future, the algorithm can apply the gained knowledge to predict the class of unknown tissue. By means of the classification procedure, the primary inhomogeneous set of CLSM samples, consisting of a mix of malignant melanoma and benign common nevi cases, is split into homogeneous subsets, which are assigned to one of the two tumour classes: common benign nevi or malignant melanoma. A homogeneous subset means that it contains only CLSM images with similar feature values, representing one specific kind of tissue. For the discrimination of the CLSM images, the CART (Classification and Regression Trees) algorithm is used [18].

The tree representation consists of different nodes and branches. There is a root node, several leaf (terminal) nodes and inner nodes (**Figure 10**). The first node in the tree is the root node. It

contains the feature values of the whole set of CLSM image samples. A leaf node is a homogeneous node which contains only samples belonging to the same class of tissue. The inner nodes contain more or less inhomogeneous sample sets. A branch in the decision tree involves the testing of one particular texture feature (binary tree). Then, the considered node, which is the parent node, is split into two child nodes (Figure 10).

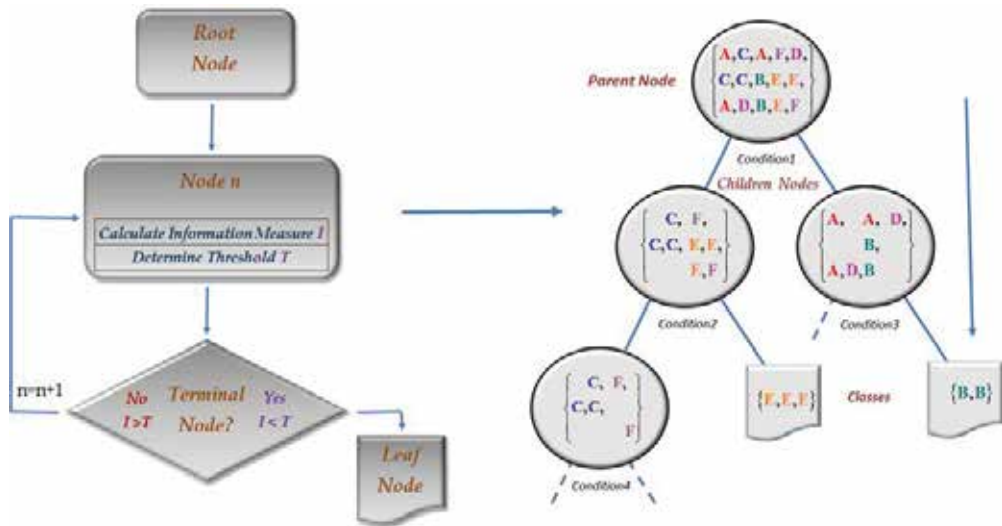


Figure 10. Generation of a decision tree.

The feature is tested by comparing its numerical value with a threshold value that divides the value range. The threshold value is selected automatically by the algorithm in such a way that the subsets of samples in the child nodes are purer than the set in the parent node. To this purpose, an information measure is used which indicates the degree of homogeneity; the value in the leaf nodes is zero and the higher the value of an inner node, the higher is its inhomogeneity. At every branch in the tree, subsets with smaller values of the information measure are generated. The decision tree is generated recursively (details are shown in: [16]). Whereby the algorithm consists in principal of three parts: the determination of the optimal splitting at every node; the decision whether the node is a leaf node or an inner node; the assignment of a leaf node to a specific class (Figure 10). To classify an unknown sample, it is routed down the tree according to the values of the different features. When a leaf node is reached, the sample is classified according to the class assigned to the leaf. The tree-based machine-learning algorithm captures the decision structure explicitly. That means the generated decision rules are 'Modus Ponens', with a precondition and conclusion part, and are intelligible in such a manner that they can be understood, discussed and used as diagnostic rules.

$$IF(\dots and.Condition1.and.Condition2)THEN(Class := A)$$

In total, 39 different features are calculated for 16 frequency bands (labelled from 0 to 15). The mean value is calculated from the first four frequency bands; therefore, 13 values result for each feature. The highest frequency bands contain only information about very fine grey level variations, such as noise, and are therefore not considered for the image analysis. The procedure for image analysis (including feature extraction and calculation) was developed with the 'Interactive Data Language' software tool IDL (IDL 7.1, ITT Visual Information Solutions). The tree classification is done by the CART analysis software from Salford Systems, San Diego, USA.

6. Biological motivation for neural networks

A neuron is an electrically excitable cell that receives, processes and transmits information as electrochemical signals. It consists of several dendrites, the soma and an axon (**Figure 11**). The soma is the cell body which contains the nucleus and all the necessary cytoplasmic cell structures. The dendrites are cytoplasmic extensions of the cell body with many branches allowing the cell to receive signals from other neurons. The axon is a special extension which carries signals away from the soma. At its terminal, the axon undergoes extensive branching, enabling communication with many target cells. The neurons maintain voltage gradients across their membranes. Ion channels, embedded in the membrane, enable the generation of intracellular-extracellular ion migrations. The resulting changes in the cross-membrane polarization generate an electrochemical pulse, known as the action potential. These changes in the cross-membrane potential are transferred as a wave of successive depolarization and repolarisation processes along the cell's axon. The axon terminal contains synapses, specialized connections to target neurons, where neurotransmitter chemicals are released. Synaptic signals may be excitatory or inhibitory. Once the pulse from the soma along the axon reaches the synapses, a neurotransmitter is released at the synaptic cleft. The neurotransmitter molecules bound at the receptors in the post-synaptic membrane (of the target neuron) and opens ion channels. Then, the electrochemical pulse is transmitted to the target neuron.

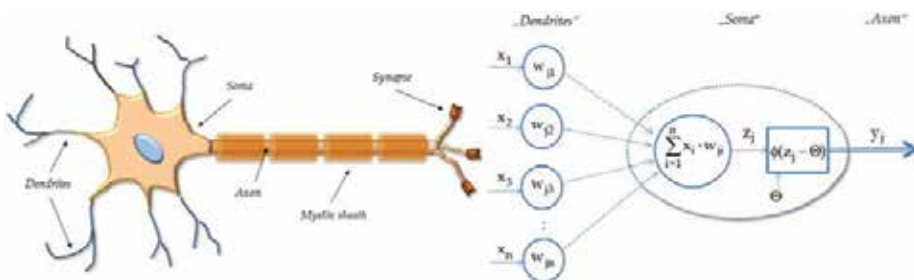


Figure 11. Microanatomy of a natural neuron (left), principle of an artificial neuron (right).

An artificial neuron is a mathematical model of a biological neuron. Artificial neurons mimic the behaviour of the biological neurons. The input of the artificial neuron is represented by a

vector: $x = (x_1, x_2, \dots, x_n)$, whereby its dimension reflects the number of contributing dendrites (**Figure 11**). In the mathematical model, each 'dendrite' contributes individually through a weighted signal to the input signal. The weight factor $w_j = (w_{j1}, w_{j2}, \dots, w_{jn})$ simulates the ratio of synaptic neurotransmitters, whereby positive values represent excitatory and negative values inhibitory behaviour (a weight value zero means that there is no connection between the involved neurons). The summation function represents the soma of the neuron j . The exciting and inhibiting signals are added in the function:

$$z_j = \sum_i x_i w_{ji}$$

The firing behaviour of the neuron is represented by the activation function. Its activation depends on the output of the summation function z_j and a threshold value Θ . If the summation function exceeds the threshold, the neuron is firing and transmits an output signal y_j :

$$y_j = \phi(z_j - \theta)$$

The biological motivation of the activation function is the threshold potential in natural neurons. Step and sigmoid functions are often used as transfer functions.

7. Artificial neural networks

Artificial neural networks consist of a number of artificial neurons, the computational units, which are interconnected. Each unit performs some small calculation based on inputs it receives from other units, whereby the associated weight factors can be tuned. This tuning occurs by allowing the network to analyse many examples of previously observed data. The most common type of neural network is the feed forward neural network (containing no loops), and in such networks, the computational units are organised into layers from an input layer, where data are fed into the network, to an output layer, where the result of the network's computation is outputted in the form of a classification result or regression result (**Figure 12**). Traditionally, each neuron in a layer is connected to all other neurons in the previous or subsequent layers (fully connected network). Between the output and input layers are hidden layers, and networks that consist of more than one hidden layer are known as *deep learning* algorithms. Such feed forward neural networks have been shown to be universal approximators, that is to say they can learn to approximate any continuous function to arbitrary precision, given enough hidden neurons [19]. Neural networks must be trained. The training data are previous observations that have been collected, and the task of the network is to learn a function which should map new input data to a classification label.

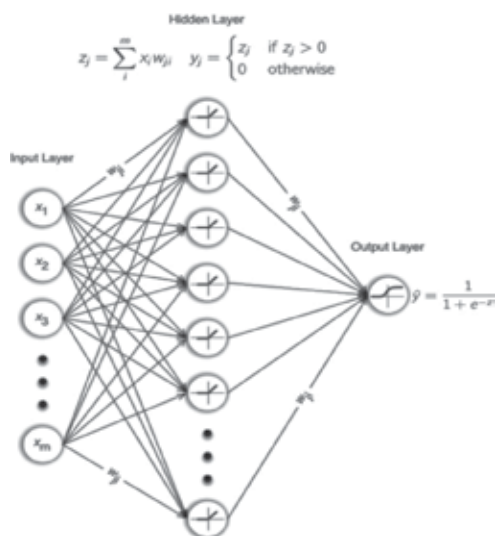


Figure 12. Structure of a feed forward artificial neural network.

In general, feed forward neural networks are supervised machine-learning algorithms. **Figure 12** shows a network with three layers: (1) an input layer, where data are fed in, (2) a hidden layer consisting of neurons that each contain an activation function that reads in data from the input neurons, performs some calculation, and outputs a value, and (3) an output layer that reads data from the hidden layer and makes a prediction based on this input. All connections between neurons have independently adjustable weights (Section 6). All layers are fully connected meaning that each neuron in the input layer is connected to every neuron in the hidden layer. The network learns by adjusting the weights between each of the connected neurons until the network makes good predictions by minimising an error function (backpropagation algorithm).

Fully connected neural networks are useful where individual features of a dataset are not very informative. In image data, where an individual pixel is not likely to be very informative taken on its own, a local combination of pixels may very well be informative and represent an object of interest. However, neural networks are also far more computationally intensive than many other machine-learning algorithms, with the number of tuneable parameters quickly growing into the millions as the network increases in depth or size. Also, neural networks typically work on image data directly, without feature reduction, meaning the dimensionality of the data being analysed by neural networks is much higher than that of other algorithms, which often work on extracted features. One could therefore summarise that neural networks are most useful for high m high n problems—problems where there exist many observations (n) of high dimensional data (m). Of late, neural networks algorithms have re-emerged as a popular technique in machine learning, especially in the field of image analysis. This re-emergence has come due to a number of recent developments in neural network design as well as independent hardware developments. In real-world applications, their usage has grown beyond image analysis and has also been shown to be useful for other tasks, such as natural

language processing and artificial intelligence [20, 21]. Nevertheless, a number of advancements in recent years resulted in an upsurge in the usage of neural networks.

First, hardware advancements have made it feasible for larger neural networks to be trained in reasonable amounts of time. As mentioned previously, neural networks that learn on very high-dimensional data require many neurons and layers, meaning networks can consist of many millions of parameters that need to be tuned. This results in large network architectures that have, for a long time, been unfeasibly difficult to train on standard desktop workstations. However, computational enhancements have meant this is no longer the case. These computational advancements are the result of rapid developments in graphics processing unit (GPU) technology due to the ever increasing requirements of the gaming industry, resulting in great improvements in the parallel processing power of GPUs. In 3D gaming, the vast majority of processing power is spent on matrix multiplications, such as transforms and perspective calculations, in order to depict the 3D worlds of games in 2D to the user. Such calculations are, for the most part, performed using matrix and vector multiplications. Such matrix calculations can be performed in parallel, and hence gaming GPUs have evolved to be particularly suited to such parallel processing tasks. To this end, GPUs typically consist of boards with many small, less powerful cores that can perform highly parallel computations. While CPUs tend to possess 2–4 large and fast cores, GPUs possess many hundreds of smaller cores. Crucially, almost 90% of the computational effort required to train a neural network is spent on vector, matrix, and tensor operations, meaning they can benefit from all the recent technological advancements in GPU technology. Indeed, with Moore's Law no longer holding, parallelised algorithms may, in future, be the only way to analyse very large data [22]. Second, empirical data have shown that neural networks with large numbers of hidden layers outperform many algorithms at several machine-learning tasks, especially in computer vision, object recognition and object detection. Deeper and deeper neural networks, with larger and larger numbers of neurons, have achieved human-level performance at very human-like tasks, such as playing video games [23] and playing the game of Go [24]. Deeper networks, however, contain more neurons, each of which needs to perform some calculation, and have its associated weight tuned, resulting in longer training times and larger memory requirements. Again, advances in hardware and optimisation techniques have meant that ever deeper networks are now trainable within reasonable timeframes [25]. Third, more and more data are permanently stored, archived and saved than ever before. This is especially true in fields such as medicine, where large amounts of data are accumulated during routine activities. In the past, these data might have been archived or stored in offline tape drives, or even discarded. However, this is no longer necessarily true as the cost per GB of storage has declined so rapidly, meaning easier access to more data and less likelihood of data being discarded. Deep learning algorithms require large amounts of data to train and access to very large datasets, and the ability for individuals to store large amounts of data has meant they are being applied to such problems more often.

Traditional feed forward neural networks consist of layers, where each neuron is connected to every other neuron in the layers above and below it. These are known as fully connected, or affine, layers. Fully connected neural networks do not consider the spatial relation between

pixels in an image. Pixels which are close together are treated exactly like pixels which are far apart when being processed by the network. For the learning of high-level features, this is suboptimal. In terms of image analysis, one particular type of neural network algorithm has stood out as being especially adept at image classification and object recognition. This is the convolutional neural network. The idea behind convolutional neural networks is to restrict the network to take inputs only from spatially nearby neurons. In other words, the layers are not fully connected, as in the example in **Figure 12**.

8. Convolutional neural networks

In the fields of image analysis, object detection and pattern recognition, convolutional neural networks are the state of the art algorithm for practical applications. Following on from our previous work, where we applied multiresolution analysis and CART as tree-based machine-learning method (Section 5), we decided to test the applicability of convolutional neural networks at a similar classification task. Because neural networks learn their own discriminatory, high-level features, the dataset requires no pre-processing or feature extraction, with the exception of image resizing and pixel value normalisation. This is in direct contrast to our previous efforts, where a dedicated feature extraction phase was necessary. Convolutional neural networks (CNN), in effect, emulate the way in which classical pattern recognition works, where local features (edges, corners, etc.) are extracted and combined to generate higher level representations that can be used for object recognition. Convolutional neural networks are locally connected, where each neuron is connected only to those that are spatially close (local receptive fields) in the previous layer, mimicking the visual cortex of some animals. Pixels that are closer to each other are more strongly correlated than those which are further away from each other, and this is something which the convolutional neural network has been designed to be able to account for through its architecture [26].

Network architectures with fully connected layers do not take into account the spatial structure of the images. Instead of using a network architecture which is *tabula rasa*, convolution neural networks (CNN) try to take advantage of spatial structures in images. They use three basic ideas: local receptive fields, shared weights and pooling. It is helpful to represent the input image as a square of neurons, whose values correspond to the pixel intensities. Then, only small, localized regions of the input image are connected to a neuron in the first hidden layer. Such a region in the input image is called the local receptive field for the corresponding hidden neuron. In other words, the hidden neuron learns to analyse its particular local receptive field. If the receptive field has a size of 5×5 pixels, then the hidden neuron is connected by 5×5 weights, which are adjusted during learning. The input of the hidden neuron is given by the summation function:

$$y_j = \sum_{l=0}^4 \sum_{m=0}^4 w_{l,m}^j b_{j+1,k+m}$$

The value $b_{x,y}$ denotes the input activation at position (x, y) . The output of the hidden neuron is given by the activation function, for example the sigmoid function. The convolutional operation can be considered as a sliding window, which travels over the image, with the window centre moving one or more pixel a time. This is defined by the stride length. If the window is moved by one pixel, the stride length is 1. For each position of the local receptive field, there is a different hidden neuron in the first hidden layer. The map from the input layer to the hidden layer (convolutional layer) is called a feature map. The weights $w_{l,m}$ defining the feature map are the shared weights. The shared weights define the convolution kernel (convolution is generally the workhorse of image processing). The pixels in the local receptive field are multiplied element-wise with the kernel. Features maps are generated using only neurons which are spatially close to each other, known as spatial connectivity. Each feature map is defined by a specific set of shared weights enabling the network to detect different kinds of features (edges, corners, etc.). The CNN therefore learns objects related to their spatial structure. For image analysis purposes, more than one feature map are required. Therefore, a complete convolutional layer consists of several different feature maps. In addition to the convolutional layers, CNNs also contain pooling layers which usually follow immediately after the convolutional layers. Pooling layers simplify the information in the output from the convolutional layer by generating a condensed feature map (this removes the positional information of the features learned, meaning the learned features are position invariant). For example, each unit in the pooling layer may summarize a region of 2×2 neurons in the previous convolutional layer. Pooling is done for each feature map separately. The final layer in the convolutional network is a fully connected layer. This layer connects every neuron from the last pooling layer to every one of the output neurons.

A depiction of a typical 7-layer convolutional neural network can be seen in **Figure 13**. Images are read into the network in the input layer. From this input, a number of feature maps (4) are generated, which are subsampled in a max-pooling phase. Then, both phases are repeated once more, before connecting to a conventional fully connected layer which is finally connected to the output layer. CNNs often contain multiple fully connected layers before the final output layer, and modern CNNs can contain many convolution/max-pooling pairs.

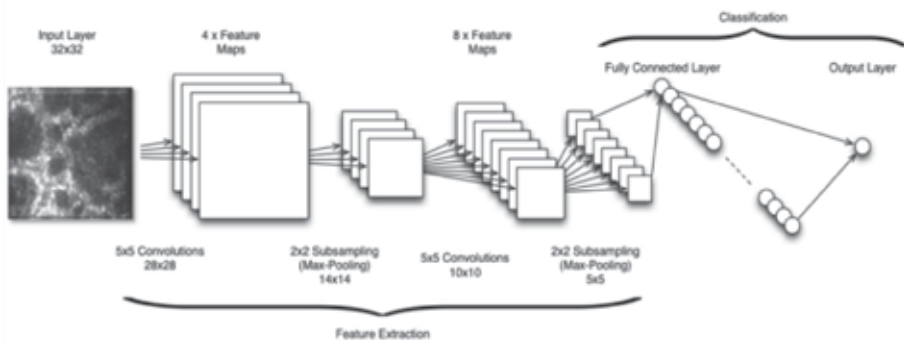


Figure 13. The structure of a typical seven-layer convolutional neural network.

Figure 14 describes the convolutional layer and max-pooling layer in more detail. The input into the convolutional neural network is a vector $\mathbf{x} \in \mathbb{R}^{1 \times m}$, and the input layer has one neuron per feature. However, the layers can be thought as having their neurons arranged as depicted in **Figures 11** and **12**. In the case above, a 5×5 kernel is used, with a stride of 1, which results in a feature map of size $32 - 5 + 1 = 28 \times 28$. Typically, a convolutional layer is followed by a max-pooling layer, which acts as a type of sub-sampling, in this case halving the size of the previous feature map (**Figure 13**).

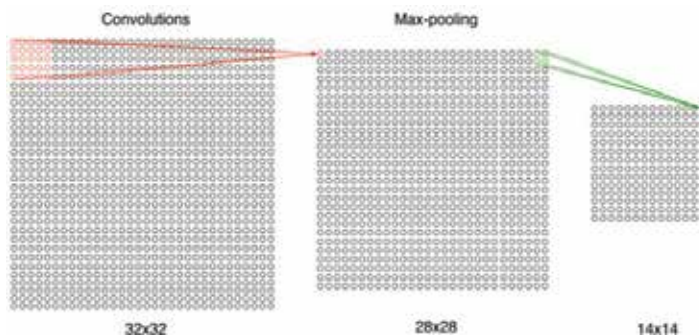


Figure 14. Principle of the convolutional layers and max-pooling layers [27].

Convolutional neural networks possess several characteristics that make them very suitable for the analysis of histological images. First, convolutional neural networks are capable of building models which are translation invariant and robust to transformations in the images, such as rotation, and they can learn features which are robust to scaling. They also generate models which are position invariant. This is especially important for microscopy imagery, where a lesion, for example, has no ‘right way up’, and cannot even be rotationally normalised.

9. Deep learning analysis of a CLSM image dataset

As stated previously, the goal was to train a model which would classify newly seen images as either malignant or benign. The neural network that was designed was based on the structure of the LeNet-5 convolutional neural network structure and was developed using the Keras deep learning library for Python [26]. The network consisted of a total of eight layers: the input layer, two pairs of convolutional and max-pooling pairs, two fully connected layers, and the output layer. The rectified linear unit (ReLU) was used throughout as the neuron nonlinearity. The ReLU is a computational unit which uses a ramp function [the rectifier $f(x) = \max(0, x)$] and is currently the most popular activation function for deep neural networks. Because of the depth of network, a graphics processing unit (GPU) was used, which greatly increases the speed at which the network can train. In terms of hardware, a mid-range NVidia gaming GPU with 2 GB of dedicated video memory and 640 cores was used for training the network. The card is capable of 1306 GFLOP/s and has a memory band-

width of 86.4 GB/s. At the time of writing, the card can be purchased for under \$150. The card was installed in a Linux workstation with 32 GB of RAM and a 3.5 GHz 6-core AMD processor running the Xubuntu 14.04 operating system. To illustrate the differences in computational power between a GPU and CPU, and to demonstrate the enormous impact using a GPU can have on training times, we benchmarked our code. Training the network over 20 epochs required 2 min 4 s of time, averaged over three runs, when using the GPU. When using the CPU, this time was 57 min 59 s for 20 epochs (also averaged over three runs), nearly 30 times slower. Experimenting with different parameters, or testing new network structures, can become very tedious when hours of computational power are required per run or experiment. The GPU reduces this time to minutes.

Dropout was used to control overfitting at two points in the network’s structure: once after the convolutional and max-pooling pairs, and once again after the first fully connected layer. Dropout helps to control overfitting by randomly setting a certain set percentage of the neurons’ weights to zero, effectively forcing the network to relearn those weights, with the intention of mitigating the learning of noise. The output of the network is finally determined by a sigmoid logistic function, squashing the results of the entire network to a value between 0 and 1. Values closer to 1 are therefore classified as being malignant, while values closer to 0 refer to a benign prediction. Such an output can also be used to examine the network’s confidence at a classification, with a value of 0.99 meaning a highly confident malignant prediction and a value of 0.51 representing an unconfident malignant prediction.

9.1. Input into the neural network

Images are read directly by the neural network. The only pre-processing which was performed was to resize the images from 640 × 480 to 64 × 64 pixels. Images are read by the neural network as a series of pixel values stored in a vector. Therefore, a single image is stored as a vector \mathbf{x} , so that one instance of an image $\mathbf{x}^{(i)} \in \mathbb{R}^{1 \times m} = [x_1^{(i)} x_2^{(i)} x_3^{(i)} \dots x_m^{(i)}]$. The dataset consisted of $n = 6897$ images, each 64 × 64 pixels in size, representing a dimensionality $m = 4096$. The entire dataset is therefore stored in an $n \times m$ matrix:

$$\mathbf{X} \in \mathbb{R}^{n \times m} = \begin{bmatrix} x_1^{(1)} & \dots & x_m^{(1)} \\ \vdots & \ddots & \vdots \\ x_1^{(n)} & \dots & x_m^{(n)} \end{bmatrix}$$

To reduce the memory footprint, neural networks are typically trained using mini-batches, which are randomly selected subsets of \mathbf{X} . Targets, or labels, are stored in an n -dimensional column vector:

$$\mathbf{y} = \begin{bmatrix} y^{(1)} \\ \vdots \\ y^{(n)} \end{bmatrix} \quad (y \in \{0, 1\} \mid 0 = \text{Benign}, 1 = \text{Malignant}).$$

Therefore, to input an image into a neural network, it must first be converted into a vector of pixel values. Each image vector's label is stored numerically in a separate target vector, \mathbf{y} . Once these have been prepared, a training matrix X_{train} , a test matrix X_{test} , and their corresponding target vectors $\mathbf{y}_{\text{train}}$ and \mathbf{y}_{test} must also be generated.

9.2. Keras

Recently, a number of frameworks have been developed for deep learning, ranging from low-level, general purpose math expression compilers, such as Theano, to higher level frameworks such as Torch. For this analysis, the Keras framework was used. Keras is written in Python and is based on the Theano framework. It offers a high level control over network construction, abstracting the low-level Theano code, making it possible to design neural network structures in a layer-wise, modular fashion. Layers and functionality are added to the network piece by piece and are finally compiled into a complete network once the desired structure has been built. Users of Python can install Keras using pip, by typing `pip install keras` at the command prompt. Keras has a number of requirements, including Theano (which can also be installed using `pip install Theano` at the command prompt). Briefly, once Keras has been correctly installed and successfully imported into the environment, a convolutional neural network is created by instantiating an object of the `Sequential` class, and then by adding layers to this object until the desired network is complete. For example, a convolutional layer can be added to the network using the `add` function: `model.add(Convolution2D(...))`. Configuring network properties, such as when to use dropout or specifying which activation function should be used, is also performed using the `add` function of the model object. The network is built in this way until the desired structure has been defined, and is then compiled using the model object's `compile` function. As Keras is based on Theano, the model is generated into Theano code, which itself is compiled into CUDA C++ code, and subsequently run on the GPU. Upon successful compilation the model, it can be trained on a dataset using the `fit` function, which takes the training data set as one of its parameters. A trained model can then be tested using the held back test data, using the trained model's `evaluate` function. Full Python source code for the generation of the model can be found in this book chapter's GitHub repository under <https://github.com/mdbloice/CLSM-classification>. This source file contains a complete implementation of the network, including the generation of all the plots and figures shown in the Section 10.

10. Results

10.1. Multiresolution analysis

Overall, 857 images of benign common nevi (408 images) and malignant melanoma (449 images) were used as study set [29]. To get more insights into the classification performance, a percentage split was performed by using 66% of the dataset for training and the remaining instances (34%) as the test set (**Table 1**). The classification results of 572 cases (276 benign

common nevi, 296 malignant melanomas) in the training set and 285 cases (132 benign common nevi, 153 malignant melanomas) in the test set.

CART	Training set			Test set		
	% Correct	Benign	Malignant	% Correct	Benign	Malignant
Benign	96.6	267	9	78.0	103	29
Malignant	98.0	6	290	84.1	24	129

Table 1. Classification results for features based on multiresolution analysis.

The CART classification shows a correct mean classification of 97.3% samples in the training set and a correct mean classification rate of 81.1% in the test set. In this study, the images were resized to 512×512 pixels. To illustrate the differences in the wavelet sub-bands of both tissues, the spectra of the wavelet coefficient standard deviations are shown for typical views of benign common nevi and malignant melanoma (**Figure 15**). The image of benign common nevi show pronounced architectural structures (so called tumour nests), whereas the image of malign melanoma show melanoma cells and connective tissue with few or no architectural structures. These visual findings are reflected by the wavelet coefficients inside the different sub-bands. The standard deviations of the wavelet coefficients in the lower and medium frequency bands (4–10) show higher values for the benign common nevi than for malignant melanoma tissue, indicating more pronounced structures at different orders of magnitude. The tissue of malignant melanoma appears more homogeneous (due to a loss of structure), and the cells are larger as in the case of benign common nevi. The standard deviations in the sub-bands with higher indices (representing finer and more pronounced structures) are lower than in the case of benign common nevi.

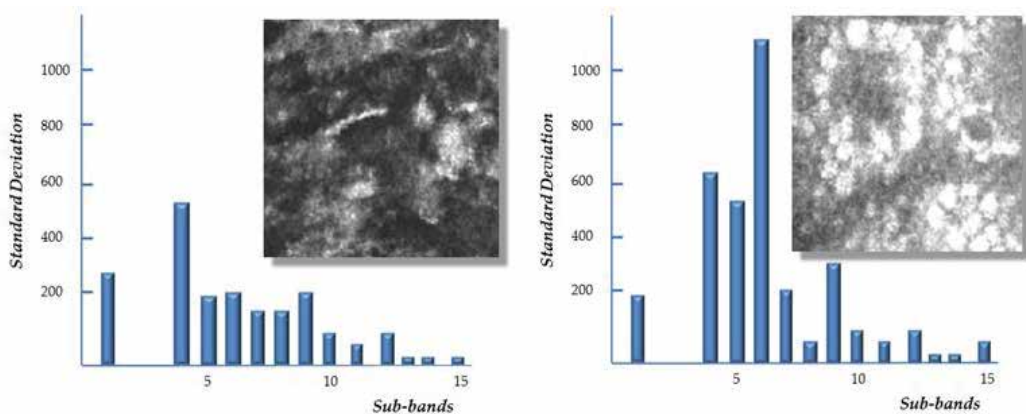


Figure 15. Sub-band spectra for benign common nevi (right) and malignant melanoma (left).

The analysis of the classification tree shows that seven classification nodes indicate benign common nevi and six nodes malignant melanoma. The visual examination of the selected nodes demonstrates characteristic monomorphic melanocytic cells and melanocytic cell nests for benign common nevi [28, 29]. Contrary polymorphic melanocytic cells, a disarray of melanocytic architecture and poorly defined or absent keratinocytic cell borders are characteristic for malignant melanomas.

10.2. Convolutional deep learning neural network

For this study, a dataset consisting of 6897 CLSM images of skin lesions was obtained from our university hospital. The dataset consisted of images of skin lesions in layers of various depths. Before training, the images were randomised and placed into a training set and test set, with the training set consisting of 5000 images and the test set consisting of 1897 images (**Table 2**). It is important to note that, in the case of this project, each image was treated individually, and not treated as belonging to one particular patient or even lesion. The test set, therefore, contained different layers or lesions from potentially the same patient as the training set, as a single patient may have had several scans or may have been examined on multiple occasions.

	Full Dataset	Training Set	Test Set
Total	6,897	5,000	1,897
Benign	3,607	2,655	952
Malignant	3,290	2,345	945

Table 2. The distribution of the classes in the whole dataset and in the training and test set.

Class imbalance occurs when a training set has far more samples of one particular class than another. For example, a small class imbalance existed in the dataset analysed in this chapter, with the samples of benign nevi slightly outnumbering the samples of malignant melanoma (there existed 317 more samples of the former compared to the latter). There are a number of techniques which can be employed to address class imbalance, such as data augmentation (generating synthetic data from your original dataset) or simply by discarding samples to better balance the dataset. In the case of our dataset, class imbalance was not at the degree as to make it problematic. When the training set and test sets were split, however, we ensured that the test set was largely balanced. Class imbalance can also affect how results, such as accuracy and precision/recall, should be perceived when analyzing a trained model on a highly imbalanced test set.

The network, after training for 20 epochs, achieved 93% accuracy on the unseen test set. The model's accuracy on the test set during training, as well as the model's error rate on the training set through each of the 20 epochs is shown in **Figure 16**.

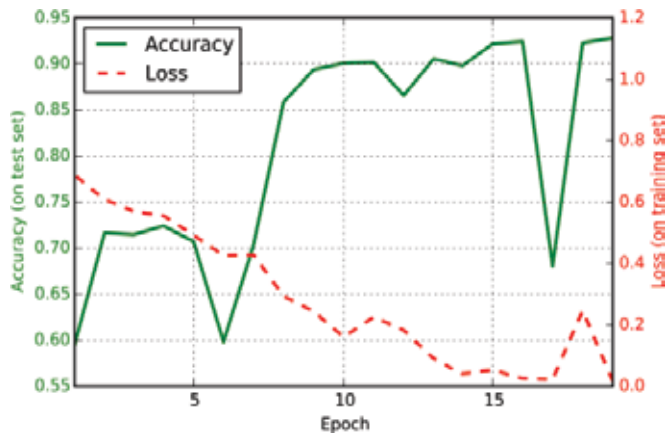


Figure 16. The model’s accuracy on the test set and its logistic loss against the training set.

Loss on the training set eventually reduces to almost 0 (meaning it is at this point overfitting heavily), while the accuracy of the model on the unseen test set fluctuates but is tending towards an accuracy of approximately 90%. The accuracy of the final model after epoch 20, when training was terminated, was 93%. A confusion matrix, shown in **Figure 17**, describes the model’s accuracy on the test set, in terms of absolute numbers of predicted and actual labels for both the benign and malignant classes.

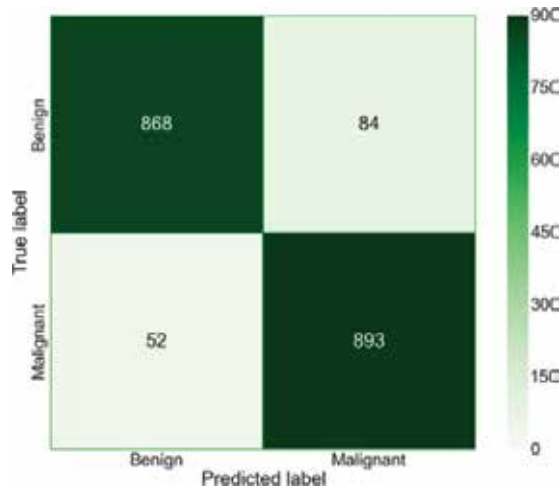


Figure 17. Confusion matrix.

Here, all true/false positives and true/false negatives can be seen. From these values, the precision, recall (sensitivity), and F_1 score (a weighted average of the precision and recall, given by $F_1 = 2 \cdot \frac{\text{precision} \cdot \text{recall}}{\text{precision} + \text{recall}}$) were calculated, as shown in **Table 3**.

	Precision	Recall (Sensitivity)	F_1 score	Support
Benign	0.94	0.91	0.93	952
Malignant	0.91	0.94	0.93	945
Avg/total	0.93	0.93	0.93	1897

Table 3. The generated model's precision, recall and F_1 score measured against the test set.

Table 4 describes the results of the model in absolute terms, with results for the model's predicted labels for both classes versus the actual labels for each class. As well as this, the total number of actual and predicted labels is shown.

Predicted	Actual		Total
	Benign	Malignant	
Benign	868	84	952
Malignant	52	893	945
All	920	977	1897

Table 4. The generated model's predicted labels versus the actual labels, measured on the test set.

10.3. Transfer learning

Transfer learning is a term that can be applied to several aspects of machine learning. In the case of neural network-based machine-learning approaches, transfer learning often refers to the act of using a pre-trained network as the starting point for a learning procedure, rather than starting with a network which has been initialized with random weights. This is often performed as a time-saving measure, but can also be done when the new data to be classified is scarce. Also, it can be performed only when the data used for pre-training is similar to the new data which should be classified. Furthermore, it constrains the practitioner into using a network which has the same architecture of the pre-trained model. Therefore, it is not useable in all situations, and it does not make sense to use, say, a network pre-trained on the ImageNet dataset (a commonly used benchmarking dataset, containing millions of samples of 1000 classes of images) in the context of CLSM lesion classification.

However, there exist several types of laser scanner-based approaches to skin lesion analysis, where the use of transfer learning may be beneficial. Other methods in the field include two photon excitation fluorescence microscopy, second harmonic imaging microscopy, fluorescence-lifetime imaging microscopy and coherent anti-stokes Raman microscopy. Whether or not transfer learning could indeed be implemented in this context would depend entirely on how well the features learned during pre-training match the features that exist in the new data (in other words, whether the learned features transfer well from one domain to the other). For example, several new methods produce colour images, which would mean the features learned in the analysis described here would likely not transfer well to this new domain (of course, colour images could be converted to greyscale). However, it is conceivable that other technol-

ogies, that also produce greyscale images, could make use of a pre-trained network, and thus benefit from pre-trained weight initialisation and therefore transfer learning.

The machine-learning community often makes available pre-trained networks for others to use, such as in the Model Zoo (<https://github.com/BVLC/caffe/wiki/Model-Zoo>). Some of the networks available on the Model Zoo took many weeks to train on powerful hardware, and is considered a very useful resource by many who do not have the time or the computational resources available to them for such an involved learning task. Of course, a pre-trained network could be made available for the CLSM or skin lesion analysis community, if the network was trained on a sufficiently large dataset and if indeed the learned features would transfer well to other domains.

11. Discussion

Confocal laser scanning microscopy is a technique for obtaining high-resolution optical images with depth selectivity. It enables the noninvasive examination of skin cancer in real-time. This makes CLSM very suitable for screening and early recognition of skin tumours, which augment the success of the therapy. The training of pathologists to acquire and refine their visual diagnostic skills is very time-consuming. To implement diagnostic capabilities on a computer, it is of considerable interest to understand how the diagnostic process unfolds and which texture features are critical for a successful diagnosis. For medical diagnosis, it is important to duplicate the automated diagnostic process.

The multiresolution approach with wavelets features mimics the diagnostic guidelines of the dermatopathologist, as they use multiscale features for the examination of CLSM views. The decision rules generated by machine-learning algorithms, such as CART, represent explicit knowledge that can be used to analyse and refine the diagnostic process. The generated rules can be implemented in viewer software which enables a visual evaluation of the diagnostic performance by the dermatologist. This can be used as a training aid for ongoing dermatologists in education. As shown in the Section 10, the algorithm performance allows a correct classification of 78.0% of the benign common nevi cases and 84.1% of the malignant melanoma in the test set. In contrast, sensitivity and specificity of 85.5 and 80.1% are reached by the human observer (overall performance 82.8%).

Although the CART algorithm discriminates the training set automatically (unsupervised), the feature extraction algorithm is predefined. Algorithms based on artificial neural networks do not perform or require hand-defined analyses of the image features with predefined (filtering) methods. Instead, they use neural computation inspired by the visual system of mammals. Neural networks process an image by use of a hierarchical processing architecture which mimics the way the visual cortex processes visual stimuli from the primary cortex (V1) to different layers (V2–V8) which are selective for different components of the visual stimuli such as orientation, colour, size, depth and motion. Neural networks are well suited for detecting similarities in images. However, the distributed representation of the acquired knowledge complicates the extraction of the diagnostic information. They deliver nothing

about the inference mechanism leading to a classification in a form that is easy readable for the human observer. Nevertheless, we can demonstrate a real example as to why artificial neural networks will play an ever more important role in automated medical diagnostic systems. A recent work reported that pigeons (*columba livia*) proved to have a remarkable ability at discriminating benign from malignant human breast histopathology images and at detecting cancer relevant micro calcifications in mammogram images after differential training with food reinforcement [30]. The discrimination was done by the pigeons via two distinctively coloured response buttons. For a correct discrimination, food was immediately provided by a dispenser. The pigeons proved not only to be capable of image memorization but were able to extend the learned skills to novel tissue images. It results that their diagnostic skills are like that of trained humans. It should be noted that the capabilities were acquired without the benefit of verbal instructions as in the case with human education. The low-level vision capabilities of pigeons appear to be equivalent to those in humans; feedforward and hierarchical processing seem to dominate. It can be assumed that pigeons do not explicitly analyse the images with predefined criteria and explicit instructions as humans do. The reinforcement training of the pigeons resembles the training of artificial neural networks. Given the high diagnostic accuracy of the pigeons they may serve as a model for the development and amelioration of artificial networks (or vice versa). We still do not know in detail how pigeons differentiate such complex visual stimuli but colour, size, shape, texture, and configurational cues seem to participate. Their visual discrimination performance may guide the basic research in artificial neural networks in order to develop computer-assisted image diagnostic systems. Experienced dermatopathologists reported that a beginner (a person in education) examines the CLSM views strictly according to the dermatological guidelines (Section 4), as the computers do by multiresolution analysis. Based on the large amount of previously viewed specimens, an experienced person reports the CLSM views more by its visual appearance (personal communication). This is similar to the image analysis performed by a trained neural network. The receptive field of a sensory neuron is a particular region in the visual system in which a stimulus will trigger the firing of that neuron. In vision research, it is known that a cat's visual cortex only develops its receptive fields if it receives visual stimuli in the first months of life [31]. The receptive fields in the primary visual cortex can be thought as 'feature detectors' or 'flexible categorizers'. This means that they learn the structure of the input patterns and become sensitive to combinations that are frequently repeated [14]. This also demonstrates the importance of convolutional neural networks in image processing and analysis.

In this work, and given the relatively small dataset size, the performance of the trained neural network model is encouraging. However, the results must be considered as a proof of concept, and not a model that could be used in a clinical setting, despite the good accuracy of the trained model. For example, the images were collected from a single department, at one hospital in a single region in Austria. To judge the potential real-world accuracy of a trained model would require a far larger dataset, collected from several regions worldwide, and carefully curated to ensure no unintentional bias is introduced (by only collecting data from patients of a certain age range, for example). By training a model on a far larger dataset such a model could be used in real-world clinical settings as a diagnosis aid.

The work here shows that deep layer neural networks have the capacity to learn the high-level discriminatory features required to classify malignant and benign skin lesions. This can be achieved without any dedicated feature engineering phase, data pre-processing or a priori domain knowledge. In the case of the CLSM image classification task presented here, all that was required was a labelled dataset of previous observations. However, what is also true is that neural networks require far more training data than traditional machine vision methods that work on extracted features. This is due to the very high dimensionality of the data, which in our case was \mathbb{R}^{4096} , in contrast to the analysis of the extracted features where the dimensionality was \mathbb{R}^{39} . To compensate for a far higher dimensionality, a much larger dataset is, therefore, a necessity. In other words, deep learning neural networks are most suitable for situations where you encounter data with ‘high m, high n’ properties—high dimensional data, like images, of which many samples exist—such datasets are common in the medical domain, meaning deep learning should be of especial interest to researchers in the area of healthcare informatics.

As parallelized hardware advances, Moore’s law begins to plateau, and the amounts of data being stored increases, algorithms that take advantage of this perfect storm will become more and more relevant. We have shown in this chapter that classical approaches to image classification can indeed be emulated by deep neural networks fed with large amounts of observed data. In fields such as medicine, where data are in such abundance, highly parallelized algorithms may be the only approach that can deal with such large data sources in a meaningful way. Fortunately, this is no longer the domain of specialized research institutes with access to cluster computing: such algorithms are trainable without large investments in hardware and can be performed on a standard desktop workstation equipped with a modestly priced GPU.

Author details

Marco Wiltgen* and Marcus Bloice

*Address all correspondence to: marco.wiltgen@medunigraz.at

Institute for Medical Informatics, Statistics and Documentation, Medical University of Graz, Graz, Austria

References

- [1] Schaller A, Sattler E, Burghof W, Röken M: Color Atlas of Dermatology. 1te ed. Thieme Verlag. Stuttgart, New York. 2012; 978–3131323415
- [2] Sterry W, Paus R: Thieme Clinical Companions Dermatology. Thieme Verlag. Stuttgart, New York. 2006 3–13–1359110

- [3] Bologna J.L, Jorrizo J.L, Schaffer J.V: *Dermatology: Expert Consult Premium Edition*. Saunders. 3 edition UK. 2012; 978-0723435716
- [4] Markovic S.N, Erickson L.A, Flotte T.J, Kottschade L.A. Metastatic malignant melanoma. *G Ital Dermatol Venereol*. 2009;144(1):1-26.
- [5] Oliveria S, Saraiya M, Geller A, Heneghan M, Jorgensen C. Sun exposure and risk of melanoma. *Arch Dis Child*. 2006;1(2):131-138.
- [6] Friedman R, Rigel D, Kopf A. Early detection of malignant melanoma: the role of physician examination and self-examination of the skin. *CA Cancer J Clin*. 1985;35(3): 130-151.
- [7] Pawley J.B. *Handbook of Biological Confocal Microscopy*. 3rd ed.. Springer, Berlin; 2006. 0-387-25921-X.
- [8] Paoli J, Smedh M, Ericson M.B. Multiphoton laser scanning microscopy—a novel diagnostic method for superficial skin cancers. *Semin Cutan Med Surg*. 2009;28(3):190-195.
- [9] Patel D.V, McGhee C.N. Contemporary in vivo confocal microscopy of the living human cornea using white light and laser scanning techniques: a major review. *Clin Exp Ophthalmol*. 2007;35(1):71-88.
- [10] Rajadhyaksha M. Confocal microscopy of skin cancers: translational advances toward clinical utility. *Conf Proc IEEE Eng Med Biol Soc*. 2009;1:3231-3233.
- [11] Hofmann-Wellenhof R, Pellacani G, Malvehy J, Soyer H.P. (eds). *Reflectance Confocal Microscopy for Skin Diseases*. Springer, Berlin Heidelberg; 2012; 978-3-642-21996-2.
- [12] Pellacani G, Cesinaro A.M, Seidenari S. In vivo assessment of melanocytic nests in nevi and melanomas by reflectance confocal microscopy. *Mod Pathol*. 2005;18:469-474.
- [13] Prasad L, Iyengar S.S. *Wavelet analysis with applications to image processing*. CRC Press, Boca Raton; 1997.
- [14] Marr D. *Vision*. W.H. Freeman, New York, 1982.
- [15] Strang G, Nguyen T. *Wavelets and Filterbanks*. Wellesley-Cambridge Press. MA USA; 1996.
- [16] Wiltgen M. Confocal laser scanning microscopy in dermatology: Manual and automated diagnosis of skin tumours. In: Chau-Chang Wang editor. *Laser Scanning, Theory and Applications*, Intech Publisher. Croatia. 2011;133-170. ISBN 978-953-307-205-0)
- [17] Murphy, K.P. *Machine learning: a probabilistic perspective*. MIT press, USA. 2012.
- [18] Breiman L, Friedman J, Olshen R.A, Stone C.F. *Classification and Regression Trees*. Chapman & Hall, New York, London; 1993.

- [19] Hornik K, Stinchcombe M, White H. Multilayer feedforward networks are universal approximators. *Neural Netw.* 1989;2(5):359–366.
- [20] Kalchbrenner N, Grefenstette E, Blunsom P. A convolutional neural network for modelling sentences. *arXiv preprint arXiv:1404.2188*, 2015.
- [21] Collobert R, Weston J, Bottou L, Karlen M, Kavukcuoglu K, Kuksa P. Natural language processing (almost) from scratch. *J Mach Learn Res.* 2011;12:2493–537.
- [22] Waldrop M.M. The chips are down for Moore’s law. *Nature.* 2016;530:144–147.
- [23] Mnih V, Kavukcuoglu K, Silver D, Rusu AA, Veness J, Bellemare MG, Graves A, Riedmiller M, Fidjeland AK, Ostrovski G, Petersen S. Human-level control through deep reinforcement learning. *Nature.* 2015;518(7540):529–33.
- [24] Silver D, Huang A, Maddison CJ, Guez A, Sifre L, van den Driessche G, Schrittwieser J, Antonoglou I, Panneershelvam V, Lanctot M, Dieleman S. Mastering the game of Go with deep neural networks and tree search. *Nature.* 2016;529(7587):484–9.
- [25] Williams DR, Hinton GE. Learning representations by back-propagating errors. *Nature.* 1986;323:533–6.
- [26] LeCun Y, Bottou L, Bengio Y, Haffner P. Gradient-based learning applied to document recognition. *Proc IEEE.* 1998;86(11):2278–324.
- [27] Michael A. Nielsen, *Neural Networks and Deep Learning*, Determination Press, USA. 2015. URL: <http://neuralnetworksanddeeplearning.com/>
- [28] Lorber A, Wiltgen M, Hofmann-Wellenhof R, Koller S, Weger W, Ahlgrimm-Siess V, Smolle J, Gerger A. Correlation of image analysis features and visual morphology in melanocytic skin tumours using in vivo confocal laser scanning microscopy. *Skin Res Technol.* 2009;15:237–241.
- [29] Wiltgen M, Gerger A, Wagner C, Smolle J. Automatic identification of diagnostic significant regions in confocal laser scanning microscopy of melanocytic skin tumours. *Methods Inf Med.* 2008;47:14–25.
- [30] Leveson R.M, Krupinski E.A, Navarro V.M, Wasserman A. Pigeons (*Columba livia*) as trainable observers of pathology and radiology breast cancer images. *Plos One* 10(11). 2015; 1–21.
- [31] Hubel DH, Wiesel TN. Period of susceptibility to physiological effects of unilateral eye closure in kittens. *J Physiol.* 1970;206(2):419–436.

Super-Resolution Confocal Microscopy Through Pixel Reassignment

Longchao Chen, Yuling Wang and Wei Song

Additional information is available at the end of the chapter

<http://dx.doi.org/10.5772/63192>

Abstract

Confocal microscopy has gained great popularity in the observation of biological microstructures and dynamic processes. Its resolution enhancement comes from shrinking the pinhole size, which, however, degrades imaging signal-to-noise ratio (SNR) severely. Recently developed super-resolution method based on the pixel reassignment technique is capable of achieving a factor of $\sqrt{2}$ resolution improvement and further reaching twofold improvement by deconvolution, compared with the optical diffraction limit. More importantly, the approach allows better imaging SNR when its lateral resolution is similar to the standard confocal microscopy. Pixel reassignment can be realized both computationally and optically, but the optical realization demonstrates much faster acquisition of super-resolution imaging. In this chapter, the development and advancement of super-resolution confocal microscopy through the pixel reassignment method are summarized, and its capabilities of imaging biological structures and interactions are represented.

Keywords: super resolution, confocal microscopy, pixel reassignment, computational realization, optical realization

1. Introduction

Better understanding of biological processes at the cellular and subcellular level is closely dependent on the direct visualization of the cellular microstructures. Among the various microscopic techniques, fluorescence microscopy takes advantage of the abilities to observe in real-time the molecular specificities in living biological samples down to the cellular and/or subcellular scale, and thus has found broad applications in the investigations of cell biology and neuroscience. However, the spatial resolution of conventional microscopy is optically diffrac-

tion-limited, restricting its lateral resolution to be ~ 250 nm and axial resolution to be ~ 600 nm (primarily determined by the numerical aperture of microscopic objective), respectively. As a result, it is very challenging to resolve the subcellular structures by the conventional microscopic technologies because their microstructures are comparable to (even finer than) the diffraction-limited resolution.

Fortunately, a number of novel fluorescence microscopic techniques with super-resolution capability have been established to break down the optical diffraction limitation in recent years, allowing the observation of many cellular and subcellular structures that are always not resolvable by the conventional fluorescence microscopy. For example, by sharpening the point-spread function of the microscope with the suppression of the fluorescence emission on the rim of a focused laser spot, stimulated emission depletion (STED) microscopy breaks the optical diffraction limitation and achieves resolution as high as ~ 30 nm [1]. Localization-based techniques, such as stochastic optical reconstruction microscopy (STORM) and photoactivated localization microscopy (PALM), enable imaging at a resolution of ~ 20 nm [2, 3]. Structured illumination microscopy (SIM) applies spatially structured light illumination for shifting the high spatial frequency to the low-frequency range, which thus can be collected by microscopy [4]. These methods achieve an order of magnitude improvement in spatial resolution over the conventional fluorescence microscopy. Therefore, the super-resolution microscopic technology opens up new windows for observing the previously unresolved cellular structures and provides great potentials for elucidating biological processes at the subcellular and molecular scale [4].

Among these high-resolution fluorescence microscopic techniques, confocal microscopy, the first super-resolution imaging technique, is one of the most widely used imaging approaches with moderately enhanced spatial resolution. Utilizing a focused laser as an excitation source in combination with a pinhole in front of the detector for blocking out out-of-focus signals, confocal microscopy is able to improve the spatial resolution by a factor of $\sqrt{2}$ in principle. However, instead of its super-resolution capability, the sectioning capability is more impressed because the spatial resolution with a factor of $\sqrt{2}$ improvement is hardly accessible in the standard confocal microscopy. The resolution of confocal microscopy relies on the pinhole diameter, that is, higher resolution comes from the smaller sized pinhole filter. Such a small pinhole rejects the unwanted out-of-focus light, while parts of the desired in-focus emission are filtered out simultaneously. As a result, the signal-to-noise ratio (SNR) is drastically decreased as the pinhole size shrinks, which, in turn, practically deteriorates the spatial resolution. Instead, the fluorescence efficiency within the biological samples is often weak, so a relatively large pinhole diameter is typically chosen concerning the imaging SNR. Therefore, the standard confocal microscopy is practically unable to provide super-resolution imaging.

In order to achieve spatial resolution improvement and better imaging SNR simultaneously in confocal microscopy, light/fluorescence signals should be detected with a nearly closed pinhole array instead of a single pinhole [5]. The images acquired by each pinhole within the array have the same resolution but different SNR levels [6]. To overcome this limitation, a method applying the pixel reassignment technique is proposed by reasonably summing the signals from each nearly closed pinhole together, which enables simultaneous improvement

of resolution and SNR. In this chapter, we present the state-of-the-art super-resolution techniques based on the pixel reassignment. Section 2 gives the principle of pixel reassignment firstly, and then two different operations realizing the pixel reassignment. Also, some representative super-resolution images in biological specimens are summarized in this section. At last, some advances in super-resolution confocal microscopy through the pixel reassignment will be discussed.

2. Super resolution by pixel reassignment

The concept of pixel reassignment is firstly proposed more than two decades ago to solve the drawbacks in standard confocal microscopy [5]. As we know, the reduction of the pinhole diameter down to zero allows the finest lateral resolution in confocal microscopy in theory, which, however, generates fluorescent images with a very low SNR due to the dramatically

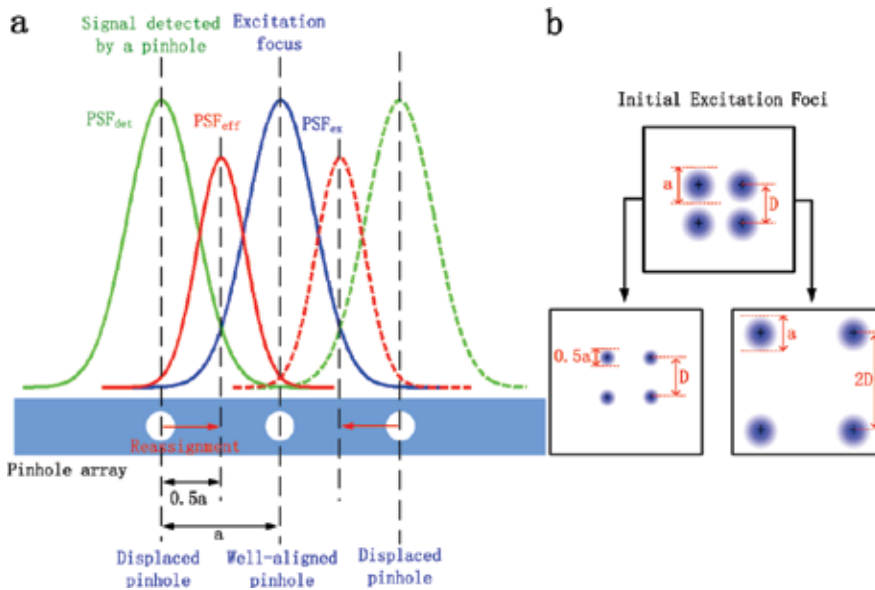


Figure 1. Schematic diagram illustrating the principles of pixel reassignment. (a) One-dimensional representation of pixel reassignment. Two pinholes (left and right) within an array displaced by a distance of 'a' from the excitation focus, which detect light signals mostly originated from the location of the peak of the product of $PSF_{det}(x-a)$ and $PSF_{ex}(x)$. In the case that PSF_{det} and PSF_{ex} are identical (i.e. neglecting the Stokes shift), the maximum in PSF_{eff} occurs at the position with a distance of $a/2$ from the excitation focus. Thus, the detected light signals from the displaced pinholes are reassigned to the well-aligned pinhole that is at the center of the excitation focus and the original detection spot. (b) Pixel realignment operation. Top panel shows the excitation foci (blue circles) created by scanning illuminating laser across the sample, where four excitation foci are with the distance of D and diameter of a . Bottom: Two pixel realignment operations for increasing the image resolution. Lower left panel represents twofold reduction of the foci without altering their distance. Lower right panel displays the increase of the foci distance to $2D$, while maintaining all foci sizes. These two implementations produce an equivalent imaging reconstruction, with only different global scaling factor.

degraded light collection efficiency. Although the pinhole size can be adjusted to one Airy unit for better imaging SNR, the lateral resolution is sacrificed. Instead of a single pinhole, a pinhole array is used for the light detection, followed by a reconstruction algorithm for the image formation. As a result, the standard confocal microscopy with the pixel reassignment operation is capable of enhancing its lateral resolution simultaneously with higher imaging SNR.

2.1. Principle of pixel reassignment

Pixel reassignment demonstrates great potentials for improving both lateral resolution and imaging SNR. Instead of summing the signals directly as the conventional imaging technologies, each signal is reassigned to a particular location where the signal most probably comes. **Figure 1(a)** gives the principle of the pixel reassignment in terms of excitation and detection point-spread function (PSF) [7]. The excitation PSF (PSF_{ex} , labeled by blue line) represents the distribution of the corresponding excitation focus. At a displaced pinhole, detection PSF (PSF_{det} , labeled by green line) is centered on the detection axis with a distributed probability of signal detection around that pinhole. The effective PSF (PSF_{eff} , labeled by red line) is contributed from the overlap (multiplication) of PSF_{det} and PSF_{ex} . The well-aligned pinhole is coaxial with the excitation focus, realizing the maximal signal detection probability. As the pinhole detector is far away from the axis of the excitation focus, the signal acquisition probability decreases because of their less overlying; consequently, these nearly closed pinhole detectors induce lower-SNR image.

In the pixel reassignment implementation, a camera (similar with a pinhole array), rather than a point detector, is commonly employed because its individual pixels are considered as infinitely narrow pinhole. Neglecting Stokes shift in single-photon fluorescence and assuming identical PSF_{det} and PSF_{ex} , a maximal probability of signal acquisition (i.e. PSF_{eff}) is at the midway of the peaks of PSF_{det} and PSF_{ex} . **Figure 1(b)** gives two methods for the pixel reassignment operation, either twofold local contraction of the excitation focus without altering the distance between them (panel in lower left of **Figure 1(b)**), or twofold increasing the distance between the foci while maintaining their original size (panel in lower right of **Figure 1(b)**) [8]. By reassigning the signals from all pixels within the detector array (i.e. all displaced pinholes as shown in **Figure 1(a)**) to the particular location, a sharper and higher-SNR image is eventually achieved.

Pixel reassignment technique is able to improve the resolution to a factor of $\sqrt{2}$ without sacrificing SNR, and the resolution can be further improved by deconvolution algorithm up to a factor of 2 [9, 10]. Although the spatial resolution of the pixel reassignment technique is still lower compared with other super-resolution methods, such as STED and STORM [1–3], it overcomes some of their shortcomings. This technique inherits all advantages of the standard confocal microscopy, including high-speed imaging rate, acceptable excitation intensity, optical sectioning capability, and a broad choice of fluorescent dyes and/or proteins, making it a readily accessible technology in a variety of biological investigations.

The pixel reassignment can be considered as an alternative method of SIM, theoretically achieving the same spatial resolution improvement compare with standard SIM through

point-like illumination feature. In contrast, the technique demonstrates better feasibility over the standard SIM, that is, the pixel reassignment operation can be easily implemented both computationally and experimentally (optical system adaptation). Unlike computational mode that is always time-consuming in raw data processing, the pixel reassignment realized with optical means is capable of obtaining super-resolution images with fast imaging acquisition. More details on these two different methods for realizing the pixel reassignment are represented as below.

2.2. Computational realization of pixel reassignment

2.2.1. Image scanning microscopy

Image scanning microscopy (ISM), proposed by C. Müller and J. Enderlein in 2009, is a super-resolution microscopic technique based on the pixel reassignment [11]. This system is modified from a standard confocal microscopy that replaces the point detector (normally a photomultiplier tube) with an Electron multiplying CCD (EMCCD) camera (labeled 9) as shown in **Figure 2(a)**. The camera takes an image of each spatial position of the scanning focus, and then an algorithm of the pixel reassignment processing is utilized by summing the raw images to reconstruct an ISM image, which improves the resolution from 244 nm to 198 nm laterally.

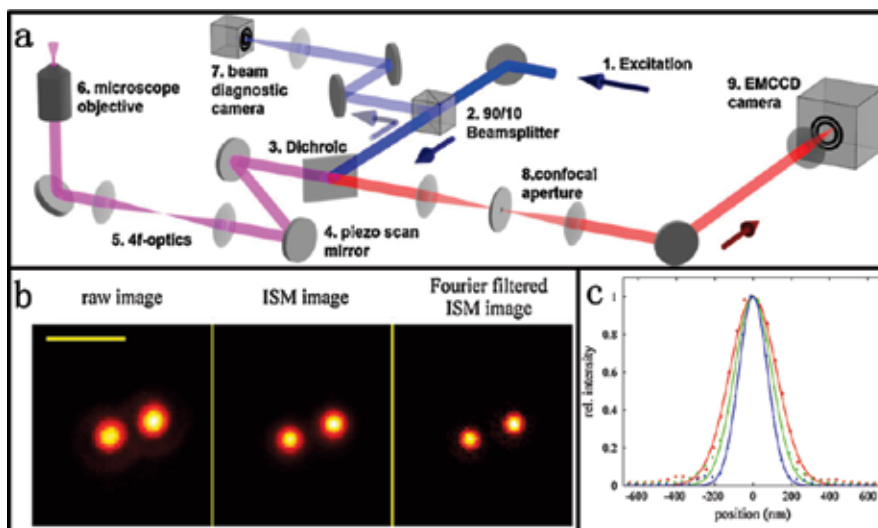


Figure 2. Super-resolution image scanning microscopy (ISM) with computational pixel reassignment. (a) The schematic diagram of ISM system. Fluorescence excitation (1); a super-continuum white light laser equipped with an acousto-optic tunable filter; nonpolarizing beam splitter cube (2); dichroic mirror (3); piezo scanning mirror (4); 4f telescope configuration (5); microscope objective (6); beam diagnostic camera (7); confocal aperture with 200 μm diameter (8); EMCCD camera for fluorescence detection (9). (b) Super-resolution imaging fluorescent beads with 100-nm diameter. Left panel: Confocal microscopy image; middle panel: ISM image; right panel: Fourier-weighted ISM image. Scale bar: 1 μm . (c) Linear cross-sectional distribution along the horizontal axis of an individual bead image in (b). Adapted with permission from reference [11].

Further, deconvolution function is used to improve its lateral resolution up to 150 nm, 1.63-fold better than the image from raw data, as shown in **Figure 2(b)** and **(c)**, respectively. Note that the pinhole in ISM (labeled 8) filters the out-of-focus light signals, maintaining the optical sectioning capability as the standard confocal microscopy. In this work, the realization of the lateral resolution improvement up to 198 nm does not entirely rely on the pinhole because of its relatively large diameter, which, however, gives a high imaging SNR. Therefore, with the computational pixel realignment ISM is able to provide images with optimization of both spatial resolution and imaging SNR.

2.2.2. Multifocal structured illumination microscopy

ISM demonstrates multiple advantages, including the optical sectioning capability as the standard confocal microscopy, the enhanced lateral resolution, and the high fluorescence collection efficiency [11]. However, it is subjected to slow frame rate due to the EMCCD camera (imaging acquisition of 10 ms with each scanning position), and is time-consuming for visualizing the three-dimensional (3D) microstructures.

In order to speed up the imaging acquisition, Shroff et al. developed multifocal structured illumination microscopy (MSIM) by using a sparse lattice of excitation foci (similar to swept-field or spinning disk confocal microscopy) in 2011 [9]. As shown in **Figure 3**, MSIM applies a digital micromirror device (DMD) for generating the sparse lattice illumination patterns.

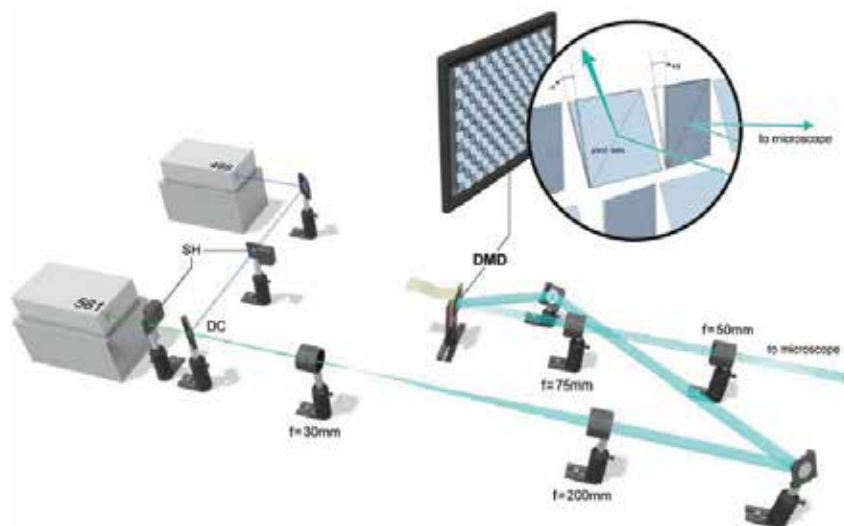


Figure 3. The schematic of multifocal structured illumination microscopy (MSIM). Lasers with 561 and 488 nm serve as illumination sources. Both laser outputs are combined with a dichroic (DC). After beam expanding, both lasers are directed onto a digital micromirror device (DMD). The resulting pattern is de-expanded by a pair of lenses, and is subsequently delivered by the tube lens and microscopic objective inside the microscope (not shown) into the samples. Mechanical shutters (SH) placed in front of the laser output are used for switching illumination on or off. Adapted with permission from reference [9].

After a series of reconstruction steps (open-source software), MSIM enables 3D subdiffraction imaging with resolution doubling, indicating a lateral resolution at 145 nm and an axial resolution at 400 nm. Moreover, it provides the capability of significantly fast imaging acquisition at one 2D image per second.

For super-resolution MSIM, the data acquisition and processing are implemented as below (please refer to **Figure 4** for detailed procedures). First, the sample is excited with a sparse, multifocal excitation pattern. Second, the resulting fluorescence image is recorded with a camera, and then the digital pinholes around each fluorescent focus are applied for rejecting the out-of-focus emission. Afterwards, the pixel reassignment with $2\times$ scaling is used to process the resulting image. Repeat the above procedures for the entire imaging region fully illuminated. Eventually, a super-resolution image with $\sqrt{2}$ -fold resolution improvement is obtained through the digital summation of all such pinholed and scaled images. Twofold resolution improvement is further achieved with deconvolution.

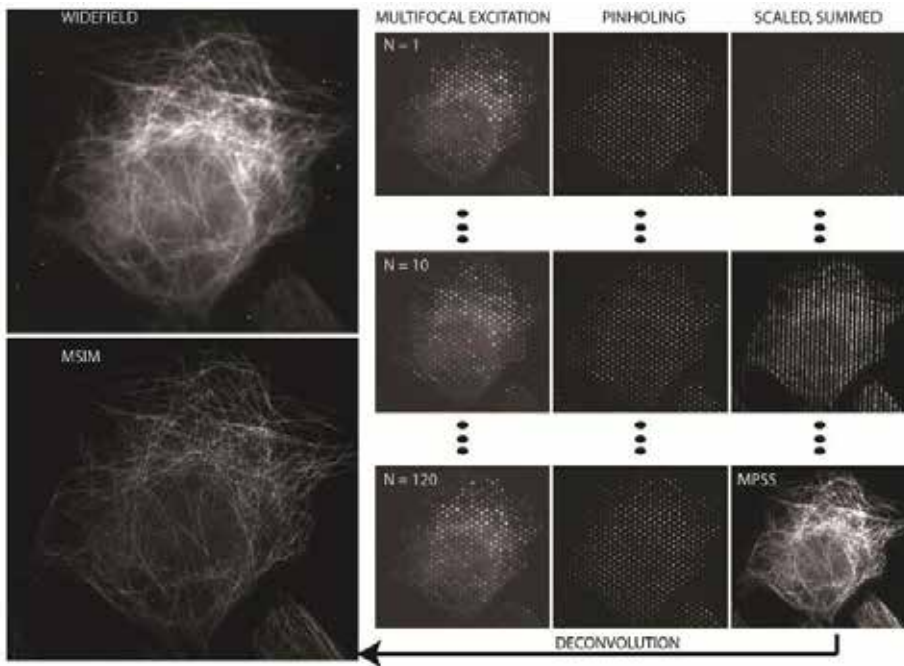


Figure 4. Super-resolution MSIM realization. Top left figure represents a wide-field image produced with a uniformly illuminated pattern onto sample. Right panel provides the reconstructed procedure for the first, tenth, and final raw images of a 120-frame sequence. Lower left figure displays the super-resolution MSIM image by deconvolving the summed image. Adapted with permission from Ref [9].

The resolution improvement of MSIM is demonstrated by imaging antibody-labeled microtubules in human osteosarcoma (U2OS) cells embedded in Fluoromount as shown in **Figure 5**. Compared to the wide-field images, the multifocal-excited, pinholed, scaled, and

summed (MPSS) images have both higher resolution and better contrast (**Figure 5(b)**). In **Figure 5(d)**, the full-width at half maximum (FWHM) of light intensity of microtubules is estimated at about 145 nm in MSIM images, giving a twofold resolution enhancement compared with the image from wide-field microscopy (~ 299 nm). Moreover, the frame rate of acquiring an image with field of view at $48 \times 49 \mu\text{m}$ is up to 1 Hz in MSIM, indicating more than 6500-fold faster acquisition over the ISM technology [11].

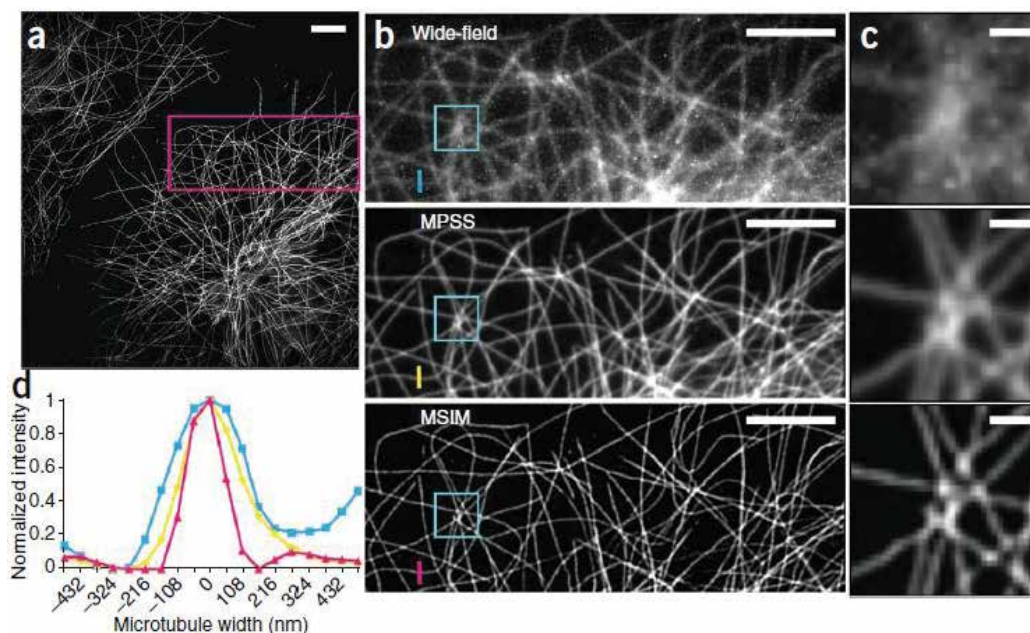


Figure 5. Resolution doubling of MSIM by imaging antibody-labeled microtubules in human osteosarcoma (U2OS) cells. (a) MSIM imaging microtubules labeled with Alexa Fluor 488 in a fixed cell. MSIM image is formed from 224 raw images taking ~ 1 s total acquisition time with 4.5 ms for each image. Scale bar: $5 \mu\text{m}$. (b) Magnified images from the boxed region in (a). Top panel showing a wide-field image, middle panel showing an MPSS image, and bottom panel showing an MPSS and deconvolved (MSIM) image. Scale bars: $5 \mu\text{m}$. (c) Close-up images of the boxed regions in (b). Scale bars: $1 \mu\text{m}$. (d) Intensity profiles along the colored lines in (b), giving FWHM values at 299 nm in wide-field microscopy, 224 nm in MPSS, and 145 nm in MSIM, respectively. Adapted with permission from reference [9].

2.3. Optical realization of pixel reassignment

The pixel reassignment implemented by the computational means is capable of doubling the resolution than wide-field imaging [9, 11]. The limitation, however, is that the methods are fundamentally time-consuming compared to the standard conventional microscopy because a large number of raw images are essentially acquired and processed. Recently, optically realized pixel reassignment has been developed to overcome the limitations by adapting the optical imaging system instead of digital data-processing operations, which produces images with comparable improvement in the spatial resolution [8, 10, 12].

2.3.1. Instant structured illumination microscopy

Instant structured illumination microscopy (ISIM) is developed by Shroff et al. in 2013 that is analogous to MSIM, while its pixel reassignment process operates optically instead of the digital computation procedures [10]. As shown in **Figure 6**, the DMD used in MSIM is replaced with a converging microlens array. As a result, a multifocal excitation pattern is generated in ISIM. Correspondingly, a matched pinhole array is added to physically reject the out-of-focus emissions. With this modification, the optical pixel reassignment is realized based on the matched microlens array for twofold local contraction of each fluorescent focus. The fluorescence emission pattern is imaged onto a camera by galvanometer scanning. Eventually, the pinholed and scaled images are optically summed, enabling $\sqrt{2}$ -fold resolution enhancement.

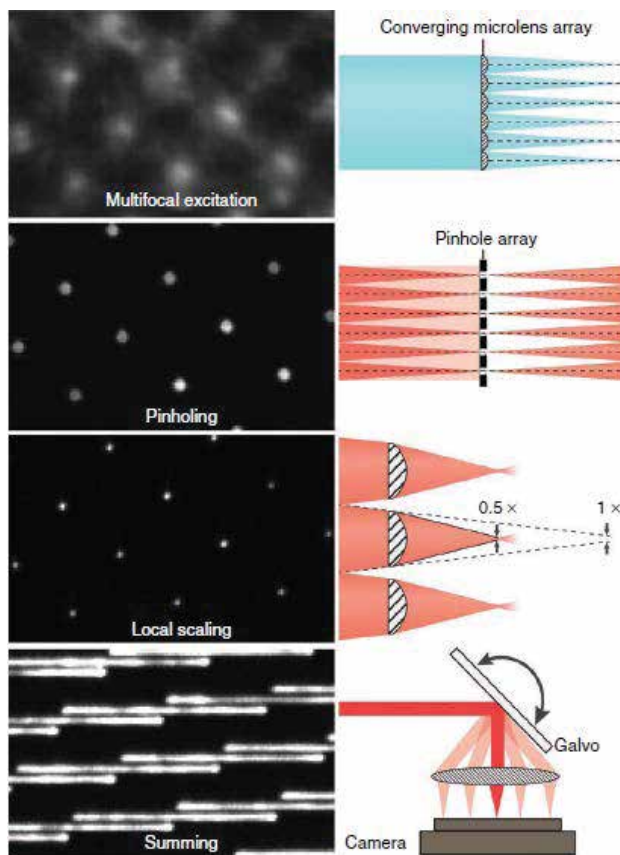


Figure 6. Principles of implementing instant structured illumination for super-resolution realization. A multifocal excitation pattern is produced with a converging microlens array. For fluorescence detection, a pinhole array that matches the microlens array rejects the out-of-focus fluorescence signals. Afterwards, a second, matched microlens array allows a twofold local contraction of each pinholed fluorescence emission. A galvanometer serves as raster scanning of multifocal excitation and summation of multifocal emission, which thus produces a super-resolution image during each camera exposure. Adapted with permission from reference [10].

ISIM demonstrates 3D super-resolution imaging with a lateral resolution of 145 nm and an axial resolution of 350 nm, nearly comparable with MSIM. Moreover, the 100 Hz frame rate comes from the optical operation of pixel realignment in ISIM, allowing super-resolution real-time imaging (almost 100-fold faster than MSIM). Taking into account the data processing duration, the speed-up factor exceeds 10000. In addition, the low illumination power in ISIM ($\sim 5\text{--}50\text{ W/cm}^2$) mitigates photobleaching. As a result, ISIM can perform imaging over tens of time points without obvious photobleaching or photodamage. In **Figure 7**, the rapid growth ($\sim 3.5\ \mu\text{m/s}$) of endoplasmic reticulum (ER) is monitored by ISIM even though less than 140 ms in the formation and growth of new ER tubules. The biological processes blur in previously developed technologies, such as MSIM and ISM [9, 11]. The capabilities make ISIM a powerful tool for time-lapse super-resolution imaging in living biological samples.

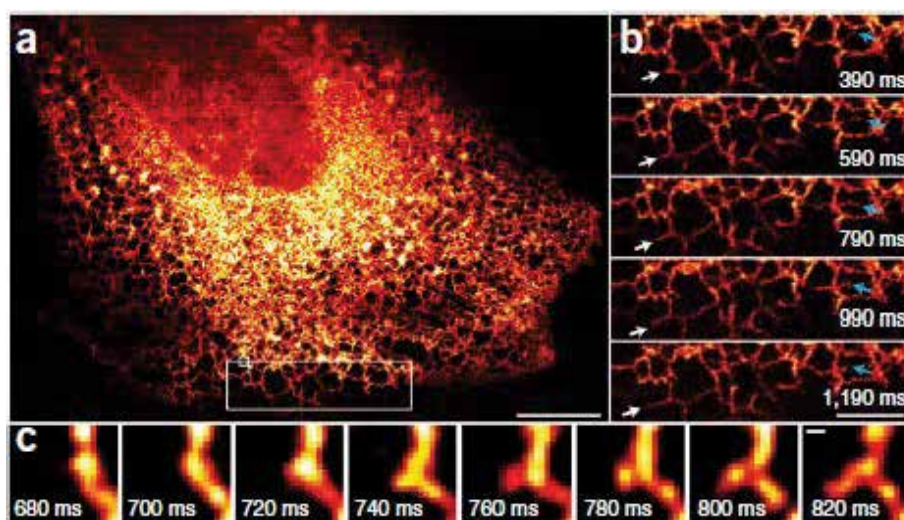


Figure 7. ISIM demonstrates high frame rate of imaging endoplasmic reticulum (ER) at 100 Hz. (a) The first image from 200 time points. ER labeled with GFP-Sec61A within MRL-TR-transformed human lung fibroblasts. Scale bar: 10 μm . (b) Magnification of image with the large white box in (a). White arrows point out the growth process of an ER tubule; blue arrows represent the remodeling of an ER tubule. Scale bar: 5 μm . (c) Magnification of the image with the small white box in (a), displaying the dynamic formation of a new tubule within 140 ms. Scale bar: 200 nm. Adapted with permission from reference [10].

2.3.2. Re-scan confocal microscopy

Rescan confocal microscopy (RCM) is another optical realization of the pixel reassignment technique, proposed by Luca et al. in 2013 [12]. Compared with ISIM, it is more easily accessible to build an RCM because this system can be readily modified from a standard confocal microscopy as shown in **Figure 8**. The optical pixel reassignment in RCM is realized as below. The focal length of the lenses L2 and L3 is adapted for twofold local contraction of the fluorescent focus spot. Alternatively, the final fluorescence image is twofold magnified while maintaining the original fluorescence foci size.

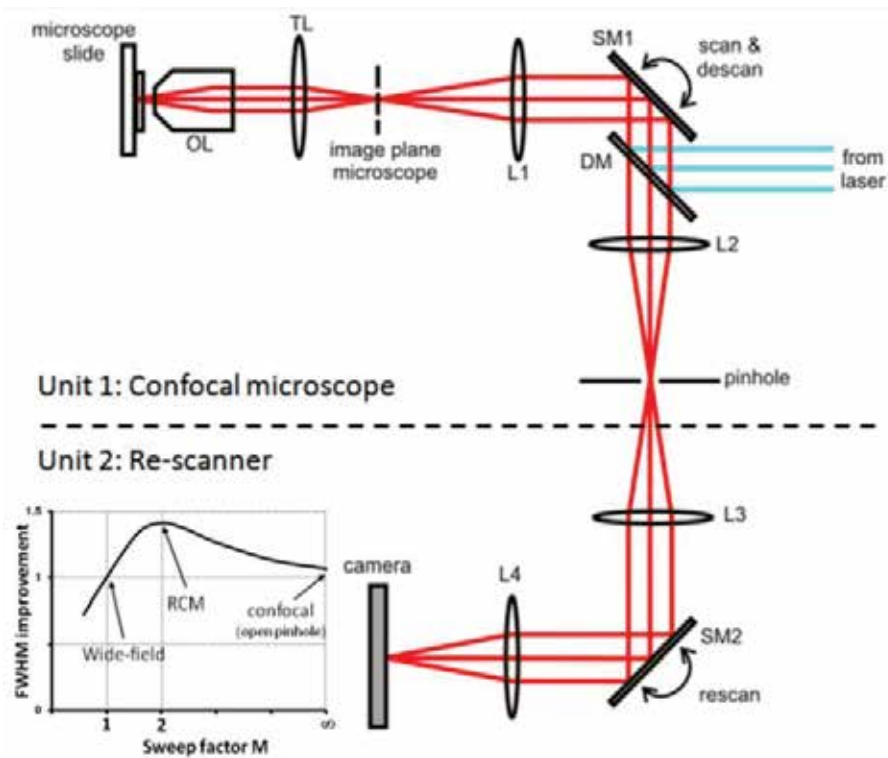


Figure 8. The schematic of rescan confocal microscopy (RCM). Unit 1: A standard confocal microscope with a set of scanning mirrors for scanning the excitation light and de-scanning the emission light. Unit 2: A re-scanning configuration for ‘writing’ the light that passes the pinhole onto the CCD-camera. Although the pinhole is in a relatively large diameter, the resolution is $\sqrt{2}$ times improved, which thus gives much more photo-efficient advantage compared to conventional confocal microscopes with the similar resolution. Adapted with permission from reference [12].

This process is accomplished by reasonably changing the angular amplitude of the rescanner. The ratio of angular amplitude of the two scanners, expressed by the sweep factor M , changes the properties of the rescan microscope. For $M = 1$ the microscope has the same lateral resolution with a wide-field microscope, defined by the well-known optical diffraction limit; it achieves the super resolution for $M = 2$. The rescanner is used to deliver the fluorescence emission onto the camera pixels. The camera is in the exposure status for optical summation of the fluorescent focus during rescanning.

The lateral resolution improvement of RCM is quantified by imaging 100-nm fluorescent beads. FWHM is found to reduce from 245 nm (15 nm) in wide-field imaging to 170 nm (± 10 nm) in RCM imaging, indicating an improvement by a factor of $\sqrt{2}$ without deconvolution. Also, the resolution improvement is concluded by visualizing fluorescently labeled microtubules of HUVEC cell in **Figure 9(a)–(f)**. To demonstrate the capability of RCM for monitoring dynamics, the time-lapse imaging of living HeLa cells expressing EB3-GFP with the growing end of microtubules is observed by RCM. As shown in **Figure 9(g)**, RCM is able to track the

fast dynamics ($0.5 \mu\text{m/s}$) with multiple advantages of improved resolution, high sensitivity, and sufficient imaging rate (1 fps).

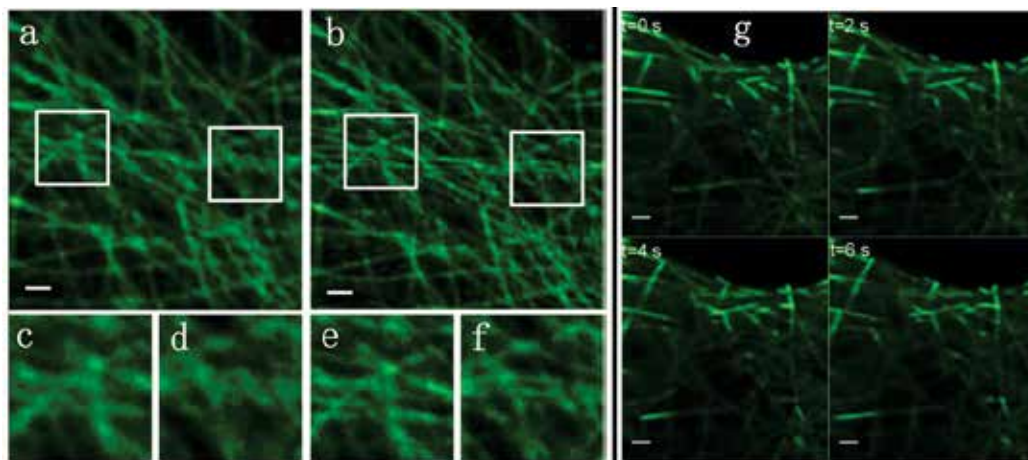


Figure 9. Fluorescently labeled microtubules in HUVEC cells imaged by RCM with sweep-factor $M=1$ (a), which gives an image with resolution of a wide-field fluorescence microscope determined by the diffraction limit. In double-sweep mode (sweep-factor $M=2$) (b) RCM gives resolution improvement by a factor of $\sqrt{2}$. Junctions of microtubules (c, e) and parallel microtubules (d, f) are unresolved with wide-field resolution (c, d), but distinguished by RCM in double sweep mode (e, f). (g) Screenshots from an RCM time lapse series of living HeLa cells at $M=2$ demonstrate the monitoring of fast dynamic structures ($0.5 \mu\text{m/s}$). Scale bars: $1 \mu\text{m}$. Adapted with permission from reference [12].

2.3.3. Two-photon instant structured illumination microscopy

RCM improves resolution by a factor of $\sqrt{2}$ compared with wide-field imaging while possessing optical sectioning capabilities as the traditional confocal microscope [8]. Two-photon excitation offers better optical sectioning capability based on the nonlinear effect. Infrared excitation light minimizes the optical scattering in the tissue, and the fluorescent signals come only from two-photon absorption. These advantages effectively increase the penetration depth and simultaneously suppress the background signal, making the two-photon excitation technique an ideal imaging tool for the thick samples.

Two-photon instant structured illumination microscopy (2P ISIM) is a combination of RCM and two-photon excitation technique, presented by Shroff et al. in 2014, as shown in **Figure 10(a)** [8]. Similarly, an additional scanning component is introduced in 2P ISIM for the optical realization of pixel reassignment. In **Figure 10(b)–(d)**, 2P ISIM provides better resolution than the diffraction-limited two-photon excitation mode by imaging the microtubules. Applying the deconvolution, the lateral resolution is further improved in **Figure 10(c)**. 2P ISIM is quantified by $\sim 150 \text{ nm}$ in the lateral resolution and by $\sim 400 \text{ nm}$ in the axial resolution, respectively, with 100-nm diameter fluorescent beads as imaging targets. A factor of 2 (with deconvolution) resolution enhancement is obtained compared with the conventional two-photon wide-field imaging ($\sim 311 \text{ nm}$).

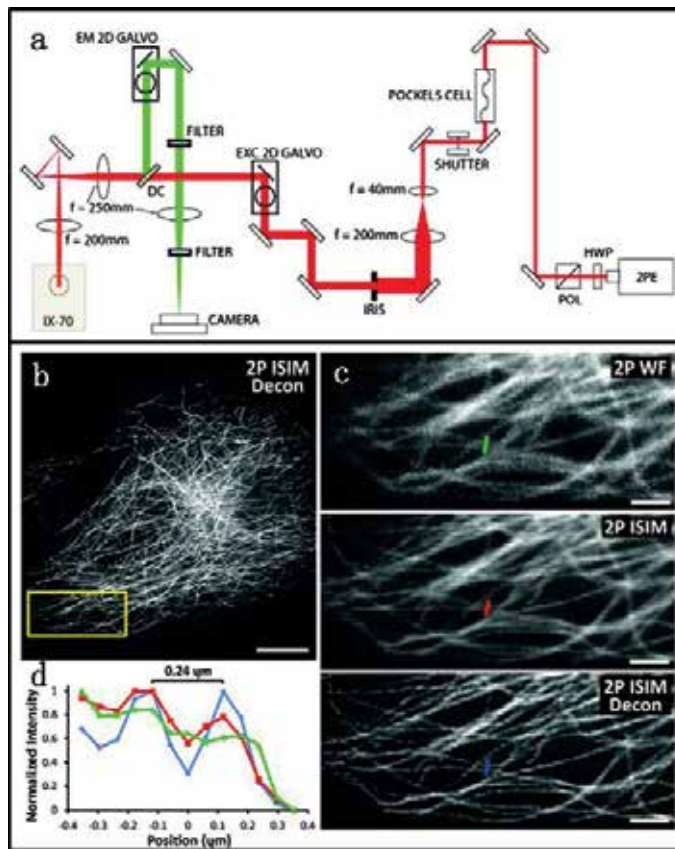


Figure 10. Schematic diagram of two-photon instant structured illumination microscopy (2P ISIM) and its imaging capabilities. (a) Pulsed femtosecond laser (2PE) serves as a two-photon excitation source (labeled by red line). Fluorescence (labeled with green line) is collected and delivered onto a camera. HWP: half-wave plate; POL: polarizer; EXC 2D GALVO: galvanometric mirror for scanning the excitation laser; DC: dichroic mirror; IX-70: microscope part housing objective and sample (not shown); EM 2D GALVO: galvanometric mirror for rescanning the fluorescence emission. (b)–(d) Resolution enhancement of 2P ISIM. (b) 2P ISIM image of immunolabeled microtubules in a fixed U2OS human osteosarcoma cell after deconvolution processing. (c) Magnified view of the yellow rectangular region in (b), indicating the resolution improvement in deconvolved 2P ISIM compared with both 2P wide-field microscopy (2P WF) and 2P ISIM. (d) Fluorescence intensity profiles of microtubules highlighted with green, red, and blue lines in (c). Scale bar: 10 μm in (b) and 3 μm in (c). Adapted with permission from reference [8].

To demonstrate the enhanced penetration ability of 2P ISIM in living thick samples, embryos of transgenic *Caenorhabditis elegans* expressing GFP-H2B are imaged in **Figure 11**. Both imaging resolution and contrast severely degrade at depths of more than $\sim 15 \mu\text{m}$ from the coverslip surface in 1P illumination due to strong scattering in deep tissue (**Figure 11(a), (b)**). The degradation is not compensated by increasing of the exposure time, which, however, mainly leads to high background noise. Two-photon excitation of 2P ISIM effectively suppresses the out-of-focus emission. Thus, the subnuclear chromatin structures are clearly observed up to the depth of $\sim 30 \mu\text{m}$ in **Figure 11(c), (d)**, where the fluorescence signals slightly reduce as the depth increases.

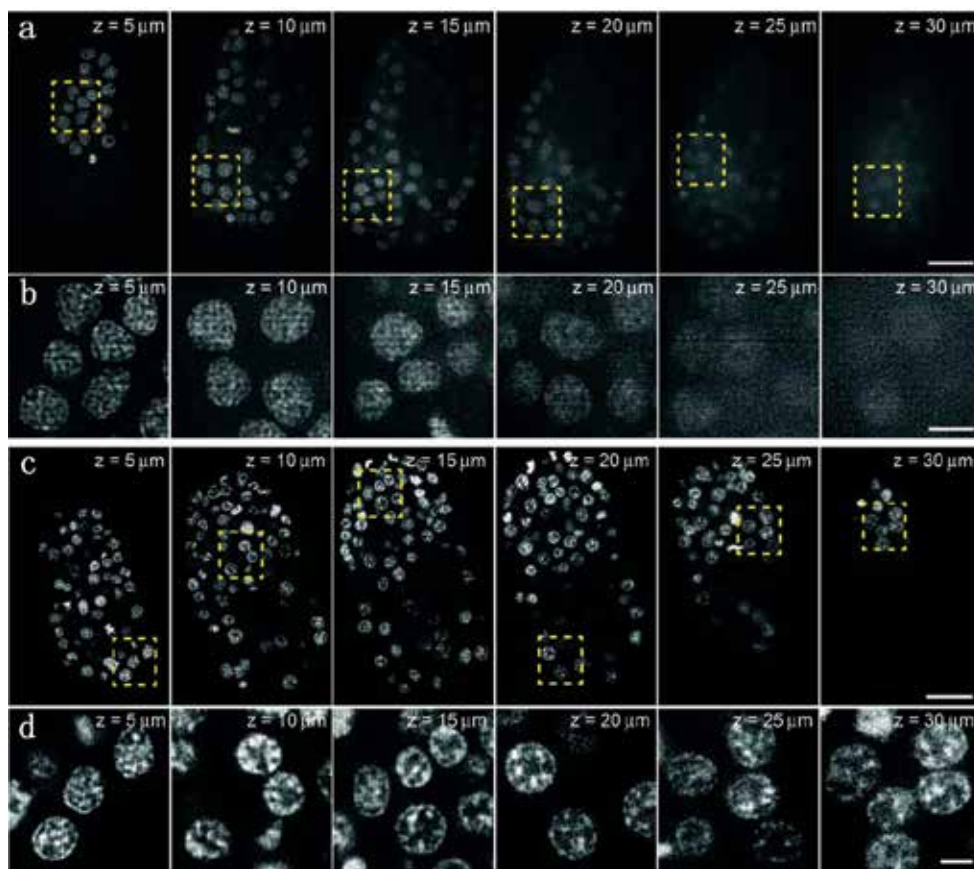


Figure 11. Enhanced penetration ability in 2P ISIM. (a, b) 1P ISIM images of a nematode embryo expressing GFP-H2B in nuclei. (a) Cross sections of the worm embryo at different axial positions. Scale bar: 10 μm . (b) Magnifications of the yellow rectangular regions in (a). Scale bar: 3 μm . The degradation in imaging contrast is observed as the depths increase. (c, d) 2P ISIM visualizes the subnuclear chromatin structure throughout nematode embryos. (c) Cross sections at the representative axial position. Scale bar: 10 μm . (d) Magnifications of yellow rectangular regions in (c), indicating better resolution, higher contrast, and larger imaging depth compared with 1P ISIM. Scale bar: 2 μm . Adapted with permission from reference [8]

3. Conclusion

In this chapter, we represent the super-resolution confocal microscopy (and two-photon microscopy) realized through the pixel reassignment methods computationally and optically. These demonstrate multiple advantages of resolution improvement, high fluorescence collection efficiency, optical sectioning capability, and fast imaging acquisition, which thus is able to investigate biological structures and processes at the cellular and even macromolecular level with 3D spatial scale. Additionally, because the method is directly established based on the standard confocal microscopy and/or two-photon microscopy, it mitigates the require-

ments in fluorescent probes and/or labeling methods that are always indispensable in some super-resolution fluorescence microscopic technologies, such as STORM and PALM [2, 3].

More importantly, the development of these techniques is not limited in the laboratorial stage. In 2015, the first commercial setup, LSM 800, is established by Carl Zeiss [13], which, in principle, is based on ISM but replaces the EMCCD camera with a 32-channel linear GaAsP-PMT array (i.e. Airyscan detector as shown in **Figure 12**). The highest imaging speed of LSM 800 with 512×512 pixels is up to 8 Hz, tremendous faster than ISM. Therefore, we expect that the super-resolution microscopy based on the pixel reassignment technique has great potentials for boosting imaging acquisition speed, and therefore further provides better understanding in intracellular molecular interactions and dynamic processes within living biological specimens.

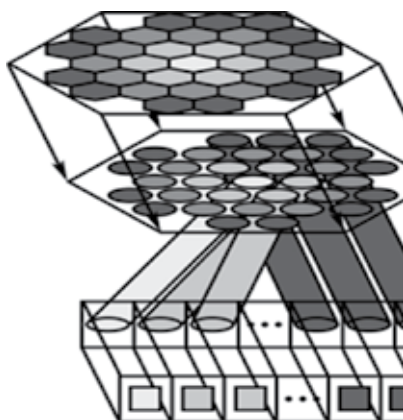


Figure 12. Schematic diagram of Airyscan detector in LSM 800. In brief, a hexagonal microlens array (a) collects incident light, which is in direct connection with the ends (b) of a fiber bundle (c). The other ends (d) of the fibers are in contact with a linear GaAsP-PMT array (e) serving as a detector. Thus, an area detector is created, onto which the Airy disk is imaged via a zoom optic configuration. Note that the single detector element, replacing the classical pinhole, acts as the separate pinholes in Airyscan detection. Adapted with permission from reference [13].

In addition to the issue of imaging acquisition speed, multicolor fluorescence microscopy is desired for investigating the interactions between different structures or biomolecules via labeling them with distinct colors. The possible interactions can be revealed by the co-localization of the different dyes and/or proteins. The standard fluorescence microscopy, however, might give inaccurate co-localization due to the diffraction-limited resolution. In combination with the pixel reassignment, the multicolor imaging technique is anticipated to provide a high-resolution imaging of the biological interaction within live cells.

In MSIM and ISIM based on the pixel reassignment approach [9, 10], both super-resolution imaging capability and color differentiation have been demonstrated, which have the advantages of easily configured optical system and weak cross-talk effect between the different colors. Switching laser lines for the excitation of different fluorophores might induce spatial mismatch in the images. Therefore, it is more preferable for simultaneously exciting all

fluorophores and synchronously collecting their fluorescence signals. Multiple detectors with appropriate dichroic mirrors and emission filters can be used to collect the different fluorescence signals with different detection channels. Alternatively, an imaging spectrometer can be applied to record the spectral feature of these fluorophores.

Synchronous imaging decreases the fluorescence photobleaching probability due to low light exposure, benefiting to long-term monitoring of living samples. However, cross-talk of the different fluorophores always occurs because of the broad and overlapping excitation and emission bands of fluorophores. Although the cross-talk effects can be removed by selecting dyes with appropriately wide and non-overlapping emission spectra, the dyes are often inaccessible, which thus restricts its application in multicolor imaging. Linear spectral unmixing analysis is a solution to eliminate the cross-talk effect in spectral imaging [14]. The spectrum of the mixed fluorescent signal is expressed as a linear integration of the component dye spectra [15], and therefore the concentration or intensity of the fluorescence from each dye can be precisely analyzed. Based on the data analysis, both spatial mismatch and cross-talk effect are mitigated in multicolor imaging of live cells.

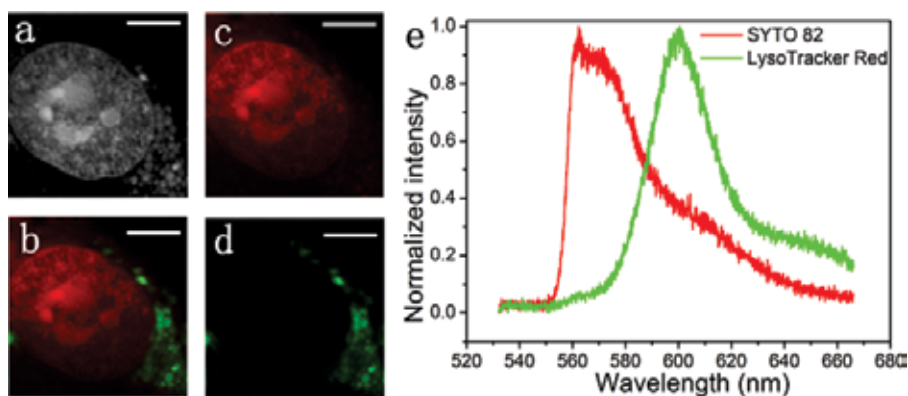


Figure 13. Multicolor RCM reveals the cellular microstructures labeled with different dyes. (a) Simultaneous RCM imaging of nucleus and lysosomes labeled with SYTO 82 and LysoTracker Red in a live bEnd.3 cell, respectively. Based on the linear spectral unmixing analysis, nucleus (c) and lysosomes (d) are differentiated according to their corresponding spectral features (e), respectively. (b) Overlaid image of the RCM images from (c) and (d). Scale bar: 5 μm .

In **Figure 13**, we establish a multicolor RCM with simultaneous excitation of different fluorophores and synchronous collection of their fluorescence. Linear spectral unmixing analysis is implemented for the spectral differentiation of the live cells stained with different dyes. SYTO 82-labeled nucleus and LysoTracker Red-stained lysosomes within live bEnd.3 cells are imaged by RCM with a spectrometer as the spectral detector. The nucleus and lysosomes are captured simultaneously, followed by the linear spectral unmixing analysis based on the known spectral features of these two dyes (severely overlapping as shown in **Figure 13(e)**). **Figure 13(b)–(d)** gives a clear separation of the two kinds of subcellular organelles. This approach is very powerful in investigation of the dynamic interactions of the subcellular structures.

Acknowledgements

This work was supported in part by the National Natural Science Foundation of China grant Nos. 61505238 and 11504042, Daqing Normal University Youth Foundation No. 12ZR12, Daqing Normal University doctor Foundation No. 15ZR03 doctor Foundation, Natural Science Foundation Project of Heilongjiang Province Nos. A200506 and QC2015066, Science and Technology Research Project of Heilongjiang Province Education Department No. 12543002, and Guidance of Science and Technology Plan Projects of Daqing City No. szdfy-2015-59.

Author details

Longchao Chen¹, Yuling Wang² and Wei Song^{1*}

*Address all correspondence to: weisong1220@gmail.com

¹ Shenzhen Institute of Advanced Technology, Chinese Academy of Sciences, Shenzhen University Town, Shenzhen, China

² School of Mechatronics Engineering, Daqing Normal University, Ranghulu District Xibin Road, Daqing, China

References

- [1] V. Westphal and S. W. Hell, "Nanoscale resolution in the focal plane of an optical microscope," *Phys. Rev. Lett.* 94(14), 143903 (2005).
- [2] M. Bates, B. Huang, G. T. Dempsey and X. Zhuang, "Multicolor super-resolution imaging with photo-switchable fluorescent probes," *Science* 317(5845), 1749–1753 (2007).
- [3] M. J. Rust, M. Bates and X. Zhuang, "Sub-diffraction-limit imaging by stochastic optical reconstruction microscopy (STORM)," *Nat. Methods* 3(10), 793–796 (2006).
- [4] B. Huang, M. Bates and X. Zhuang, "Super resolution fluorescence microscopy," *Annu. Rev. Biochem.* 78, 993 (2009).
- [5] C. Sheppard, "Super-resolution in confocal imaging," *Optik* 80(2), 53–54 (1988).
- [6] I. J. Cox, C. J. Sheppard and T. Wilson, "Improvement in resolution by nearly confocal microscopy," *Appl. Opt.* 21(5), 778–781 (1982).
- [7] J. McGregor, C. Mitchell and N. Hartell, "Post-processing strategies in image scanning microscopy," *Methods* 88, 28–36 (2015).

- [8] P. W. Winter, A. G. York, D. Dalle Nogare, M. Ingaramo, R. Christensen, A. Chitnis, G. H. Patterson and H. Shroff, "Two-photon instant structured illumination microscopy improves the depth penetration of super-resolution imaging in thick scattering samples," *Optica* 1(3), 181–191 (2014).
- [9] A. G. York, S. H. Parekh, D. Dalle Nogare, R. S. Fischer, K. Temprine, M. Mione, A. B. Chitnis, C. A. Combs and H. Shroff, "Resolution doubling in live, multicellular organisms via multifocal structured illumination microscopy," *Nat. Methods* 9(7), 749–754 (2012).
- [10] A. G. York, P. Chandris, D. Dalle Nogare, J. Head, P. Wawrzusin, R. S. Fischer, A. Chitnis and H. Shroff, "Instant super-resolution imaging in live cells and embryos via analog image processing," *Nat. Methods* 10(11), 1122–1126 (2013).
- [11] C. B. Müller and J. Enderlein, "Image scanning microscopy," *Phys. Rev. Lett.* 104(19), 198101 (2010).
- [12] G. M. De Luca, R. M. Breedijk, R. A. Brandt, C. H. Zeelenberg, B. E. de Jong, W. Timmermans, L. N. Azar, R. A. Hoebe, S. Stallinga and E. M. Manders, "Re-scan confocal microscopy: scanning twice for better resolution," *Biomed. Opt. Express*. 4(11), 2644–2656 (2013).
- [13] J. Huff, "The Airyscan detector from ZEISS: confocal imaging with improved signal-to-noise ratio and super-resolution," *Nat. Methods* 12(12), (2015).
- [14] T. Haraguchi, T. Shimi, T. Koujin, N. Hashiguchi and Y. Hiraoka, "Spectral imaging fluorescence microscopy," *Genes. Cells* 7(9), 881–887 (2002).
- [15] H. Tsurui, H. Nishimura, S. Hattori, S. Hirose, K. Okumura and T. Shirai, "Seven-color fluorescence imaging of tissue samples based on Fourier spectroscopy and singular value decomposition," *J. Histochem. Cytochem.* 48(5), 653–662 (2000).

Second Harmonic Generation Microscopy: A Tool for Quantitative Analysis of Tissues

Juan M. Bueno, Francisco J. Ávila, and Pablo Artal

Additional information is available at the end of the chapter

<http://dx.doi.org/10.5772/63493>

Abstract

Second harmonic generation (SHG) is a second-order non-linear optical process produced in birefringent crystals or in biological tissues with non-centrosymmetric structure such as collagen or microtubules structures. SHG signal originates from two excitation photons which interact with the material and are “reconverted” to form a new emitted photon with half of wavelength. Although theoretically predicted by Maria Göpert-Mayer in 1930s, the experimental SHG demonstration arrived with the invention of the laser in the 1960s. SHG was first obtained in ruby by using a high excitation oscillator. After that starting point, the harmonic generation reached an increasing interest and importance, based on its applications to characterize biological tissues using multiphoton microscopes. In particular, collagen has been one of the most often analyzed structures since it provides an efficient SHG signal. In late 1970s, it was discovered that SHG signal took place in three-dimensional optical interaction at the focal point of a microscope objective with high numerical aperture. This finding allowed researchers to develop microscopes with 3D submicron resolution and an in depth analysis of biological specimens. Since SHG is a polarization-sensitive non-linear optical process, the implementation of polarization into multiphoton microscopes has allowed the study of both molecular architecture and fibrillar distribution of type-I collagen fibers. The analysis of collagen-based structures is particularly interesting since they represent 80% of the connective tissue of the human body. On the other hand, more recent techniques such as pulse compression of laser pulses or adaptive optics have been applied to SHG microscopy in order to improve the visualization of features. The combination of these techniques permit the reduction of the laser power required to produce efficient SHG signal and therefore photo-toxicity and photo-damage are avoided (critical parameters in biomedical applications). Some pathologies such as cancer or fibrosis are related to collagen disorders. These are thought to appear at molecular scale before the micrometric structure is affected. In this sense, SHG imaging has emerged as a powerful tool in biomedicine and it might serve as a non-invasive early diagnosis technique.

Keywords: second harmonic microscopy, biomedical imaging, collagen, polarization, adaptive optics

1. Principles of second harmonic generation

Non-linear optical microscopy refers to all microscopy techniques based on non-linear optics, in which light-matter interactions violate the linear superposition principle. These techniques can be divided in two main categories: incoherent and coherent. Although in the former, the phase of the emitted optical signal is random, in coherent techniques it depends on a wide variety of factors, including those related to the exciting light or associated with the geometric distribution of the radiating molecules. One of these phenomena is the so called Second Harmonic Generation (SHG).

SHG is a coherent non-linear process where two incident photons at their fundamental frequency interacting with a medium are directly converted into a single photon of exactly the same total energy at double of frequency, without absorption or reemission of photons [1]. This process is carried out via an intermediate virtual state in a single quantum event. **Figure 1** compares this SHG process with the typical linear fluorescence phenomenon.

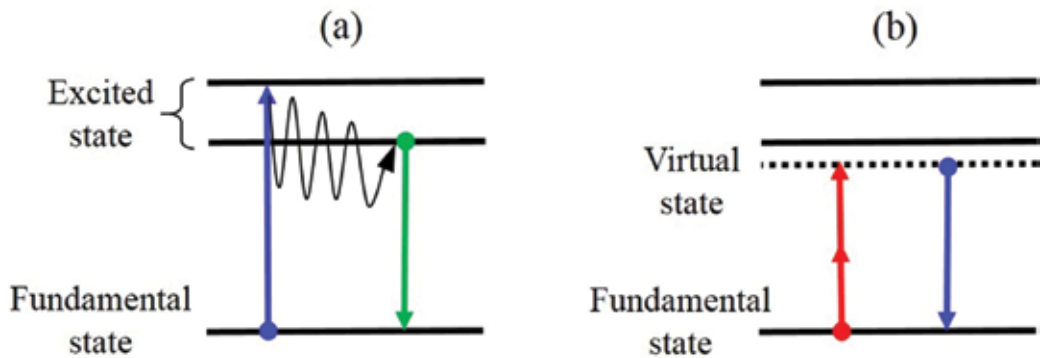


Figure 1. Diagrams of linear fluorescence (a) and SHG (b).

According to the non-linear optics theory, an incident electric field \vec{E}_ω with a frequency ω induces a second-order polarization $\vec{P}_{2\omega,i}$ at 2ω in the i th direction given by [1]:

$$\vec{P}_{2\omega,i} = \epsilon_0[\chi^{(1)}\vec{E} + \chi^{(2)}\vec{E}\vec{E} + \chi^{(3)}\vec{E}\vec{E}\vec{E} + \dots] \quad (1)$$

where ϵ_0 is the vacuum permittivity and $\chi^{(n)}$ is the n th-order non-linear susceptibility tensor. The first term of Equation (1) describes the normal absorption and reflection of light, and the second the SHG. Since the term $\chi^{(2)}$ depends on the polarization of the excitation source, the SHG emission is sensitive to polarization [2]. In a medium with hexagonal symmetry, the non-null coefficients $d_{ij} = \frac{1}{2} \epsilon_0 \chi_{ij}^{(2)}$ are d_{31} , d_{33} , d_{15} and d_{14} [3].

These coefficients contain the non-linear optical properties of the material and sum zero for inversion symmetry [4]. Moreover, if Kleinman and cylindrical symmetries are assumed, $d_{14}=0$ and $d_{15} = d_{31}$ [5].

SHG was demonstrated in crystalline quartz in 1962 by Kleinman, and since then this has been commonly used to frequency-double pulsed lasers to obtain shorter wavelengths [5]. Moreover, SHG signal is sensitive to bulk non-centrosymmetric spatial arrangements such as collagen structures or birefringent crystals [6]. The lack of a center of symmetry in an organized material strongly affects the second-order susceptibility and therefore the efficiency of SHG signals [7].

Unlike two-photon excitation fluorescence, SHG is energy conserving (it does not involve an excited state), strongly directional and preserves the coherence of the laser light [8]. Then, a medium is able to provide efficient SHG signal when its structure is organized at the scale of the laser wavelength and lacks a center of symmetry. Further details on the advantages of using SHG imaging (especially for biological applications) will be presented along this chapter.

2. SHG microscopy of biological samples

In 1971, Fine and Hansen proposed that SHG signal could also be produced by biological tissues [9]. In 1974, Hellwarth and Christensen implemented SHG into an optical microscope to visualize the microscopic crystal structure of polycrystalline ZnSe [10]. Later, Gannaway and Sheppard presented SHG images of a lithium niobate crystal by using a laser scanning microscope [11]. These images showed features and contrast levels not seen in regular (linear) microscopy.

However, to our knowledge, the first biological SHG image was reported by Freund in 1986. He imaged a rat tail tendon with high resolution SHG scanning microscopy [12]. More than a decade was necessary to consistently apply SHG microscopy to visualize biological specimens. In particular, a laser scanning microscope was combined with a Ti-Sapphire femtosecond laser to acquire live cell images based on SHG [13].

Other biological specimens imaged using SHG microscopy include membranes [7], proteins [13] and collagen-based structures [14] among others. **Figure 2** shows a sample containing starch grains imaged with SHG microscopy.

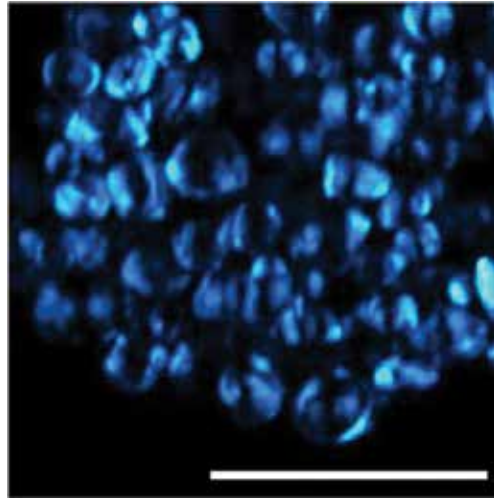


Figure 2. SHG image of starch grains. These are plant polysaccharides with a convenient radial structure. It can be found in both a non-organized (dry) and an organized (hydrated) form. Scale bar: 50 μm .

According to the non-linear nature of harmonic generation, the intensity of the SHG signal depends on the square of the excitation laser intensity, and occurs intrinsically confining the focus of the microscope objective. Since this event takes place in both transversal and axial directions, SHG imaging microscopy provides intrinsic 3D sectioning capabilities with excellent Z-resolution. This property allows optical sectioning of biological samples with reduced out-of-plane photo-toxicity (see **Figure 3**).

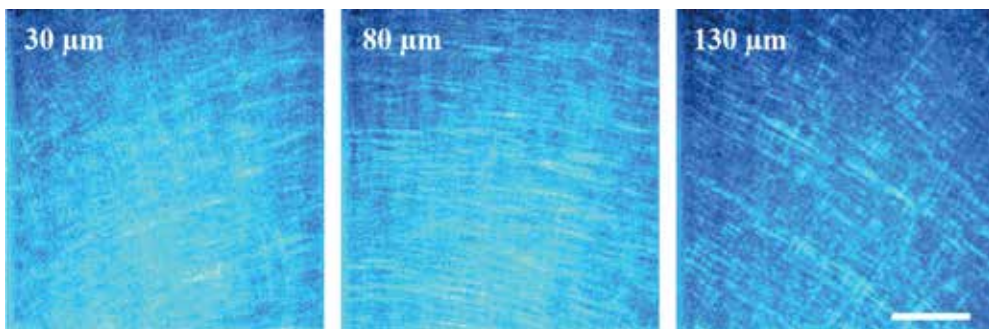


Figure 3. SHG images of an eagle cornea acquired at three different depth locations. Scale bar: 50 μm .

Apart from this inherent property, during the last ten years SHG microscopy has gained increasing popularity in biomedicine mainly due to the provided possibilities for endogenous contrast imaging (staining procedures are not required), reduced tissue damage, sensitivity to molecular architecture organization, preservation of phase information and polarization dependence [15].

SHG is restricted to molecules with non-centrosymmetric organization and is emitted by different biological tissues containing collagen [1], myosin [16] or tubulin (which polymerizes into microtubules) [17]. Type-I collagen is the most abundant structural protein of the human body [18], and due to its presence in connective tissue, SHG signal can be effectively obtained from the cornea, the skin, bones or tendons [19–27]. Collagen plays an important role within the human body and has been studied under many different experimental conditions. Its presence in connective tissues constitutes 6% of the dry weight of the body [28].

The basic structural unit of collagen is the molecule of tropocollagen, presenting a helical structure, formed by three polypeptide chains coiled around each other to form a spiral (see **Figure 4**). These molecules are cross-linked to form collagen fibrils.

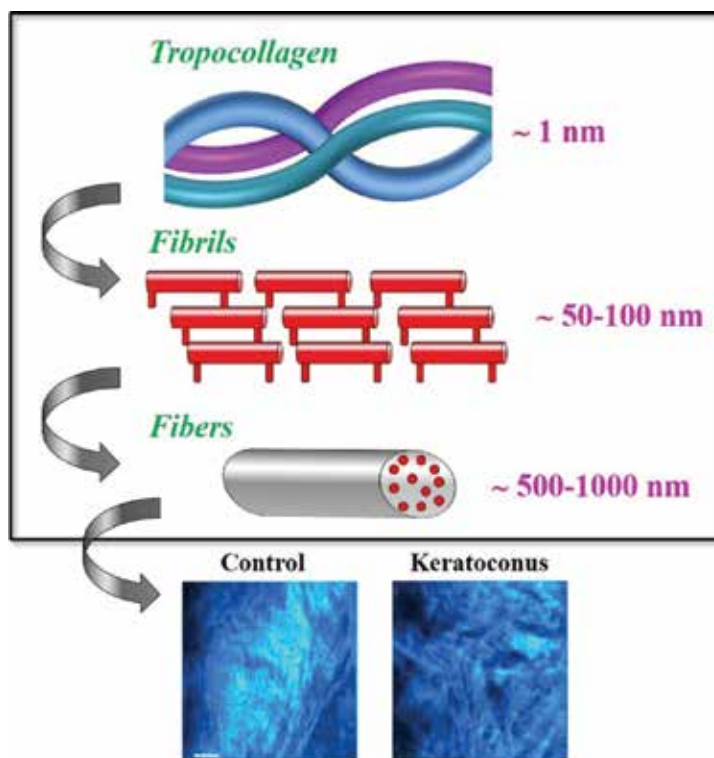


Figure 4. Schematic representation of the collagen structure and SHG images of two human corneas with different collagen distributions. Bar length: 50 μm .

These fibrils are assembled into parallel beams to form collagen fibers [18]. The origin of the SHG signal in collagen arises from its molecular chirality, where the molecules possess permanent dipole moments with high order alignment, ensuring the generation of harmonic signal as a consequence of the non-symmetrical oscillation of the electrons [15]. On the other hand, the intrinsic chirality of the triple-helix of molecular collagen increases the asymmetry of the assembly increasing the non-linear response.

As above explained, the SHG signal can be characterized by the non-linear susceptibility tensor [4]. This depends on the induced dipole moment of the molecules and therefore on the organization of the collagen tissue. If a collagen triple-helix is excited along its main axis, each bond contribution is summed coherently to the SHG signal [29]. When the molecules with the same orientation—or polarity—are assembled to form fibrils, the SHG signal is amplified significantly [30]. Then, the total intensity is the coherent sum of the signal from individual collagen fibrils.

However, in some collagen-based tissues the polarity of the fibrils within the fiber varies randomly [31]. In those cases the organization presents contributions to the axial momentum altering the coherent process of the SHG. Theoretically, the phase matching condition for which the non-linear process is strictly coherent is given by [15]:

$$\vec{\Delta k} = \vec{k}_{2\omega} - 2\vec{k}_{\omega} = 0 \quad (2)$$

where $\vec{k}_{2\omega}$ is the wave vector for the SHG emission and $2\vec{k}_{\omega}$ is the wave vector of the incident light. Then, a second harmonic conversion is maximum if $\vec{\Delta k} = 0$. Experimentally, only birefringent crystals have been found to verify this condition [32]. In biological samples, and particularly in collagen-based tissues, the SHG signal is a quasi-coherent process which SHG efficiency conversion depends on how aligned within the fiber the fibrils are.

SHG images at the bottom of **Figure 4** compare the collagen distribution in a normal healthy human cornea and another affected by a pathology called keratoconus. This is a real example on how the coherence of SHG signal is an efficient detector of collagen organization within a sample. Although the control tissue displays a fairly regular distribution of collagen fibers along a preferential direction, these are randomly distributed in the pathologic case. The

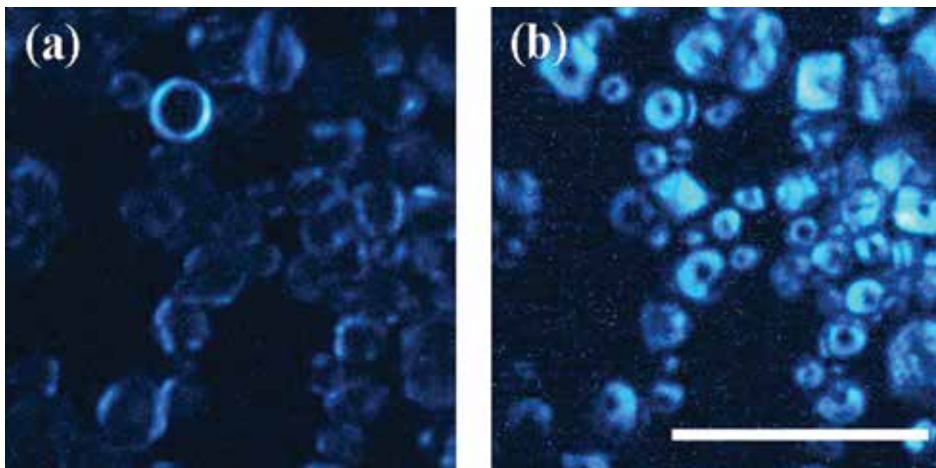


Figure 5. Comparison of SHG images acquired in the backward (a) and forward (b) directions. The differences between the two acquisition directions are readily visible due to the behavior of the SHG emission. Scale bar: 50 μm .

control tissue provides a more efficient SHG conversion because Δk is significantly lower than in the pathologic case. Changes in collagen morphology are firstly produced at molecular level (tropocollagen), which number of aligned dipoles coherently sum, affecting the fibril organization and therefore the distribution of the fibers finally imaged with SHG microscopy.

On the other hand, the emission directionality has an effect in both SHG signal conversion efficiency and observed morphology. This is easily observed in the starch grains presented in **Figure 5**.

In collagen-based tissues, this effect is due to the size and the organization of the collagen fibers, since both affect the phase mismatch and the amplification of the SHG intensity [15]. In general, SHG directionality depends on the distribution of the induced dipoles in the focal volume where the non-linear process takes place [33]. In this sense, the directionality effects of the SHG signal can be appreciated in the visualization of continuous structures (fibers) in the backward channel (i.e. backscattered emission), and a higher segmentation or discrete distribution in the forward directed emission [34]. This implies that the choice of the detection direction in the experimental device will depend on the desired scale of observation. However, since changes in collagen fibers can be observed in the backward configuration [1], this configuration has become suitable for biomedical imaging.

3. Imaging ocular tissues with SHG microscopy

As stated above, the human body is plenty of tissues composed of collagen. These tissues are often the main component of different organs. In particular, the eye is one of them. Although this is not a vital organ (such as the heart or the liver, for instance), it is necessary to have a regular way of living (both humans and animals). Since the middle of nineteenth century, there have been a number of instruments to visualize ocular structures in order to improve the diagnosis and treatment of eye's diseases. Since most ocular elements are transparent, staining procedures are usually required and, under certain experimental conditions, the existing clinical techniques are sometimes not totally appropriate. In that sense, SHG microscopy might be used as a new tool to improve the imaging of some ocular tissues.

The sclera and the cornea are the two structures are the eye's outer tunic, mainly composed of type-I collagen. The former is an opaque connective tissue acting as protective element that gives stability to the ocular globe. Unlike the sclera, the cornea presents high transparency which originates from particular arrangements of the collagen fibers (localized within the stroma, which occupies about 90% of whole corneal thickness). Corneal collagen assembles to form long fibrils with a diameter of approximately 25 nm (in humans) [35]. These are uniformly spaced forming larger bundles or fibers termed "corneal lamellae" (tens of microns in size). In contrast, scleral fibrils have various diameters ranging between 25 and 230 nm [35]. These collagen fibrils also form bundles, however these are not parallel arranged but entangled in individual bundles.

Since type-I collagen is an effective second harmonic generator, both ocular elements can be visualized with SHG imaging microscopy without using labeling techniques. However, the

sclera does not have any contribution to the vision function and this is probably the reason because SHG studies on the sclera are scarce. To our knowledge, Han and colleagues were the first to show SHG images of the sclera [36]. The sclera collagen distribution was analyzed through these images in forward and backward directions. They concluded that the sclera presents inhomogeneous, tube-like structures with thin hard shells, maintaining the high stiffness and elasticity of the tissue. SHG imaging was used by Teng and co-authors to resolve the difference in structural orientations between the collagen fibers of the cornea and the sclera: the corneal collagen is organized in a depth-dependent fashion, whereas the sclera collagen is randomly packed [37]. As an example, **Figure 6** shows SHG images of healthy tissues corresponding to a human cornea and a sclera. A simple visual inspection reveals the evident difference in collagen distribution.

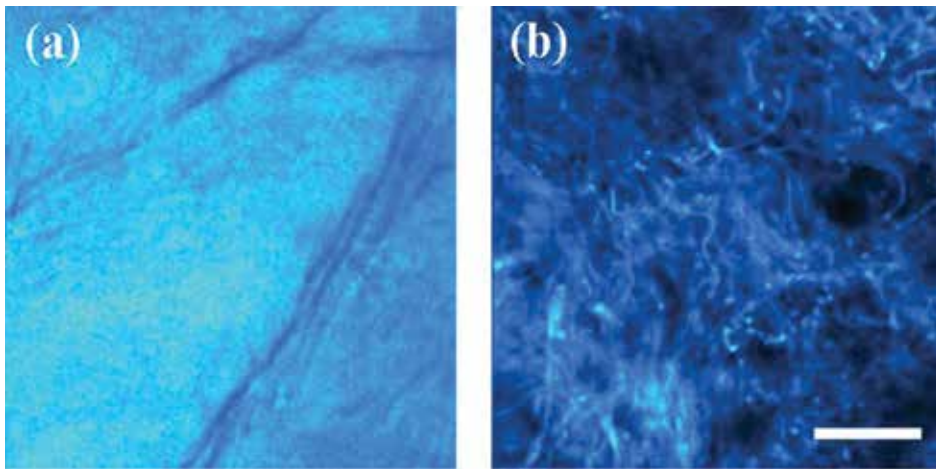


Figure 6. Comparison of collagen distributions in SHG images of a human cornea (a) and a piece of human sclera (b). Although the fibers in the sclera present always a non-organized pattern, in the cornea the arrangement depends on a number of factors as explained below. Scale bar: 50 μm .

SHG images of the sclera as a function depth have also been analyzed. At shallow planes collagen bundles were roughly aligned parallel to the limbus. At deeper locations the fibers did not have a specific orientation of alignment [38]. At the posterior pole this arrangement differed. On the external surface undulating thick bundles without a notable major orientation were found. These also had interwoven structures with various orientations. On the internal surface of the sclera fine collagen bundles were observed. These bundles were frequently branched and intermingled. As already mentioned, the sclera has not a direct implication in visual function, however its structures are related to ocular biomechanics and the changes with intraocular pressure or surgery might be interesting in clinical applications.

Unlike the sclera, the cornea has been analyzed with SHG microscopy by many different authors. Since Yeh et al. obtained SHG images in rabbit corneas without exogenous dyes [19] the corneal structure has been studied in a number of animal models (including humans) under several experimental conditions (see for instance [39] and references therein). SHG images of

the cornea have been compared in both forward and backward scattering directions [36]. Although images showed different information, collagen fibers always showed a regular packaging [36, 37]. However, this regular pattern has been shown to change with pathologies [40, 41] or after surgical procedures [42–44]. The corneal stroma also suffers alterations due to scars [45] or changes in the intraocular pressure [46] that have been explored through SHG imaging.

Although SHG microscopy has been used to image the cornea under different experimental conditions, two aspects are really important: (1) the response of the SHG signal to polarized light and (2) the measurement of the stroma organization. Moreover, an objective characterization of structural abnormalities is of great interest to distinguish normal from pathological corneas and the key for possible clinical applications. The next section deals with this topic.

4. Measurement of collagen organization in ocular tissues

As previously mentioned, the collagen arrangement could be compromised due to pathological processes, mechanical trauma or denaturation (aging). Due to this, both classification and quantification of collagen arrangement might be a powerful tool in biomedicine as well as in medical diagnosis, in particular for those pathologies associated with collagen disorders occurring at early stages of the disease.

The analysis of the collagen organization has usually been carried out in a qualitative manner. A quantitative analysis would lead to understand changes in corneal stroma caused by intraocular pressure [46], pathological processes [47, 48] or surgery [49] among others. Although there are several techniques to analyze the spatial distribution of collagen, the bi-dimensional fast Fourier transform (2D-FFT) has often been used for this goal [50].

In particular, the 2D-FFT method has been used with SHG images to compute the degree of organization in corneal collagen in the presence of pathologies [26] or after physical damage

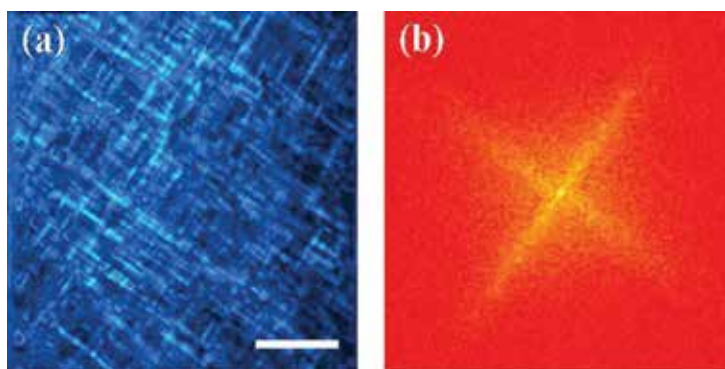


Figure 7. (a) SHG images of an eagle cornea with two preferential directions of the collagen fibers (crosshatched pattern) and (b) the associated 2D-FFT image. As expected, the 2D-FFT presents a cross shape as a result of the distribution of the fibers within the imaged corneal layer. Scale bar: 50 μm .

[51]. If the SHG image shows a structure with a preferential orientation, the spatial frequencies of the 2D-FFT spectrum are aligned along the direction orthogonal to that preferential orientation [52]. Nevertheless, the resolution of the 2D-FFT is limited by the noise of the SHG image and an image filtering is often required. The distribution of the spatial frequencies on the 2D-FFT is also generally fitted by an ellipse, and the ratio between its axes is used as a parameter to quantify the collagen organization. However, when a collagen distribution is arranged in a more complex and heterogeneous pattern (interwoven, crosshatched, ...), the best fit is a circle and this operation may lead to erroneous conclusions that require a complicate post-processing [53]. **Figure 7** shows a SHG image with a crosshatched appearance of collagen fibers, together with the corresponding 2D-FFT.

In this sense an alternative procedure based on the structure tensor has recently been presented by these authors as a useful tool to classify the spatial distribution of collagen-based tissues through SHG images [54]. The technique has the advantage of differentiate areas with maximum organization from those locations where the orientation of the collagen fibers is not significant. The structure tensor provides relevant parameters such as the spatially-resolved degree of isotropy (DoI) and the histogram of orientation distribution. The former ranges between 0 and 1 and its value increases with the order of the structure (i.e. the more aligned the fibers the higher the DoI). In the latter, it is verified that the narrower the data, the higher the presence of a dominant orientation. Apart from their quantitative information, a visual inspection of both the DoI map and the orientation histogram permits to discriminate between quasi-aligned and non-organized collagen distributions. For a better understanding of this tool, **Figure 8** shows two SHG images with different spatial distributions and the correspond-

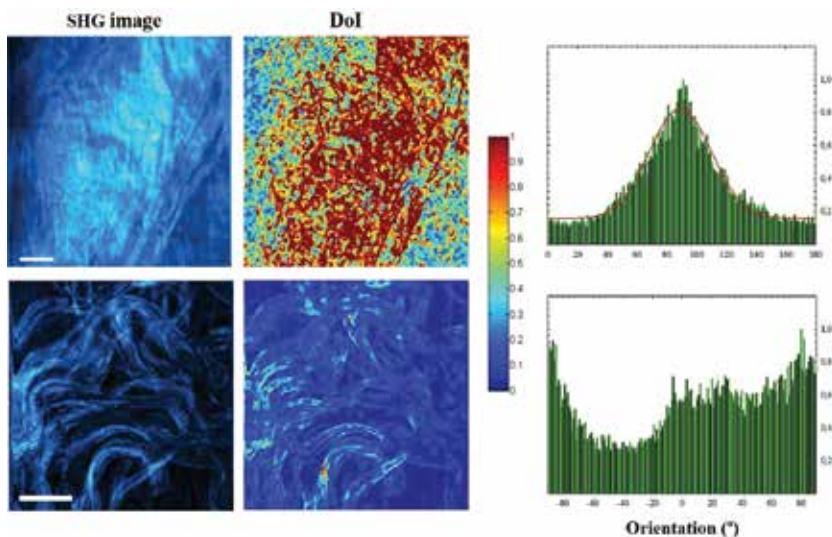


Figure 8. SHG images of a human cornea (upper row) and bovine sclera (bottom row) and their respective spatially-resolved DoI and orientation histogram computed through the structure tensor. Detailed information on how these parameters were computed can be found in [54]. Scale bar: 50 μm .

ing structure tensor parameters. At this point, it is important to notice that the combination of SHG microscopy and the structure tensor could help in the diagnosis of abnormal structures and in the tracking of pathologies related to corneal stroma disorders.

5. Adaptive optics SHG imaging

Despite optical sectioning capabilities and inherent confocality of SHG microscopy, the imaging of thick samples (3D imaging) is limited by the specimen-induced aberrations. When a femtosecond laser beam is focused into a specimen, the deeper the layer to be imaged, the larger the focal spot size. This leads to a reduction in the effectiveness of the SHG process (i.e. lower SHG signal) and a decrease in the quality of the acquired images, both contrast and resolution (**Figure 9**).

To overpass this, adaptive optics (AO) techniques combining a wavefront sensor and an adaptive device (deformable mirror or spatial light modulator) have been used [55–58]. Most authors have been interested in improving two-photon excitation fluorescence images through AO and experiments dealing with AO-SHG imaging are scarce in the literature [59–62].

Although the ideal situation is to compute and correct for the plane-by-plane aberrations, this is experimentally difficult [63]. In that sense, wavefront sensor-less techniques combined with multiphoton microscopy have been reported [58, 59, 61, 62]. With this approach, at a certain plane within the sample the AO element pre-compensates for the “unknown” aberrations without measuring them, but finding the best image according to a pre-defined image quality metric. Although these are time-consuming procedures due to the use of iterative algorithms such as genetic learning, hill-climbing or stochastic, they have provided significantly improved images with more visible details.

Moreover, the dominant aberration term at deeper layers is the spherical aberration [55, 58, 64]. In order to correct for (or minimize) this unwanted spherical aberration, objective correc-



Figure 9. SHG images of a rabbit cornea at different depth locations (10, 100 and 100 μm). The reduction in SHG signal is readily visible. This decrease in SHG effectiveness is mainly due to specimen-induced aberrations and scattering. Scale bar: 50 μm .

tion collars [64, 65] and wavefront sensor-less AO devices [55, 58, 62] have been used. The former is a manual method only valid for a defined set of cover thickness values. The latter is faster than usual since only the spherical aberration term has to be corrected. An alternative technique has recently been reported to improve 3D multiphoton imaging [66]. This is based on the manipulation of the spherical aberration pattern of the incident beam while performing fast tomographic SHG imaging. As expected, when inducing spherical aberration the image quality is reduced at best focus, however at deeper planes a better image quality is obtained. This increases the penetration depth and enables improved 3D SHG images even with non-immersion objectives.

Although these AO techniques can be applied to both non-biological and biological samples, there is a special interest when imaging ocular tissues, the cornea in particular. For this ocular structure the features of interest (especially when analyzing pathologies) might be close to the surface or located deep into it. For shallow planes, SHG images are usually of high quality. However when the plane to be imaged is located at a deeper position AO-SHG can be used as a powerful technique to noticeably enhance SHG images corresponding to those deep corneal layers (see **Figure 10** as an example). Those images will have enough contrast and resolution to observe the collagen bundles [66], and any possible abnormal distribution of them across

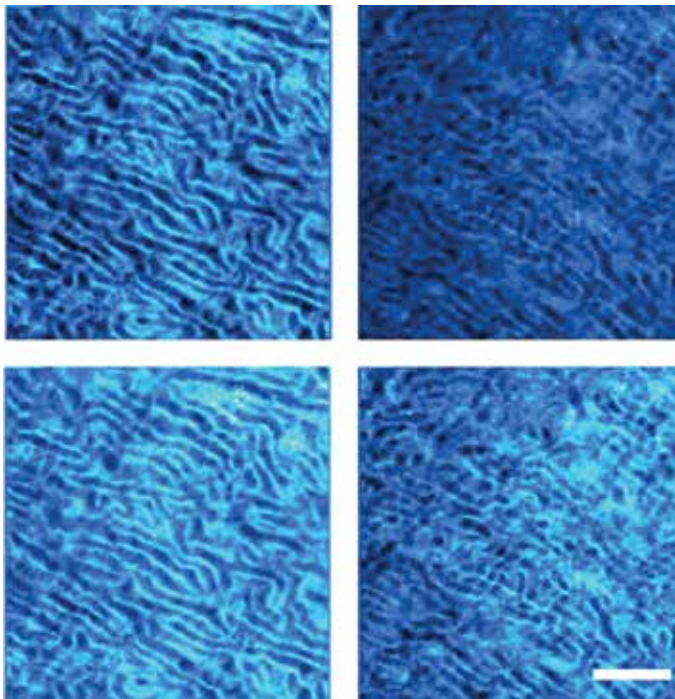


Figure 10. Comparison of SHG images before (upper panels) and after (bottom panels) using AO for two different locations within the sample (porcine cornea). It can be observed how AO improves the quality of the images at both locations. However this is more noticeable for deeper locations within the sample. Scale bar: 50 μm .

the imaged area. Future clinical instruments can also benefit from this implementation which leads to a better visualization of the layered ocular structures.

6. Polarization-sensitive SHG microscopy

The dependence between polarization and SHG signals in collagen is well recognized [67–69]. The combination of non-linear microscopy and polarization allowed detecting changes in collagen arrangement [70] and has been proposed to characterize collagen-based tissues [71, 72]. Type-I collagen fibers exhibit structural anisotropy that can be characterized by the ratio of hyperpolarizabilities or polarization anisotropy $\rho = \beta_{xxx}/\beta_{xyy}$ which provides information about the internal collagen structure [33, 73].

The polarization anisotropy depends on the orientation of the collagen triple-helix and the orientation of the induced dipoles along the peptide bonds and the values have been reported to be in the range [-3, 3] [33]. Low values of ρ are associated with immature collagen [67], aging [69] or loss of arrangement in the collagen distribution [1]. Therefore, polarization-sensitive SHG microscopy provides information about the dipolar distribution within the collagen fibers.

SHG intensity has been reported to vary with the angle between the optical axis of the polarizer and the main orientation of the collagen fibers [33, 69]. Moreover, depending on the spatial distribution of collagen fibers the SHG signal will be differently affected by the incoming polarization state [72, 74, 75] (see **Figure 11** as an example). This fact might be of great importance in SHG imaging not only because the total signal varies (for instance) when changing from linear to circular polarization, but also because more details and extra features might be visible for certain polarization states (see **Figure 12**) [72].

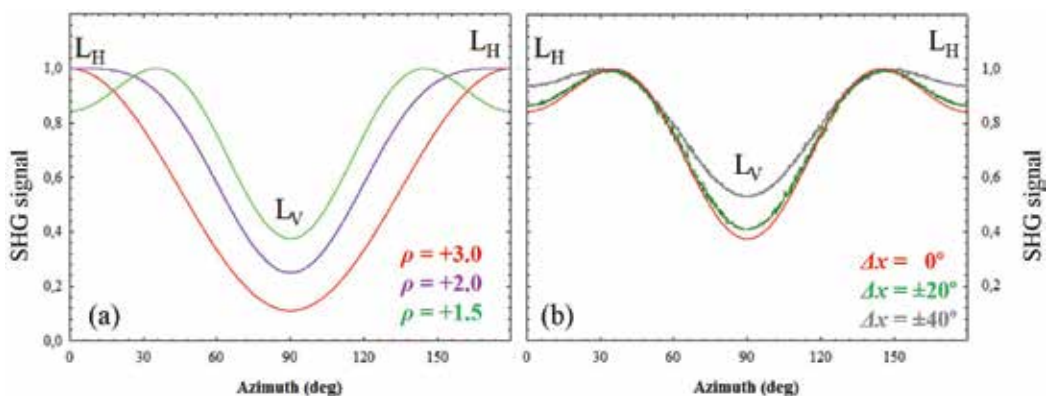


Figure 11. SHG intensity as function of the incident linear polarization for three values of ρ and parallel-arranged collagen fibers (a), and for three different values of structural dispersion, Δx , and $\rho = +1.5$ (b). Further details on this can be found in [72].

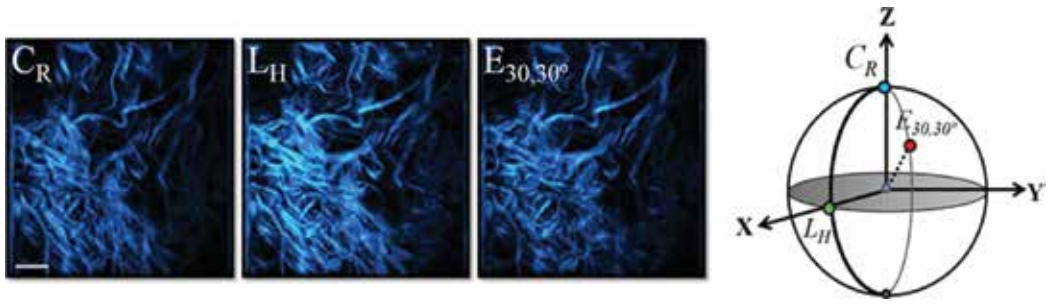


Figure 12. SHG images of a bovine sclera recorded for three different incident polarization states. L_H , linear horizontal; C_R , right circular and $E_{30,30^\circ}$ right elliptical. The location of these polarization states over the Poincaré sphere are shown on the right. Scale bar: 50 μm .

The combination of polarization and SHG signal allows obtaining information about the hierarchical architecture of collagen at molecular scale [76, 77]. This has been used in biopsies to discriminate normal breast from malignant tissue [78], and analyze cancerous ovarian tissues [79].

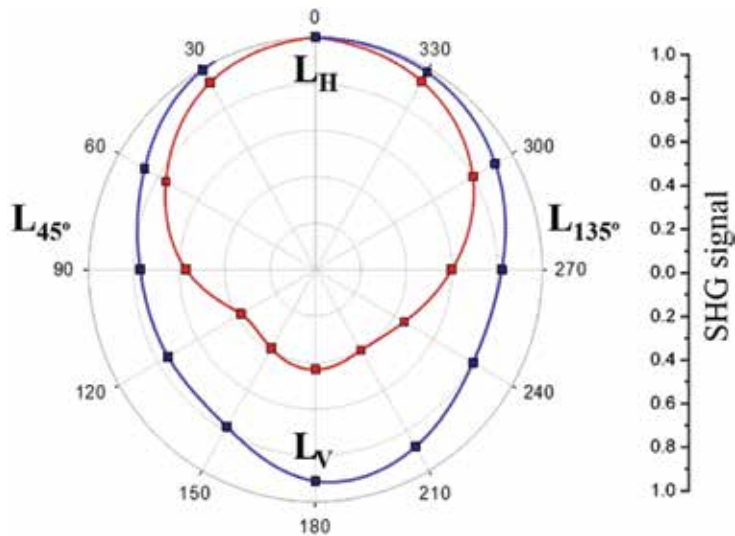


Figure 13. Polar diagram representing the normalized SHG intensity distribution as function of incoming polarization of a control (red) and a keratoconus (blue) cornea. The dependence of SHG intensity with incident polarization is stronger in the former probably due to the presence of a dominant direction of the collagen fibers. This does not exist in the latter and the SHG signal hardly depends on the polarization state.

Pathological alterations of the cornea could seriously compromise vision. In this sense polarization-sensitive SHG microscopy has been proved to be effective to detect structural alterations in keratoconus [40]. It has also been employed to analyze the molecular changes produced by high levels of intraocular pressure and to investigate how these modifications produced within the lamellae affect the stroma thickness [80]. As a possible clinical application,

Figure 13 compares the response to incident linear polarization of a human control and a keratoconus cornea (those presented in **Figure 4**). It can be observed how the SHG signal from the pathological case presents lower dependence with polarization.

7. Conclusions

Along this chapter, the principles of SHG processes and the application to biological imaging have been reviewed. SHG microscopy is a non-linear modality with inherent confocality that allows visualizing non-stained tissues composed of collagen and shows features not seen with regular microscopy. SHG intensity depends on both the size and organization of the collagen fibers. Since SHG directionality depends on the distribution of the induced dipoles within the fibers, the registration of the signal in a backscattered direction can be used to observe the collagen architecture within the specimens (**Figure 13**).

In particular, this is a useful tool to image connective ocular tissues such as the sclera and the cornea with high resolution as function of depth. These tissues can be characterized attending the organization of their collagen fibers. Unlike the sclera that usually presents a non-organized distribution, the arrangement of the corneal fibers depends on numerous factors. These collagen organizations have been discussed and a novel method based on the structure tensor to perform quantitative analyses has been proposed. This permits to classify the spatial distribution of the fibers from the SHG images, and can be used for diagnoses of pathologies related to collagen disorders.

However, the efficiency of SHG imaging of thick samples reduces with depth, as the specimen itself induces aberrations and scattering. To overcome this limitation, AO procedures have been implemented into SHG microscopes. The manipulation of the aberration pattern of the incident laser beam has allowed increasing the image quality of SHG images especially at deeper locations.

On the other hand, SHG signal from collagen structures is polarization dependent. This modulation depends on both collagen internal structure (parameter ρ) and the arrangement of the fibers (external organization). The combination of polarization and SHG microscopy has been reported to be effective in detecting structural changes in collagen-related pathological processes. The technique could then be a powerful tool in biomedicine and/or in clinical diagnoses.

Author details

Juan M. Bueno*, Francisco J. Ávila, and Pablo Artal

*Address all correspondence to: bueno@um.es

Laboratorio de Optica, Universidad de Murcia, Murcia, Spain

References

- [1] R. M. Williams, W. R. Zipfel and W. W. Webb. Interpreting second-harmonic generation images of collagen I fibrils. *Biophys. J.* 2005; 88(2): 1377–1386.
- [2] A. Erikson, J. Ortegren, T. Hompland, C. L. Davies and M. Lindgren. Quantification of the second-order non-linear susceptibility of collagen I using a laser scanning microscope. *J. Biomed. Opt.* 2009; 12(4):044002.
- [3] P. N. Butcher and D. Cotter. *The elements of nonlinear optics.* Cambridge University Press. Cambridge, 1991.
- [4] R. W. Boyd. *Non-linear optics.* Academic Press. San Diego, USA, 1992.
- [5] D. A. Kleinman. Theory of second harmonic generation of light. *Phys. Rev.* 1962; 128(4): 1761–1775.
- [6] T. Verbiest, S. Van Elshocht, M. Kauranen, L. Hellemans, J. Snauwaert, C. Nuckolls, T. J. Katz and A. Persoons. Strong enhancement of nonlinear optical properties through supramolecular chirality. *Science.* 1999; 282(5390):913–915.
- [7] L. Moreaux, O. Sandrea and J. Mertz. Membrane imaging by second harmonic generation microscopy. *J. Opt. Soc. Am. B.* 2000; 17(10):1685–1689.
- [8] P. J. Campagnola, A. C. Millard, M. Terasaki, P. E. Hoppe, C. J. Malone and W. Mohler. Three-dimensional high-resolution second-harmonic generation imaging of endogenous structural proteins in biological tissues. *Biophys. J.* 2002; 82(1):493–508.
- [9] S. Fine and W. P. Hansen. Optical second harmonic generation in biological systems. *Appl. Opt.* 1971; 10(10):2350–2353.
- [10] R. Hellwarth and P. Christensen. Nonlinear optical microscopic examination of structure in polycrystalline ZnSc. *Opt. Commun.* 1974; 12(3):318–322.
- [11] J. N. Gannaway and C. J. R. Sheppard. Second harmonic imaging in the scanning optical microscope. *Opt. Quantum Electron.* 1978; 10(5):435–439.
- [12] I. Freund and M. Deutsch. Second harmonic microscopy of biological tissues. *Opt. Lett.* 1986; 11(2):94–96.
- [13] P. J. Campagnola, M. D. Wei, A. Lewis and L. M. Loew. High resolution nonlinear optical microscopy of living cells by second harmonic generation. *Biophys. J.* 1999; 77(6):3341–3349.
- [14] P. J. Campagnola and L. M. Loew. Second-harmonic imaging microscopy for visualizing biomolecular arrays in cells, tissues and organisms. *Nat. Biotechnol.* 2003; 21(11): 1356–1360.
- [15] R. LaComb, O. Nadiarnykh, S. S. Townsend and P. J. Campagnola. Phase matching considerations in second harmonic generation from tissues: effects on emission

- directionality, conversion efficiency and observed morphology. *Opt. Commun.* 2008; 281(7):1823–1832.
- [16] S. V. Plotnikov, A. Millard, P. Campagnola and W. Mohler. Characterization of the myosin-based source for second-harmonic generation from muscle sarcomeres. *Biophys. J.* 2006; 90(2):328–339.
- [17] D. A. Dombeck, K. A. Kasischke, H. D. Vishwasrao, M. Ingelsson, B. T. Hyman and W. W. Webb. Uniform polarity microtubule assemblies imaged in native brain tissue by second-harmonic generation microscopy. *Proc. Natl. Acad. Sci. U.S.A.* 2003; 100(12): 7081–7086.
- [18] H. Lodish, A. Berk, C. A. Kaiser, M. Krieger, A. Bretscher, H. Ploegh, A. Amon and M. P. Scott. *Molecular cell biology.* W.H. Freeman and Company, New York, 2013.
- [19] A. T. Yeh, N. Nassif and B. J. Tromberg. Selective corneal imaging using combined second-harmonic generation and two-photon excited fluorescence. *Opt. Lett.* 2002; 27(23):2082–2084.
- [20] G. Cox, E. Kable and M. D. Gorrel. Three-dimensional imaging of collagen using second harmonic generation. *J. Struct. Biol.* 2003; 141(1):53–62.
- [21] S. J. Lin, S. H. Jee and C. Y. Dong. Discrimination of basal cell carcinoma from normal derma stroma by quantitative multiphoton imaging. *Opt. Lett.* 2006; 31(18):2756–2758.
- [22] H. S. Lee, S. W. Teng and C. Y. Dong. Imaging human bone marrow stem cell morphogenesis in polyglycolic acid scaffold by multiphoton microscopy. *Tissue Eng.* 2006; 12(10):2835–2841.
- [23] P. J. Campagnola. Second harmonic generation imaging microscopy: applications to diseases diagnostic. *Anal. Chem.* 2011; 83(9):3224–3231.
- [24] I. Gusachenko, V. Tran, Y. G. Houssen, J. M. Allain and M. C. Schanne-Klein. Polarization-resolved second-harmonic generation in tendon upon mechanical stretching. *Opt. Express.* 2012; 102(9):2220–2229.
- [25] X. Chen, O. Nadiarynkh, S. Plotnikov and P. J. Campagnola. Second harmonic generation microscopy for quantitative analysis of collagen fibrillar structure. *Nat. Protoc.* 2012; 7(4):654–669.
- [26] W. Lo, W. L. Chen, C. M. Hsueh, A. A. Ghazaryan, S. J. Chen, D. H. K. Ma, C. Y. Dong and H. Y. Tan. Fast Fourier transform-based analysis of second-harmonic generation Image in keratoconic cornea. *Invest. Ophth. Vis. Sci.* 2012; 53(7):3501–3507.
- [27] H. Yuan-Tan, Y. L. Chang, W. Lo, C. M. Hsueh, W. L. Chen, A. A. Ghazaryan, P. S. Hu, T. H. Young, S. J. Chen and C. Y. Dong. Characterizing the morphologic changes in collagen crosslinked-treated corneas by Fourier transform-second harmonic generation imaging. *J. Cat. Refract. Surg.* 2013; 39(5):779–788.

- [28] R. Seeley, T. Stephens and P. Tate. *Anatomy and physiology*. McGraw-Hill, Phoenix, 2003.
- [29] A. Deniset-Besseau, J. Duboisset, E. Benichou, F. Hache, P. F. Brevet and M. C. Schanne-Klein. Measurement of the second order hyperpolarizability of the collagen triple helix and determination of its physical origin. *J. Phys. Chem. B*. 2009; 248(4951):73–76.
- [30] K. E. Kadler, D. F. Holmes, J. A. Trotter and J. A. Chapman. Collagen fibril formation. *Biochem. J*. 1996; 316:1–11.
- [31] D. A. D. Parry and A. S. Craig. Quantitative electron microscope observations of the collagen fibrils in rat-tail tendon. *Biopolymers*. 1977; 16(5):1015–1031.
- [32] A. Yariv. *Quantum electronics*. Wiley, New York, 1989.
- [33] P. Stoller, P. Celliers, K. Reiser and A. Rubenchik. Quantitative second-harmonic generation microscopy in collagen. *Appl. Opt.* 2003; 42(25):5209–5219.
- [34] I. J. Su, W. L. Chen, Y. F. Chen and C. Y. Dong. Determination of collagen nanostructure from second-order susceptibility tensor analysis. *Biophysical J*. 2011; 100(8):2053–2062.
- [35] Y. Komai and T. Ushiki. The three-dimensional organization of collagen fibrils in the human cornea and sclera. *Invest. Ophthalmol. Vis. Sci*. 1991; 32(8):2244–2258.
- [36] M. Han, G. Giese and J. F. Bille. Second harmonic generation imaging of collagen fibrils in cornea and sclera. *Opt. Exp.* 2005; 13(15):5791–5797.
- [37] S. W. Teng, H. Y. Tan, J. L. Peng, H. H. Lin, K. H. Kim, W. Lo, Y. Sun, W. C. Lin, S. J. Lin, S. H. Jee, P. T. So and C. Y. Dong. Multiphoton autofluorescence and second-harmonic generation imaging of the ex vivo porcine eye. *Invest. Ophthalmol. Vis. Sci*. 2006; 47(3):1216–1224.
- [38] M. Yamanari, S. Nagase, S. Fukuda, K. Ishii, R. Tanaka, T. Yasui, T. Oshika, M. Miura and Y. Yasuno. Scleral birefringence as measured by polarization-sensitive optical coherence tomography and ocular biometric parameters of human eyes in vivo. *Biomed. Opt. Express*. 2014;5(5):1391–1402.
- [39] J. M. Bueno, E. J. Gualda and P. Artal. Analysis of corneal stroma organization with wavefront optimized nonlinear microscopy. *Cornea*. 2011; 30(6):692–701.
- [40] H. Y. Tan, Y. Sun, W. Lo, S. J. Lin, C. H. Hsiao, Y. F. Chen, S. C. Huang, W. C. Lin, S. H. Jee, H. S. Yu and C. Y. Dong. Multiphoton fluorescence and second harmonic generation imaging of the structural alterations in keratoconus ex vivo. *Invest. Ophthalmol. Vis. Sci*. 2006; 47(12):5251–5259.
- [41] C. M. Hsueh, W. Lo, W. L. Chen, V. A. Hovhannisyan, G. Y. Liu, S. S. Wang, H. Y. Tan and C. Y. Dong. Structural characterization of edematous corneas by forward and backward second harmonic generation imaging. *Biophys. J*. 2009; 97(4):1198–1205.

- [42] T.-J. Wang, W. Lo, C. M. Hsueh, M. S. Hsieh, C. Y. Dong and F. R. Hu. Ex vivo multiphoton analysis of rabbit corneal wound healing following conductive keratoplasty. *J. Biomed. Opt.* 2008; 13(3):034019.
- [43] E. J. Gualda, J. R. Vázquez de Aldana, M. C. Martínez-García, P. Moreno, J. Hernández-Toro, L. Roso, P. Artal and J. M. Bueno. Femtosecond infrared intrastromal ablation and backscattering-mode adaptive-optics multiphoton microscopy in chicken corneas. *Biomed. Opt. Express.* 2011; 2(11):2950–2960.
- [44] J. M. Bueno, E. J. Gualda, A. Giakoumaki, P. Pérez-Merino, S. Marcos and P. Artal. Multiphoton microscopy of ex-vivo corneas after collagen cross-linking. *Invest. Ophthalmol. Vis. Sci.* 2011; 52(8):5325–5331.
- [45] S. W. Teng, H. Y. Tan, Y. Sun, S. J. Lin, W. Lo, C. M. Hsueh, C. H. Hsiao, W. C. Lin, S. C. Huang and C. Y. Dong. Multiphoton fluorescence and second-harmonic-generation microscopy for imaging structural alterations in corneal scar tissue in penetrating full-thickness wound. *Arch. Ophthalmol.* 2007; 125(7):977–978.
- [46] Q. Wu and A. T. Yeh. Rabbit cornea microstructure response to changes in intraocular pressure visualized by using nonlinear optical microscopy. *Cornea.* 2008; 27(2):202–208.
- [47] N. Morishige, A. J. Wahlert, M. C. Kenney, D. J. Brown, K. Kawamoto, T. Chikama, T. Nishida and J. V. Jester. Second-harmonic imaging microscopy of normal human and keratoconus cornea. *Invest. Ophthalmol. Vis. Sci.* 2007; 48(3):1087–1094.
- [48] N. Morishige, N. Yamada, X. Zhang, Y. Morita, N. Yamada, K. Kimura, A. Takahara and K. H. Sonoda. Abnormalities of stromal structure in the bullous keratopathy cornea identified by second harmonic generation imaging microscopy. *Invest. Ophthalmol. Vis. Sci.* 2012; 53(8):4998–5003.
- [49] K. Plamann, F. Aptel, C. L. Arnold, A. Courjaud, C. Crotti, F. Deloison, F. Druon, P. Georges, M. Hanna, J. M. Legeais, F. Morin, É. Mottay, V. Nuzzo, D. A. Peyrot and M. Savoldelli. Ultrashort pulse laser surgery of the cornea and the sclera. *J. Opt.* 2010; 12(8):084002.
- [50] H. G. Adelman. Butterworth equations for homomorphic filtering of images. *Comp. Biol. Med.* 1998; 28(2):169–181.
- [51] P. Matteini, F. Ratto, F. Rossi, R. Cicchi, C. Stringari, D. Kapsokalyvas, F. S. Pavone and R. Pini. Photothermally-induced disordered patterns of corneal collagen revealed by SHG imaging. *Opt. Express.* 2009; 17(6):4868–4878.
- [52] J. C. Russ. *The image processing handbook.* CRC Press, Boca Raton, 2007.
- [53] J. M. Bueno, R. Palacios, M. K. Chessey and H. Ginis. Analysis of spatial lamellar distribution from adaptive-optics second harmonic generation corneal images. *Biom. Opt. Express.* 2013; 4(7):1006–1013.

- [54] F. J. Avila and J. M. Bueno. Analysis and quantification of collagen organization with the structure tensor in second harmonic microscopy images of ocular tissues. *Appl. Opt.* 2015; 54(33):9848–9854.
- [55] L. Sherman, J. Y. Ye, O. Albert and T. B. Norris. Adaptive correction of depth-induced aberrations in multiphoton scanning microscopy using a deformable mirror. *J. Microsc.* 2002; 206:65–71.
- [56] P. Marsh, D. Burns and J. Girkin. Practical implementation of adaptive optics in multiphoton microscopy. *Opt. Express.* 2003; 11(10):1123–1130.
- [57] M. Rueckel, J. A. Mack-Bucher and W. Denk. Adaptive wavefront correction in two-photon microscopy using coherence-gated wavefront sensing. *P. Natl. Acad. Sci. U. S. A.* 2006; 103(46):17137–17142.
- [58] D. Debarre, E. J. Botcherby, T. Watanabe, S. Srinivas, M. J. Booth and T. Wilson. Image-based adaptive optics for two-photon microscopy. *Opt. Lett.* 2009; 34(16):2495–2497.
- [59] A. Jesacher, A. Thayil, K. Grieve, D. Debarre, T. Watanabe and T. Wilson. Adaptive harmonic generation microscopy of mammalian embryos. *Opt. Lett.* 2009; 34(20):3154–3156.
- [60] J. M. Bueno, E. J. Gualda and P. Artal. Adaptive optics multiphoton microscopy to study ex vivo ocular tissues. *J. Biomed. Opt.* 2010; 15(6):066004.
- [61] J. Antonello, T. van Werkhoven, M. Verhaegen, H. H. Truong, C. U. Keller and H. C. Gerritsen. Optimization-based wavefront sensorless adaptive optics for multiphoton microscopy. *J. Opt. Soc. Am. A.* 2014; 31(6):1337–1347.
- [62] M. Skorsetz, P. Artal and J. M. Bueno. Performance evaluation of a sensorless adaptive optics multiphoton microscope. *J. Microscopy.* 2015; doi: 10.1111/jmi.12325.
- [63] M. Skorsetz, P. Artal and J. M. Bueno. Performance evaluation of a sensorless adaptive optics multiphoton microscope. *J. Microsc.* 2015; 261(3):246–258
- [64] W. Lo, Y. Sun, S. J. Lin, S. H. Jee and C. Y. Dong. Spherical aberration correction in multiphoton fluorescence imaging using objective. *J. Biomed. Opt.* 2005; 10(3):034006.
- [65] P. A. Muriello and K. W. Dunn. Improving signal levels in intravital multiphoton microscopy using an objective correction collar. *Opt. Commun.* 2008; 281(7):1806–1812.
- [66] J. M. Bueno. Adaptive optics multiphoton microscopy: probing the eye more deeply. *Opt. Photo. News.* 2014; 25(1):48–55.
- [67] S. Roth and I. Freund. Second harmonic generation in collagen. *J. Chem. Phys.* 1979; 70(4):1637–1643.
- [68] S. Roth and I. Freund. Optical second-harmonic scattering in rat-tail tendon. *Biopolymers.* 1981; 20(6):1271–1290.

- [69] I. Freund, M. Deutsch and A. Sprecher. Connective tissue polarity: optical second-harmonic microscopy, crossed-beam summation, and small-angle scattering in rat-tail tendon. *Biophys. J.* 1986; 50(4):693–712.
- [70] P. Stoller, K. M. Reiser, P. M. Celliers and A. M. Rubenchik. Polarization-modulated second harmonic generation in collagen. *Biophys. J.* 2002; 82(6):3330–3342.
- [71] C. H. Lien, K. Tilbury, S. J. Chen and P. J. Campagnola. Precise, motion-free polarization control in second harmonic generation microscopy using a liquid crystal modulator in the infinity space. *Biom. Opt. Express.* 2013; 4(10):1991–2002.
- [72] F. J. Ávila, O. Barco and J. M. Bueno. Polarization dependence of collagen-aligned tissues imaged with second harmonic generation microscopy. *J. Biom. Opt.* 2015; 20(8): 086001.
- [73] I. Gusachenko, G. Latour and M. C. Schanne-Klein. Polarization-resolved Second Harmonic microscopy in anisotropic thick tissues. *Opt. Express.* 2010; 18(18):19339–19352.
- [74] O. Nadiarnykh and P. J. Campagnola. Retention of polarization signatures in SHG microscopy of scattering tissues through optical clearing. *Opt. Express.* 2009; 17(7): 5794–5806.
- [75] O. del Barco and J. M. Bueno. Second harmonic generation signal in collagen fibers: role of polarization, numerical aperture, and wavelength. *J. Biom. Opt.* 2012; 17(4): 045005.
- [76] F. Tiaho, G. Recher and D. Rouède. Estimation of helical angles of myosin and collagen by second harmonic. *Opt. Express.* 2007; 15(19):12286–12295.
- [77] W. L. Chen, T. H. Li, P. J. Su, C. K. Chou, P. T. Fwu, S. J. Lin, D. Kim, P. T. C. So and C. Y. Dong. Second-order susceptibility imaging with polarization-resolved, second harmonic generation microscopy. *Proc. SPIE.* 2010; 7569(75691):1–7.
- [78] R. Ambekar, T. Y. Lau, M. Walsh, R. Bhargava and K. C. Toussaint. Quantifying collagen structure in breast biopsies using second-harmonic generation imaging. *Biom. Opt. Express.* 2012; 3(9):2021–2035.
- [79] K. Tilbury and P. J. Campagnola. Applications of second-harmonic generation imaging microscopy in ovarian and breast cancer. *Perspect. Medicin. Chem.* 2015; 16(7):21–32.
- [80] A. Benoit, G. Latour, S. K. Marie-Claire and J. M. Allain. Simultaneous microstructural and mechanical characterization of human corneas at increasing pressure. *J. Mech. Behav. Biomed. Mater.* 2015; 60:93–105.

Nonlinear Microscopy Techniques: Principles and Biomedical Applications

Javier Adur, Hernandes F. Carvalho,
Carlos L. Cesar and Víctor H. Casco

Additional information is available at the end of the chapter

<http://dx.doi.org/10.5772/63451>

Abstract

Nonlinear optical microscopy techniques have emerged as a set of successful tools within the biomedical research field. These techniques have been successfully used to study autofluorescence signals in living tissues, structural protein arrays, and to reveal the presence of lipid bodies inside the tissular volume. In the first section, the nonlinear contrast technique foundations is described, and also, a practical approach about how to build and combine this setup on a single confocal system platform shall be provided. In the next section, examples of the usefulness of these approaches to detect early changes associated with the progression of different epithelial and connective tissular diseases are presented.

Finally, in the last section, we attempt to review the present-day most relevant analysis methods used to improve the accuracy of multimodal nonlinear images in the detection of epithelial cancer and the supporting stroma. These methods are presented as a set of potential valuable diagnostic tools for early cancer detection and to differentiate clinical subtypes of *osteogenesis imperfecta* disorders, being highly advantageous over present classical clinical diagnostic procedures.

In this chapter, it is proposed that the combination of nonlinear optical microscopy and informatics-based image analysis approaches may represent a powerful tool to investigate collagen organization in skin diseases and tumor cell morphology.

Keywords: nonlinear microscopy, second harmonic generation, third harmonic generation, image analysis, early diagnosis

1. Principles of nonlinear microscopy techniques

The notable advances in cell and molecular biology science have induced the need to imagine cells in an intact-live whole organism. Therefore, the need for real-time observation of cell (and their subcellular components) behavior in whole tissues has become crucial to understanding cellular physiology. During the past decades, imaging techniques have been improved to pursue this goal. One of these techniques is fluorescence imaging. The use of confocal microscopy allows the examination of subcellular material with three-dimensional resolution but is restricted by the effective imaging depth (usually less than 200 μm) and phototoxicity, which is caused by using a short wavelength laser (principally continuous wave (CW) laser) [1]. Recent advances in nonlinear optical processes of multiphoton microscopy overcome single-photon linear microscopy technologies, such as confocal microscopy, by their capacity of tissular penetration, clean images production, minimal invasiveness, and chemical selectivity [2]. Therefore, multiphoton fluorescence (MPF) and nonlinear optical (NLO) microscopy in recent year has become one of the key imaging modes and evolved as an alternative to conventional single-photon confocal microscopy. The best-known nonlinear microscopy techniques are two-photon excited fluorescence (TPEF) microscopy, second harmonic generation (SHG) and third harmonic generation (THG) microscopy, and coherent anti-Stokes Raman scattering (CARS) microscopy.

These nonlinear technologies provide several advantages, namely high depth penetration by using a near infrared (pulsed) laser as excitation source, intrinsic tridimensional sectioning and resolution, due to the spatial confinement of the signal to the laser focus, multiple nonlinear processes, and the possibility to use numerous endogenous molecular markers and low phototoxicity that allows the investigation of living processes, without significant perturbation [3]. Together, these advantages allow analyzing the complex relations between tissue and organ function and its structure in complex diseases [4].

To understand this new microscopy instruments, it is advisable to think in classical optical tool. In conventional optical imaging, contrast mechanisms consist of interactions such as absorption, reflection, scattering, and fluorescence, and the response recorded is linearly dependent on the intensity of the incident light. Thereby, there is a linear relationship between the strength of electric field of the light and the induced object polarization. At moderately low incident intensity, the optical response can be approximated to the first-order response as $P = \chi^{(1)} \otimes E$, where $\chi^{(1)}$ is the linear susceptibility, P is the polarization of a material, and E is the strength of an applied optical field. By contrast, nonlinear optical effects occur when a biological tissue interacts with an intense laser beam exhibiting a nonlinear response to the applied field strength. In this situation, the induced polarization vector P of the material subject to the vectorial electric field E can be expressed as $P = \chi^{(1)} \otimes E + \chi^{(2)} \otimes E \otimes E + \chi^{(3)} \otimes E \otimes E \otimes E + \dots$, where $\chi^{(i)}$ is the i^{th} order nonlinear susceptibility tensor and \otimes represents a combined tensor product and integral over frequencies [5]. The bulk nonlinear optical susceptibilities $\chi^{(2)}$ and $\chi^{(3)}$ are obtained from the corresponding high-order molecular nonlinear optical coefficients (hyperpolarizability) β and γ by using a sum of the molecular coefficients over all molecule sites. Typically, materials with conjugated π -electron structures exhibit large optical

nonlinearities. The usual linear susceptibility $\chi^{(1)}$ contributes to the single-photon absorption and reflection of the light in tissues. The $\chi^{(3)}$ corresponds to third-order processes such as two-photon absorption, THG, and CARS, while SHG results from $\chi^{(2)}$ [6].

Another way is to think nonlinear optical processes in terms of particles called photons discovered by Einstein, such as processes involving more than one photon. All these processes have some characteristics in common. First, it only occurs if multiple photons coincide in time and space or, in chemical terms, at high concentration of photons. The speed V of a chemical reaction of n elements $f + f + f + f + \dots \rightarrow f_n$ depends on the concentration f elevated to the n^{th} degree, that is, $V \propto [f]^n$ where $[f]$ is the concentration of f . In optics, the concentration is proportional to the laser beam intensity, $I = \text{power/area} = (\text{energy/time}) / \text{area}$. Thus, the efficiency of a one-photon process is I , and for two-photon would be I^2 , and generalizing for n photons I^n . Therefore, it is not surprising that the first nonlinear optical empirical results were materialized only after the advent of pulsed lasers. The NLO microscopes come with the advent of Ti:Sa lasers which produce pulses typically in the range of 100 femtoseconds [$\text{fs} = 10^{-15}$ sec], with an average power of 2 watts and repetition time of 12 nanoseconds [$\text{ns} = 10^{-9}$ sec]. In this case, the peak power will be 240 kilowatts, although the pulse energy is just 24 nanoJoule. The pulsed laser, therefore, increased the peak power of 2 watts for a CW laser to 240 kilowatts, while keeping the same average power and low energy per pulse. In other words, the very high potencies are obtained by decreasing the pulse duration instead of increasing the pulse energy. Thus, nonlinear effects occur avoiding the potential sample damage. The smaller the temporal pulse duration, greater the efficiency of nonlinear processes, so femtosecond lasers are preferable to picosecond lasers.

The pulsed laser ensures the coincidence of photons in time, but not in the space. The concentration of photons but will be greater the smaller the area of the laser beam, i.e., is maximum in the laser focus. The total generation of events caused by one photon processes is constant, independent of the laser focusing position, because if the process is linear with I , the total number of events is proportional to I multiplied by the area, i.e., $N \text{ events} \propto (\text{power/area}) \times \text{area} = \text{power}$. As power is constant along the beam, the number of events does not depend on the axial position [along the lens axis—defined as the z -axis]. The processes with more than one photon are proportional to I^n and therefore are inherently confocal. In this case, the amount of events depends very strongly on the beam area, because now $N \text{ events} \propto I^n \times \text{area} = (\text{power}^n / \text{area}^{n-1})$. Two-photon processes decay inversely with the area, whereas a three-photon does so with the square of the area. This means that events can occur only in the vicinity of the lower area, i.e., the laser focus, that is, the light generated by the nonlinear optical process are generated at the focus of the laser, which becomes intrinsically a confocal microscope. The laser focus is on the operator microscope control and can be used for 3D image reconstruction.

One way to visualize the various nonlinear optical processes is by arrows with length proportional to the photon energy. **Figure 1** schematically depicts a number of nonlinear optical effects, produced for the specimen if the energy density at the focal spot of an objective lens is sufficiently large and also are compared with lineal process produced for a CW laser. Principal contrast mechanisms and characteristics of TPEF, SHG, THG, and CARS modalities are described below.

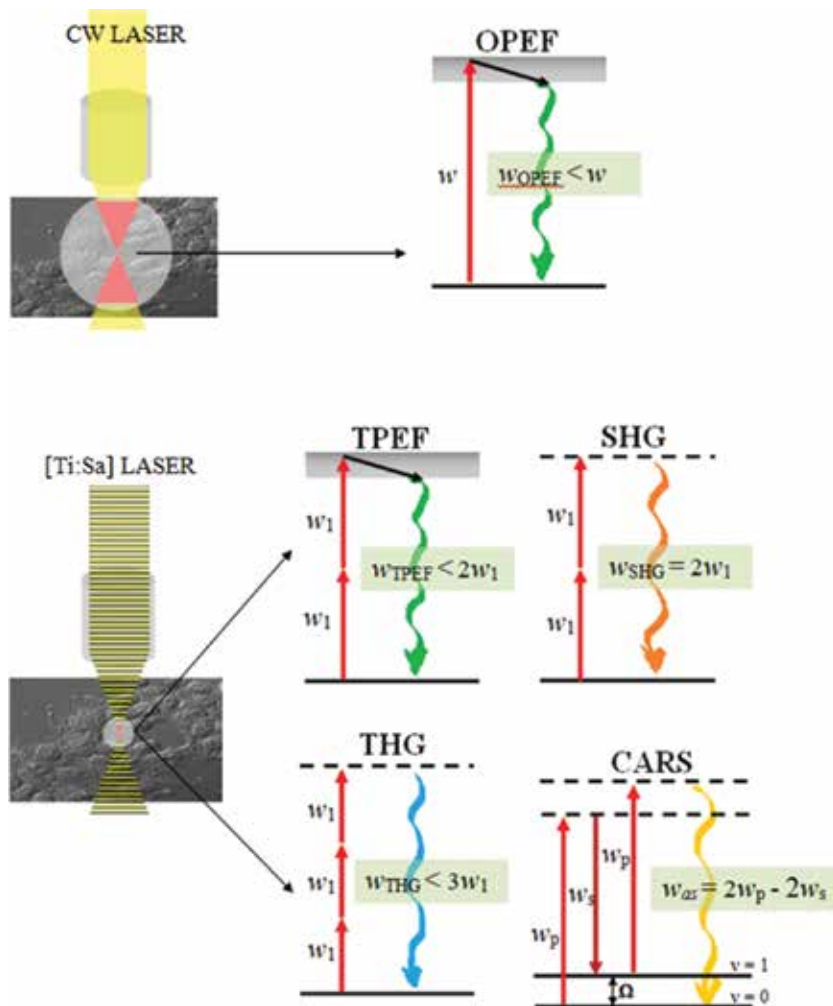


Figure 1. Energy diagrams of linear and nonlinear optical process. Solid lines represent electronic and vibrational states of molecules, while dashed lines denote virtual states. The straight arrows are excitation beams, whereas wavy arrows are the output signal beams. The black arrow represents relaxation in electronically excited states, and red hourglass represents the excitation volume. ω_1 and ω_2 symbolize the two beams available in CARS microscope. $\omega_p = \omega_1$ and $\omega_s = \omega_2$ in CARS. $v = 0$: vibrational ground state, $v = 1$: vibrational excited state, and Ω is a frequency of vibrational transition between $v = 0$ and $v = 1$. ω_1 = pump beams and ω_2 = Stokes beam from the laser sources. ω_3 is a long wavelength beam for THG obtainable on OPO systems for CARS microscope. Abbreviations: CW: continuous wave, OPEF: one-photon excited fluorescence, OPO: optical parametric oscillator.

TPEF microscopy is a third-order nonlinear optical resonant process where two photons excite an electron from the ground state. It is an inelastic process where photon energy is released at the sample. Two-photon absorption happens only when the energy of the incident photons falls into the two-photon excitation band which is specific for each fluorescent marker. The two-photon excitation band is not exactly half of the one photon excitation band because the selection rules are different. The fact that TPE depends on the square of the incident light

provides its confocal features, that is, a process happening only at a focal point volume. Photobleaching is smaller in two-photon excited fluorescence (TPEF) compared to single photon excitation because the excited volume is smaller. Multicolor imaging is allowed to excite different fluorophores simultaneously through different order processes with a single wavelength, in which emissions are spectrally shifted by hundreds of nanometers and uninterrupted for collection. Consequently, multiphoton microscopy is especially appropriate for physiological and pathophysiological studies since it is able to excite endogenous auto-fluorescent components and thus to obtain specific signals such as nicotinamide adenine dinucleotide (NADH) and flavin adenine dinucleotide (FAD) [6].

On the contrary, SHG and THG are coherent second/third-order elastic nonlinear optical processes, respectively. Because two/three photons generate another photon with two/three times the energy of the incident photons, there is no energy released to the medium, meaning out of focus cell photodamages are not expected from these processes. Both SHG/THG can be segregated from fluorescence signals by the wavelength or even by time gating, because the coherent processes are practically instantaneous. The fact that SHG signal is proportional to I^2 , while THG signal is proportional to I^3 , where I , is the incident light intensity, provides confocality for both techniques. For the same wavelength of the incident light, THG has better optical sectioning resolution than SHG or TPEF but is also more sensitive to changes in the intensity of the light in the focused spot, such as those caused by laser instability or by scattering or defocusing the illumination [7]. The first images of high-resolution SHG were reported in 1998 by Sheppard's group [8], and shortly afterward in 2001, Chu and co-workers showed a multimodal imaging study, including TPEF+SHG+THG [9]. Usually, the third-order nonlinear susceptibility (χ^3), responsible for THG, is much smaller than the second-order one (χ^2), responsible for SHG. In principle, this would mean that THG should be much harder to observe. However, χ^2 , as well as any other even susceptibility coefficients, must be null in the presence of inversion symmetry. Therefore, SHG shall be zero in the presence of centrosymmetric molecules, unless an external parameter, such as electric fields or interfaces, breaks the symmetry.

By contrast, all materials have non-zero third-order susceptibility χ^3 . Moreover, χ^3 can be several orders of magnitude larger or smaller for different materials. However, THG is null in a homogeneous material, no matter how high χ^3 could be, because the Gouy-phase shift of π across the focus of a Gaussian excitation beam creates a destructive interference between signals generated before and after the focus [10]. Nevertheless, for a nonhomogeneous focal volume, a measurable amount of third harmonic is generated [11]. Since in biological samples, heterogeneity is more common than homogeneity, THG provides an important tool for bioimaging, with the warning that it tends to be brighter at the interface of large granules, lipid droplets, or similar biostructures, compared to the internal signal [6]. SHG imaging modality can probe molecular organization, molecular symmetry, orientation, molecular alignments, and ultrastructure on the micro, as well as the nanoscale. Natural structures are mostly unarranged (optically isotropic) and do not generate any SHG signal. Hardly, some few biological assemblies are ordered and can produce harmonic signal. One of the best known SHG structures in biology is collagen, the major protein of the extracellular matrix. Collagen

fibrils often aggregate into larger, cable-like bundles, several micrometers in diameter. This regularly staggered packing order provides the needed structural conditions for efficient SHG [12]. Other examples are acto-myosin assemblies in muscle and microtubule structures in living cells [13, 14]. Discontinuities in refraction index of the optical dispersion properties of biological tissues are able to generate THG signals [15, 16]. The THG can be used to study optical cell interfaces such as those at cell membranes or organelle surfaces. For example, the surface of the erythrocyte can generate significant THG [17]. In contrast to the chemical specificity that characterizes fluorescence images, harmonic generation (SHG and THG) provides an imaging modality specific for structural configuration. In the study of cancer tumors, our experience with both techniques is that SHG is an excellent tool to observe collagen network of extracellular matrix, while THG allows to clearly display the nuclei, which are two key parameters for pathologists [4, 18–20].

Characteristics	TPEF	SHG	THG	CARS
Application in bioscience	1990	1986	1997	1982
Number of photons	2	2	3	3
Susceptibility	χ^3	χ^2	χ^3	χ^3
Advantages	Deeper imaging with less phototoxicity Spatial localization for fluorescence excitation	Coherent process, symmetry selection Probing well-ordered structures, functions of membranes, nonfluorescence tissues No absorption of light	Coherent process, no symmetry requirement No absorption of light Imaging both in bulk and at surfaces for extended conjugation of pi electrons	Coherent process Inherent vibrational contrast for the cellular species, requires no endogenous or exogenous fluorophores Vibrational and chemical sensitivities
Contrast mechanics	Electronics levels of the molecules	Nonlinear properties of the medium	Nonlinear properties of the medium	Vibrational levels of the molecules
Information	Autofluorescence of some biological substances (NADH, FAD, etc.)	Noncentrosymmetric molecules with spatial organization (collagen, elastin, etc.)	Interfaces, optical inhomogeneities, (cell edges, lipids, membranes)	Chemical information (lipids, DNA, proteins)

Table 1. Characteristics of nonlinear optical microscopy.

In addition to harmonic generation microscopy, CARS microscopy is another 3D high-resolution imaging approach that circumvents exogenous probes. CARS is a four-wave mixing

process in which a pump beam at frequency w_p , a Stokes beam at frequency w_s , and a probe beam at frequency w'_p are interacted with a sample to result in an anti-Stokes signal at $w_{as} = 2w_p - w_s$. In nearly all experiments, the pump and the probe beams are derived from the resonant oscillation when the beat frequency ($w_p - w_s$) matches the frequency of a particular Raman active molecular vibration mode. Furthermore, due to its coherent nature, CARS signal production only occurs when the field-sample interaction length is less than the coherence length. The generated CARS signal is proportional to $(\chi^{(3)})^2 I_p^2 I_s$, having a quadratic dependence on the pump field intensity and a linear dependence on the Stokes field intensity. These properties provide it a 3D-sectioning capability [6]. First CARS microscopy setup was described at the nineties [21] and has now matured into a powerful method for biological imaging. CARS microscopy is more informative than SHG and THG microscopy since it contains rich spectroscopic information about specific molecular species.

To summarize the first section, a description of the physical properties, characteristics, and principal contrast mechanisms of each nonlinear optical imaging method described are summarized in **Table 1**.

2. Nonlinear optical technique implementation

Today, there are multiples ways to assemble a nonlinear microscopy platform. The engineering challenge is to integrate the different modalities on a single platform. In response to this challenge, manufacturers have designed microscopes with multiple input and output ports and increased infinity space for the introduction of customized optics. Coming up next, some laser sources, detectors, and confocal body microscopies routinely used in this technology are enumerated, and a setup configuration by our group is described in some detail.

As was described in the introductory section, for high harmonic generation and multiphoton fluorescence microscopies, short femtoseconds pulses of high peak power are required. While ultrashort few cycle pulses are spectrally very broad, they allow for simultaneous excitation of different chromospheres with spectrally separated absorption bands. Available lasers that conjugate these features are the titanium:sapphire (Ti:Sa) (wavelength range 700–980 nm, pulse width 100 fs, and 76–100 MHz repetition rate), the Cr:forsterite laser (wavelength range 1230–1270 nm, pulse width 65 fs, and 76–120 MHz repetition rate), the Nd:glass laser (wavelength range 1053–1064 nm, pulse width 150 fs, and 70–150 MHz repetition rate), and the femtosecond ytterbium laser (wavelength range 1030 nm, pulse width 200 fs, and 50 MHz repetition rate).

The SHG wavelength excited by a Ti:Sa femtosecond laser operating at 940 nm will be in the blue at 470 nm, and the TPEF will be in the region above 470 nm. While that THG signal generated by a 940 nm principal beam, will be in the UV region at 330 nm. As a result, the THG signal will suffer from the high UV absorption of the principal biological specimens making signal detection difficult. In contrast, using the Cr:forsterite laser operating in the range of 1230 nm allows SHG (615 nm), THG (410 nm), and TPEF (>615 nm), all to fall within the visible spectrum. Additionally, the lowest light attenuation in biological material is generally found in the 1000–1300 nm. In recent years other ultrafast laser systems appeared, such as InSight TM DeepSee TM (wavelength range 680–1300 nm, pulse width <120 fs, and repetition rate 80

MHz), which also can be an excellent light source for multi-modality microscopy. Moving the excitation wavelength to 1200 nm, not only the visible but also the NIR spectrum is open for signal recording.

Nonlinear microscopes share many common features with confocal laser scanning microscopes. In fact, many research groups have implemented multimodal nonlinear platform by coupling source lasers described previously into a confocal scanning microscope. Practically, many scan head models of different manufactures have been used with this proposal, such as Olympus FV300 [22], Olympus FV1000 [23], Zeiss LSM Meta 510 [24], Zeiss LSM 710 [25], Nikon C1 [26], Leica TCS-SP5 [27], and Zeiss LSM 780 [28]. In general, the generated nonlinear signals can be collected with the same microscope objective, separated by a dichroic mirror, which is expressly selected for the given fundamental and fluorescence or harmonic emission wavelengths and focused with a lens through the filter onto detector. If Ti:Sa laser is used, the wavelengths fall within the sensitivity range of high quantum efficiency (QE) silicon-based detectors and photomultiplier tube (PMT) photocathodes that are the currently used detectors. If the source laser used are Nd:glass or Cr:forsterite, special NIR detectors (i.e., indium gallium arsenide (InGaAs) photodiode) are needed. For more data about the optical characteristics of the different detectors, readers can find excellent information in [7].

In our setup (**Figure 2**), we used an inverted Zeiss Axio Observer.Z1 and confocal LSM 780. Briefly, this device is equipped with a UV-lamp, for classical epi-fluorescence operation mode; five lines of CW laser, for confocal studies; and femtosecond (fs) and picosecond (ps) pulsed laser, for nonlinear microscope modalities. The fs laser source is a tunable, Ti:sapphire laser emitting around 690–1040 nm both for efficient TPEF and higher SHG/THG spatial resolution. The picosecond (ps) source is obtained from a synchronously pumped optical parametric oscillator (OPO) system to obtain THG signal in the visible range and high spectral resolution CARS microscopy. The OPO can be easily and continuously tuned over a wide spectral range from 690 to 990 nm for the signal and between 1150 and 2450 nm for the idler output. The fs laser is combined with the scan head through an acousto-optic modulator (AOM) and a collimating telescope (T1) to regulate the beam diameter in the objective back-aperture and the focus position on the microscope focal point. The five wavelengths (signal and idler for each OPO plus the fundamental 1064 nm) are controlled independently with dedicated telescopes (T2, T3, T4, T5, and T6). Delay lines on the five beam paths ensure temporal overlap between the beams. These beams necessary for CARS microscopy are temporally synchronized, recombined (P), and sent onto the backward excitation port of the scan head. The scan head of the LSM780 has a spectral gallium arsenide phosphide (GaAsP) detector with 32 in-line elements and 2 adjacent PMTs. The motorized collimators, the scanners, and the pinhole precisely positionable and the highly sensitive detectors are arranged to provide optimum specimen illumination and efficient collection of the emitted light. The Raman line width is comparable to the spectral width of a picosecond pulse, so that the excitation energy is fully used to take full advantage of the vibrational resonant CARS signal. Working with 1~3 ps spectral pulse widths is possible to obtain the optimal signal-to-background ratio for typical Raman band [29]. A pulse width of a few picoseconds provides a good compromise between the spectral resolution and the peak power and improves the signal-to-background ratio. The

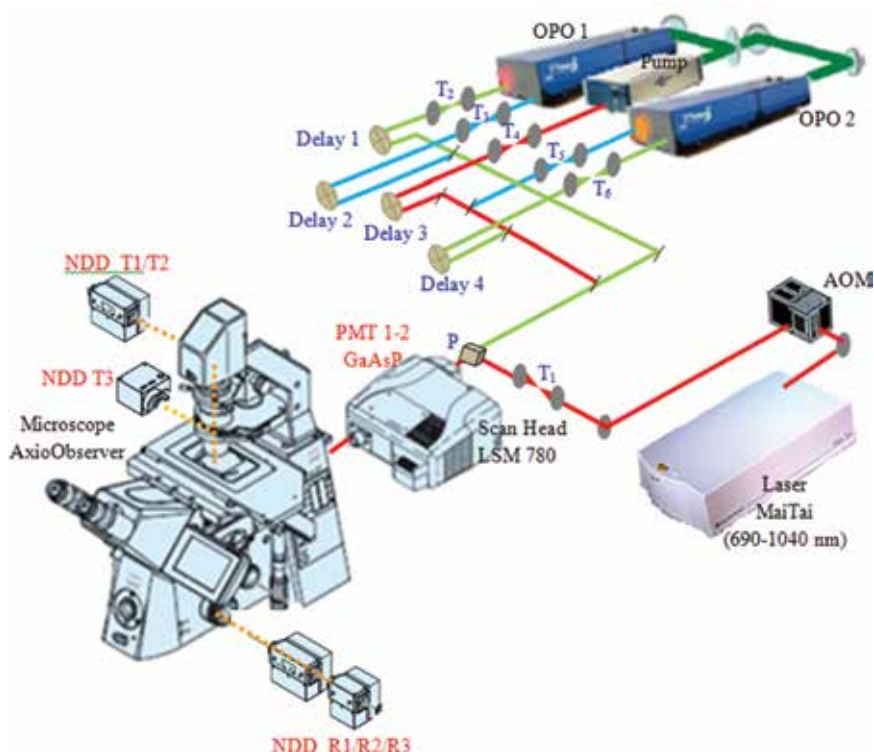


Figure 2. Schematic setup of a multimodal NLO microscope using a femtosecond laser source (Mai-Tai) and picoseconds (OPOs system) pulsed laser. Lasers are coupled to a commercial confocal system platform (inverted Zeiss Axio Observer.Z1 and confocal LSM 780). Principal optics elements are shown with blue letterings (telescope, delay lines, and recombination) and detectors with red letterings. Solid and dashed lines represent excitation and emission paths, respectively. AOM, acousto-optic modulator; T, telescope lens; P, recombine; NDD T, nondescanned detector (transmitted way); NDD R, nondescanned detector (reflective way); PMT, photomultiplier tube.

OPO light source for CARS that we used has already been reported to perform time resolved CARS [30] to improve the sensitivity or to cover the full vibrational Raman spectrum. In our setup, the frequency doubled Nd:YVO generates 8 W of green light (532 nm) and pumps two OPOs with 4 W each. Although the full system can provide up to five wavelengths simultaneously (signal and idler for each OPO plus the fundamental 1064 nm), we normally use three colors. The two signals coming from each OPO are recombined with the fundamental 1064 nm beam from the Nd:YVO oscillator. The power, polarization state, and divergence of each beam are controlled independently with dedicated polarization optics and telescopes. Delay lines on two of the beam paths (signal and 1064 nm) assure temporal overlap between the three beams. The backward detection is achieved with internal GaAsP detector of scan head. A set of dedicated filters is placed before the detectors to select the relevant spectral domains.

The generated signals can be collected with the same microscope objective (reflected or epi-detected), splitted by dichroic mirrors, which were specifically chosen for the given funda-

mental and fluorescence or harmonic emission wavelengths and focused onto specific detectors. Interference or band pass filters are used in front of the detector for filtering scattered fundamental light and spurious signals outside the desired bandwidth. For epi-detection, the system has two internal PMT plus GaAsP avalanche photodiodes inside the scan head (PMT 1-2, **Figure 2**). Also, three non-descanned detectors (NDDs) are available for epi-detection of nonlinear signals (NDD R1/R2/R3). It is also possible to detect the signals in the forward direction. Either one detector with appropriate filters or several detectors recording different signals separated by dichroic mirrors can be used. The system shown here has three NDD detectors (NDD T1/T2/T3). T3 detector was placed right after the sample, holding it as close to the sample as possible. With this system, many configurations can be used and different, linear, and/or nonlinear signals can be simultaneously detected. For example, we can observe CARS signal with internal GaAsP detector of scan head, forward THG, SHG and TPEF with NDD T1/T2/T3, and reflected SHG and TPEF with NDD R1/R2.

3. Biomedical applications

Over the past years, life science interdisciplinary research has routinely used nonlinear microscopy techniques. The combination of SHG, THG, and CARS is used in the production of chemical maps of complex tissues. NLO techniques allow inspecting the assembly of single cells, tissues, and organs as well as monitoring structural and chemical changes related to diverse diseases. Here a few examples of the use of our setup in two applications are shown, epithelial cancer detection and diagnosis of *osteogenesis imperfecta*.

3.1. Cancer detection

Cancer is still a threat to human life [31]. Modern clinically used imaging methods for cancer diagnosis comprise x-ray, CT, MRI, and OCT [32, 33]. The facilities of these technologies are restricted by either low spatial resolution or a lack of chemical specificity, making it difficult to identify the edges of the tumor. Today, new image-based instruments are necessary as diagnostic tool to evaluate structural features with subcellular resolution that are closely linked with tumor malignancy. The combination of different image approaches described in this chapter may represent a powerful combination of tools to study both malignant cells and stromal environment. One of the main examples of such an objective is the collagen organization changes analysis, the remodeling matrix and alterations in epithelial/stromal interface. Highly valuable, structural information revealed by each nonlinear contrast approach can be isolated and analyzed separately, while their superposition allows a better comparison and understanding of the spatial tissue organization. Thus, TPEF and THG can be used to image a variety of well-documented morphologic and architectural alterations, moreover, combined TPEF-SHG can be applied to analyze alterations in epithelial cells and the supporting stroma, and CARS microscopy can be used to understand lipid and proteins composition in tumor tissues.

Figure 3A exemplifies this combination, where NLO techniques were applied to differentiate between normal and malignant (fibroadenoma and invasive lobular carcinoma (ILC)) human breast tissue. The characteristic microscopic appearance of each type of tissue and relationship between cells and stromal compartment can be identified in the SHG/THG combination. The differential orientation and distribution of collagen fibers can be clearly identified in stromal region with SHG image. **Figure 3B** shows a comparative analysis of CARS images of breast tissue. Adipose and fibrous structures of normal tissue possess strong CARS signals. Fibroadenoma exhibits the compressed duct with linear branching pattern, whereas ILC presents single or rows of cells invading into the stroma. Based on examples such as this and our previous work [19], we have established that it is possible to have both qualitative parameters of differences between each kind of breast tumor and to demonstrate the advantage of the integration of as many NLO approaches as possible to analyze breast cancer.

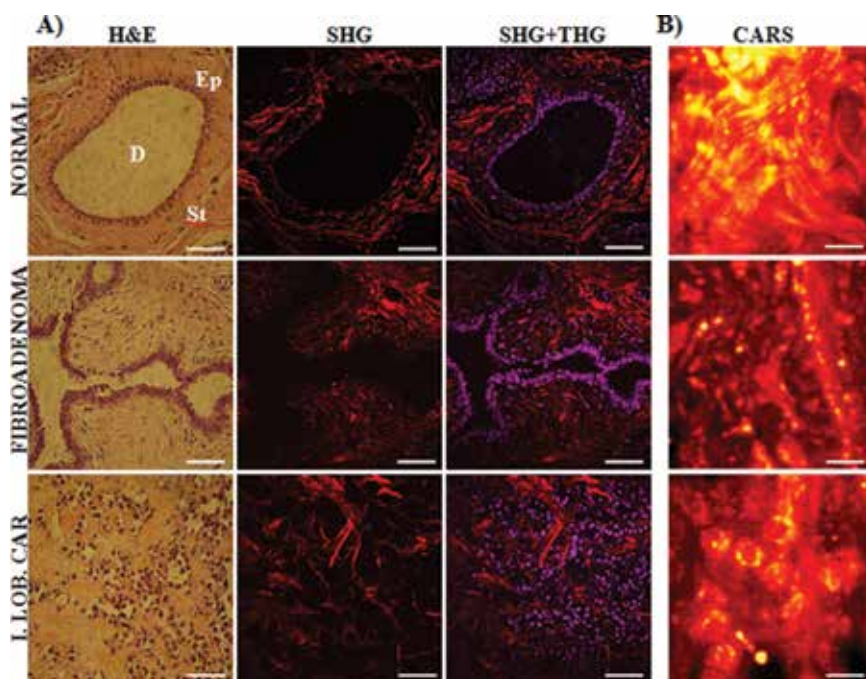


Figure 3. Multimodal NLO approach applied to human breast tumor. (A) Representative H&E-stained and SHG, and SHG+THG cross-sectional images of breast tissues diagnosed as normal (first row), fibroadenoma (second row), and invasive lobular carcinoma (third row). Scale bar = 20 μm . (B) Representative CARS cross-sectional images of breast tissues. Scale bar = 20 μm . D, duct; Ep, epithelium; St, stroma; Fibroad, fibroadenoma; Lob. Carc., lobular carcinoma; I.Lob.Carc, invasive lobular carcinoma. **Figure 3A** from Adur et al., [19].

Human ovarian tumors are shown in **Figure 4**. TPEF signal (green) represents stromal connective tissues. The SHG signal (red) shows collagen fibers, while THG (cyan) enhances the nuclei. The information revealed by each mode can be directly compared, providing a better understanding of the tissue. For example, SHG/THG-merged signals can be used to distinguish the epithelial/stromal interface. It is worth mentioning that these differences and

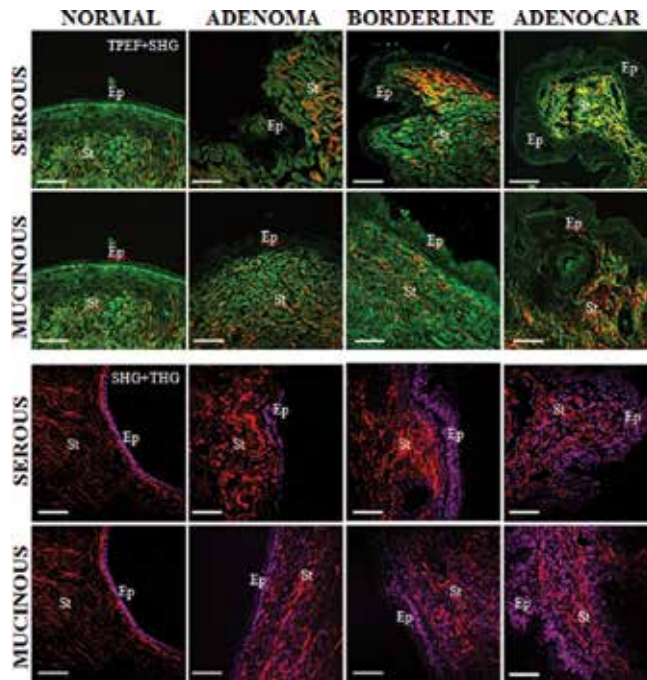


Figure 4. Multimodal NLO approach applied to human ovarian tumor. Representative merges of TPEF (green) and SHG (red) cross-sectional images of ovarian tumor tissues diagnosed as serous-type tumor and mucinous-type tumor; and representative merges of SHG (red) and THG (cyan) cross-sectional images. All scale bar = 20 μm . Ep, epithelium; St, stroma; n, nucleus; c, collagen; Ade, adenoma; Bord, borderline; Adenocar, adenocarcinoma. Reproduced figures from Adur et al. [34] (open access).

contrasts could be automatically and digitally done for quantification (see next section). These data confirm the fact that normal ovaries are more organized tissues than the adenocarcinoma samples. Finally, using THG signal, it was possible to evaluate the differences in the surface epithelium of each tumor type. In normal ovary, cells were arranged in one cell layer. Serous adenoma samples display elevated ciliated and non-ciliated cuboidal epithelial cells with lengthened nuclei, also in one regularly single cell layer. Besides, the serous borderline tumor and serous adenocarcinoma samples are absolutely different from the previous ones, showing epithelial surface with cells of altered sizes lying in multiple layers, including cellular atypia and proliferation. Mucinous tumor samples are similar to borderline/adenocarcinoma, with different size cells forming up multiple layers, but having rich cytoplasmic mucin and basal nuclei.

Figure 5 summarizes the combined uses of these techniques in the analysis of human colon cancer. NLO images clearly demonstrate the circular arrangement pattern of control colonic crypts registered from crypt-cross sections, characterized by epithelial columnar cells and interspersed goblet cells. TPEF (green) revealed the typical foveolar pattern of colon mucosa glands, displaying crypts with rounded luminal openings. SHG (red) specifically traces the collagen scaffold within lamina propria. The evaluation of colonic tissue by SHG microscopies

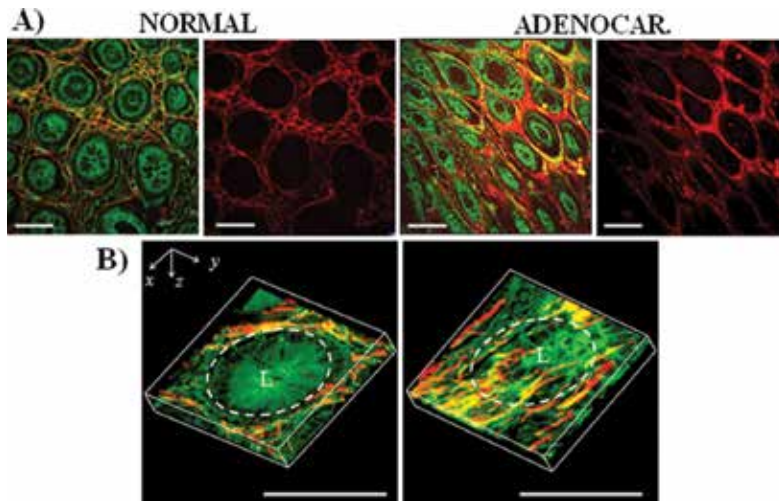


Figure 5. Multimodal NLO approach applied to human colon tumor. (A) Representative TPEF+SHG and SHG cross-sectional images of normal and tumor colon tissues. Scale bars = 20 μm . (B) Maximum projection of 60 images separated 0.5 μm each of normal and adenocarcinomas colonic tissues. Epithelial-stromal interface is indicated (white outline). Scale bars = 50 μm . L, luminal crypt orifice; Adenocar, adenocarcinoma. Reproduced figures from Adur et al. [37] (open access).

rapidly and clearly allows differentiating between adenocarcinoma and normal tissue states. Whereas individual crypts were easily identified with TPEF, the interspersed connective tissue was detected via SHG of collagen (**Figure 5A**). As was previously stated, in tumoral tissues, SHG images highlight changes in the surrounding fibrous stroma. Another key aspect of NLO techniques in relation to the classical H&E ones is that they have high potential to produce 3D reconstructions and stereological studies. **Figure 5B** shows three-dimensional representations that allow the visualization of indistinguishable features in classical two-dimensional procedures. Using 3D SHG representation, it was possible to detect the tilt and invasiveness of collagen fibers of adenocarcinomas compared to normal colon. Those features are not easily visible in standard two-dimensional H&E-stained sections. In others works, NLO microscopy approaches, especially when combined, can reveal information not distinguishable in H&E stained sections. Different changes in collagen fibers are parameters that can be consistently quantified, which allows to predict an enormous clinical potential in colon cancer. These results show important changes of collagen fiber morphology, alignment, and density in colon tumor tissue, suggesting that collagen fiber inclination angles are a key factor in tumor progression. In agreement with these results, previous reports on human colon and other tissues suggest that the epithelial cells preferentially invade tissues where the collagen fibers became perpendicularly aligned, instead of arbitrarily organized ones [35, 36].

3.2. Osteogenesis imperfecta

Osteogenesis imperfecta (OI) is a heterogeneous disorder of connective tissues (see **Table 2** for types of OI) with an incidence of 1/15000 [38, 39] and disease severity spanning from subclinical

osteoporosis to intrauterine lethality. Dominant mutation in collagen type I is the most common cause (>90%). Type I collagen is the most abundant extracellular matrix (ECM) protein in humans and the major structural protein in many organs, for example in skin. It is a heterotrimer consisting of two α 1-chains and one α 2-chain, encoded by COL1A1 and COL1A2, respectively. Mutations in the genes encoding type I procollagen produce a range of disorders, which include autosomal dominant (AD) OI. Currently, more than 1000 heterozygous COL1A1/2 mutations have been identified (<https://oi.gene.le.ac.uk>) [40, 41]. Mutation type and position influence the phenotype and as such genotype-phenotype relations exist to some extent. Mainly, two types of mutations in collagen I cause classical dominant OI: quantitative and qualitative collagen defects. These collagen I mutations are reflected in some way on fibril collagen assembly that can be finally observed in an organ, such as the skin. For example, in patients suffering from OI, skin collagen fibers could be smaller and more randomly packed. These disorders in collagen fibrils could be quantified using SHG microscopy.

Type	I	II	III	IV	V	VI
Characteristic						
Severity	Mild	Perinatal lethal	Severe	Moderate	Moderate	Moderate
Congenital fractures	NO	YES	Usually	Rarely	NO	NO
Bone deformity	Rarely	Very severe	Severe	Mildly moderate	Moderate	Moderate
Stature	Normal	Severely short	Very short	Variable short	Variable	Mildly short
Hearing loss	60% of cases	NA	Common	42% of cases	NO	NO
Respiratory complications	NO	YES	YES	NO	NO	NO

NA: not available

Table 2. Clinical characteristics of osteogenesis imperfecta.

Figure 6 depicts representative images acquired using previous setup, displaying representative TPEF (green) and SHG (red) images. TPEF signals are generated fundamentally by the eosin fluorescence and, in every case, this signal was used to detect just the skin epithelium (dashed white line). The non-contamination confirmation of the SHG signal was established by the wavelength range, half of the excitation, of the signal, by using the avalanche photodiodes (APD) array of the LSM-780 Zeiss scan head CCD. Besides the difference found in the collagen extent, a visual examination of the SHG images of **Figure 6** reveals that the normal skin has thinner collagen fibers that weave in all directions round the hair follicles. The skin from OI patients exhibits changes in collagen fiber thickness when compared to the normal skin. Skin images from the more severe forms of OI result in thicker, broken, and wavy collagen fibers that are firmly packed following the same direction. Moreover, using fresh skin, one can identify a marked reduction in the density of the collagen fibers network in the 3D illustration of SHG images from severe OI patient's samples (**Figure 6B** and **6C**), when compared with 3D SHG images from normal skin fresh biopsies (**Figure 6A**). These skin images are just a basic representative example about how the SHG tool can be used for optical evaluation of OI.

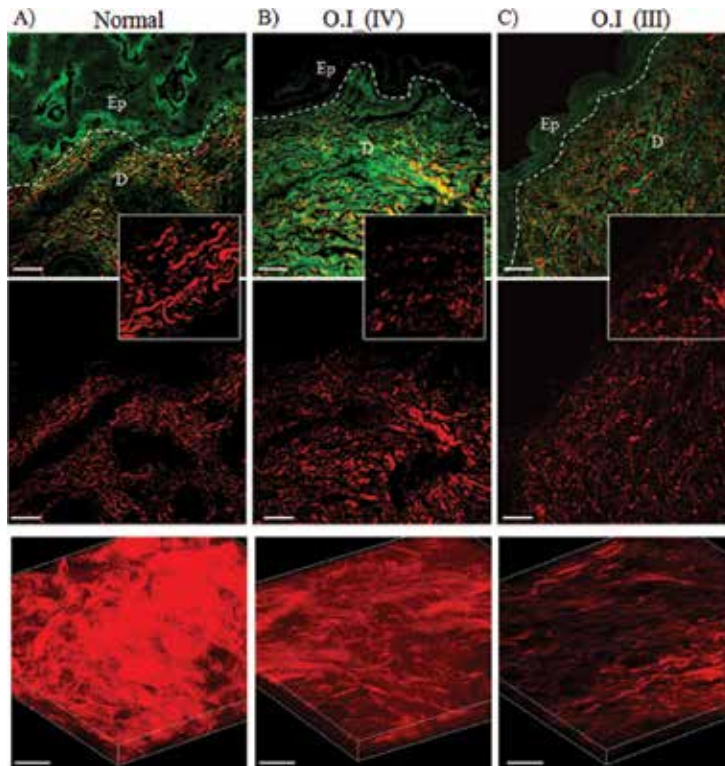


Figure 6. Representative cross-sectional images for TPEF (green) and SHG (red) analyses of normal (A), OI type IV (B), and OI type III (C) skin human tissues. Epidermis/dermis interface is signposted by white outline. Insets highlight visual differences of fiber collagen. Ep, epidermis; D, dermis; and representative 3D maximum projection (40 images at intervals of 1 μm) of SHG images from fresh skin biopsies. Scale bars = 20 μm . Reproduced figures with permission from Journal of Biomedical Optics, 2012 [19].

However, to offer a more accurate diagnostic method, it is necessary to develop reliable quantitative tools that allow discriminating between different OI types. The following section aims to demonstrate that the texture analysis (one of the analyses method presented below), which is the first step to provide SHG image quantitation tool, providing important information about collagen fiber organization.

4. Analysis methods used as diagnostic tools

As was previously mentioned, different processing methods can be used to obtain the relationship between signals of epithelial cells and the collagen matrix obtained with NLO microscopy techniques [4, 42]. Some of the methods that are currently used and others potentially implementable with free software, such as ImageJ (NIH, Bethesda, Maryland, USA), are described below.

4.1. Ratio between collagen and elastic tissue (SAAID)

The second harmonic to autofluorescence aging index of dermis (SAAID) value is a measure of the ratio between collagen and elastic fiber network [4, 43]. As the stroma is composed primarily of collagen and elastic fibers allows the use of nonlinear optical signals to discriminate between altered connective tissue regions near tumor area [44–46]. Specifically, collagen fibers are strong second harmonic signal generators, whereas elastic fibers are only autofluorescent emitters. This parameter can be applied when TPEF and SHG microscopy are simultaneously used [47, 48]. The SAAID index is defined as $SAAID = (I_{SHG} - I_{TPEF}) / (I_{SHG} + I_{TPEF})$, where I equals the intensity of each signal, SHG/TPEF are above preselected threshold intensities [43]. For example, to obtain this index, we have used the collagen-elastic tissue ratio map in the whole image of ovarian tissue (**Figure 7A, B**). The whole stroma region was selected as one ROI for each image. It has been demonstrated that collagen content was increased within the tumor stroma. The quantification of these observations is showed by the SAAID bar graph (**Figure 7C**). The corresponding SAAID of adenocarcinoma type exhibits statistically significant ($p < 0.05$, t -test) higher values (-0.38 ± 0.03) compared to normal stroma (-0.63 ± 0.06) due to the high SHG (collagen) signal and low TPEF signal in this region. To demonstrate the utility of this index, it was applied to images of ovarian cancer showed in **Figure 4** and represented by bar graph in the **Figure 7D**. The corresponding SAAID of both adenocarcinoma types presented statistically significant ($p < 0.05$, t -test) higher values compared to normal stroma due to both the high SHG (collagen) and low TPEF signals in this region [34].

4.2. Tumor-associated collagen signatures (TACS)

This parameter is frequently used to determine the collagen fiber orientation at the tumor stroma boundary [4]. At present, there are three well-characterized TACS. They are reproducible during defined stages of tumor progression: TACS-1 (presence of dense collagen localized around small tumors during early disease), TACS-2 (collagen fibers arranged parallel to the tumor boundary—around 0°), and TACS-3 (collagen fibers disposed perpendicularly to the tumor boundary—around 90° , when the disease becomes invasive) [49]. The collagen-fiber angle calculation (relative to the tumor boundary) is required to know the epithelial zone having abnormal appearance. After this manual selection, fiber angle could be measured using the angle tool option from ImageJ toolbar. This tool measures the angle demarcated by three points. The first is an arbitrary point-guide along the fibril; the second one is the fibril extreme, closer to edge of the tumor; and the third one is any point that connects to the first draws with a path parallel to the epithelium [20]. Using this parameter, for example, to analyze collagen transformation in ovarian cancer, the fiber angle relative to the epithelium has been quantified. SHG images have been used along with collagen orientation, instead of the SHG signal (**Figure 7E, F**). The TACS-2, straightened (taut) collagen fibers, stretched around the epithelium (**Figure 7E**), and TACS-3, identifying radially aligned collagen fibers, that may provide the scaffolding of local invasion (**Figure 7F**), has been found. In normal ovary tissue, collagen fibers were mainly distributed around 0° (see white arrows). Approximately 75% of these fibers are parallel to the epithelium (angle $\leq 20^\circ$). In contrast, serous adenocarcinoma exhibits incipient

regions of local invasion (TACS-3) with a set of realigned fibers, most of which are disposed around 90° (see white arrows) with respect to epithelium (**Figure 7G**) [4, 20].

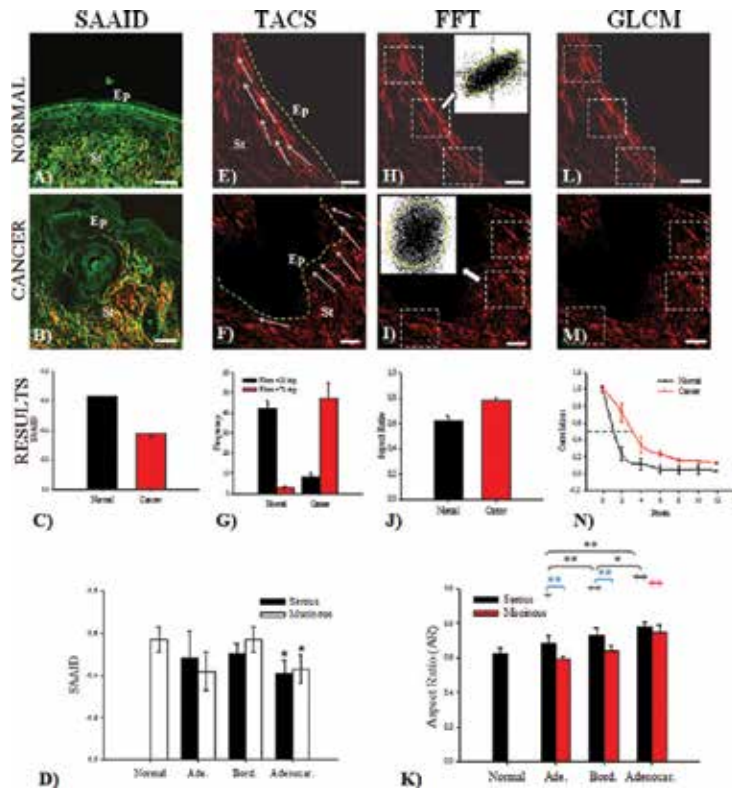


Figure 7. Depicting several applications of different methods to analyze NLO signals. The panel shows representative TPEF (green) and SHG (red) images of (A, E, H, L) normal and (B, F, I, M) cancer ovary. From the TPEF+SHG combination (first column), it is possible to calculate (C) the SAAID ratio. From the SHG image (remaining columns) and using regions near the epithelial/stromal interface (yellow line), it is possible to calculate: (G) TACS (measuring the collagen fiber angle relative to the epithelium); (J) FFT transforms (and fit to ellipse to estimate the anisotropy); and (N) GLCM (correlation value). (D) Bar graphs represent SAAID index quantitative analysis of ovarian tissues. Asterisks indicate a significant increase as compared to the nontumor tissues ($p < 0.05$, t -test). (K) Bar graphs represent anisotropy (aspect ratio) quantitative analysis of ovarian tissues. Comparisons with normal tissues are indicated with +, * indicates a statistically significant ($p < 0.05$) difference and ++, ** indicates a statistically very significant ($p < 0.01$) difference following ANOVA. Ep, epithelium; St, stroma; white arrows, collagen fibers; white squares, regions of interest (ROI). Reproduced figures from Adur et al. [4] (open access).

4.3. Fast Fourier transform (FFT) analysis

The FFT has proven to be a good method to assign the degree of image organization [42, 50]. Thereby, the FFT of a set of aligned fibers will have higher values along the orthogonal path to the direction track of the fibers, and its intensity plot seems to have an ellipsoidal shape. If the fibers are perfectly aligned, the ellipse will collapse into a line. For randomly oriented fibers, the intensity plot of the corresponding FFT image looks like a circle. Therefore, the anisotropy

of the image can be calculated by performing an elliptic fit on the thresholded FFT images, and then calculating the ratio between its short and long axes, i.e., its aspect ratio (AR) [51]. One sample will be more anisotropic as the AR goes to zero, whereas it will be more isotropic when the AR is closer to one.

To perform anisotropy calculations, squared ROI in the SHG images are usually selected, with the only requirement that they must be placed upon the collagen network around the epithelium, since this is the region responsible for the stroma invasion. The square ROI is required by the FFT procedure of ImageJ, based on an implementation of the 2D Fast Hartley Transform [52]. The FFT can be carried out with the homonymous command of the ImageJ menu [4]. The anisotropy on the ovary SHG image of stromal region has been estimated using this methodology (**Figure 7H, I**). Three ROIs of 150×150 pixels side squared have been used to ensure that the collagen network in the vicinity of the epithelium is registered. **Figure 7J** shows the AR value averaged on all the examined samples. In serous-type tumors, it was found that the AR index turned out to be significantly increased ($p < 0.05$, *t*-test) from normal (0.62 ± 0.04) to adenocarcinoma samples (0.78 ± 0.03).

Using this method, serous and mucinous ovarian cancer samples were analyzed (**Figure 4**). In serous-type tumors, AR increased progressively and significantly ($p < 0.05$, ANOVA) from normal to adenocarcinoma, and in mucinous-type tumors (by contrast), AR showed statistically very significant differences only for adenocarcinomas ($p < 0.01$, ANOVA) (**Figure 7K**). These results confirm the fact that normal ovaries are more organized tissues as compared to adenocarcinoma. By using this tool, it was possible to discriminate between serous adenoma from mucinous adenoma and serous borderline from mucinous borderline subtypes [48]. Unlike ovarian serous tumors, which are relatively homogeneous in their cellular composition and differentiation degree, mucinous tumors are frequently heterogeneous, with mixtures of benign, borderline, and malignant elements often found within the same neoplasm. The heterogeneity in these mucinous tumors suggests that malignant transformation is sequential and slow, progressing from cystoadenoma to borderline tumor and, finally, to invasive carcinoma [46]. This slow behavior is probably reflected in a more organized stroma [53].

4.4. Gray level co-occurrence matrix (GLCM) analysis

The GLCM analysis method allows the classification of different tissues based on the evaluation of geometrical collagen arrangement [4, 42]. It provides information on the spatial relationships between pixel brightness values in a given image. The GLCM is constructed by counting the number of occurrences of a gray level adjacent to another gray level, at a specified pixel distance “*d*” and dividing each counting by the total counting number to obtain a probability. The result is a matrix with rows and columns representing gray levels and elements containing the probability $P_d[i, j]$ of the gray-level co-occurrence between pixels. The matrix is usually averaged in opposite and different orientations (0–180°, 45–225°, 90–270°, and 135–315°) unless one-dimensional feature dominates overall possible ones, in which case, the 0–180 average is sufficient. A detailed explanation on how this matrix is created from the original image can be found in [54].

The GLCM analysis can be carried out by different methods; they are commonly classified as contrast methods, orderliness methods, and statistical methods. Contrast methods can be used in order to give quantitative information on the intensity fluctuations in the image [4, 34, 42]. Among the contrast methods, homogeneity is the weighted sum of the GLCM pixel values. The weights are values nonlinearly decreasing according to the distance from the GLCM matrix diagonal increases. The homogeneity parameter gives information about the similitude of two neighboring pixel values, against all the other pair of pixels of the image. Orderliness methods are particularly suitable to images with fibrous structures, such as SHG images of collagen. This approach can be used in order to give a quantitative measurement on the mutual orientation of collagen fiber bundles. The energy parameter, for example, is the root-squared sum of the GLCM pixel values. Considering that it gives higher weight to the hot spots of the GLCM matrix, that parameter can be considered as a measure of the sample orderliness. Statistical methods are based on the statistical analysis of pixel value dependence and can be used for determining repetition of a certain pattern within a tissular image. Among them, the correlation method probably represents the most powerful approach to be applied to SHG images of collagen. Mathematically the parameters are defined in **Table 3**.

Parameters	Interpretation	Mathematical expression
Correlation	Linear dependency of gray levels on those of neighboring pixels	$-\sum_{i,j=0}^{N-1} P_{i,j} \left[\frac{(i-\mu)(j-\mu)}{\sigma^2} \right]$
Contrast	Representation of pixels entirely similar to their neighbor	$\sum_{i,j=0}^{N-1} (i-j)^2 P_{i,j}$
Energy	Degree of image's texture directions according to the perception of human eyes	$\sum_{i,j=0}^{N-1} P_{i,j}^2$
Homogeneity	Measure of the amount of local uniformity present in the image	$\sum_{i,j=0}^{N-1} \frac{P_{i,j}^2}{1+(i-j)^2}$

Table 3. GLCM parameters and its mathematical expressions.

The texture analyses can be performed with Image-J GLCM Texture plugin, which was described by Walker and collaborators [55]. Also other parameters such Contrast, Entropy, Inertia, and Variance could be estimated from the GLCM approach [42]. Here a characterization of tissues by estimating the typical dimensions in which collagen maintains its organization is showed. For example, the correlation of the image itself with a pixel separation translated from 1 to 12 or 18 pixels (**Figure 7L–N**) was used. The feature was averaged at angles $\theta = 0, 90, 180,$ and 270 degrees to take into account the fact that these images do not have a specific spatial orientation. The distance where correlation falls to $1/2$ expressed in microns was measured [4]. To perform the calculations, three ROIs (100×100 pixel side squared) in the SHG images near the epithelium were selected. Correlation and entropy were measured using GLCM-Texture plugin from ImageJ, which was previously described by Walker and collaborators [55]. **Figure 7N** shows that the correlation of normal fibrils fall off sharply with distance,

indicating distinct, linear fibrils, whereas correlation for the fibrils in adenocarcinomas remained elevated for larger distances, implying less-defined fibrillar structure. Consistent with qualitative appearances, the correlation was found to remain higher in malignant tissues with the Corr50, the pixel distance where the correlation dropped below 50% of the initial value, significantly greater in adenocarcinomas (3.4 pixels) compared with normal ovarian (1.7 pixels) (**Figure 7N**; $p < 0.05$, t -test). In the same ROI, the entropy values were 6.26 ± 0.31 and 7.40 ± 0.58 from normal and adenocarcinoma, respectively. This means that normal tissues exhibit a lesser complexity or higher organization than malignant ones [34].

Following the impact of GLCM analysis, the method in the evaluation of patients with OI is showed. Skin samples from healthy and from patients with OI were obtained from the Laboratory of Pediatric Endocrinology, Campinas, SP, Brazil. Biopsies were analyzed and classified as normal (4 cases) or OI (5 cases). OI patients were classified according to clinical observations in mild OI (Type I—1 case), moderately affected and severe OI (Type III or Type IV—4 cases). Normal samples were obtained from eyelid plastic surgery discarded tissue, and patient biopsies were obtained from growing skin. Fresh skin samples in Phosphate Buffer Solution (PBS) were analyzed by 3D SHG representations within 6 hours of the excision. From the mounted SHG pictures, images located in the dermis were taken. Nonsymmetric GLCMs were computed using 256 gray levels. Because collagen fiber orientation changed from sample to sample, four orientations average were used. This scoring method was competent to satisfactorily discriminate the different OI patients according to their clinical severity [56]. Using fresh biopsies, one could detect a marked density decrease of the collagen fibers network in the 3D representations of SHG images from severe OI patient's samples (**Figure 8B** (Type III) and **Figure 8C** (Type IV)), when compared with the 3D representation of SHG images taken from normal skin fresh biopsies (**Figure 8A**). Furthermore, energy value of GLCM texture analysis could not only discriminate type I and type III OI samples from normal skin (**Figure 8D**), but it could also differentiate (with statistical significance) between patients with varying degrees of OI, including Type IV OI (**Figure 8E**). It is well known that dermis collagen fibers have diameter ranges around 0.5 to 3 μm . Therefore, it is expected that GLCM analysis would show a repeating structure with distances of about 1.5–8 pixels corresponding to the 0.5–3 μm range. Considering that OI patients exhibit thicker fibers than normal skin samples, GLCM correlation signals could be to drop on a longer scale. The values of decay length are obtained by fitting the correlation data with a double exponential decay function. The decay length values using the Corr50 (the pixel distance where the correlation dropped below 50% of the initial value) obtained are between 1.3 and 2.5 μm (3.8–7 pixels), confirming that patient D had thicker collagen fiber $\approx 2.5 \mu\text{m}$ (7 pixels). Using this pixel distance as comparison, the energy parameter shows values of 0.15 ± 0.02 (normal), 0.13 ± 0.04 (Patient (Pat.) A), 0.20 ± 0.03 (Pat. B), 0.24 ± 0.04 (Pat. C), 0.29 ± 0.03 (Pat. D), and 0.33 ± 0.04 (Pat. E), with significant differences ($p < 0.05$) when normal skin was compared with OI patient's (B, C, D, and E) skin. This means that this texture parameter clearly allows the identification of each patient pattern. Interestingly, by using this method, it was possible to discriminate one case of type IV patient, exhibiting a more severe phenotype (Patient D) than the others. SHG images of these patient skins display a more compacted collagen pattern (thicker collagen fiber), intermediate between type III, and the two remaining type IV patients. The preliminary results allow auguring that

these nonlinear microscopy techniques in association with specific scoring method (energy-GLCM) will be an excellent diagnostic tool to clinically distinguish different types of OI in human skin [56].

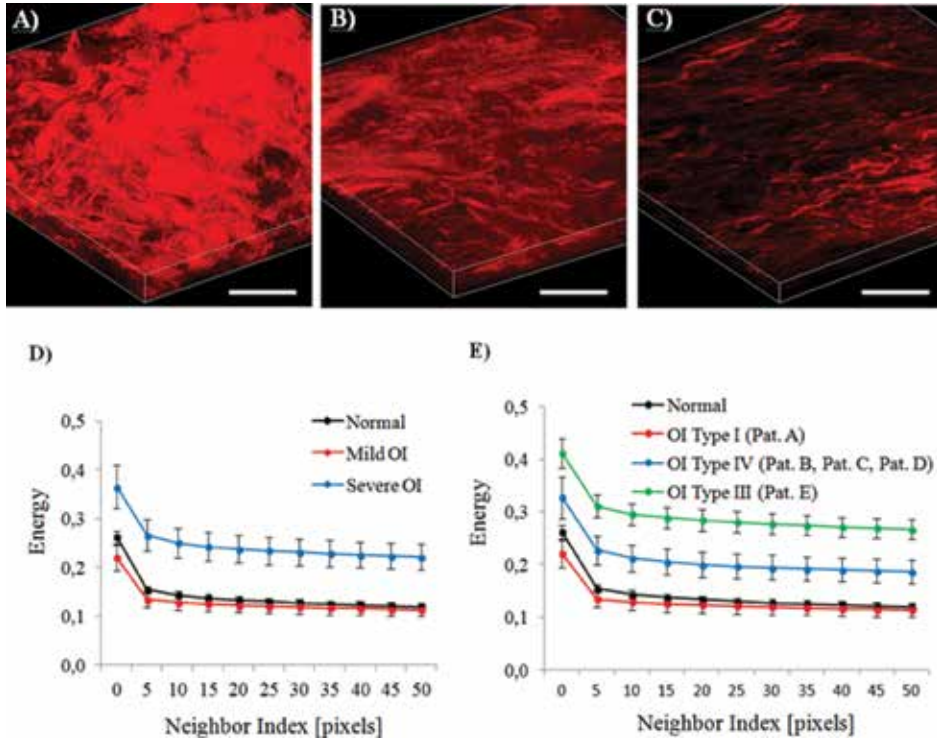


Figure 8. Representative 3D maximum projection (40 images at 1µm interval) of SHG images from fresh skin biopsies, (A) normal skin, (B) OI type III (Patient E), and (C) OI type IV (Patient D). Texture analysis (D, E) using GLCM. Energy values were calculated in dermis tissues versus distance pixels; ranging from 1 to 50 pixels (0.35 µm–17.30 µm) in 0, 45, 90, and 135° directions of image (d): $n = 12$ normal, $n = 3$ mild OI, and $n = 12$ severe OI; and (e) $n = 12$ normal, $n = 3$ OI type I, $n = 9$ OI type IV, $n = 3$ OI type III). Pat: patients. Reproduced figures from Adur et al. [56] (open access).

5. Conclusions

This chapter summarizes several nonlinear microscopy techniques that can be combined and the images acquired analyzed by a set of quantitative tools. This may allow the implementation of new diagnostic procedures for early detection of various diseases. The integration of a set of microscopy techniques is one of the evolving areas in bioimaging that promises to have a strong impact on the understanding and early detection of diverse pathologies. As has been described and exemplified in the sections of this chapter, the advantages of the techniques are numerous, namely high depth penetration (due to Near Infrared (NIR) laser), intrinsic 3D

sectioning and 3D resolution (due to the spatial confinement of the signal to the laser focus), multiple nonlinear processes summed to the possibility to detect several endogenous molecular markers, and low phototoxicity. Additionally, these techniques allow the investigation of living processes in the native environment without major perturbations. All these advantages allow us to postulate that in the near future the NLO techniques together with nonlinear signal processing methods can be very useful in the field of medical diagnosis. In combination with sophisticated animal models and computer-assisted data analysis, NLO microscopy techniques and image processing methods are opening new doors to the study of tumor biology, facilitating the development of new strategies for early tumor diagnosis and other diseases.

As is shown in this chapter, by integrating the strengths of each NLO imaging modality, different structures, and their interactions in a complex biological system can be simultaneously visualized. Additionally, the possibility of obtaining images at high speed and with chemical specificity makes NLO microscopy a powerful tool to evaluate the dynamic behavior of *in vivo* disease progression [57]. CARS microscopy should allow longitudinal studies of lipid metabolism in the same living model organisms over time. Other auspicious application is the label-free imaging of organogenesis and drug delivery. Also, CARS can provide structural information and it has been useful in analyzing molecular orientations in myelin [58], single lipid bilayer [59], cellulose fiber [60], and crystal of clean fourth-order symmetry [61].

In translational research, NLO microscopy has demonstrated the ability of diagnosing diseases of live organisms [62]. Recently, it has been found that changes occurring in collagen deposit and arrangement, in early tumor development and during their progression, can be used as predictable tools of the disease status. The ovary examples in this work demonstrate that AR and correlation analysis have the ability to predict the disease degree in human patients. Therefore, if more experiments are successful, SHG may eventually provide a more rapid, real-time substitute for traditional histopathological processing and analyses. For this disease, mortality rates are elevated because an efficient screening test does not exist presently. Approximately, 15% of ovarian cancers are found before metastasis has occurred. If ovarian cancer is found and treated before this process is triggered, the 5-year survival rate will be around 94%. Thus, an early diagnostic test to detect premalignant changes would save many lives. In this sense, the unique attributes of NLO microscopy described here render these methods as a promising imaging modality for disease diagnostics in the clinic. Also, the medical utility of these optical methods could be improved by the continuous development and refinement of methods to obtain objective, quantitative information. These will be in the form of analysis algorithms such as Helmholtz analysis, wavelet analysis, and with numerical parameters relating to image frequency content and second-order gray-level statistics. Further, a classification scheme could be developed by using a support vector machine.

The effort to develop new diagnosing methods that could better identify early lesions and consequently lead to an early diagnosis is a challenge and a stimulus for research in this area. The outcomes of different works indicate that the combination of diverse image analysis approaches summarized here represent a combination of powerful tools to investigate epithelial cells transformation, collagen organization, and extracellular matrix remodeling in epithelial tumors and *osteogenesis imperfecta* in skin. About OI, it was demonstrated in this

chapter that nonlinear microscopy techniques, in combination with image analysis approaches, represent a powerful tool to investigate the collagen organization in skin dermis in patients with OI and having the potentiality to distinguish the different types of OI. The procedure used here requires a skin biopsy, which is almost painless as compared to the bone biopsy commonly used in conventional methods. The data presented here are complementary of existing clinical diagnostic approaches and can be used as a procedure to confirm the disease and evaluate its severity and treatment efficacy.

In cancer diagnosis, there is a growing need for the development of a multimodal imaging-based diagnostic tool to objectively evaluate morphological features with subcellular resolution and molecular compositions that are closely associated with tumor malignancy. With this perspective, NLO microscopy has proven to be useful in cancer research. These techniques have recently emerged as a valuable tool for high-resolution, nondestructive, chronic imaging of living tumors. Moreover, multimodal microscopy can provide a powerful tool for investigating the dynamics of structure-function relationships both at the subcellular and molecular levels.

Today, the application of multimodal nonlinear imaging is recognized in basic research in the biological and biomedical sciences; however, regular applications in clinics are still rare, mainly because of their high cost. Multimodal platforms are still complex and require specialized personnel for its operation. So, mainly technological progresses are required for miniaturization, enhancement of the ease of control, automated data processing, and extraction of significant information. To achieve this goal, the modification of typical clinical endoscopes for in vivo multimodal nonlinear imaging is necessary. The development of nonlinear optical endoscopy, which allows imaging under conditions in which a conventional nonlinear optical microscope cannot be used, will be the primary goal to extend applications of nonlinear optical microscopy toward clinical ones. There are several key challenges involved in the pursuit of in vivo nonlinear optical endoscopy. A few of them are the necessity of obtaining efficient ultrashort pulse laser liberations into a remote place, the need to enhance scan rates for monitoring biological processes, and the miniaturization of the laser-scanning mechanisms to the millimeter scale. Finally, the design of a nonlinear optical endoscope based on micro-optics with great flexibility, and compact enough to be incorporated into endoscopes, will become an evolution of these microscopy platforms. With the continuous advancement in this endoscopic techniques and new laser sources, we have reason to believe that these particularly promising techniques in conjunction with efficient image analysis algorithm will open up many new possibilities for the diagnosis and treatment of different diseases in the near future.

Acknowledgements

HFC acknowledges funding from FAPESP (Grant no. 2009/16150-6). The authors are grateful to FAPESP (Grant no. 2011/51591-3), CEPOF (Optics and Photonics Research Center, FAPESP), INFABIC (National Institute of Photonics Applied to Cell Biology, FAPESP, and CNPq), and PICTO UNER-INTA-CAFECS (Grant no. 2009-209).

Author details

Javier Adur^{1,2,3*}, Hernandes F. Carvalho^{3,4}, Carlos L. Cesar^{3,5,6} and Víctor H. Casco^{1,2}

*Address all correspondence to: jadur@bioingenieria.edu.ar

1 CITER—Centro de Investigación y Transferencia de Entre Ríos, UNER-CONICET, FI-UNER, Argentina

2 Microscopy Laboratory Applied to Molecular and Cellular Studies, School of Bioengineering, National University of Entre Ríos, Argentina

3 INFABiC—National Institute of Science and Technology on Photonics Applied to Cell Biology, Campinas, Brazil

4 Department of Structural and Functional Biology, Biology Institute, State University of Campinas, Brazil

5 Biophotonic Group, Optics and Photonics Research Center (CEPOF), Institute of Physics “Gleb Wataghin”, State University of Campinas, Brazil

6 Department of Physics of Federal University of Ceara (UFC), Brazil

References

- [1] Provenzano PP, Eliceiri KW, Keely PJ. Multiphoton microscopy and fluorescence lifetime imaging microscopy (FLIM) to monitor metastasis and the tumor microenvironment. *Clin. Exp. Metastasis*. 2009; 26:357–370. doi: 10.1007/s10585-008-9204-0
- [2] Masters BR, So PTC. The genesis of nonlinear microscopies and their impact on modern developments. In: Master and So, Editors. *Handbook of Biomedical Nonlinear Optical Microscopy*. New York: Oxford University Press, 2008. p. 5–28.
- [3] Meyer T, Schmitt M, Dietzek B, Popp J. Accumulating advantages, reducing limitations: multimodal nonlinear imaging in biomedical sciences – the synergy of multiple contrast mechanisms. *J. Biophotonics*. 2013; 6:887–904. doi: 10.1002/jbio.201300176
- [4] Adur J, Carvalho HF, Cesar CL, Casco VH. Nonlinear optical microscopy signal processing strategies in cancer. *Cancer Inf*. 2014; 13:67–76. doi: 10.4137/CIN.S12419
- [5] Shen YR. *The principles of nonlinear optics*. New York, John Wiley, 1984.
- [6] Gu M, Bird D, Day D, Fu L, Morrish D. eds. *Nonlinear optical microscopy*. In: *Femtosecond Biophotonics Core Technology and Applications*. New York: Cambridge University Press, 2010. p. 9–34.

- [7] Cheng PC, Sun CK. Nonlinear (harmonic generation) optical microscopy. In: Pawley JB, Editor. *Handbook of Biological Confocal Microscopy*, 3rd edn. 2006. Springer. New York. p. 703–721.
- [8] Gauderon R, Lukins PB, Sheppard CJ. Three-dimensional second-harmonic generation imaging with femtosecond laser pulses. *Opt. Lett.* 1998; 23:1209–1211.
- [9] Chu SW, Chen IH, Liu TM, Chen PC, Sun CK, Lin BL. Multimodal nonlinear spectral microscopy based on a femtosecond Cr:forsterite laser. *Opt. Lett.* 2001; 26:1909–1911.
- [10] Boyd R. *Nonlinear Optics*, 1st edn. New York, Academic Press, 1992.
- [11] Debarre D, Beaurepaire E. Quantitative characterization of biological liquids for third harmonic generation microscopy. *Biophys. J.* 2007; 92:603–612.
- [12] Williams RM, Zipfel WR, Webb WW. Interpreting second-harmonic generation images of collagen I fibrils. *Biophys. J.* 2005; 88:1377–1386.
- [13] Campagnola PJ, Millard AC, Terasaki M, Hoppe PE, Malone CJ, Mohler WA. Three-dimensional high-resolution second-harmonic generation imaging of endogenous structural proteins in biological tissues. *Biophys. J.* 2002; 82:493–508.
- [14] Chu SW, Chen SY, Chern GW, Tsai TH, Chen YC, Lin BL, Sun CK. Studies of chi(2)/chi(3) tensors in submicron-scaled bio-tissues by polarization harmonics optical microscopy. *Biophys. J.* 2004; 86:3914–3922.
- [15] Müller M, Squier J, Wilson KR, Brakenhoff GJ. 3D microscopy of transparent objects using third-harmonic generation. *J. Microsc.* 1998; 3:266–274.
- [16] Moreaux L, Sandre O, Blanchard-Desce M, Mertz J. Membrane imaging by simultaneous second-harmonic generation and two-photon microscopy. *Opt. Lett.* 2000; 25:320–322.
- [17] Sun CK, Chu SW, Chen SY, Tsai TH, Liu TM, Lin CY, Tsai HJ. Higher harmonic generation microscopy for developmental biology. *J. Struct. Biol.* 2004; 147:19–30.
- [18] Adur J, Pelegati VB, Costa LF, Pietro L, de Thomaz AA, Almeida DB, Bottcher-Luiz F, Andrade LA, Cesar CL. Recognition of serous ovarian tumors in human samples by multimodal nonlinear optical microscopy. *J. Biomed. Opt.* 2011; 16:096017. doi: 10.1117/1.3626575
- [19] Adur J, Pelegati VB, de Thomaz AA, D'Souza-Li L, Assunção Mdo C, Bottcher-Luiz F, Andrade LA, Cesar CL. Quantitative changes in human epithelial cancers and osteogenesis imperfecta disease detected using nonlinear multicontrast microscopy. *J. Biomed. Opt.* 2012; 17:081407-1. doi: 10.1117/1.JBO.17.8.081407
- [20] Adur J, Pelegati VB, de Thomaz AA, Baratti MO, Andrade LA, Carvalho HF, Bottcher-Luiz F, Cesar CL. Second harmonic generation microscopy as a powerful diagnostic imaging modality for human ovarian cancer. *J. Biophotonics.* 2014; 7:37–48. doi: 10.1002/jbio.201200108

- [21] Duncan MD, Reintjes J, Manuccia TJ. Scanning coherent anti-Stokes Raman microscope. *Opt. Lett.* 1982; 7:350–352.
- [22] Pelegati VB, Adur J, De Thomaz AA, Almeida DB, Baratti MO, Andrade LA, Bottcher-Luiz F, Cesar CL. Harmonic optical microscopy and fluorescence lifetime imaging platform for multimodal imaging. *Microsc. Res. Tech.* 2012; 75. doi: 10.1002
- [23] Hu W, Zhao G, Wang C, Zhang J, Fu L. Nonlinear optical microscopy for histology of fresh normal and cancerous pancreatic tissues. *PLoS One.* 2012; 7:e37962. doi: 10.1371
- [24] Hompland T, Erikson A, Lindgren M, Lindmo T, de Lange Davies C. Second-harmonic generation in collagen as a potential cancer diagnostic parameter. *J. Biomed. Opt.* 2008; 13. doi: 10.1117.054050, doi: 10.1117/1.2983664
- [25] Sivaguru M, Durgam S, Ambekar R, Luedtke D, Fried G, Stewart A, Toussaint KC Jr. Quantitative analysis of collagen fiber organization in injured tendons using Fourier transform-second harmonic generation imaging. *Opt. Express.* 2010; 18:24983–93. doi: 10.1364/OE.18.024983
- [26] Mouras R, Rischitor G, Downes A, Salter D, Elfick A. Nonlinear optical microscopy for drug delivery monitoring and cancer tissue imaging. *J. Raman Spectrosc.* 2010; 41:848–852.
- [27] Bianchini P, Diaspro A. Three-dimensional (3D) backward and forward second harmonic generation (SHG) microscopy of biological tissues. *J. Biophotonics.* 2008; 1:443–450. doi: 10.1002/jbio.200810060
- [28] Adur J, Carvalho HF, Cesar CL, Casco VH. Nonlinear imaging microscopy: Methodological setup and applications for epithelial cancers diagnosis. In: Fred Wilkins Ed, Nova Science Publishers. *Nonlinear optics: fundamentals, applications and technological advances.* New York, Nova Publishers, 2014. p. 97–136.
- [29] Cheng JX, Xie XS. Coherent anti-Stokes Raman scattering microscopy: instrumentation, theory, and applications. *J. Phys. Chem. B.* 2004; 108:827–840.
- [30] Volkmer A, Book LD, Xie XS. Time-resolved coherent antiStokes Raman scattering microscopy: imaging based on Raman free induction decay. *Appl. Phys. Lett.* 2002; 80: 1505–1507.
- [31] American Cancer Society. *Cancer Facts & Figures 2009.* Atlanta, American Cancer Society, 2009.
- [32] Tsuboi M, Ueda T, Ushizawa K, Ezaki Y, Overman SA, Thomas GJ. Raman tensors for the tryptophan side chain in proteins determined by polarized Raman microspectroscopy of oriented N-acetyl-L-tryptophan crystals. *J. Mol. Struct.* 1996; 379:43–50.
- [33] Tearney GJ, Brezinski ME, Bouma BE, Boppart SA, Pitris C, Southern JF, Fujimoto JG. In vivo endoscopic optical biopsy with optical coherence tomography. *Science.* 1997; 276:2037–2039.

- [34] Adur J, Pelegati VB, de Thomaz AA, Baratti MO, Almeida DB, Andrade LA, Bottcher-Luiz F, Carvalho HF, Cesar CL. Optical biomarkers of serous and mucinous human ovarian tumor assessed with nonlinear optics microscopies. *PLoS One*. 2012; 7:e47007. doi:10.1371/journal.pone.0047007
- [35] Zhuo S, Zhu X, Wu G, Chen J, Xie S. Quantitative biomarkers of colonic dysplasia based on intrinsic second-harmonic generation signal. *J. Biomed. Opt.* 2011; 16:120501.
- [36] Birk JW, Tadros M, Moezardalan K, Nadyarnykh O, Forouhar F, Anderson J, Campagnola P. Second harmonic generation imaging distinguishes both high-grade dysplasia and cancer from normal colonic mucosa. *Dig. Dis. Sci.* 2014; 59:1529–1534. doi: 10.1007/s10620-014-3121-7
- [37] Adur J, Bianchi M, Pelegati VB, Viale S, Izaguirre MF, Carvalho HF, Cesar CL, Casco VH. Colon adenocarcinoma diagnosis in human samples by multicontrast nonlinear optical microscopy of hematoxylin and eosin stained histological sections. *J. Cancer Ther.* 2014; 5:1259–1269. <http://dx.doi.org/10.4236/jct.2014.513127>
- [38] Kuurila K, Kaitila I, Johansson R, Grenman R. Hearing loss in Finnish adults with osteogenesis imperfecta: a nationwide survey. *Ann. Otol. Rhinol. Laryngol.* 2002; 111:939–1946.
- [39] Stoll C, Dott B, Roth MP, Alembik Y. Birth prevalence rates of skeletal dysplasias. *Clin. Genet.* 1989; 35:88–92.
- [40] Dalgleish R. The human type I collagen mutation database. *Nucleic Acids Res.* 1997; 25:181–187.
- [41] Dalgleish R. The human collagen mutation database 1998. *Nucleic Acids Res.* 1998; 26:253–255.
- [42] Tilbury K, Campagnola PJ. Applications of second-harmonic generation imaging microscopy in ovarian and breast cancer. *Perspect. Med. Chem.* 2015; 7:21–32. doi: 10.4137/PMC.S13214
- [43] Cicchi R, Sacconi L, Pavone F. Nonlinear imaging of tissues. In: Tuchin VV, Editor. *Handbook of photonics for biomedical science*. New York, CRC Press, 2010. p. 509–545.
- [44] Cicchi R, Massi D, Sestini S, Carli P, De Giorgi V, Lotti T, Pavone FS. Multidimensional non-linear laser imaging of basal cell carcinoma. *Opt. Express.* 2007; 15:10135–10148.
- [45] Cicchi R, Sestini S, De Giorgi V, Massi D, Lotti T, Pavone FS. Nonlinear laser imaging of skin lesions. *J. Biophotonics.* 2008; 1:62–73. doi: 10.1002/jbio.200710003
- [46] Lin SJ, Jee SH, Kuo CJ, Wu RJ, Lin WC, Chen JS, Liao YH, Hsu CJ, Tsai TF, Chen YF, Dong CY. Discrimination of basal cell carcinoma from normal dermal stroma by quantitative multiphoton imaging. *Opt. Lett.* 2006; 31:2756–2758.
- [47] Koehler MJ, König K, Elsner P, Bückle R, Kaatz M. In vivo assessment of human skin aging by multiphoton laser scanning tomography. *Opt. Lett.* 2006; 31:2879–2881.

- [48] Lin SJ, Wu R Jr, Tan HY, Lo W, Lin WC, Young TH, Hsu CJ, Chen JS, Jee SH, Dong CY. Evaluating cutaneous photoaging by use of multiphoton fluorescence and second-harmonic generation microscopy. *Opt. Lett.* 2005; 30:2275–2277.
- [49] Provenzano PP, Inman DR, Eliceiri KW, Knittel JG, Yan L, Rueden CT, White JG, Keely PJ. Collagen density promotes mammary tumor initiation and progression. *BMC Med.* 2008; 6:11. doi: 10.1186/1741-7015-6-11
- [50] Sivaguru M, Durgam S, Ambekar R, Luedtke D, Fried G, Stewart A, Toussaint KC Jr. Quantitative analysis of collagen fiber organization in injured tendons using Fourier transform-second harmonic generation imaging. *Opt Express.* 2010; 18:24983–24993. doi: 10.1364/OE.18.024983
- [51] Matteini P, Ratto F, Rossi F, Cicchi R, Stringari C, Kapsokalyvas D, Pavone FS, Pini R. Photothermally-induced disordered patterns of corneal collagen revealed by SHG imaging. *Opt Express.* 2009; 17:4868–4878.
- [52] Arlo RA. Thesis for the degree of Master of Science by Thayer School of Engineering [master's thesis]. New Hampshire, Dartmouth College Hanover, 1990.
- [53] Zhuo S, Zhu X, Wu G, Chen J, Xie S. Label-free monitoring of colonic cancer progression using multiphoton microscopy. *Biomed. Opt. Express.* 2011; 2:615–619. doi: 10.1117/1.3659715
- [54] English RS, Shenefelt PD. Keloids and hypertrophic scars. *Dermatol Surg.* 1999; 25:631–638.
- [55] Walker RF, Jackway PT, Longstaff ID. Genetic algorithm optimisation of adaptive multi-scale in GLCM features. *Int. J. Pattern Recogn.* 2003; 17:17–39.
- [56] Adur J, DSouza-Li L, Pedroni MV, Steiner CE, Pelegati VB, de Thomaz AA, Carvalho HF, Cesar CL. The severity of Osteogenesis imperfecta and type I collagen pattern in human skin as determined by nonlinear microscopy: proof of principle of a diagnostic method. *PLoS One.* 2013; 8:e69186. doi: 10.1371/journal.pone
- [57] Huff TB, Cheng JX. In vivo coherent anti-Stokes Raman scattering imaging of sciatic nerve tissue. *J. Microsc.* 2007; 225:175–182.
- [58] Kennedy AP, Sutcliffe J, Cheng JX. Molecular composition and orientation of myelin figures characterized by coherent anti-Stokes Raman scattering microscopy. *Langmuir.* 2005; 21:6478–6486.
- [59] Potma EO, Xie XS. Detection of single lipid bilayers with coherent anti-Stokes Raman scattering (CARS) microscopy. *J. Raman Spectrosc.* 2003; 34:642–650.
- [60] Zimmerley M, Younger R, Valenton T, Oertel DC, Ward JL, Potma EO. Molecular orientation in dry and hydrated cellulose fibers: a coherent anti-Stokes Raman scattering microscopy study. *J. Phys. Chem. B.* 2010; 114:10200–10208. doi: 10.1021/jp103216j

- [61] Munhoz F, Rigneault H, Brasselet S. High order symmetry structural properties of vibrational resonances using multiple-field polarization coherent anti-Stokes Raman spectroscopy microscopy. *Phys. Rev. Lett.* 2010; 105:123903.
- [62] Wang HW, Langohr IM, Sturek M, Cheng JX. Imaging and quantitative analysis of atherosclerotic lesions by CARS-based multimodal nonlinear optical microscopy. *Arterioscler. Thromb. Vasc. Biol.* 2009; 29:1342–1348. doi:10.1161/ATVBAHA.109.189316

Skin Wound Healing Revealed by Multimodal Optical Microscopies

Gitanjal Deka, Shi-Wei Chu and Fu-Jen Kao

Additional information is available at the end of the chapter

<http://dx.doi.org/10.5772/64088>

Abstract

Skin is the largest organ of our body serving as the first line defense against pathogens and toxicity. The skin can heal itself if any damage in it occur. Wounds, if not taken care properly, can become chronic and can even cause death. In the field of cosmetics and plastic reconstructive surgery, wounds, are major cause of trauma and costs, which demand proper diagnosis that can help in appropriate treatment. In conventional medicine, wound diagnosis mostly relied on the expertise and experience of physicians on the basis of non-quantitative observation of clinical signs, or invasive histochemical assessment of biopsies.

Methodologies based on light-matter interaction can provide quantitative, noninvasive and real time assessment of a tissue section based on imaging. Depending on the nature of interaction, various contrasts can be achieved by either absorption, scattering, or fluorescence, enabling observation of structural or molecular components of tissue sections. Development of multiphoton nonlinear optical detection techniques provide better resolution and tissue penetration depth with optical sectioning ability by using molecular and structural contrasts simultaneously. This chapter discusses and evaluates various optical approaches with special emphasis on multimodal multiphoton imaging of skin tissue components in correlation to physiological processes that affects the wound healing.

Keywords: skin, wound healing, optical microscopy, NADH, collagen, fluorescence, second harmonic generations

1. Introduction

Skin wounds and their treatment lead to major medical expenses in cosmetic surgery. Chronic wounds, including diabetic ulcers and pressure ulcers, present a significant health and economic concern for individual patients as well as the healthcare system. The diabetic ulcer is a major complication of diabetes mellitus, a disease which afflicts more than 350 million people worldwide. Among them foot ulceration is the leading cause for hospitalization [1]. Acute cutaneous burn wounds are also a serious health-related issue in the global community. Nearly 11 million flame burns occur annually and burn deaths rank in the top 15 causes of death for individuals 5–29 years of age. Around 60% of these burn patients heal with debilitating hypertrophic or keloid scarring [2]. Additionally, the cutaneous burn wound can left deep and large scar in comparison to normal wound after healing. All these scars are formed due to over deposition of collagen fibers to fill up the wound gaps, which are structurally and molecularly different to each other and need different approaches for their diagnosis and management. Improper management of wound may cause serious tissue disfigurement that may cause serious physical and psychological problems in patients.

Wound healing is a widely studied biomedical problem regarding tissue systems. To address the situation of wounds and their assessment of healing potential requires insight of what occurs to the components of skin at cellular and molecular level. Specifically, epithelial cell migration and collagen regeneration by fibroblast cells in the skin were found to have great effects on accelerated wound healing [3]. The entire wound healing process is a complex series of events that starts at the moment of injury and can continue for months even years in a few sequential yet overlapping phases. The characterization of wounds, their healing, and also the timeline of these sequential phases have major clinical significance in assessing severity, healing potential, and determining the correct treatment for all wound types. Traditionally, wound assessment has relied on visual evaluation by trained clinicians, with techniques based on laboratory biopsies providing objective assessment modalities [4, 5]. Currently, histological analysis of the tissue remains the gold standard for precise quantitative and qualitative assessment of wound depth and status. However, the biopsy process is invasive, can be painful, and in some cases can cause additional trauma and worsen scarring [4, 5]. Additionally, the processing required for histochemical observation usually distorts the structural integrity of the tissue.

In contrast to the abovementioned traditional wound assessment procedures, noninvasive imaging by optical means does not require destructive tissue sectioning; it preserves all layers of the skin. By collecting the information through light and tissue interaction, optical imaging assesses wound severity, healing potential, and progress in a rapid, objective, and noninvasive manner. Optical microscopic techniques use various biomolecules as marker to observe skin and its physiology. Various imaging modalities detect scattering and absorption of light by these markers, aiding the qualitative and quantitative evaluation of cell regeneration, metabolic activity, collagen remodeling, blood flow, inflammation, vascular structure, and water content. For example, absorption by hemoglobin provides contrast of veins in technique such as laser Doppler imaging (LDI); reflection and scattering by extracellular matrix provide

structural contrast achieved by optical coherence tomography (OCT) and reflectance confocal laser scanning microscopy (RCLM) and fluorescence from molecules such as NADH, FAD [6], and tryptophan [7] provide molecular contrasts for fluorescence imaging of cells that constitute the epidermal layers of the skin. Some molecules, such as collagen and elastin found in the skin dermis, are also known to have autofluorescence [8, 9]. Along with fluorescence, collagen is better known as a strong SH generator that can provide structural contrast while imaging the dermis [9].

In clinical setting, optical imaging with these contrast mechanisms has been or has the potential to study skin wound healing noninvasively. Spectrally resolved tissue imaging with confocal or multiphoton microscopy enables 3D imaging of tissues through depth sectioning and can be used to study skin wound healing [10]. In comparison to other conventional optical microscopies, multiphoton microscopy offers a number of advantages. Nonlinear excitation limits the sample excitation to the focal volume and optical scanning with very small excitation volume results in high-contrast images. Lower scattering of IR light enables deeper penetration in tissue. Large spectral separation between the multiphoton excitation and emission provides easier discrimination of entire emission spectrum [11]. Among the modalities of multiphoton microscopy, two-photon fluorescence (2PF) and SHG present as the most effective ones in tissue imaging for diagnosis and prognosis in skin wound healing.

In this chapter we will discuss recent advancements in optical microscopic techniques for imaging skin tissue and its regeneration during wound healing. We will put forward a comparative idea of various techniques in their specific objectives of skin observations. In doing so we will briefly discuss the wound healing processes at various phases and the corresponding molecular components involved that can be used as biomarkers. Our main emphasis of the chapter is on the analysis of wound healing enabled by multiphoton microscopy (MPM), mainly 2PF and SHG imaging, and their prospects in clinical settings. However, we will also cover other popular methodologies for optical imaging of skin, highlighting their potentials in wound healing study.

2. Skin and wound healing phases

Skin is the largest organ of our body which protects us from excessive water loss and invasion of outside pathogens, senses changes in environment, etc. Before discussing the diagnostic methodologies of skin wound healing, it is very important to understand the anatomy and the molecular basis of skin and how the healing processes are related. In this section we will introduce the skin's anatomic layers and the molecules present in these layers that are potential markers for optical imaging. Various phases of wound healing and the molecular components involve in the process are also discussed in the later part of the section.

From an anatomic point of view, skin is a multilayered tissue as represented in **Figure 1(b)**. It weighs about 10% of our total body weight and thickness is approximately ranged from .5 to 2 mm [12]. The thickness of skin varies in deferent region of the body. Skin is composed of three primary layers:

(1) The epidermis, which preserves body fluid and serves as a barrier to infection, is mainly a stratified squamous epithelium composed of proliferating basal and differentiated keratinocytes. Keratinocytes are the major cells in epidermis constituting 95% of it. It is composed of five stratified layers, namely, stratum corneum, stratum granulosum, stratum spinosum, and stratum germinativum, ranging from 0.05 to 1.5 mm thick [13]. As cells possess autofluorescing chromophores, such as NADH, FAD, and tryptophan, the epidermal physiology can be observed through fluoresce microscopy.

(2) *The dermis* is the layer beneath the epidermis separated by the basement membrane and consists of connective tissues deposited in a space of 0.3–3.0 mm thickness that cushions the body from stress and strain. The connective tissues in dermis are composed mainly of extracellular matrix fibers such as elastin and collagens, ground substances, and specialized cells such as fibroblasts and adipocytes. The main components of extracellular matrix (ECM), collagen, and elastin have autofluorescence, which makes them very useful markers for wound diagnosis. However, collagen being a noncentrosymmetric molecule, SHG is the more popular way of collagen imaging. Additionally, the fibroblasts in dermis play an important role in the wound healing process, which can also be monitored with fluorescence imaging techniques [13].

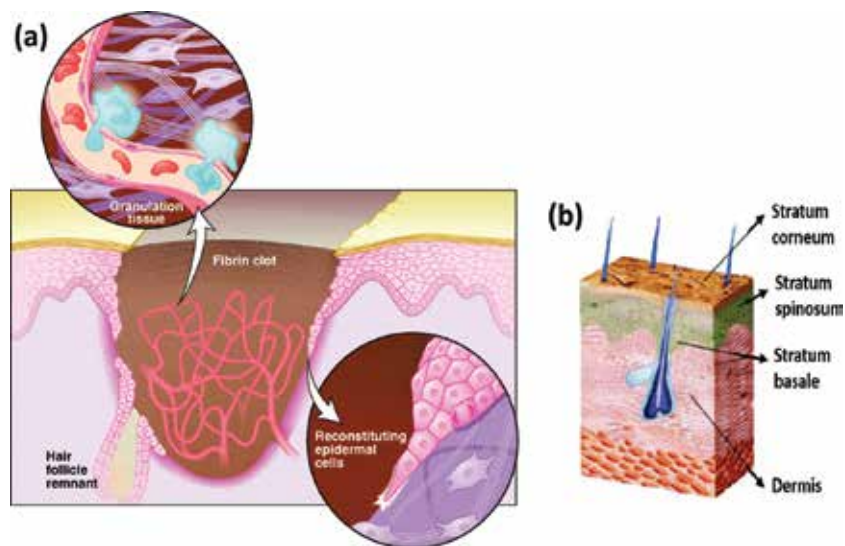


Figure 1. (a) Representative image of the key players in the healing of a skin wound [3]. The wound gap is temporarily plugged with fibrin clot that protects the wound from outside environment along with providing provisions for a dense capillary plexus of new granulation tissue and inflammatory as well as fibroblast cell migration. Reconstructing epidermal cells migrates under the fibrin clot to construct the wound bed that helps in granulation tissue formation to fill the wound gap. (b) Schematic representation of skin anatomy with its different layers [25].

(3) *Hypodermis*: Hypodermis is the layer that lies below the dermis. However, it is not considered to be a part of the skin. It helps joining the skin with the underlying muscles, bones, and blood vessels, as well as nerves. It is mainly composed of loose connective tissues and elastin.

Fibroblasts, macrophages, and adipocytes are the main cells that comprise the hypodermis. Body fat that serves as the insulator of the body also lies in this layer [13].

In normal skin, the epidermis and dermis exist in steady-state equilibrium, forming a protective barrier against the external environment. Once the protective barrier is broken, the normal process of wound healing starts immediately. Wound healing involves sequential phases of cellular initiation and secretion of molecules triggered by specific growth factors and signaling molecules [3]. Initially, a fibrin clot is formed that plugs the defects, which provides a provisional platform for cell migration as depicted in **Figure 1(a)**. In subsequent days, the wound heals completely by forming a dynamic scar tissue rich in collagen [3]. Classical model of wound healing divides the processes into several vital sequential yet overlapping stages, such as (1) hemostasis, (2) inflammation, (3) proliferation, and (4) remodeling.

Hemostasis starts immediately after the wound formation. At this stage, blood changes from liquid state to solid state to stop excessive blood loss, which is termed as blood clotting [14, 15], followed by bacteria and cell debris at the wound site being phagocytosed and removed by macrophages and white blood cells. During this phase the wound site appears red and hotter than the adjacent area marking the onset of inflammation [16–18]. Additionally, at this stage tissue matrix metalloproteinase enzymes start to degrade surrounding ECM proteins such as collagen and necrotic cellular macromolecules to provide a platform for epithelial cells migration [3]. The proliferative phase begins only when the wound is covered by re-epithelium which will migrate to central region of the wound to cover the wound defect. Angiogenesis, collagen deposition, granulation tissue formation, epithelialization, and wound contraction are the signatures of the proliferative phase [19]. The final phase of wound healing is remodeling. It is characterized by the maturation of collagen by rearrangement, intermolecular cross-linking, and alignment along the wound tension line [16]. The remodeling phase may last for a year or even longer with respect to wound size and type [20]. As the wound maturation progresses, the tensile strength of the wound increases, ultimately becoming as strong as 80% of normal tissue [20]. The wound scar gradually flattens and becomes less prominent and more pale and supple. Since activity at the wound site is reduced, consequently blood vessels that are no longer needed are removed by apoptosis and the scar loses its red appearance [21]. The wound healing normally progresses in a predictable, timely manner if not interrupted by any means; otherwise healing may progress inappropriately to transform into a chronic wound or pathological scarring such as a keloid [22, 23]. These scars consist mainly of poorly reconstructed thick parallel bundles of collagens [24]. There are mainly three different kinds of scar tissues depending upon the deposition of ECM [24]: (a) Keloids, (b) hypertrophic scar, and (c) normal scar.

Clinically, keloids are defined as scars growing beyond the confines of original wounds, which rarely regress over time. Hypertrophic scars, on the other hand, are raised scars that remain within the boundaries of the wound and frequently regress spontaneously. Histologically, collagen bundles in the dermis of normal scar tissues appear relatively relaxed and arranged in random arrays, but keloids and hypertrophic scars have collagen bundles that appear much stretched and aligned on the same plane as the epidermis.

3. Current methodologies of wound diagnosis

In clinical practice wound diagnosis is carried out by clinical signs based on the practice and expertise of the physician. For more quantitative and qualitative assessment, histochemical biopsies are employed. Some methodologies commonly used by the clinicians for wound diagnoses are as follows:

(a) *Use of clinical signs:* The clinical signs of infection are erythema, edema, heat, pain, foul odor, and wound breakdown [4]. A physician has to make a firm decision of a wound status on the basis of his or her experience. However, there are several intrinsic limitations to diagnosing a wound through these techniques as all of them are non-quantitative.

(b) *Clinical biopsies:* A biopsy is a medical examination commonly performed by a pathologist involving slice of tissue sections from a diseased or inflamed body part for insights into possible cancerous and inflammatory conditions. It is the medical removal of tissue from a living subject, which is processed into thin slices stained for observation under a microscope or analyzed by biochemical means. This kind of diagnosis has the disadvantage that the method can enlarge the wound. Moreover the time required from biopsy collection to analysis can influence the data and interfere with the wound [5, 26].

(c) *Needle aspiration:* It is a diagnostic procedure used to investigate superficial inflammation, lumps, or masses. In this technique, a thin, hollow needle is inserted into the mass and a portion of the tissue is recovered. The recovered tissue with the cells is stained and examined under a microscope. Needle aspiration biopsies are minor surgical procedures and safe. In spite of being considered as the next best method for microbiological culturing of abscesses and closed wounds, there is a risk, because the biopsy is very small (only a few cells), that the problematic cells may be missed, resulting in a false-negative result [5, 27] that prohibits a definitive diagnosis.

Recently noninvasive approaches have been brought in for assessing skin lesions that include magnetic resonance, ultrasound, and photoacoustic and optical techniques with which intravital imaging of the alterations or aberrations in the skin below the surface has been materialized [28]. Among them optical microscopic techniques provide cost effective and wider range of applications of skin tissue imaging.

4. Optical techniques used in skin observations

Optical imaging techniques are based on the principles of light and tissue interaction for collecting information that is further analyzed to reconstruct an image of the respective tissue section. Depending on the nature of interactions, such as scattering, absorption, or fluorescence, various information can be extracted to reveal anomalies in the tissue sections. The physiological events associated with such structural anomalies also determine the choice of optical modality needed to address the problem noninvasively. In a few excellent reviews,

various optical approaches in skin imaging are listed and discussed depending on the skin conditions [28–31].

Optical modalities are comparatively advantageous for their low-cost, easy to use, non-ionizing, mostly noninvasive, and non-contacting attributes. Some of the optical methodologies can provide 3D imaging capability by optical sectioning with high resolution [32–35]. Optical techniques may also be useful in real-time functional imaging regarding skin physiology [36]. Additionally, most of the skin optical imaging techniques use near-infrared (NIR) or infrared (IR) wavelengths, which are less absorbed in tissue, hence penetrating deeper, enabling the imaging of the whole skin layer [37–39]. Most common optical imaging modalities include LDI, tissue spectral imaging (TSI), and OCT, which are useful in imaging macro-masses in skin (macro-imaging modalities). Optical techniques that are useful in imaging at molecular domain or micro contrasts (micro-optical modalities) are RCLM, Raman spectro-microscopy, and laser scanning fluorescence and SHG microscopy. In this section, we are going to discuss the recent advancements in optical techniques that have been applied to evaluate skin wound-related problems noninvasively or hold potential in this regard. The following is separated into two subsections: the macro-optical modalities and micro-optical modalities.

4.1. Macro-optical imaging modalities

4.1.1. Dermoscopy

Dermoscopy or dermatoscopy, also known as epiluminescence microscopy, is the most common basic handheld magnifying tool that aids in first-line optical observation of morphological abnormalities. Recent dermoscopes use polarized light to illuminate the tissue section to visualize horizontal morphological features that are not visible to naked eye [40]. Dermoscopy has been useful in qualitative visualization of skin-related abnormalities such as rosacea [41], diagnosis of hair and scalp diseases [41–43], diagnosis of warts caused by human papillomavirus [44], and determination of the surgical margin of hard to define skin cancers [41].

This method has been widely used in observing skin lesions based on the presence of certain architectural characteristics of the lesion, which provide promising possibilities in skin wound healing study, mainly in collagen regeneration during wound remodeling phase [45]. A dermoscope is easy to use and represents a relatively low-cost first-line diagnostic tool for skin-related issues; however it is not quantitative and requires expertise and experience to have fair diagnostic judgment [46]. Its resolution is only enough to see small lumps and lesions in the skin. Additionally, no functional information can be gathered with this technique. Commercial dermoscopes are available in the market for quite a few time. Companies such as Optilia, WelchAllyn, CALIBER, HYMED, and FotoFinder are manufacturing dermoscopy products of various specifications and models with attached digital cameras to it that are capable of videography also.

4.1.2. Laser Doppler imaging

In LDI, laser light is used to illuminate the tissue section and the backscattered as well as reflected light is collected to image any moving object within the tissue section. With this technique blood flow through superficial skin layer can be calculated based on the Doppler shift introduced by moving blood cells [47, 48]. It is useful in measuring blood perfusion unit [48], which can be applied in extracting useful functional information to assess angiogenesis and endothelial functioning during wound healing [49].

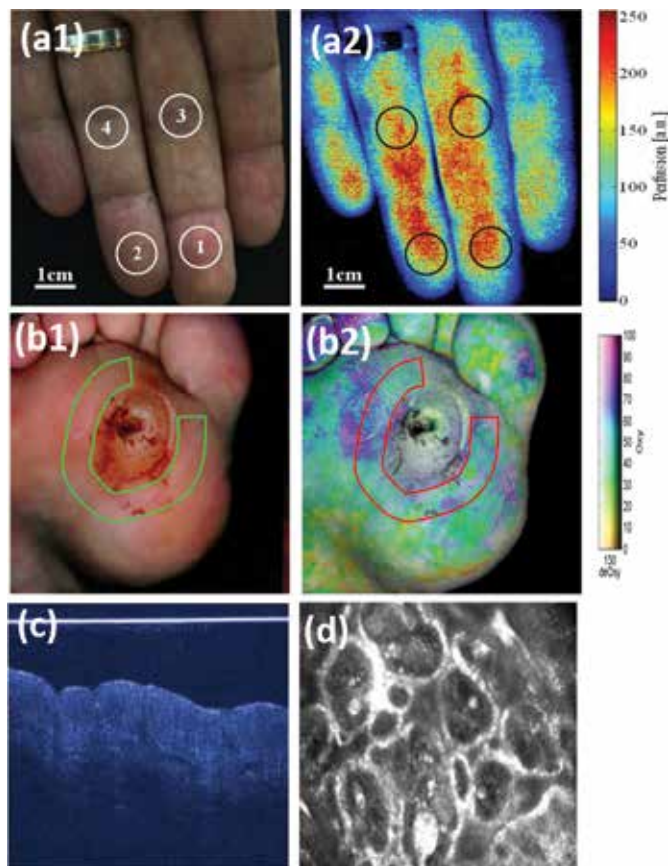


Figure 2. (a1) Visible color image of fingertips and (a2) color-coded blood perfusion map [51]. (b1) Visible and (b2) hyperspectral image of a healing diabetic foot ulcer taken with the HTOM system. HTOM values are 60, 53, and 53% for oxy, deoxy, and StO₂, respectively [57]. (c) OCT signals using a super luminescent NIR diode [25] and (d) reflectance confocal microscopy image at wavelength 830 nm of a human nevus detected by VivaScope [25].

LDI is a low-cost, easy to use noninvasive imaging modality compatible with classical medical instrumentation, where discomfort and risk to patients are minimal. A typical LDI system has a resolution of about 2 mm × 2 mm with an average imaging depth of 200–240 μm [50, 51]. **Figure 2(a1)** and **(a2)** depicts a representative comparison of visible **(a1)** and color-coded blood

perfusion map (**a2**) [51]. LDI has been reported to be used in imaging microcirculation in burned skin and monitoring blood flow recovery in a skin flap during reconstructive surgery demonstrating its potential for clinical wound assessment applications [47]. There are several other reports of burn wound depth and healing assessment with LDIs in clinical and research settings both on human and animals [50, 52, 53].

Commercial instruments based on the principle of LDI are made available by company such as Moor Instruments for skin perfusion assessments. The moorLDI2-IR laser Doppler blood flow imager can image an area up to 50 cm × 50 cm in one scan in less than 5 minutes. Due to the large area scanning possibility, this method has been very useful in burn wound depth and healing assessment based on angiogenesis.

The main disadvantage of this technique is its limited application only in observation of blood flow, similar to that of laser spackle imaging. It is unable to provide any other functional as well as structural information of skin integrities. The poor resolution in millimeter range is another major limitation of this technique in comparison with other optical techniques. Additionally, the use of visible light illumination in LDI limits its applicability in deep dermal wound assessments.

4.1.3. Tissue spectral imaging

Tissue spectral imaging (TSI) is a technique where a tissue of interest is illuminated by a broadband light and collects the reflected or diffused light through selective narrowband filters in front of the detection unit. This technique thus yields several images of specific wavelengths on the same area, providing quantitative measures of the absorbers or scatterers present [54]. Skin has several chromophores such as hemoglobin, melanin, collagen, and other biomolecules which absorb or scatter light and are responsible for skin physiology.

Diffused multispectral imaging (DMSI) is a type of TSI in which the diffused light through a tissue section was collected with a narrow band-pass filter in front of the detection unit. Based on peak absorption, specific wavelengths were chosen to reconstruct an image that can provide physiological information. It is a widely used technique in imaging hemoglobin as it can discriminate oxygenated and deoxygenated hemoglobin by their spectral signature [28]. Most of the DMSI uses NRI wavelength (700–1,100 nm) for quantitative spectroscopic analysis of structural and chemical integrity of cutaneous tissue, especially oxygen saturation, hemoglobin content, and water content. Careful assessment of the absorption spectra can be applied to monitor the wound severity and healing. Reports at preclinical setting have demonstrated the potential of this technique in differentiating superficial-, intermediate-, deep-, and full-thickness burn wounds based on measurement of water content, oxygen saturation, and total hemoglobin concentration [55, 56]. It has also been found useful in diabetic ulcer assessment and predicting diabetic wound healing as well as differentiating diabetic wounds from nondiabetic wounds [37, 38].

Hyperspectral imaging (HSI) is an effective technique that can capture and map detailed spectroscopic information for every pixel in an image. A single pixel in a hyperspectral image provides information in two-spatial dimension and one spectral dimension creating a 3D data

cube [30]. HSI has been reported to be used in diagnosing diabetic foot ulcers [57, 58] and burn wound edemas [59] where cutaneous tissue oxygenation is observed by assessing oxy- and deoxy-hemoglobin as spectroscopic contrasts. Based on HSI of hemoglobin oxygenation in wound site and areas adjacent to ulcer, wound healing index has been developed [58]. HSI using broadband visible light-emitting diodes has been reported to generate tissue anatomical oxygen map that predicts the risk of diabetic foot ulceration in pre-ulceration tissue [60]. **Figure 2(b1)** and **(b2)** depicts a representative comparison of visible and hyperspectral image of a healing diabetic foot ulcer taken with the hyperspectral tissue oxygenation mapping (HTOM) system [57].

Spectrophotometric intracutaneous analysis (SIAscope) is a kind of TSI technique based on back-reflected light of wavelength within the range of 400–1000 nm. It is a portable, fast device that predicts burn wound depth by creating a quantitative map of specific chromophores [61]. TSI based on reflectance has also found to have potential in assessing hematomas on the basis of hemoglobin destruction quantification that can determine the age of hematomas in vivo [62]. This information can also be crucial in identifying the layer of skin that sustains the hematoma [63].

Orthogonal polarization spectral imaging (OPSI) uses linearly polarized light to illuminate the skin tissue and collect the emergent depolarized light scattered by the skin components through an analyzer positioned orthogonal to the plane of illumination light polarization [64]. By analyzing the depolarized light, hemoglobin in microcirculation can be visualized to quantify the microvasculature during cutaneous wound healing [65–68].

Thermographic spectroscopy is a spectroscopic imaging technique based on the principle that all the objects including the skin have a heat signature that radiates in IR wavelength. This emission can be detected by using appropriate detector and construct color-coded images that correlate the relative temperature of the specific skin area [69–71]. Usually superficial burn wounds are warmer than uninjured skin due to increased inflammatory processes while deeper burns are cooler than uninjured skin due to structural damage to the vasculature. By using this basic principle, burn wound depth and healing progress over time can be predicted [71, 72].

A number of modalities of TSI have been commercialized by companies such as HySpex and Specim's AisaFENIX. The TSI technique can provide better resolution than LDI, typically up to 0.4–1 μm . Being a wide-field imaging technique, TSI is unable to provide a detailed 2D sectioned image with better resolution; rather it only can provide a molecular map in a certain area. It also suffers from scattering blur and diffraction limitations and has low penetration depth. Additionally, to gather a meaningful spectral information, it requires enough photon information which makes it a relatively slow method. Even with these limitations, this technique holds potential for functional imaging of blood clotting, blood flow during wound inflammation phase, and angiogenesis during superficial skin wounds. Recent advancements in computational methodologies have shown great promises in real-time quantitative functional imaging with improved resolution [54].

4.1.4. *Optical coherence tomography (OCT)*

OCT is a technique that captures 3D images of a tissue. OCT uses reflected light from tissue to construct cross-sectional images from deeper part of the skin. Most common OCTs use IR illumination, which after scattering from tissue is superimposed with a reference light to generate an interferometric pattern that provides high-resolution 3D depth information by scanning the tissue section in all directions [73–76].

OCT has been an established imaging modality in medical diagnosis and research field. Although it is most popularly used in ophthalmology [77], it has also gripped its root in dermatology [78] study such as keratosis [79], skin cancers [80], skin fibrosis [81], and wound healing. Other than that, it has also been reported to be used in other dermatological problems such as inflammatory diseases and parasitic infection and those of the nails [75, 76]. Recent advancement in OCT allows use of polarized light to image extracellular matrix and other connective tissues in the skin layer that are polarization sensitive [82, 83]. Reports also suggest use of phase-resolved OCT for imaging blood flow in the skin [84]. There are a few excellent reviews that have listed and discussed various applicable possibilities for OCT in dermatology [83, 85, 86].

In diagnosis of wound healing, there are reports of comparing healing assessment of acute wound [87] and superficial wound caused by bacterial infection on mice by OCT to histological findings [88]. A study had reported quantitative evaluation of healing kinetics at real time after fractional laser therapy by OCT demonstrating excellent correlation with findings from histopathological observations [89]. In an *in vivo* study, OCT has effectively evaluated the various stages of wound healing in 12-day long healing process recognized by re-epithelialization in the early stage, followed by thickening of the epithelial layer around 10th day and formation of scar tissue composed of extracellular matrix along with thickening of epidermal layer in the final stage [90].

OCT's most promising advantage is its ability of axial sectioning and 3D imaging of a tissue mass. OCT techniques using IR light sources are suitable imaging modalities for deep tissue topographical imaging of skin disfigurement. Although the resolution of OCT is lower compared to CLSM or 2PFM or SHG microscopy, the associated resolution degradation with depth is much smaller. OCT cannot produce images at cellular or fibrous molecular resolution; hence it is incapable of imaging a single-cell structure or fibrous collagen structure in the skin dermis [30]. However, in comparison to other macro-optical methodologies, OCT exhibits better resolution. In fact, with sophisticated design, OCT can also achieve a resolution of few tens of micrometer. OCT was also reported to provide even more detailed structural information of a larger mass of tissue than 2PFM at depth of 2–3 mm while imaging thermally injured wounds [91]. OCT is a useful noninvasive technique that has huge potential for wound healing research and assessment. **Figure 2(c)** represents a typical OCT image [25].

OCT has been commercialized by companies such as Optovue, NinePoint Medical, and Thorlabs; two such models from Thorlabs are Ganymede II IR-OCT system and Telesto series spectral domain OCT systems. These systems are mainly operated in IR domain with line scan rate within the range of 5.5–76 KHz.

4.2. Micro-optical modalities

4.2.1. Raman spectro-microscopy

Microscopic imaging based on Raman vibrational spectroscopic contrast provides a useful noninvasive approach for visualizing skin tissues and the corresponding architecture with molecular specificity. A typical Raman microscope detects vibrational scattering changes introduced by the Raman-active molecules in tissue. Molecules rich in CH₂ bonds, such as protein and lipid, are good Raman contrast agents and can be interpreted to visualize structural changes occurring in different skin strata [92–94]. An automated Raman micro-spectrometer in confocal settings was reported to be used to determine water concentrations in hydrated and non-hydrated stratum corneum, showing the capacity of this method [95]. However, spontaneous Raman signal is very weak. The Raman detection can be significantly enhanced by CARS. It can visualize structural fibers such as collagen and elastin that constitutes the human dermis along with subcutaneous layer rich in lipids, due to the high density of CH₂ bonds [96–98]. CARS microscopy is the method of choice for studies that require visualization of fat in tissues, which can very effectively characterize obesity in murine skin *in vivo* [99]. While imaging superficial tissue layers, CARS can provide strong signal from the fat component of the skin that allow video-rate imaging.

Video-rate CARS imaging can be used for imaging lipid lamellae of the stratum corneum, sebaceous glands, and dermal adipocytes, and the fat-containing cells of the subcutaneous layer with imaging depths of up to several hundred micrometers, promising a potential methodology for noninvasive molecular imaging [97]. Recently CARS has also been used in studying transdermal delivery of retinol in mouse ear, a drug with strong CARS signal that stimulates collagen growth in skin and was located in corneocytes of stratum corneum [100].

König and his group have reported a CARS tomography system for skin imaging suitable for clinical environments that is capable of *in vivo* histology with subcellular resolution and chemical contrast toward patients suffering from psoriasis and squamous cell carcinoma [101]. Their system also has the potential to be used in studying skin wound healing. Although Raman imaging in the form of CARS can provide high-contrast functional imaging with subcellular resolution, it is, however, mostly limited to Raman-active molecules only. In comparison, the Raman scattering cross section is very small which translates to very weak signal intensities, thus requiring very high density of molecules or very long acquisition times in order to acquire a meaningful image.

4.2.2. Laser scanning microscopy techniques:

A commonly used wide-field microscope provides a two-dimensional image, typically in histological observations of biopsies. However it has several drawbacks, including low resolution, low penetration depth, slow imaging rate, and inability to have functional imaging. It delivers poorer image contrast and lacks optical sectioning capability. In contrast, a laser scanning microscope (LSM) provides a few numbers of platforms for imaging that are improved with respect to all aspects mentioned above. Among them confocal microscopy in linear domain and two-photon fluorescence microscopy (2PFM) and SHG in nonlinear domain

are most prominent. Confocal laser scanning microscopy (CLSM) has several advantages over traditional microscopy, including faster data acquisition, optical sectioning of cells and tissues for 3D imaging, and significantly improved spatial resolution [39, 102, 103]. The pioneering work of Minsky, in the year 1957, initiated the development and the first commercialized CLSM was realized in 1987 [104]. However, CLSM has a relatively lower penetration depth compared to MPM, due to the shorter wavelength used. Single-photon confocal microscopy obtains an image section at the expense of photon efficiency, attributing to the spatial filtering pinhole [39, 105, 106]. The overexposure would cause photo bleaching of the sample. As a result, only highly photostable fluorophores work well with this technique. In comparison, MPM uses IR excitation which reduces photo bleaching in a confined way and allows imaging depths of up to ~ 2 mm. The nonlinear effect forms a virtual pinhole and saves the trouble of precision alignment needed for a physical pinhole [39, 106].

4.2.2.1. Reflectance confocal laser scanning microscopy (RCLSM)

In RCLSM, a pinhole at the confocal image plane eliminates out-of-focus signal to realize optical sectioning for 3D imaging. It uses a focused laser beam for excitation and forms the image by point to point scanning, usually by a pair of computer-controlled galvano mirrors [32, 33]. The reflected light signal is collected by a photo detector after the pinhole. The reflected signal is de-scanned by the same pair of galvano mirrors so the alignment of pinhole is straightforward [107]. The configuration is widely used in commercially available confocal microscopes for skin imaging [33, 107]. It has also been used for assessing and monitoring cutaneous wound healing by evaluating the cellular and morphological parameters of wound bed and wound margins noninvasively over the course of healing [102]. In the reported study, patients with chronic leg ulcers and skin cancers receiving split skin graft were evaluated against healthy individuals, in which various physiological signatures of wound healings at different phases were documented. For example, appearance of inflammatory cells in the epidermis during the early stage of wound healing, proliferative keratinocytes and their migration during granulation and re-epithelialization phases, and the networks of connective tissues during remodeling phases were observed with reflectance CLSM [102].

A commercially available CLSM in reflectance mode is VivaScope®1500 that has planar and axial resolution of 1.25 and 5.0 μm , respectively, with an imaging depth up to 200 μm . Its image acquisition speed of 9 frames per second allows real-time videography of wound healing. **Figure 2(d)** represents a reflectance confocal microscopy image by detecting backscattered 830 nm light from a human nevus with the system [25].

Although these instruments are widely used, they are limited to surface imaging only. Therefore, they are not suitable for evaluating deep dermal wounds. Nevertheless, they can image wound margins, which may provide crucial semiquantitative information regarding wound healing with a resolution comparable to that of histological analysis [30]. The reflection contrast-based CLSM is frequently used for structural imaging but is incapable of molecular functional imaging. A typical CLSM has much improved resolution and faster scanning rate than OCT. However, it may be limited by photo bleaching and diffraction blurring when compared to multiphoton techniques.

4.2.2.2. Confocal fluorescence microscopy

Confocal fluorescence microscopy is a technique that allows imaging of living tissue by collecting fluorescence emission from the chromophores present in the tissue. In single-photon fluorescence imaging, a fluorophore absorbs a single photon to be excited into a higher energy state before emitting the fluorescence, and comes down to original lower energy state. The simplest fluorescence imaging instrumentation uses a laser to illuminate the skin at a specific excitation wavelength and collects the filtered fluorescence emission with a detector bearing an optical filter in front of it.

Fluorescence imaging can be done with either staining the tissue by exogenous fluorescent materials or imaging endogenous fluorescence from skin's natural fluorophores. Indocyanine green (ICG) is one commonly used exogenous fluorescence dye that can be located in systemic circulation, which allows the imaging of vascularization and the determination of imaging depth [108]. This technique has been shown to quantitatively measure blood flow in the cutaneous wound that is well correlated with the histological assessment of burn depth [108]. As mentioned in Section 2, endogenous fluorophores, NADH, FAD, and collagen are all important markers in wound healing processes that can be used for wound diagnosis [36, 109].

Along with NADH and FAD, collagen is another abundant molecule present in the skin dermis that is autofluorescing. It can serve as a marker upon exposure to the 325 nm He-Cd laser treatment ($\sim 2 \text{ J/cm}^2$) during skin tissue regeneration, as shown in mouse model by detecting the collagen autofluorescence intensity [110]. In another comparative ex vivo and in vivo study of wound granulation by the same group, normalized NADH/collagen autofluorescence intensity was used to assess collagen deposition during healing [111].

Confocal fluorescence microscopy can provide real-time functional imaging of cells and tissues with improved resolutions. However single-photon imaging may be limited by photo bleaching and low penetration depth. Alternatively, MPF imaging would improve photo stability with deeper penetration.

4.2.2.3. Multiphoton microscopy (MPM)

In multiphoton imaging a simple confocal laser scanning microscope is used with an ultrafast NIR laser source. The pinhole is usually removed and the detection unit is modified with specialized filters. Multiphoton laser technique greatly improves resolution and penetration depth than macro-optical modalities. Its optical sectioning ability does not require a pinhole, which reduces alignment difficulty and the volume of photo bleaching. Additionally, the NIR excitation wavelengths are shown to extend the limit of deep tissue imaging up to 2 mm.

In tissue imaging, commonly used multiphoton techniques are 2PFM and SHG imaging. In 2PFM, the fluorophores absorb two photons simultaneously to be excited to a higher energy real state before emitting the fluorescence, while in SHG, the two photons of the same energy would combine to form a new photon of twice the energy of the incident photon. Biomolecules such as collagen and muscle myosin with noncentrosymmetric molecular structures have the ability to generate SHG signal [8, 112–114]. Skin can be imaged with both fluorescence and SHG contrasts simultaneously with the help of a laser scanning MPM [36, 115]. Zoumie et al.

in their study of a tissue model have described spectrally resolved imaging of different parts of the skin layers by a combined 2PFM and SHG setup [115]. They detected fluorescence from cellular NADH and SHG from collagen. The study of wound healing with fluorescence and SHG is discussed in the following paragraphs.

Cellular NADH autofluorescence in two-photon modality has been used as marker for morphological characterization of epithelia both in vivo [116–118] and ex vivo [119] for animal and human tissues as well as fresh biopsies [120]. It enables optical microscopic imaging being equivalent to histochemical analysis. With the help of 2PFM imaging, various epidermal layers of in vivo skin were discriminated at subcellular spatial resolution based on cellular morphological features [31]. Additionally, the time-correlated single-photon counting technique in conjunction with 2PFM has made functional imaging possible by measuring the lifetime of fluorophores. This technique, termed as fluorescence lifetime imaging (FLIM), is very effective in determining real-time cellular metabolic activity in vivo by measuring the fluorescence lifetime decay of NADH. Cells located in the basal layer exhibit the strongest metabolic activities, while epidermal surface layered cells are found to have lower metabolic activities. FLIM has demonstrated its capacity in characterizing epithelial tissue involved in wound healing and other pathological conditions [31].

NADH, being a metabolic coenzyme, is associated with the cellular metabolic activities through the electron transport chain (ETC) of oxidative phosphorylation. NADH has two functional forms, free and bound. During the process of energy generation, free NADH is bound to mitochondrial membrane proteins [36]. Although the fluorescence emission spectra of both free and bound forms of NADH fall in a very narrow band, their fluorescence lifetimes are well separated. When NADH binds to a protein, its lifetime increases from ~0.4 to ~2.5 ns [121–123]. Therefore by evaluating the contribution of free and bound states to the combined double exponential lifetime, the relative concentrations of individual states can be predicted. In simple words, a cell with higher metabolic activity has a higher concentration of bound NADH than a cell with lower metabolic activity. In addition to that the ratio of bound form NADH to bound form of FAD, termed as cellular redox ratio, can also be a marker for relative metabolic activity determination [124].

The cellular metabolic parameters are viable markers for evaluating wound healing. We have demonstrated on live rat models that the cellular metabolic rate correlates well with wound healing phases [36]. In the study, artificially created incisional wound by punch biopsy was used to evaluate the wound healing from the day of wound formation to scar formation in a 20-day healing course with 2PFM and SHG microscopy. The relative metabolic activities of cells involved in the process of wound healing as time progresses were evaluated by the NADH bound to free ratio, while the changes in collagen concentration are correlated with SHG intensity. These findings suggest the metabolic activities at the wounded sites increase during inflammatory and granulation phases and gradually decrease as wound heals (**Figure 3(b)**). Interestingly, in the beginning of healing, SHG intensity decreases (or collagen concentration), indicating the degradation of collagen in the dermal layer during cell migration. Once new collagens were formed, SHG signal started to increase gradually (**Figure 3(c)**). In general, wounds heal gradually from the edge toward the center; hence the metabolic activities are

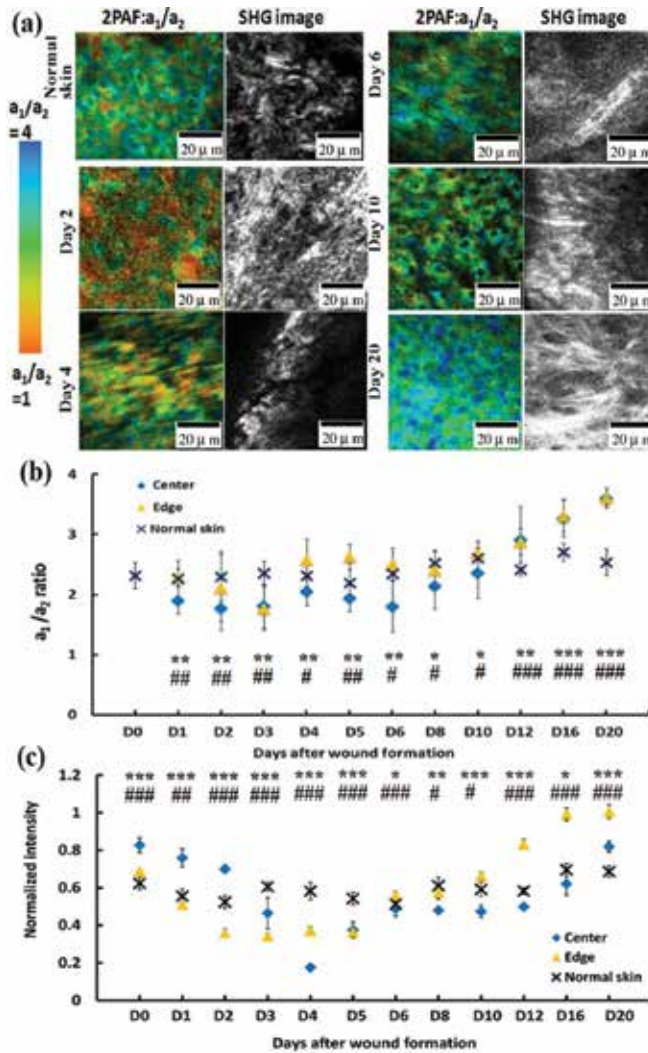


Figure 3. (a) Representative color-coded NADH free/bound (a_1/a_2) lifetime ratio images (left column) and gray-scale SHG intensity images (right column) of collagen regeneration during wound healing [132]. (b) Scatter plot of NADH a_1/a_2 distribution peak value with healing progress both at the center and edge, averaged over 15 wounds at each day of wound observation. The ratio NADH a_1/a_2 is inversely proportional to metabolic activity of cells. Two-side Student's *t*-test evaluated significant differences of NADH a_1/a_2 values at the center from normal skin that are indicated by *, $P > 0.05$; **, $0.05 > P > 0.001$; and ***, $P < 0.001$. The significant differences of a_1/a_2 values at the edge from the normal skin are designated as #, $P > 0.05$; ##, $0.05 > P > 0.001$; and ###, $P < 0.001$ [132]. (c) Scatter plot of normalized SHG intensity with respect to the maximum intensity observed at the edge on day 20. The changes in SHG intensity elucidate the relative degradation and regeneration of collagen at the center and the edge in the course of wound healing. Two-side Student's *t*-test evaluated significant differences of SHG intensity at center from normal skin that are indicated by *, $P > 0.05$; **, $0.05 > P > 0.001$; and ***, $P < 0.001$ for center. The significant differences of SHG intensity values at edge from normal skin are designated as #, $P > 0.05$; ##, $0.05 > P > 0.001$; and ###, $P < 0.001$. *P* value less than 0.05 was considered significant [132].

higher at the edge in the early stages of wound healing, marked by the higher bound to free NADH ratio in lifetime measurement. However, in the proliferative phase the center has higher metabolic activity than the edge since the edge has entered the remodeling phase, in which cell activity decreases and collagen is deposited to fill the wound gap, marked by the increase of SHG intensity. Following the proliferative phase, the whole wound is filled with granulation tissues, mainly collagen, and the cellular metabolism decreases gradually. The wound then heals into a scar, composed of connective tissues marked with higher SHG signal intensity than that from a normal tissue. The lack of cells in scar tissue reduces the need for blood influx, which results in removal of blood vessels by apoptosis and leaves a scar tissue characterized by lower metabolic activity and higher collagen deposition.

The changes of the NADH free to bound ratio (**Figure 3(b)**) and the collagen SHG intensity (**Figure 3(c)**) exhibit as the signature of the various phases in wound healing, which can be used for crucial diagnosis and proper treatment. With the simultaneous measurements of 2PFM and SHG, a correlation between cellular metabolic activities and collagen regeneration can be observed. In **Figure 3(a)**, the morphological features of cells and their gradual appearance in wound region and structural evolution of collagen in a healing wound, acquired by 2PFM and SHG, respectively, are demonstrated. The disordered collagen in normal skin is degraded and more structured collagens are deposited in the process of scar formation as shown in **Figure 3(a)**.

Similar results have also been reproduced by other researchers using combined SHG and 2PFM imaging, where disorganized collagen in fibrin clots and inflammatory cells involved during the early stage of wound healing are distinguished from more organized and aligned collagens in regenerated new skin [125].

SHG is also used in showing the orientation of collagen fibers and their structural changes in the healthy tissues of human dermis [126–129] as well as in *in vivo* tissue constructs [130]. The efficiency of SHG signal is highly sensitive to the collagen orientation when the incident light is polarized. Along with intensity measurements, polarization-resolved SHG provides information on collagen alignment and orientation during regeneration, which is correlated to wound closure and the way scar tissue forms [131].

Polarization-resolved SHG indicates that collagens are more organized and fibrillary during the proliferative phase, to aid in wound closure when the margins are pulled together by them [132]. In this way, the anisotropic variation of collagen during wound healing can be monitored by collecting the parallel (I_{par}) and the perpendicular (I_{perp}) components of the polarized SHG signals with respect to the incident polarization. **Figure 4** demonstrates representative I_{par} (first row) and I_{perp} (second row) polarization-resolved SHG intensity images from biopsy samples taken after discrete days of wound formation along with corresponding anisotropy images (third row) defined by $(I_{par} - I_{perp}) / (I_{par} + 2I_{perp})$. Anisotropy value equal to 0 corresponds to complete random arrangement of the scatterers, and if it is equal to 1, it corresponds to having a well-aligned, well-structured scattered system [132, 133]. Anisotropic observation of *ex vivo* rat skin biopsies has revealed maximum anisotropy value of collagen during wound contraction and closure. When the wound gap is filled with matured collagen, the anisotropy decreases gradually [132].

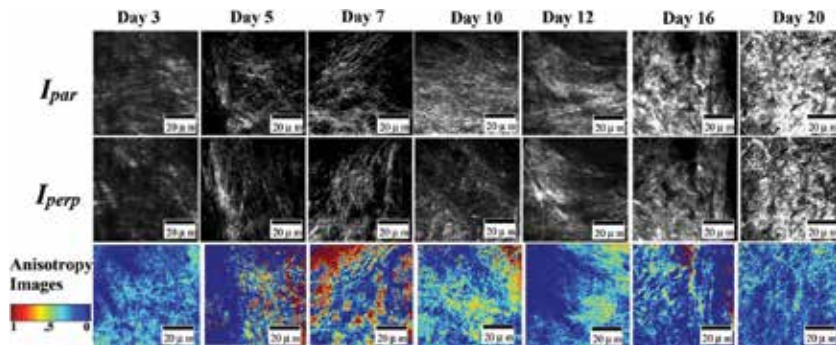


Figure 4. Representative polarization-resolved SHG intensity images of wound biopsy samples taken at different healing stages. The first row depicts the images with the parallel (I_{par}) component. The second row depicts the images with the perpendicular (I_{perp}) component. The third row depicts the corresponding anisotropy images defined by $(I_{par} - I_{perp}) / (I_{par} + 2I_{perp})$ [132].

In clinical setting, multiphoton imaging of human epidermis and upper dermis has been achieved by commercial system such as DermaInspect™ that is able to scan an area of $350 \mu\text{m} \times 350 \mu\text{m}$ with special resolution of $1 \mu\text{m}$ in lateral and $2 \mu\text{m}$ in axial directions [25]. The system provide non-invasive in vivo optical biopsies of skin at subcellular resolution by detecting autofluorescence from biomolecules such as NADH, flavins, porphyrins, elastin and melanin and SHG signals from collagens.

5. Conclusion

Wound healing is an important physiological process that follows a certain sequential order. Migration of various cells and the involvement of certain molecules at the wound site characterize the various phases during healing progression. Detailed quantitative and qualitative information of these components at a specific time provides critical insights on wound healing. Optical methodologies are versatile and include techniques that can gather a wide variety of information on multiple components noninvasively, which presents tremendous future prospects in terms of clinical implications. The available modalities present enormous potentials to supplement clinical assessment and to aid research in the field of cutaneous healing and skin tissue regeneration.

The versatile optical modalities discussed in this chapter have their own significance in assessing specific wound-related problems. Some modalities are simple and easy to operate, which provide relatively low-cost first-line diagnosis. More complex techniques can provide better resolution and sophisticated structural information. By judiciously combining various contrasts from the skin components, these optical techniques can address a wide variety of skin wound-related issues. These can include observations of subsurface morphological features using dermoscope, blood flow using LDI, molecular and functional signatures using TSI, structural revelation using OCT, RCLM and SHG microscopy, or molecular identification with Raman and fluorescence imaging. Each technique would provide unique yet complementary information.

Multimodal MPM presents the most sophisticated approach for quick, qualitative, and quantitative skin wound healing study as it integrates multiple contrast mechanisms for imaging the skin. Specifically, 2PFM and SHG are favorable in wound assessment for their high-resolution, better penetration depth, optically sectioned 3D imaging with the provision of structural and real-time molecular functional signature.

Emerging super resolution imaging based on saturation excitation (SAX) of scattering from metallic nanoparticles may extend the possibilities of super resolving the skin abnormalities [134]. Ointments and sunscreen lotion could effectively carry the nanoparticles into skin epidermis to facilitate the new optical techniques. With the ongoing rapid advancements in photonics and imaging, one can expect new and novel techniques will find unprecedented and enlightening applications in dermatology in the coming future.

Author details

Gitanjal Deka^{1*}, Shi-Wei Chu¹ and Fu-Jen Kao²

*Address all correspondence to: gitanjal@yahoo.com

¹ Department of Physics, National Taiwan University, Taipei, Taiwan

² Institute of Biophotonics, National Yang Ming University, Taipei, Taiwan

References

- [1] H. Brem, and M. Tomic-Canic, "Cellular and molecular basis of wound healing in diabetes," *J. Clin. Invest.* 117, 1219-1222 (2007).
- [2] M. Peck, J. Molnar, and D. Swart, "A global plan for burn prevention and care," *Bull. World. Health. Organ.* 87, 802-803 (2009).
- [3] P. Martin, "Wound healing--aiming for perfect skin regeneration," *Science* 276, 75-81 (1997).
- [4] S. E. Gardner et al., "A tool to assess clinical signs and symptoms of localized infection in chronic wounds: development and reliability," *Ostomy. Wound Manag.* 47, 40-47 (2001).
- [5] G. Dow et al., "Infection in chronic wounds: controversies in diagnosis and treatment," *Ostomy. Wound Manag.* 45, 23-40 (1999).
- [6] T. Y. Buryakina, P.-T. Su, W.-J. Syu, C. A. Chang, H.-F. Fan, and F.-J. Kao, "Metabolism of HeLa cells revealed through autofluorescence lifetime upon infection with enterohemorrhagic *Escherichia coli*" *J. Biomed. Opt.* 17, 101503 (2012).

- [7] B. Banerjee, T. Renkoski, L. R. Graves, N. S. Rial, V. L. Tsikitis, V. Nfonsam, J. Pugh, P. Tiwari, H. Gavini, and U. Utzinger, "Tryptophan autofluorescence imaging of neoplasms of the human colon," *J. Biomed. Opt.* 17, 016003 (2012).
- [8] W. R. Zipfel, R. M. Williams, R. Christie, A. Y. Nikitin, B. T. Hyman, and W. W. Webb, "Live tissue intrinsic emission microscopy using multiphoton-excited native fluorescence and second harmonic generation," *Proc. Natl. Acad. Sci. U. S. A.* 100, 7075-7080 (2003).
- [9] X. Jiang, J. Zhong, Y. Liu, H. Yu, S. Zhuo, and J. Chen, "Two-photon fluorescence and second-harmonic generation imaging of collagen in human tissue based on multiphoton microscopy," *Scanning* 33, 53-56 (2011).
- [10] W. Denk, J. H. Strickler, and W. W. Webb, "Two-photon laser scanning fluorescence microscopy," *Science* 248, 73-76 (1990).
- [11] P. T. So, C. Y. Dong, B. R. Masters, and K. M. Berland, "Two-photon excitation fluorescence microscopy," *Annu. Rev. Biomed. Eng.* 2, 399-429 (2000).
- [12] Y. Lee, and K. Hwang, "Skin thickness of Korean adults," *Surg. Radiol. Anat.* 24, 183-189 (2002).
- [13] L. A. Baden, "Surgical Anatomy of the Skin," *Arch. Dermatol.* 125, 719-719 (1989).
- [14] G. C. Troy, "An overview of hemostasis," *Vet. Clin. North Am. Small Anim. Pract.* 18, 5-20 (1988).
- [15] T. A. Springer, "Biology and physics of von Willebrand factor concatamers," *J. Thromb. Haemost.* 9, 130-143 (2011).
- [16] H. P. Lorenz, and M. T. Longaker, "Wounds: biology, pathology, and management," in *Essential Practice of Surgery* (Springer, 2003), pp. 77-88.
- [17] F. H. Epstein, A. J. Singer, and R. A. Clark, "Cutaneous wound healing," *N. Engl. J. Med.* 341, 738-746 (1999).
- [18] S. A. Eming, T. Krieg, and J. M. Davidson, "Inflammation in wound repair: molecular and cellular mechanisms," *J. Invest. Dermatol.* 127, 514-525 (2007).
- [19] K. S. Midwood, L. V. Williams, and J. E. Schwarzbauer, "Tissue repair and the dynamics of the extracellular matrix," *Int. J. Biochem. Cell Biol.* 36, 1031-1037 (2004).
- [20] R. F. Diegelmann, and M. C. Evans, "Wound healing: an overview of acute, fibrotic and delayed healing," *Front. Biosci.* 9, 283-289 (2004).
- [21] D. G. Greenhalgh, "The role of apoptosis in wound healing," *Int. J. Biochem. Cell Biol.* 30, 1019-1030 (1998).
- [22] R. O'leary, E. Wood, and P. Guillou, "Pathological scarring: strategic interventions," *Eur. J. Surg.* 168, 523-534 (2002).

- [23] A. Desmoulière, C. Chaponnier, and G. Gabbiani, "Tissue repair, contraction, and the myofibroblast," *Wound. Repair. Regen.* 13, 7-12 (2005).
- [24] T.-L. Tuan, and L. S. Nichter, "The molecular basis of keloid and hypertrophic scar formation," *Mol. Med. Today.* 4, 19-24 (1998).
- [25] K. König, "Clinical multiphoton tomography," *J. Biophotonics* 1, 13-23 (2008).
- [26] L. Brentano, and D. L. Gravens, "A method for the quantitation of bacteria in burn wounds," *J. Appl. Microbiol.* 15, 670 (1967).
- [27] N. S. Levine, R. B. Lindberg, A. D. Mason JR, and B. A. Pruitt JR, "The quantitative swab culture and smear: A quick, simple method for determining the number of viable aerobic bacteria on open wounds," *J. Trauma. Acute. Care. Surg.* 16, 89-94 (1976).
- [28] B. Dasgeb, J. Kainerstorfer, D. Mehregan, A. Van Vreede, and A. Gandjbakhche, "An introduction to primary skin imaging," *Int. J. Dermatol.* 52, 1319-1330 (2013).
- [29] D. W. Paul, P. Ghassemi, J. C. Ramella-Roman, N. J. Prindeze, L. T. Moffatt, A. Alkhalil, and J. W. Shupp, "Noninvasive imaging technologies for cutaneous wound assessment: a review," *Wound. Repair. Regen.* 23, 149-162 (2015).
- [30] H. Albert, "A survey of optical imaging techniques for assessing wound healing," *Int. J. Intell. Control Syst.* 17, 79-85 (2012).
- [31] R. Cicchi, D. Kapsokalyvas, and F. S. Pavone, "Clinical nonlinear laser imaging of human skin: a review," *BioMed Res. Int.* 2014, 903589 (2014).
- [32] S. Paddock, T. Fellers, and M. Davidson, *Confocal Microscopy*, Humana Press, Springer, New York (2001).
- [33] M. Rajadhyaksha, S. González, J. M. Zavislan, R. R. Anderson, and R. H. Webb, "In vivo confocal scanning laser microscopy of human skin II: advances in instrumentation and comparison with histology," *J. Invest. Dermatol.* 113, 293-303 (1999).
- [34] J. Fredrich, "3D imaging of porous media using laser scanning confocal microscopy with application to microscale transport processes," *Phys. Chem. Earth. Pt. A* 24, 551-561 (1999).
- [35] J. Lawrence, D. Korber, B. Hoyle, J. Costerton, and D. Caldwell, "Optical sectioning of microbial biofilms," *J. Bacteriol.* 173, 6558-6567 (1991).
- [36] G. Deka, W.-W. Wu, and F.-J. Kao, "In vivo wound healing diagnosis with second harmonic and fluorescence lifetime imaging," *J. Biomed. Opt.* 18, 061222 (2013).
- [37] M. S. Weingarten, E. Papazoglou, L. Zubkov, L. Zhu, G. Vorona, and A. Walchack, "Measurement of optical properties to quantify healing of chronic diabetic wounds," *Wound. Repair. Regen.* 14, 364-370 (2006).

- [38] E. S. Papazoglou, L. Zubkov, L. Zhu, M. S. Weingarten, S. Tyagi, and K. Pourrezaei, "Monitoring diabetic wound healing by NIR spectroscopy," in *Conf. Proc. IEEE. Eng. Med. Biol. Soc. (IEEE, 2005) Shanghai, China*, pp. 6662-6664.
- [39] A. Diaspro, *Confocal and Two-photon Microscopy: Foundations, Applications and Advances*, Wiley-VCH; New York, (2001).
- [40] E. Ruocco, G. Argenziano, G. Pellacani, and S. Seidenari, "Noninvasive imaging of skin tumors," *Dermatol. Surg.* 30, 301-310 (2004).
- [41] G. Micali, F. Lacarrubba, D. Massimino, and R. A. Schwartz, "Dermatoscopy: alternative uses in daily clinical practice," *J. Am. Acad. Dermatol.* 64, 1135-1146 (2011).
- [42] S. Inui, T. Nakajima, and S. Itami, "Significance of dermoscopy in acute diffuse and total alopecia of the female scalp: review of twenty cases," *Dermatology* 217, 333-336 (2008).
- [43] M. Wu, S. Hu, and C. Hsu, "Use of non-contact dermoscopy in the diagnosis of scabies," *Dermatol. Sinica.* 26, 112-114 (2008).
- [44] E.-M. De Villiers, C. Fauquet, T. R. Broker, H.-U. Bernard, and H. zur Hausen, "Classification of papillomaviruses," *Virology* 324, 17-27 (2004).
- [45] G. Argenziano, H. P. Soyer, S. Chimenti, R. Talamini, R. Corona, F. Sera, M. Binder, L. Cerroni, G. De Rosa, and G. Ferrara, "Dermoscopy of pigmented skin lesions: results of a consensus meeting via the Internet," *J. Am. Acad. Dermatol.* 48, 679-693 (2003).
- [46] G. Pagnanelli, H. Soyer, G. Argenziano, R. Talamini, R. Barbati, L. Bianchi, E. Campione, I. Carboni, A. Carrozzo, and M. Chimenti, "Diagnosis of pigmented skin lesions by dermoscopy: web-based training improves diagnostic performance of non-experts," *Br. J. Dermatol.* 148, 698-702 (2003).
- [47] M. Leutenegger, E. Martin-Williams, P. Harbi, T. Thacher, W. Raffoul, M. André, A. Lopez, P. Lasser, and T. Lasser, "Real-time full field laser Doppler imaging," *Biomed. Opt. Express* 2, 1470-1477 (2011).
- [48] K. Wårdell, A. Jakobsson, and G. E. Nilsson, "Laser Doppler perfusion imaging by dynamic light scattering," *IEEE Trans Bio-Med Eng* 40, 309-316 (1993).
- [49] S. Kubli, B. Waeber, A. Dalle-Ave, and F. Feihl, "Reproducibility of laser Doppler imaging of skin blood flow as a tool to assess endothelial function," *J. Cardiovasc. Pharmacol.* 36, 640-648 (2000).
- [50] Z. Niazi, T. Essex, R. Papini, D. Scott, N. McLean, and M. Black, "New laser Doppler scanner, a valuable adjunct in burn depth assessment," *Burns* 19, 485-489 (1993).
- [51] M. Leutenegger, E. Martin-Williams, P. Harbi, T. Thacher, W. Raffoul, M. André, A. Lopez, P. Lasser, and T. Lasser, "Real-time full field laser Doppler imaging," *Biomed. Opt. Express* 2, 1470-1477 (2011).

- [52] S. A. Pape, C. A. Skouras, and P. O. Byrne, "An audit of the use of laser Doppler imaging (LDI) in the assessment of burns of intermediate depth," *Burns* 27, 233-239 (2001).
- [53] E. Droog, W. Steenbergen, and F. Sjöberg, "Measurement of depth of burns by laser Doppler perfusion imaging," *Burns* 27, 561-568 (2001).
- [54] J. M. Kainerstorfer, M. Ehler, F. Amyot, M. Hassan, S. G. Demos, V. Chernomordik, C. K. Hitzengerger, A. H. Gandjbakhche, and J. D. Riley, "Principal component model of multispectral data for near real-time skin chromophore mapping," *J. Biomed. Opt.* 15, 046007 (2010).
- [55] M. G. Sowa, L. Leonardi, J. R. Payette, J. S. Fish, and H. H. Mantsch, "Near infrared spectroscopic assessment of hemodynamic changes in the early post-burn period," *Burns* 27, 241-249 (2001).
- [56] K. M. Cross, L. Leonardi, M. Gomez, J. R. Freisen, M. A. Levasseur, B. J. Schattka, M. G. Sowa, and J. S. Fish, "Noninvasive measurement of edema in partial thickness burn wounds," *J. Burn. Care. Res.* 30, 807-817 (2009).
- [57] A. Nouvong, B. Hoogwerf, E. Mohler, B. Davis, A. Tajaddini, and E. Medenilla, "Evaluation of diabetic foot ulcer healing with hyperspectral imaging of oxyhemoglobin and deoxyhemoglobin," *Diabetes care* 32, 2056-2061 (2009).
- [58] L. Khaodhiar, T. Dinh, K. T. Schomacker, S. V. Panasyuk, J. E. Freeman, R. Lew, T. Vo, A. A. Panasyuk, C. Lima, and J. M. Giurini, "The use of medical hyperspectral technology to evaluate microcirculatory changes in diabetic foot ulcers and to predict clinical outcomes," *Diabetes Care* 30, 903-910 (2007).
- [59] M. A. Calin, S. V. Parasca, R. Savastru, and D. Manea, "Characterization of burns using hyperspectral imaging technique – a preliminary study," *Burns* 41, 118-124 (2015).
- [60] D. Yudovsky, A. Nouvong, K. Schomacker, and L. Pilon, "Assessing diabetic foot ulcer development risk with hyperspectral tissue oximetry," *J. Biomed. Opt.* 16, 026009 (2011).
- [61] H. Tehrani, M. Moncrieff, B. Philp, and P. Dziewulski, "Spectrophotometric intracutaneous analysis: a novel imaging technique in the assessment of acute burn depth," *Ann. N Y. Acad. Sci.* 61, 437-440 (2008).
- [62] V. Hughes, P. Ellis, T. Burt, and N. Langlois, "The practical application of reflectance spectrophotometry for the demonstration of haemoglobin and its degradation in bruises," *J. Clin. Pathol.* 57, 355-359 (2004).
- [63] M. Bohnert, R. Baumgartner, and S. Pollak, "Spectrophotometric evaluation of the colour of intra-and subcutaneous bruises," *Int. J. Dermatol.* 113, 343-348 (2000).
- [64] W. Groner, J. W. Winkelman, A. G. Harris, C. Ince, G. J. Bouma, K. Messmer, and R. G. Nadeau, "Orthogonal polarization spectral imaging: a new method for study of the microcirculation," *Nat. Med.* 5, 1209-1212 (1999).

- [65] S. Langer, F. Born, R. Hatz, P. Biberthaler, and K. Messmer, "Orthogonal polarization spectral imaging versus intravital fluorescent microscopy for microvascular studies in wounds," *Ann. N Y. Acad. Sci.* 48, 646-653 (2002).
- [66] O. Goertz, A. Ring, A. Köhlinger, A. Daigeler, C. Andree, H.-U. Steinau, and S. Langer, "Orthogonal polarization spectral imaging: a tool for assessing burn depths?" *Ann. N Y. Acad. Sci.* 64, 217-221 (2010).
- [67] S. M. Milner, "Predicting early burn wound outcome using orthogonal polarization spectral imaging," *Int. J. Dermatol.* 41, 715-715 (2002).
- [68] S. M. Milner, S. Bhat, S. Gulati, G. Gherardini, C. E. Smith, and R. J. Bick, "Observations on the microcirculation of the human burn wound using orthogonal polarization spectral imaging," *Burns* 31, 316-319 (2005).
- [69] A. Renkielska, A. Nowakowski, M. Kaczmarek, and J. Ruminski, "Burn depths evaluation based on active dynamic IR thermal imaging—a preliminary study," *Burns* 32, 867-875 (2006).
- [70] N. J. Prindeze, P. Fathi, M. J. Mino, N. A. Mauskar, T. E. Travis, D. W. Paul, L. T. Moffatt, and J. W. Shupp, "Examination of the early diagnostic applicability of active dynamic thermography for burn wound depth assessment and concept analysis," *J. Burn. Care. Res.* 36, 626-635 (2015).
- [71] R. N. Lawson, G. Wlodek, and D. Webster, "Thermographic assessment of burns and frostbite," *Can. Med. Assoc. J.* 84, 1129-1131 (1961).
- [72] A. Renkielska, A. Nowakowski, M. Kaczmarek, M. K. Dobke, J. Grudziński, A. Karmolinski, and W. Stojek, "Static thermography revisited—an adjunct method for determining the depth of the burn injury," *Burns* 31, 768-775 (2005).
- [73] A. F. Fercher, "Optical coherence tomography—development, principles, applications," *Zeitschrift Med. Phys.* 20, 251-276 (2010).
- [74] D. Huang, E. A. Swanson, C. P. Lin, J. S. Schuman, W. G. Stinson, W. Chang, M. R. Hee, T. Flotte, K. Gregory, and C. A. Puliafito, "Optical coherence tomography," *Science* 254, 1178-1181 (1991).
- [75] E. Sattler, R. Kästle, and J. Welzel, "Optical coherence tomography in dermatology," *J. Biomed. Opt.* 18, 061224 (2013).
- [76] A. Pagnoni, A. Knuettel, P. Welker, M. Rist, T. Stoudemayer, L. Kolbe, I. Sadiq, and A. Kligman, "Optical coherence tomography in dermatology," *Skin. Res. Technol.* 5, 83-87 (1999).
- [77] L. M. Sakata, J. DeLeon-Ortega, V. Sakata, and C. A. Girkin, "Optical coherence tomography of the retina and optic nerve—a review," *Clin. Experiment. Ophthalmol.* 37, 90-99 (2009).

- [78] S. Chua, "High-Definition Optical Coherence Tomography for the Study of Evolution of a Disease," *Dermatol. Bullet.* 26, 2-3 (2015).
- [79] V. R. Korde, G. T. Bonnema, W. Xu, C. Krishnamurthy, J. Ranger-Moore, K. Saboda, L. D. Slayton, S. J. Salasche, J. A. Warneke, and D. S. Alberts, "Using optical coherence tomography to evaluate skin sun damage and precancer," *Lasers Surg. Med.* 39, 687-695 (2007).
- [80] M. Mogensen, L. Thrane, T. M. Jørgensen, P. E. Andersen, and G. B. Jemec, "OCT imaging of skin cancer and other dermatological diseases," *J. Biophotonics* 2, 442-451 (2009).
- [81] O. Babalola, A. Mamalis, H. Lev-Tov, and J. Jagdeo, "Optical coherence tomography (OCT) of collagen in normal skin and skin fibrosis," *Ann. N.Y. Acad. Sci.* 306, 1-9 (2014).
- [82] S. Sakai, M. Yamanari, Y. Lim, N. Nakagawa, and Y. Yasuno, "In vivo evaluation of human skin anisotropy by polarization-sensitive optical coherence tomography," *Biomed. Opt. Express* 2, 2623-2631 (2011).
- [83] M. C. Pierce, J. Strasswimmer, B. H. Park, B. Cense, and J. F. de Boer, "Advances in optical coherence tomography imaging for dermatology," *J. Invest. Dermatol.* 123, 458-463 (2004).
- [84] Y. Zhao, Z. Chen, C. Saxer, S. Xiang, J. F. de Boer, and J. S. Nelson, "Phase-resolved optical coherence tomography and optical Doppler tomography for imaging blood flow in human skin with fast scanning speed and high velocity sensitivity," *Opt. Lett.* 25, 114-116 (2000).
- [85] J. Welzel, "Optical coherence tomography in dermatology: a review," *Skin. Res. Technol.* 7, 1-9 (2001).
- [86] T. Gambichler, A. Pljakic, and L. Schmitz, "Recent advances in clinical application of optical coherence tomography of human skin," *Clin. Cosmet. Investig. Dermatol.* 8, 345-354 (2015).
- [87] N. Greaves, B. Benatar, S. Whiteside, T. Alonso-Rasgado, M. Baguneid, and A. Bayat, "Optical coherence tomography: a reliable alternative to invasive histological assessment of acute wound healing in human skin?" *Br. J. Dermatol.* 170, 840-850 (2014).
- [88] K. Sahu, Y. Verma, M. Sharma, K. Rao, and P. Gupta, "Non-invasive assessment of healing of bacteria infected and uninfected wounds using optical coherence tomography," *Skin. Res. Technol.* 16, 428-437 (2010).
- [89] E. C. E. Sattler, K. Poloczek, R. Kästle, and J. Welzel, "Confocal laser scanning microscopy and optical coherence tomography for the evaluation of the kinetics and quantification of wound healing after fractional laser therapy," *J. Am. Acad. Dermatol.* 69, e165-e173 (2013).

- [90] M. J. Cobb, Y. Chen, R. A. Underwood, M. L. Usui, J. Olerud, and X. Li, "Noninvasive assessment of cutaneous wound healing using ultrahigh-resolution optical coherence tomography," *J. Biomed. Opt.* 11, 064002 (2006).
- [91] J. G. Fujimoto, C. Pitris, S. A. Boppart, and M. E. Brezinski, "Optical coherence tomography: an emerging technology for biomedical imaging and optical biopsy," *Neoplasia* 2, 9-25 (2000).
- [92] G. Zhang, D. J. Moore, C. R. Flach, and R. Mendelsohn, "Vibrational microscopy and imaging of skin: from single cells to intact tissue," *Anal. Bioanal. Chem.* 387, 1591-1599 (2007).
- [93] H. Lui, J. Zhao, D. McLean, and H. Zeng, "Real-time Raman spectroscopy for in vivo skin cancer diagnosis," *Cancer. Res.* 72, 2491-2500 (2012).
- [94] Y. Li, R. Chen, H. Zeng, Z. Huang, S. Feng, and S. Xie, "Raman spectroscopy of Chinese human skin in vivo," *Chin. Opt. Lett.* 5, 105-107 (2007).
- [95] P. Caspers, G. Lucassen, H. Bruining, and G. Puppels, "Automated depth-scanning confocal Raman microspectrometer for rapid in vivo determination of water concentration profiles in human skin," *J. Raman Spectro.* 31, 813-818 (2000).
- [96] H.-W. Wang, T. T. Le, and J.-X. Cheng, "Label-free imaging of arterial cells and extracellular matrix using a multimodal CARS microscope," *Opt. Commun.* 281, 1813-1822 (2008).
- [97] C. L. Evans, E. O. Potma, M. Puoris' haag, D. Côté, C. P. Lin, and X. S. Xie, "Chemical imaging of tissue in vivo with video-rate coherent anti-Stokes Raman scattering microscopy," *Proc. Natl. Acad. Sci. U. S. A.* 102, 16807-16812 (2005).
- [98] M. N. Slipchenko, T. T. Le, H. Chen, and J.-X. Cheng, "High-speed vibrational imaging and spectral analysis of lipid bodies by compound Raman microscopy," *J. Phys. Chem. B* 113, 7681-7686 (2009).
- [99] D. Haluszka, R. Szipocs, N. Wikonkal, and A. Kolonics, "Characterization of obesity in murine skin in vivo by CARS and SHG microscopy using a cost efficient, fiber laser based wavelength extension unit," in 6th EPS-QEOD Europhoton Conference. Neuchatel, Switzerland (2014).
- [100] P. D. Pudney, M. Mélot, P. J. Caspers, A. Van Der Pol, and G. J. Puppels, "An in vivo confocal Raman study of the delivery of trans retinol to the skin," *Appl. Spectrosc.* 61, 804-811 (2007).
- [101] M. Weinigel, H. Breunig, M. Kellner-Höfer, R. Bückle, M. Darwin, M. Klemp, J. Lademann, and K. König, "In vivo histology: optical biopsies with chemical contrast using clinical multiphoton/coherent anti-Stokes Raman scattering tomography," *Laser Phys. Lett.* 11, 055601 (2014).
- [102] S. Lange-Asschenfeldt, A. Bob, D. Terhorst, M. Ulrich, J. Fluhr, G. Mendez, H.-J. Roewert-Huber, E. Stockfleth, and B. Lange-Asschenfeldt, "Applicability of confocal

laser scanning microscopy for evaluation and monitoring of cutaneous wound healing," *J. Biomed. Opt.* 17, 076016 (2012).

- [103] M. Rajadhyaksha, M. Grossman, D. Esterowitz, R. H. Webb, and R. R. Anderson, "In vivo confocal scanning laser microscopy of human skin: melanin provides strong contrast," *J. Invest. Dermatol.* 104, 946-952 (1995).
- [104] M. Minsky, "Memoir on inventing the confocal scanning microscope," *Scanning* 10, 128-138 (1988).
- [105] T. Wilson, "The role of the pinhole in confocal imaging system," in *Handbook of Biological Confocal Microscopy*, Springer, New York, pp. 167-182 (1995).
- [106] F. Helmchen, and W. Denk, "Deep tissue two-photon microscopy," *Nat. Methods* 2, 932-940 (2005).
- [107] P. Calzavara-Pinton, C. Longo, M. Venturini, R. Sala, and G. Pellacani, "Reflectance confocal microscopy for in vivo skin imaging," *Photochem. Photobiol.* 84, 1421-1430 (2008).
- [108] J. Still, E. Law, K. Klavuhn, T. Island, and J. Holtz, "Diagnosis of burn depth using laser induced indocyanine green fluorescence: a preliminary clinical trial," *Burns* 27, 364-371 (2001).
- [109] M. E. Gschwandtner, E. Ambrózy, S. Marić, A. Willfort, B. Schneider, K. Böhler, U. Gaggli, and H. Ehringer, "Microcirculation is similar in ischemic and venous ulcers," *Microvasc. Res.* 62, 226-235 (2001).
- [110] V. Prabhu, S. B. Rao, E. M. Fernandes, A. C. Rao, K. Prasad, and K. K. Mahato, "Objective assessment of endogenous collagen in vivo during tissue repair by laser induced fluorescence," *PloS One* 9, e98609 (2014).
- [111] V. Prabhu, S. B. Rao, S. Chandra, P. Kumar, L. Rao, V. Guddattu, K. Satyamoorthy, and K. K. Mahato, "Spectroscopic and histological evaluation of wound healing progression following Low Level Laser Therapy (LLLT)," *J. Biophotonics* 5, 168 (2012).
- [112] S.-J. Lin, R.-J. Wu, H.-Y. Tan, W. Lo, W.-C. Lin, T.-H. Young, C.-J. Hsu, J.-S. Chen, S.-H. Jee, and C.-Y. Dong, "Evaluating cutaneous photoaging by use of multiphoton fluorescence and second-harmonic generation microscopy," *Opt. Lett.* 30, 2275-2277 (2005).
- [113] T. Luo, J. Chen, S. Zhuo, K. Lu, X. Jiang, and Q. Liu, "Visualization of collagen regeneration in mouse dorsal skin using second harmonic generation microscopy," *Laser Phys.* 19, 478-482 (2009).
- [114] E. Brown, T. McKee, A. Pluen, B. Seed, Y. Boucher, and R. K. Jain, "Dynamic imaging of collagen and its modulation in tumors in vivo using second-harmonic generation," *Nat. Med.* 9, 796-800 (2003).

- [115] A. Zoumi, A. Yeh, and B. J. Tromberg, "Imaging cells and extracellular matrix in vivo by using second-harmonic generation and two-photon excited fluorescence," *Proc. Natl. Acad. Sci. U. S. A.* 99, 11014-11019 (2002).
- [116] B. R. Masters, P. T. So, and E. Gratton, "Multiphoton excitation microscopy of in vivo human skin: functional and morphological optical biopsy based on three-dimensional imaging, lifetime measurements and fluorescence spectroscopy," *Ann. N.Y. Acad. Sci.* 838, 58-67 (1998).
- [117] B. Masters, P. So, and E. Gratton, "Optical biopsy of in vivo human skin: multi-photon excitation microscopy," *Lasers Med. Sci.* 13, 196-203 (1998).
- [118] J. A. Palero, H. S. De Bruijn, H. J. Sterenberg, and H. C. Gerritsen, "Spectrally resolved multiphoton imaging of in vivo and excised mouse skin tissues," *Biophys. J.* 93, 992-1007 (2007).
- [119] L. H. Laiho, S. Pelet, T. M. Hancewicz, P. D. Kaplan, and P. T. So, "Two-photon 3-D mapping of ex vivo human skin endogenous fluorescence species based on fluorescence emission spectra," *J. Biomed. Opt.* 10, 024016 (2005).
- [120] J. Paoli, M. Smedh, A.-M. Wennberg, and M. B. Ericson, "Multiphoton laser scanning microscopy on non-melanoma skin cancer: morphologic features for future noninvasive diagnostics," *J. Invest. Dermatol.* 128, 1248-1255 (2008).
- [121] W. R. Zipfel, R. M. Williams, and W. W. Webb, "Nonlinear magic: multiphoton microscopy in the biosciences," *Nat. Biotechnol.* 21, 1369-1377 (2003).
- [122] A. Gafni, and L. Brand, "Fluorescence decay studies of reduced nicotinamide adenine dinucleotide in solution and bound to liver alcohol dehydrogenase," *Biochemistry* 15, 3165-3171 (1976).
- [123] M. Wakita, G. Nishimura, and M. Tamura, "Some characteristics of the fluorescence lifetime of reduced pyridine nucleotides in isolated mitochondria, isolated hepatocytes, and perfused rat liver in situ," *J. Biochem.* 118, 1151-1160 (1995).
- [124] M. C. Skala, K. M. Riching, A. Gendron-Fitzpatrick, J. Eickhoff, K. W. Eliceiri, J. G. White, and N. Ramanujam, "In vivo multiphoton microscopy of NADH and FAD redox states, fluorescence lifetimes, and cellular morphology in precancerous epithelia," *Proc. Natl. Acad. Sci. U. S. A.* 104, 19494-19499 (2007).
- [125] J. Chen, C. Guo, F. Zhang, Y. Xu, X. Zhu, S. Xiong, and J. Chen, "In-vivo monitoring rat skin wound healing using nonlinear optical microscopy," *Proc. of SPIE BiOS (International Society for Optics and Photonics, 2014) San Francisco, California, United States*, 894820-894827.
- [126] R. Cicchi, S. Sestini, V. De Giorgi, D. Massi, T. Lotti, and F. Pavone, "Nonlinear laser imaging of skin lesions," *J. Biophotonics* 1, 62-73 (2008).

- [127] P. Stoller, K. M. Reiser, P. M. Celliers, and A. M. Rubenchik, "Polarization-modulated second harmonic generation in collagen," *Biophys. J.* 82, 3330-3342 (2002).
- [128] R. Cicchi, D. Kapsokalyvas, V. De Giorgi, V. Maio, A. Van Wiechen, D. Massi, T. Lotti, and F. S. Pavone, "Scoring of collagen organization in healthy and diseased human dermis by multiphoton microscopy," *J. Biophotonics* 3, 34-43 (2010).
- [129] T. Yasui, Y. Tohno, and T. Araki, "Characterization of collagen orientation in human dermis by two-dimensional second-harmonic-generation polarimetry," *J. Biomed. Opt.* 9, 259-264 (2004).
- [130] B. A. Torkian, A. T. Yeh, R. Engel, C.-H. Sun, B. J. Tromberg, and B. J. Wong, "Modeling aberrant wound healing using tissue-engineered skin constructs and multiphoton microscopy," *Arch. Dermatol.* 6, 180-187 (2004).
- [131] L. Cuttle, M. Nataatmadja, J. F. Fraser, M. Kempf, R. M. Kimble, and M. T. Hayes, "Collagen in the scarless fetal skin wound: detection with Picrosirius-polarization," *Wound. Repair. Regen.* 13, 198-204 (2005).
- [132] G. Deka, K. Okano, W.-W. Wu, and F.-J. Kao, "Multiphoton microscopy for skin wound healing study in terms of cellular metabolism and collagen regeneration," in *SPIE BiOS (International Society for Optics and Photonics, 2014)*, pp. 894820-894820-894827.
- [133] P. J. Campagnola, A. C. Millard, M. Terasaki, P. E. Hoppe, C. J. Malone, and W. A. Mohler, "Three-dimensional high-resolution second-harmonic generation imaging of endogenous structural proteins in biological tissues," *Biophys. J.* 82, 493-508 (2002).
- [134] S.-W. Chu, T.-Y. Su, R. Oketani, Y.-T. Huang, H.-Y. Wu, Y. Yonemaru, M. Yamanaka, H. Lee, G.-Y. Zhuo, and M.-Y. Lee, "Measurement of a saturated emission of optical radiation from gold nanoparticles: application to an ultrahigh resolution microscope," *Phys. Rev. Lett.* 112, 017402 (2014).

Automated Identification and Measurement of Haematopoietic Stem Cells in 3D Intravital Microscopy Data

Reema Adel Khorshed and Cristina Lo Celso

Additional information is available at the end of the chapter

<http://dx.doi.org/10.5772/64089>

Abstract

Image analysis and quantification of Haematopoietic stem cells (HSCs) position within their surrounding microenvironment in the bone marrow is a fast growing area of research, as it holds the key to understanding the dynamics of HSC-niche interactions and their multiple implications in normal tissue development and in response to various stress events. However, this area of research is very challenging due to the complex cellular structure of such images. Therefore, automated image analysis tools are required to simplify the biological interpretation of 3D HSC microenvironment images. In this chapter, we describe how 3D intravital microscopy data can be visualised and analysed using a computational method that allows the automated quantification of HSC position relative to surrounding niche components.

Keywords: intravital microscopy, 3D image analysis, bone marrow visualisation, haematopoietic stem cell niche, object segmentation and classification

1. Introduction

Somatic stem cells have the extraordinary ability to maintain their own pool, while replenishing dead cells and regenerating tissues after injuries throughout our lifetime. Dividing stem cells have the potential to differentiate into other cell types such as blood cells, skin cells or brain cells, or maintain themselves through a process called “self-renewal”. The stem cells that form blood and immune cells are called haematopoietic stem cells (HSCs). These stem cells are responsible for turnover and maintenance of red blood cells, platelets and immune cells. During

differentiation, HSCs generate multi-potent and lineage-committed progenitor cells prior to attaining maturity, which results in the generation of billions of new blood cells every day [1].

The bone marrow (BM) is the main site, where HSCs and their immediate progeny reside, precisely contained in a regulated and a very complex environment called the niche. The niche microenvironment has a direct impact on the function of HSCs, determined by the interaction of the HSCs themselves with particular cellular and molecular components in their surroundings [1, 2].

To observe and understand such interactions, single-cell resolution intravital microscopy of fluorescent HSCs and niche components is a vital tool, allowing the study of stem cells, their behaviour and interactions during steady state, aging and disease [3, 4]. This method has been successfully utilised to directly observe the HSCs with their niche in mouse bone marrow. Fluorescent dyes were used to label HSCs prior to transplantation into transgenic reporter mice that expressed GFP under the control of an osteoblast-specific promoter. Osteoblast cells reside on the bone marrow endosteal surface and contribute to the formation of bone [5]. This kind of fluorescent niche component served as a fundamental tool for the visualisation of the HSC endosteal niche and resulted in multiple observations indicating that functional HSCs localise near osteoblastic cells [5–7]. Intravital microscopy of HSCs injected into wild type and other bone marrow stroma/haematopoietic reporters indicated the importance of Galpha5 receptor subunit on homing HSCs [8], of interactions with nestin-positive mesenchymal stem and progenitor cells [9] and with regulatory T cells [10]. Time-lapse imaging has revealed that infection-exposed HSCs interact with larger endosteal niches [7, 11] and that aged HSCs interact with the bone marrow differently than young ones [12]. However, a clear understanding of how the coordinated action of multiple niche components regulates HSC fate is not clear, and considering the localization of HSCs relative to multiple surrounding cellular and structural constituents of the bone marrow microenvironment is the first step towards unravelling HSCs dynamics and signal exchanges.

Even though manual distance measurement of HSCs to other niche components is possible [1, 6, 13], it suffers from various limitations including the extensive time spent on conducting such manual analysis as well as intra- and inter-researcher inconsistencies and human error. Therefore, a specialised image analysis tool capable of completing such tasks will add the great benefits of producing consistent unbiased results, and will simplify the interpretation of the biological microenvironment events of the bone marrow niche.

During the last decade, several attempts have been made to develop image analysis approaches to automate the quantification of medical and biological images, from cell segmentation and detection to tumour diagnosis and classification [14–16]. However, the direct application of such methods to three-dimensional (3D) intravital microscopy images of the bone marrow is not possible. This is due to the complex structure of the tissue, decreased signal with increased depths, unpredictable scattering of both the excitation and emission photons and the irregular encasing bone structure, which restricts the resolution of intravital microscopy images when compared to *ex vivo* and soft tissue imaging.

Consequently, we developed an image analysis pipeline, to specifically tackle all the main challenges associated with intravital microscopy 3D images of bone marrow. The approach starts by detecting and segmenting HSCs and surrounding niche components, for instance, the bone and osteoblast. Then it classifies each segmented HSCs and assigns them into one of three classes, and finally it quantifies them based on their location to surrounding niche components. This analysis will allow the extraction of variable quantitative features, which could potentially reveal novel aspects of HSC biology, and especially their relation to the bone marrow microenvironment [11].

This chapter is organised as follows: first an introduction of the bone marrow and haematopoietic stem cells niche highlighting the importance of intravital microscopy and automated image analysis is provided (Section 2), followed by a detailed description of intravital microscopy of the bone marrow and the main challenges faced during the image analysis stage (Section 3). The automated image analysis tool is then described (Section 4), detailing how the three main segmentation parameters can be optimised for a particular cell or niche component (Section 5). Finally, a description of how a supervised machine learning classifier can be used to classify both HSCs and vasculature is presented (Section 6), followed by a brief description of how to obtain 3D positional measurements of HSCs to other niche components (Section 7).

2. Intravital microscopy of mouse bone marrow

In vivo imaging of stem cells is a growing field, providing unique insights of their behaviour and especially of their interaction with their surrounding microenvironment. This approach has been instrumental in producing new hypotheses and revealed a number of novel findings concerning the regulation of fate decision of multiple somatic stem cells [17, 18], including HSCs [1, 3, 4].

Nevertheless, how multiple niche components affect and regulate HSCs fate is still a significant question that scientists are attempting to answer. Recording the localization of HSCs relative to multiple surrounding cellular and structural constituents of the bone marrow microenvironment is the first step towards understanding such phenomena.

Confocal fluorescence and second harmonic generation microscopy of HSCs and their niche components in the mouse calvarium (top of the skull) bone marrow provides a powerful tool to observe cellular interactions and has been successfully used to detect and study fluorescently labelled HSCs and GFP expressing osteoblasts and other niche components in transgenic reporter mice [7, 11].

Confocal microscopy provides a better 3D optical resolution than epifluorescence microscopy because it restricts the light that reaches the photomultiplier through a pinhole. While in epifluorescence microscopy in-focus image objects are mixed with out-of-focus image information arising from regions outside the focal plane, in confocal microscopy the pinhole blocks out-of-focus signal. This technology has allowed major advances in the field of biological imaging, due to its cost-effective solution and ease of use. In addition, confocal microscopes

have improved sensitivity, resolution and intensity compared to epifluorescent microscopes. Confocal microscopy is also less phototoxic and can therefore be used to generate not only static but also dynamic data of living cells within their tissues, through time-lapse acquisition. All these qualities make confocal microscopes an ideal instrument for *in vivo* studies.

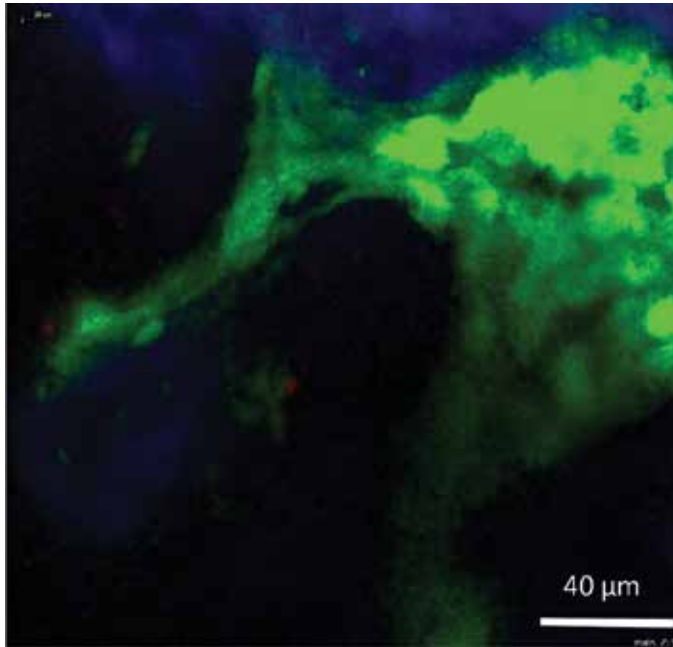


Figure 1. Maximum intensity projection of a 3D stack example of raw bone marrow *in vivo* images including DiD signal (red), GFP signal from osteoblastic cells (green) and bone collagen SHG signal (blue). Confocal microscopy was used to generate the signal for both DiD-labelled HSCs and osteoblasts using 633 and 488 nm lasers, respectively. Second harmonic generation (SHG) signal was obtained using 840-nm excitation of collagen to resolve bone structures.

Two-photon excitation of a fluorophore provides 3D optical sectioning similar to confocal imaging. However, it uses a wavelength roughly twice the length of the absorption peak of the specimen being imaged. In this chapter, we describe a particular application of two-photon excitation, named second harmonic generation (SHG). This takes advantage of a characteristic specific to certain molecules, such as collagen, which is the emission of photons at half of the wavelength of the exciting photons. Because collagen is one of the main components of bone, SHG signal allows detection of calvarium bone without the need to use specific transgenic fluorescent reporter mouse strains. An example of raw bone marrow *in vivo* images containing HSCs, osteoblast and SHG bone signal is presented in **Figure 1**. Two-photon excitation is also widely used to detect signal from multiple fluorophores, including GFP and tomato fluorescent protein [17], and signal obtained from two-photon excitation fluorescence microscopy can be analysed with the same computational algorithm we describe below.

3. Application and challenges of bone marrow intravital microscopy image analysis

The combination of confocal and SHG microscopy has greatly simplified high-resolution fluorescence imaging of animal tissues and organs. In Section 2, we have briefly described the advantages of the combination of confocal/SHG microscopy. Here, we describe the experimental set-up used and the challenges posed by the intravital images when they have to be further analysed. In the following sections, we describe in details how HSCs and bone marrow components can be automatically segmented, classified and measured.

To visualise HSCs, they were first labelled *ex vivo* using lipophilic membrane dyes such as 1,1'-Dioctadecyl-3,3,30,30-Tetramethylindodicarbocyanine (DiD) to generate a bright fluorescent signal [1, 5]. DiD-labelled HSCs were then injected into Col2.3GFP recipient mice, which allow the visualisation of osteoblasts as GFP-positive cells. Confocal microscopy was used to generate the signal for both DiD-labelled HSCs and osteoblasts using 633 and 488 nm lasers, respectively. Second harmonic generation (SHG) signal was obtained from 840-nm excitation of collagen to resolve bone structures. Acquisition setting (e.g. gain, laser powers, step and stack size) can vary between multiple users, leading to overall brighter/dimmer images and a range of field of view sizes and depths. Such variance imposes a challenge for automated image analysis. Therefore, developing an image analysis tool that can deal with the variability of setting preferences is a crucial point.

Another challenge imposed on image analysis from *in vivo* microscopy data is the decreased signal at increased depths. This results in non-uniform intensity and brightness of objects. In addition, light scattering caused by the surrounding tissue and bone restricts the resolution of *in vivo* microscopy of bone marrow compared to that of other soft tissues or *ex vivo* techniques.

To address these issues, we developed a local heterogeneity-based image segmentation (LHSEG) approach [11] that employs multi-resolution segmentation [19] and mean intensity difference to neighbour thresholding. The approach works by comparing local morphological and intensity characteristics of objects, which most often are smaller than the cells and structures recorded. These detected objects are then grouped based on their homogeneity with other neighbouring objects within a defined distance. Because the method is applied to each 2D slide, it ensures reliable edge detection and segmentation across cells and structures with high intensity heterogeneity, despite the decreased signal (intensity) at increasing depths.

DiD labelling produces a bright fluorescent signal of HSCs [1, 5]. However, this and other related dyes have a number of limitations when associated with intravital microscopy:

1. The dye often diffuses from the labelled cells into the surroundings, and is diluted upon cell division, resulting in a loss of brightness and intensity of signal.
2. Labelling HSCs does not always provide a homogenous staining, which can result in some HSCs being brighter than others.
3. The dye often leads to background noise as result of cell debris and aggregate signal.

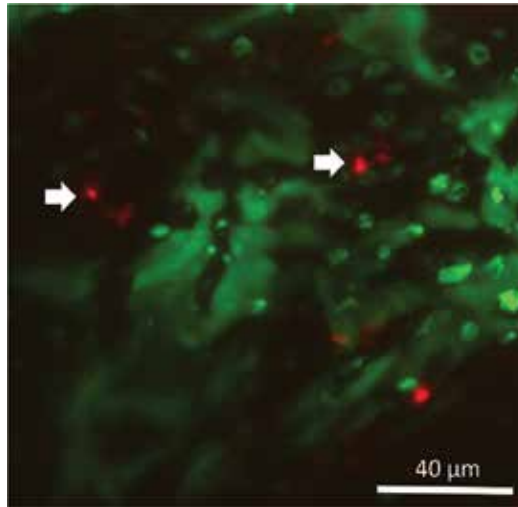


Figure 2. Maximum intensity projection of a 3D stack example representing the challenges for automated analysis of raw bone marrow *in vivo* images. DiD signal is in red. Arrows point at single DiD-labelled HSCs with varying intensity levels and sizes; the remaining red signal represents debris and background noise. Osteoblast cells (green) show non-uniform intensity levels too.

Figure 2 shows examples of the points listed above.

To overcome these issues, LH-SEG detects cells with variable intensities and signal brightness. Moreover, a machine learning classification protocol based on morphological and textural features recognises and classifies all segmented DiD signal, to differentiate real HSCs from cell debris and aggregate.

4. Image analysis

Image analysis is the process of extracting meaningful information from images, using manual or automated methods (the latter known as computer vision techniques) [20, 21]. The selection of the appropriate image analysis method for a certain type of images determines the success rate of the analysis. Therefore, understanding the challenges associated with the images acquired is the first step towards developing an effective image analysis solution.

Automated image analysis has a number of advantages over the human manual analysis. Human vision can easily be biased by pre-conceived concepts, affecting the output results and the rigorous testing of hypothesis. Manual analysis can also be time-consuming compared to automated analysis tasks, in which large datasets can be batch processed without the need of human monitoring, allowing users to perform other tasks while the analysis is being carried out.

Microscopy images are often complex, with a range of artefacts and background noise, which require variable image processing steps before any meaningful quantification can be extracted

from objects and region of interests. An overall image analysis protocol, including image processing, analysis and data output, needs to be designed and tailored according to the targeted image datasets. A general outline of the image analysis pipeline described in this chapter is provided in **Figure 3**.

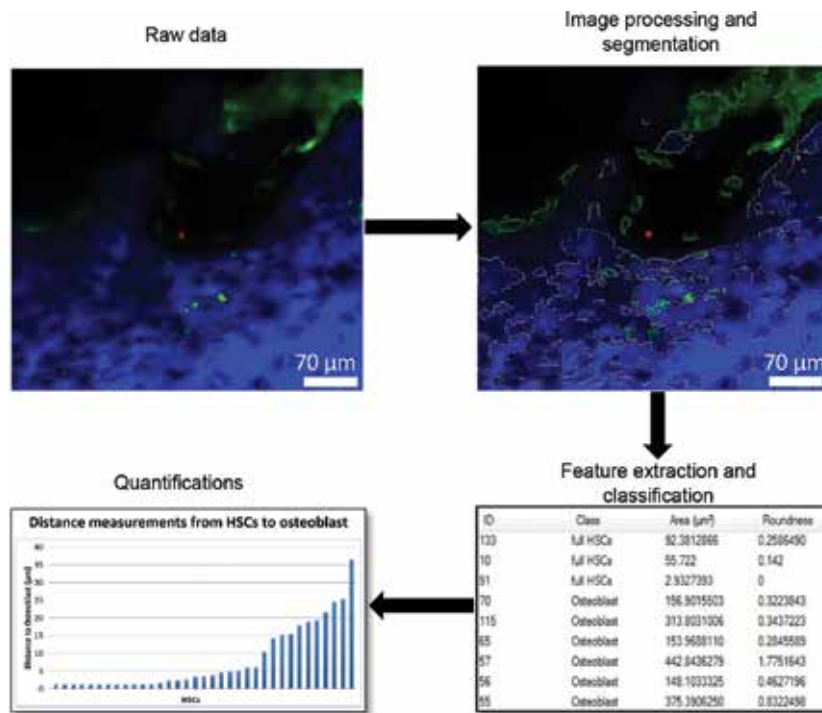


Figure 3. Outline of our image analysis protocol, starting from raw data and applying image processing and segmentation, feature extraction and classification, and finally distance measurements.

4.1. Image acquisition and processing

Image acquisition is the process of obtaining the raw image data using a microscope. Such data usually contain a number of imperfections, for example, due to oversaturation, out of focus signal and uneven excitation due to the irregular structure of the tissue itself.

To overcome these issues, filtering techniques are usually introduced to the image analysis as a pre-processing step. Smoothing and de-noising filters such as the median filter and Gaussian filter are applied to enhance image quality and reduces the noise introduced by the image acquisition process.

In the case of our *in vivo* bone marrow images, we applied Gaussian blur [22] to handle fluorescence intensity heterogeneity. The blur is typically used to smooth images detail and

reduce noise from uneven signal intensity. A small kernel size of (3×3) was used to reduce noise while avoiding over-smoothing of image objects.

4.2. Image segmentation

Object detection is a crucial step, as it determines the objects of interest in an image. This step ultimately governs the quality of quantifications extracted from each object. A very effective method of object detection is image segmentation. Segmentation is the process of dividing an image into smaller meaningful segments, by selecting a group of pixels to represent a region, or an object, contained within a border. Objects are segmented such that the pixels enclosed within one border share certain characteristics that define them as an object.

Successful segmentation is dependent on the method used, which critically needs to be tailored for each particular set of images. Images with a high level of contrast between objects of interests and background and with uniform intensities can be segmented using simple thresholding and edge detection approaches. More complex images with high intensity heterogeneity and intricate structures such as *in vivo* single cell resolution images require a more sophisticated segmentation approach.

The main challenges imposed upon segmentation of bone marrow *in vivo* images are the heterogeneity of fluorescent intensity as represented in GFP and DiD signal in **Figure 2**, the loss of signal with increasing depths and the unpredictable shape of stroma components. To overcome these issues, we have developed a two-step method of segmentation (LH-SEG). This method combines two powerful approaches: the multi-resolution segmentation and mean intensity difference to neighbourhood thresholding (MDN).

This segmentation approach was mainly developed to minimise artefacts due to loss of signal with increased depths. The first step of LH-SEG, multi-resolution segmentation, starts by dividing each 2D slice of the 3D stack into smaller segments grouped by their homogeneity in shape and texture. Homogeneity for each pixel is then calculated by selecting a scale parameter α . The parameter α is optimised for each object type (HSC, osteoblast and bone), taking into consideration their morphological and textural characteristics. Optimisation of this parameter for each object type is described in detail in Sections 4.3 and 5.

Adjacent homogeneous image segments are then merged based on their mean intensity difference to neighbourhood (MDN) threshold. MDN threshold calculates the difference between an image segment and its neighbouring image segments using the mean intensity values described in [11] as follows:

$$T_{\Delta k}^-(v) = \frac{1}{w} \sum_{u \in N_v(d)} w_u (\bar{c}_k(v) - \bar{c}_k(u)) \quad (1)$$

where w is the image channel weight. Images are weighted by the distance between the segmented image objects, defined as follows:

$$w = \sum_{u \in N_v(d)} w_u \quad (2)$$

where v and u are two segmented image objects, N_v is the direct neighbour to the segmented image object v . u is defined as a direct neighbour to v if the minimum distance between them is less than or equal to d . d is the distance between neighbouring segments and defined as the radius of the segmented image object perimeter in pixel. w_u is the weight of the segmented image object defined by the difference of the mean intensity value between v and u in a given distance d . \bar{c}_k is the mean intensity value of channel k . The appropriate MDN threshold for $T_{\bar{\Delta}_k}$ and distance featured d need to be selected for effective segmentation of each image object category (HSC, osteoblast and bone) (from [11]).

Figure 4 shows how, at the end of this process, segmented images on each z plane are then linked together to generate a 3D rendering of the whole stack.

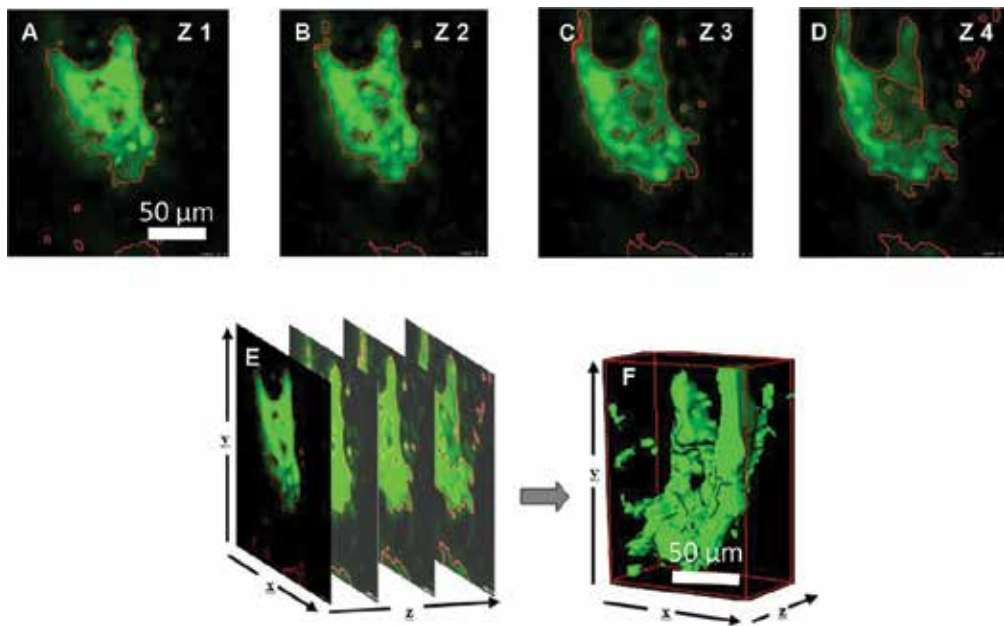


Figure 4. (A–D) segmented regions of osteoblast 2D slices using the LH_SEG method before they are merged (E) for the 3D rendering (F).

4.3. Parameter optimisation

Image segmentation is a fundamental step of image analysis, which ultimately determines the level of success of the overall quantification. Automated image analysis approaches can only perform sufficiently well when their parameters are optimally set for a certain type of images or dataset. In this section, we describe how the optimal settings can be selected for datasets containing intravital microscopy bone marrow 3D stacks. Three fundamental parameters are

targeted: (1) the multi-resolution segmentation scale parameter α ; (2) MDN threshold $T_{\bar{\Delta}_k}$; and (3) the MDN distance between neighbouring image segments d . The optimisation of parameters will be discussed in detail for each image object category (HSCs, osteoblast and bone) in Section 5.

The selection of the scale parameter α depends on the physical and textural structure of the objects. Different values of parameter α for the multi-resolution segmentation influence the output of the segmentation process. Selecting high scale parameters results in fewer, larger segments that can be bigger than the object observed, while lower scale parameter values result in smaller objects. To illustrate the consequences of using a range of parameter values for α on the resulting segmentation, we will present parameter values that would represent excessive cases of error when increasing or decreasing the scale parameter, as shown in **Figure 5**.

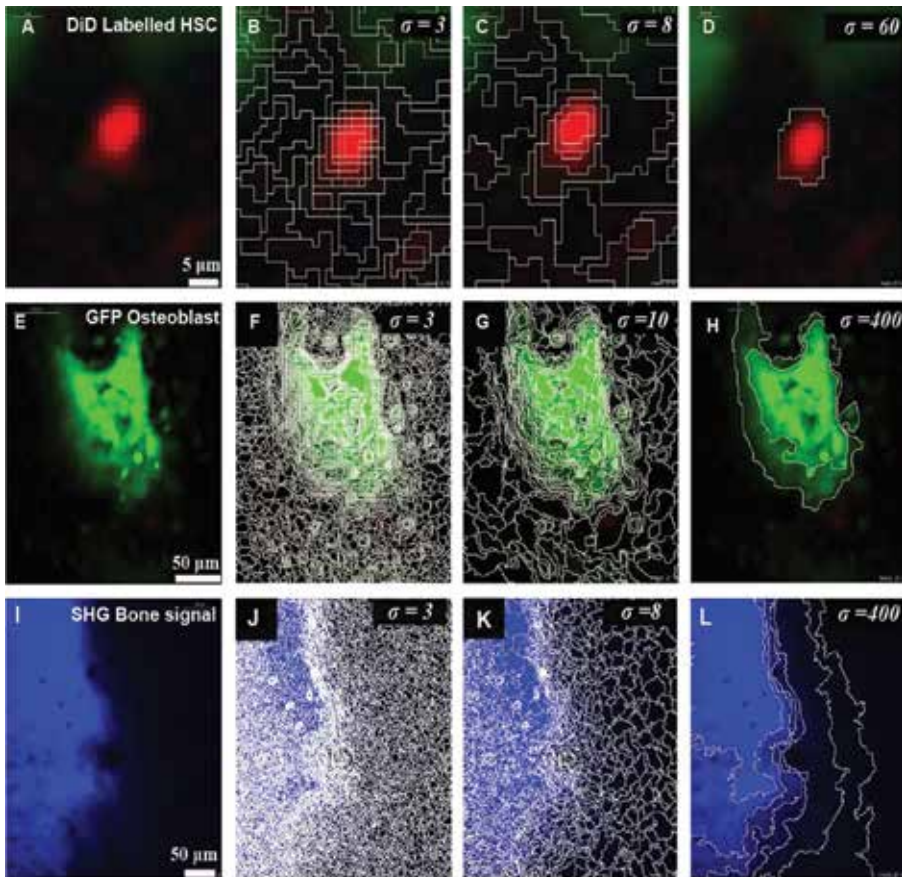


Figure 5. Optimisation of the multi-resolution segmentation parameter α for each image object category. Column (A–I) represent the data of each object category after smoothing with the convolution filter. Column (B–J) represent region segmentation error when decreasing the α parameter. Column (C–K) represent correct region segmentation with the optimal parameter α . Column (D–L) represent region segmentation error when increasing the α parameter.

MDN threshold has two parameters: MDN threshold value $T_{\bar{\Delta}_k}$ and the distance to neighbouring image segments d . Results of all three parameters optimisation for each component type (HSCs, osteoblast and bone), together with examples of the consequences of using excessively high or low parameter values, are described in Section 5 and presented in **Figures 6** and **7**.

5. Parameter optimisation

In this section, we present examples of the results obtained when different parameter values for α , $T_{\bar{\Delta}_k}$ and d are selected, to help the reader apply the same decision process to his/her own image dataset.

5.1. Multi-resolution parameter α

5.1.1. α for HSCs

Selecting a small value such as $\alpha = 3$ results in the region of the image corresponding to an HSC being divided in small segments (irregular boxes delimited by white lines, **Figure 5**) and increases the running time of the overall process. On the other hand, a scale parameter of $\alpha = 8$ leads to larger and fewer segments, covering the area occupied by the HSC and, once combined, describing its edges, therefore, serves as the optimal parameter for HSCs. Increasing the scale parameter α will result in even fewer, larger segments comprising areas of heterogeneous intensity and causing some background signal to be included in the HSC segment region (**Figure 5A–D**).

5.1.2. α for osteoblasts

Selecting a small value such as $\alpha = 3$ results in the osteoblastic cell region being divided in very small segments (irregular boxes delimited by white lines) and increases the running time of the overall process. A scale parameter of $\alpha = 10$ leads to fewer, larger segments, which cover the area occupied by the osteoblastic cells and combined describe their edges. Having fewer segments reduces the processing time. Therefore, $\alpha = 10$ serves as the optimal parameter for osteoblasts. Increasing the scale parameter α marginally did not have a major change in the segments produces, however, increasing the parameter extensively to e.g. $\alpha = 400$ results in larger segments comprising areas of heterogeneous intensity and causing some background signal to be included in the osteoblastic segment region (**Figure 5E–H**).

5.1.3. α for bone

Selecting a small value such as $\alpha = 3$ results in the bone region being divided into small segments (irregular boxes delimited by white lines) and increases the running time of the overall process. Similarly to osteoblasts, a scale parameter $\alpha = 8$ leads to fewer, larger segments covering the area occupied by the bone and bone cavities and, once combined, describing its edges. Again,

dealing with fewer segments reduces the processing time. Therefore, $\alpha = 8$ serves as the optimal parameter for bone. Increasing the scale parameter α marginally did not have a major impact on the segments produced, however, increasing the parameter extensively to e.g. $\alpha = 400$ results in larger segments comprising areas of heterogeneous intensity and causing some background signal to be included in the bone segment region **Figure 5I–L**.

5.2. MDN threshold value $T_{\bar{\Delta}_k}$

5.2.1. $T_{\bar{\Delta}_k}$ for HSCs

The optimisation of the MDN threshold value depends on the correct detection of HSC edges. To observe the effects of changing the MDN threshold on HSC segmentation, we set $\alpha = 8$ and $d = 30$, then change the parameter $T_{\bar{\Delta}_k}$. Selecting $T_{\bar{\Delta}_k} \geq 10$ resulted in some background signal being included in the HSC segment region, while $T_{\bar{\Delta}_k} \geq 68$ resulted in correct segmentation of the HSC region. On the other hand, selecting a threshold value of $T_{\bar{\Delta}_k} \geq 200$ resulted in restricting the selection of segments to only those which have $T_{\bar{\Delta}_k} \geq 200$ mean intensity difference value to their neighbouring segments and excluded HSC segments of lower intensity from the final HSC object. Hence selection of low threshold values for the MDN will result in increased segment region sizes, while selecting higher MDN threshold values will restrict the selection of segments to regions of smaller size (**Figure 6A–C**).

5.2.2. $T_{\bar{\Delta}_k}$ for osteoblasts

To observe the effects of changing the MDN threshold on osteoblastic cell segmentation, we set $\alpha = 8$ and $d = 30$, then change the MDN threshold parameter $T_{\bar{\Delta}_k}$. $T_{\bar{\Delta}_k} \geq 0$ resulted in some background signal being included in the osteoblastic cell segment regions, while $T_{\bar{\Delta}_k} \geq 8$ resulted in correct segmentation of the osteoblastic cell regions. $T_{\bar{\Delta}_k} \geq 100$ resulted in restricting the selection of segments to only those which have $T_{\bar{\Delta}_k} \geq 100$ mean intensity difference to their neighbouring segments and excluded osteoblast segments of lower intensity from the final osteoblastic cell objects. Hence selection of low threshold values for the MDN will result in increased segment regions, while selecting higher MDN threshold values will restrict the selection of segments (**Figure 6D–F**).

5.2.3. $T_{\bar{\Delta}_k}$ for bone

To observe the effects of changing the MDN threshold on bone segmentation, we set $\alpha = 8$ and $d = 70$, then change the MDN threshold parameter $T_{\bar{\Delta}_k}$, while $T_{\bar{\Delta}_k} \geq 0$ resulted in some background signal being included in the bone segment region. $T_{\bar{\Delta}_k} \geq 4$ resulted in correct segmentation of the bone region, $T_{\bar{\Delta}_k} \geq 80$ resulted in restricting the selection of segments to only those which have ≥ 80 mean intensity difference to their neighbouring segments and excluded bone segments of lower intensity from the final bone object. Hence selection of low

threshold values for the MDN will result in increased bone segment regions, while selecting higher MDN threshold values will restrict the selection of segments (**Figure 6G–I**).

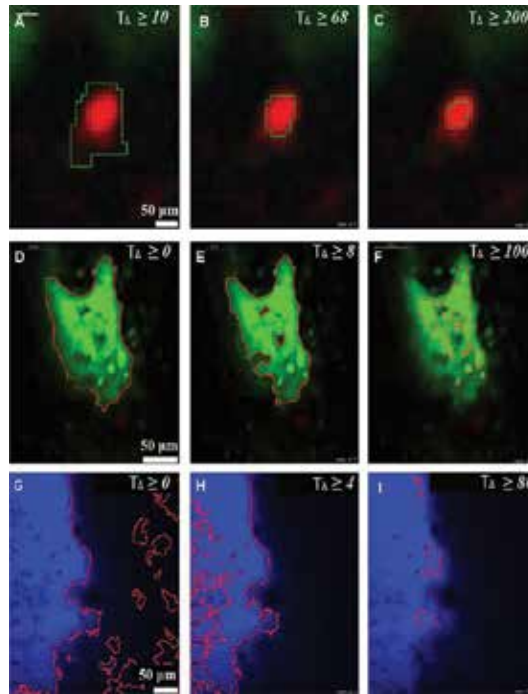


Figure 6. Optimisation of the MDN threshold parameter T_{Δ} for each image object category. Column (A–G) represent object segmentation error when decreasing the T_{Δ} parameter. Column (B–H) represent correct object segmentation with the optimal parameter T_{Δ} . Column (C–I) represent object segmentation error when increasing the T_{Δ} parameter.

5.3. Distance to neighbour d parameter

5.3.1. d for HSCs

To illustrate the process of selecting the optimal distance to neighbour d parameter, we use varying distance d between neighbouring segments as follows:

We set the optimal multi-resolution scale parameter $\alpha = 8$ and MDN $T_{\Delta_k} \geq 68$, then select the neighbourhood size. Small neighbourhood size such as $d = 2$ restricts the selection to fewer segments, specifically to those within a two pixels radius from the centre of the HSC region. As a result, the edges of the HSC are excluded from the final object. On the other hand, increasing the neighbouring distance to $d = 30$ resulted in correct selection of segments belonging to the HSC and elimination of segments containing background signal. Increasing the neighbouring distance further to about $d = 120$ resulted in some background signal being included in the final HSC region (**Figure 7A–C**).

5.3.2. d for osteoblasts

To show the effects of changing the neighbourhood size d on osteoblast segmentation, we use the optimal multi-resolution scale parameter $\alpha = 8$ and MDN threshold to $T_{\bar{\Delta}_k} \geq 8$, then select the neighbourhood size d . Selection of small neighbourhood size such as $d = 2$ restricted the selection of segments, resulting in fragmented segments scattered across the osteoblastic cell regions and failed to detect actual osteoblast regions. On the other hand, $d = 2$ resulted in correct selection of segments belonging to the osteoblasts and elimination of segments containing background signal. Increasing the neighbouring distance to $d = 120$ resulted in some background signal being included in the final osteoblast region (**Figure 7D–F**).

To demonstrate the effect of the selection of the value of parameter d on low intensity osteoblast regions, we selected images from lower slices of the same 3D stack of images (**Figure 7G–I**).

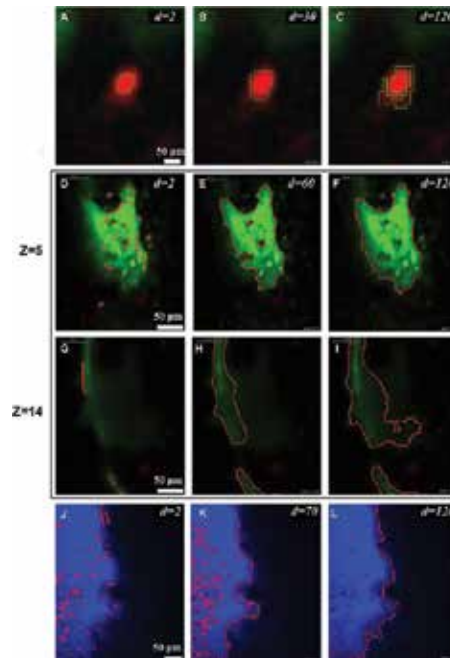


Figure 7. Optimisation of Distance to neighbour d parameter for each image object category. Column (A–J) represent object segmentation error when decreasing the d parameter. Column (B–K) represent correct object segmentation with the optimal parameter d . Column (C–L) represent object segmentation error when increasing the d parameter. Row (G–I) represent images from lower slices of the same 3D stack of images (D–F).

5.3.3. d for bone

To show the effect of changing the neighbourhood size d on bone segmentation, we use the optimal multi-resolution scale parameter $\alpha = 8$ and MDN threshold to $T_{\bar{\Delta}_k} \geq 4$, then select the neighbourhood size d . Selection of small neighbourhood size such as $d = 2$ restricted the

selection of segments, resulting in fragmented segments scattered across the bone regions and failed to detect actual bone regions. As a result, the edges of the bone are excluded from the final object. On the other hand, $d = 70$ resulted in correct selection of segments belonging to the bone and elimination of segments containing background signal. Increasing the distance to $d = 120$ resulted in some background signal being included in the final bone region and missing small detail of bone cavities (Figure 7J–L).

Note: Parameter selection can be further observed on the YZ and XZ dimensions to ensure accurate selection of the optimal parameters (Figure 8). To optimise the parameters for further niche components and cell types (e.g. vasculature), the same steps can be followed as described for the HSCs, osteoblasts and bone.

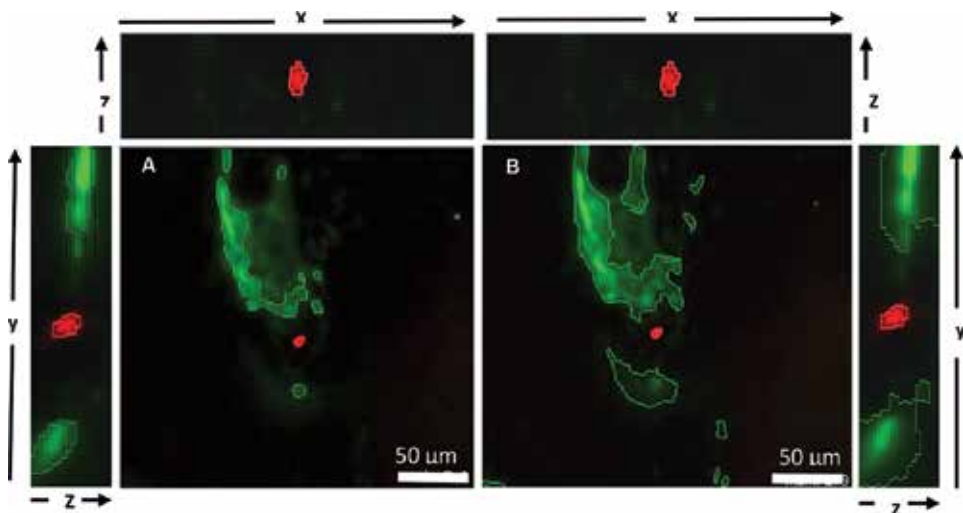


Figure 8. Examples of different dimensions view to observe the segmentation results following selecting different parameter values for α , $T_{\bar{\Delta}_k}$ and d .

6. Machine learning

Machine learning (ML) has become a valuable artificial intelligence tool, increasingly used for analysis of complex image data [23, 24]. ML serves two main objectives: classification and regression. Classification approaches are performed when a computer is given a set of options and is expected to divide them into a subset of categories. Regression is the process of selecting the appropriate response to a particular situation from a set of possible responses. Furthermore, ML classifiers can be categorised into two main models: supervised and unsupervised classifiers. Unsupervised approaches utilise a clustering technique, where ML looks for resemblances across data, and then splits the same data into clusters. Clusters are then used to define the classes. Conversely, supervised approaches require a training set, where the ML

learns information by extracting a set of features from that particular set, and the ML classifier is then expected to classify a new set of data and categorise it into a k number of classes based on the discriminative features extracted from the training set. Supervised classifiers are capable of identifying a set of complex features, suitable for classifying heterogeneous imaging data such as HSCs and vasculature from *in vivo* bone marrow 3D images, and then use them to perform such classification.

6.1. Decision tree classifier

The decision tree (DT) classifier is a structured approach that builds classification models from an input dataset to predict the output of an unknown dataset. The DT classifier starts the classification procedure structurally from the top node and uses the feature vectors to split it into further nodes [25, 26]. The selection of the feature vectors is measured by the purity of a particular subset, such that if a pure subset is produced, the splitting stops, otherwise splitting continues until a pure subset is allocated. Impurity of a specific subset is calculated by the entropy and is defined in [27] as follows:

$$E(S) = -\sum_{c \in C} p(c) \log_2 p(c) \quad (3)$$

where S is the dataset for which the entropy is calculated, c the set of classes in set S , $p(c)$ the proportion of the number of elements belonging to class c to the number of elements in set S . Pure subsets will generate a value of 0, while impure subsets will generate a value of 1.

$$I(S, F) = \sum_i \frac{|S_i|}{|S|} E(S_i) \quad (4)$$

where F is a feature. When a feature F splits the set S into subsets S_i , the average entropy is computed and the sum compared to the entropy of the original set S ; from [28].

$$Gain(S, F) = E(S) - I(S, F) = E(S) - \sum_i \frac{|S_i|}{|S|} E(S_i) \quad (5)$$

In this chapter, we describe the application of the DT classifier for classifying DiD signal (potential HSCs) and vasculature structures. The DT classifier was selected in this study due to its computational simplicity and illustrative attributes represented in the DT output. The classifier also has the advantage of being able to select discriminative features without a prior step of feature optimisation, allowing the incorporation of a wide range of features for testing at the training stage.

6.2. Training and testing the classifier

6.2.1. HSCs

LH-SEG provides a sufficient level of DiD objects detection. However, not all the DiD objects are HSCs. This is due to cell debris and the diffusion of the dye, which could lead to aggregates producing signal similar in shape and intensity to that of the HSCs.

In order to identify HSCs, we propose the use of DT classifier. We first trained our classifier to distinguish three classes of DiD objects: Class-1 represents HSCs distinguished by their smoother, round surface and high intensity as observed for quiescent HSCs; Class-2 comprises HSCs that have less rounded shapes and present small uropod-like protrusions [27], as previously observed in time-lapse images of migratory HSCs [7]; and Class-3 contains DiD objects that are not HSCs and characterised by their exceedingly uneven morphology. A selection of objects was manually selected for each category and fed into the classifier as training set. The exact number of objects needed for training each class depends on the variability of the structures contained, such that objects with regular, predictable characteristics such as Class-1 HSCs would require fewer objects for training, while irregular objects containing high variability such as class-3 would require a higher number of objects for training to ensure the classifier collects sufficient numbers of characteristics to handle the complexity and inconsistency of objects. After training, the classifier is tested on different datasets from those used for training with a 3-fold cross-validation approach. Classification results provided a high accuracy for all classes and successfully classified the DiD object to the three proposed classes as described in [11] and **Figure 9A and B**.

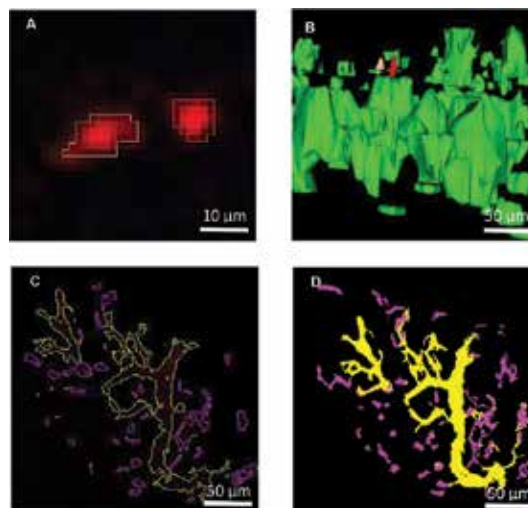


Figure 9. (A) Classification results of DiD objects using our proposed approach: two DiD-labelled HSCs were classified as HSC class 1 (red) and 2 (moccasin). (B) 3D rendering of DiD HSCs represented in (A) inside their microenvironment. (C) Classification results of vasculature using our proposed approach, showing small sinusoids (magenta) and large sinusoids (yellow). (D) 3D rendering of the 3D stack containing the slice shown in (C).

6.2.2. Vasculature

Blood vessels inside the bone marrow are another component that plays a vital role in the maintenance of HSCs. Interactions between vasculature and HSCs have become one of the main headlines for many recent studies [29, 30]. As demonstrated in our previous study, segmentation of vasculature of *in vivo* images was possible using the LH-SEG [11]. However, the automated identification of the variable components of the BM vascular network is a challenging task due to the complex and interlinked structure of blood vessels. Therefore, the selection of effective thresholds for classifying the vasculature into different regions based on their appearance and morphology is a challenging task. To overcome these issues, we propose a DT Classifier to define distinct features of the different types of vasculature and classify them into four categories based on their morphological and topological characteristics inside the BM space [28]. Blood vessels share mutual features in relation of their complexity and interlinking physical structure. Consequently, we manually select different 2D segmented from the vasculature region to create the training sets for four classes of blood vessels: (1) large sinusoids: larger blood vessels in comparison to other sinusoids and positioned mostly towards the periphery of the BM space; (2) small sinusoids: blood vessels smaller in section when compared to the large sinusoids, spread across bone marrow space; (3) the central sinus: a large venous vessel situated in the centre of the bone marrow space; and (4) the bifurcation of the central sinus, which results from the central sinus branching out towards either sides of the BM space in its frontal area. The number of samples was optimised for each class to avoid under-fitting and over-fitting the classifier. Three-fold cross validation was used in this experiment. Morphological and topological features were fed to the classifier for extraction of discriminative values. Classification results provided a high accuracy for all classes and successfully classified all vessels into one of the four classes as described in [23] and presented in **Figure 9C** and **D**. This demonstrates the applicability of ML classification approaches to 3D *in vivo* images of the bone marrow, which escalates the throughput of intravital imaging and our understanding of the complexity of the HSC and their interaction with multiple niche components.

7. 3D positional measurements

Following segmentation and classification of DiD-labelled HSCs, HSCs position relative to their nearest osteoblast and bone is measured as described in [11], and could be measured to their nearest vessel or other segmented bone marrow components. The overall automated distance measurements from HSCs to osteoblast and bone were equivalent to previously published data obtained using manual distance measurements and described in [5, 6]. Further quantitative measures such as the morphological and textural characteristics of each segmented and classified object can also be obtained using this tool.